Radiation Asymmetry and MHD Activity in Rapid Shutdowns on Alcator C-Mod

by

Geoffrey Michael Olynyk

B.Sc. (Eng.), Queen's University, Kingston, Canada (2007)

Submitted to the Department of Nuclear Science and Engineering
in partial fulfillment of the requirements for the degree of

Doctor of Philosophy in Applied Plasma Physics and Fusion Energy

at the

MASSACHUSETTS INSTITUTE OF TECHNOLOGY

September 2013

Author .....
Department of Nuclear Science and Engineering
Friday, August 9, 2013

Certified by .....
Dennis G. Whyte
Professor, Department of Nuclear Science and Engineering
Thesis Supervisor

Certified by .....
Robert S. Granetz
Principal Research Scientist, Alcator Project
Thesis Reader

Accepted by .....
Mujid S. Kazimi
TEPCO Professor of Nuclear Engineering
Chair, Department Committee on Graduate Students

Radiation Asymmetry and MHD Activity in Rapid Shutdowns on Alcator C-Mod

by

Geoffrey Michael Olynyk

Submitted to the Department of Nuclear Science and Engineering
on Friday, August 9, 2013, in partial fulfillment of the
requirements for the degree of
Doctor of Philosophy in Applied Plasma Physics and Fusion Energy

Abstract

Disruptions, the sudden termination of tokamak fusion plasmas by instabilities, have the potential to cause severe material wall damage to large tokamaks like ITER. The mitigation of disruption damage is an essential part of any fusion reactor system. Massive gas injection (MGI) rapid shutdown is a technique in which large amounts of noble gas are injected into the plasma in order to safely radiate the plasma energy evenly over the entire plasma-facing first wall. However, it has been observed that this energy is not radiated evenly: it can have significant asymmetries, which could cause melting in large devices even in the case of a successful rapid shutdown. The first rapid shutdown experiments using multiple gas injectors on any tokamak were conducted on Alcator C-Mod. A dedicated toroidal array of fast ultraviolet photodiodes was installed in order to diagnose toroidal radiation asymmetries during the thermal quench (TQ). It is found that the radiation asymmetry is controlled by a low-n brightness mode in the TQ phase of rapid shutdowns. This mode sometimes rotates, and the rate of rotation sets the integrated radiation asymmetry in the TQ. It is proposed that this brightness feature is caused by the transport of energy from the hot plasma core to the radiative edge by the MHD flow at one phase of an $n = 1$ global MHD mode. This phenomenology is confirmed by extended MHD simulation using the NIMROD code. An exponentially growing $n = 1$ magnetic mode is observed during the pre-TQ phase of MGI rapid shutdowns; the saturation of this mode marks the beginning of the thermal quench. It is proposed that this mode is a magnetic island caused by a radiative tearing mode; the predicted growth rate is compared to the predictions of analytic theory. This magnetic island then couples to other global $n = 1$ MHD modes, causing the energy transport during the TQ. An important implication of this result is that simply adding more gas injectors cannot guarantee a symmetric rapid shutdown: the asymmetry is controlled by the behavior of the core MHD activity during the TQ. The implications of this rotating radiation asymmetry during the TQ of MGI rapid shutdown for the beryllium wall of ITER are discussed.

Thesis Supervisor: Dennis G. Whyte
Title: Professor, Department of Nuclear Science and Engineering

Thesis Reader: Robert S. Granetz
Title: Principal Research Scientist, Alcator Project

Explanations exist: they have existed for all times, for there is always an easy solution to every problem – neat, plausible and wrong.

— H.L. Mencken, "The Divine Afflatus", in the *New York Evening Mail*, November 16, 1917

Il semble que la perfection soit atteinte non quand il n'y a plus rien à ajouter, mais quand il n'y a plus rien à retrancher.

— Antoine de Saint-Exupéry, *L'Avion*

Real power is limited to those who have facts.

— Joe Clark, Prime Minister of Canada, 1979–1980

Science is but a perversion of itself unless it has as its ultimate goal the betterment of humanity.

— attributed to Nikola Tesla, 1919

First, there is a mountain, then there is no mountain, then there is.

— Traditional Buddhist saying, via Donovan (1967)

Acknowledgments

The person to whom I owe the most for helping me through this process is my wife. Jackie, you are a constant source of encouragement, strength, and good advice. I love you more than I am capable of expressing.

I would like to thank my supervisors, Dennis Whyte and Bob Granetz. Your expertise, wisdom, and supportiveness were more than any graduate student could hope for. I have learned a great deal from each of you.

I am indebted to the skilled engineers, electricians, technicians, machinists, and other technical staff at the Plasma Science and Fusion Center. I would particularly like to thank Ron Rosati, Tom Toland, Bill Parkin, Dan Coronado, Rui Vieira, Charlie Cauley, Bill Forbes, Willy Burke, Jim Zachs, and Ned Mucic.

There are several other plasma physicists to whom I owe my gratitude. I would like in particular to thank Matt Reinke who, in addition to originally suggesting the topic for this thesis, spent a lot of time helping me with photodiodes, data acquisition, and IDL code. I would like to thank Val Izzo for many hours of help with the NIMROD code, and Jacob King and Scott Kruger at Tech-X for their aid in getting it compiled and working on the Loki compute cluster. Acknowledgement is also given to Luis Delgado-Aparicio for valuable discussions regarding radiative tearing modes.

To the administrators at the PSFC, in the Alcator C-Mod project, and in the NSE Department: Jessica Coco, Valerie Censabella, Heather Barry, Clare Egan, and Alisa Cabral, thank you for your patience and your assistance with the bureaucracy.

To my office-mates, Bob Mumgaard, Dan Brunner, and Mike Garrett: I think we had the best office relationship of any set of co-workers in history. I'm hono(u)red to have you all as friends. It will be interesting to meet up in ten years and see where we all are. And to all the other graduate students that I have been lucky enough to work with on Alcator C-Mod and elsewhere at the PSFC: thank you for being fantastic colleagues and fostering such a rich intellectual environment.

Finally, to my parents, Peter and Susan Olynyk, thank you for encouraging my interest in science and engineering through my entire childhood, and for supporting and helping Jackie and me in so many ways as we navigated the stressful world of living abroad. When Ernest Rutherford was awarded his baronetcy in England, he cabled his mother in New Zealand: "Now Lord Rutherford, more your honour than mine." My sentiment is the same.

This work was financially supported by the United States Department of Energy under Contract N$^{\underline{o}}$ DE-FC02-99ER54512 and by the Natural Sciences and Engineering Research Council of Canada (NSERC) PGS D program.

— Geoff Olynyk, August 1, 2013.

Author biography and contact information

Geoffrey M. Olynyk was born April 6, 1984 in Burlington, Ontario, Canada. He lived in Burlington for his entire childhood, attending Fairfield Public School from kindergarten to grade 4, John T. Tuck Public School from grades 5–8, and Aldershot High School (now Aldershot School) for grades 9–12 and OAC, graduating with a high school diploma (OS:IS) in 2003. (The Ontario Academic Credit was "grade 13" in that province; it was phased out in 2003.)

Geoff then attended Queen's University in Kingston, Ontario from 2003–2007, where he earned a Bachelor's of Science in Engineering (B.Sc. (Eng.)) degree, with a concentration in Engineering Physics. The Eng Phys program requires students to choose a concentration in a particular discipline of engineering (mechanical, electrical, etc.) – Geoff's concentration was Mechanical Engineering.

While at Queen's, he held summer jobs at Walters Inc., a steel design, fabrication, and construction company in Hamilton, Ontario, Primary Fluid Systems Inc., a maker of valves and other flow control equipment in Burlington, Ontario, and between his 3rd and 4th year of school, was a summer research assistant at the Royal Military College (RMC) in Kingston, Ontario. While at RMC, Geoff worked on two topics related to hydrogen fuel cells for military applications. It was after this, in his fourth year of studies at Queen's, that Geoff "caught the fusion bug". The proximate cause was a lecture given by Dr. Amanda Hubbard, a graduate of Queen's Engineering, and a Principal Research Scientist on the Alcator C-Mod project at the MIT Plasma Science and Fusion Center.

After graduation, Geoff worked for a year as a junior engineer at Hatch, Inc., a large engineering consulting company in Mississauga, Ontario. In 2008, he left Hatch and entered the Ph.D. program in the Department of Nuclear Science and Engineering at MIT, where he has been ever since. Geoff's permanent email address is geoff (at) olynyk.name.

Note on typesetting

The body of this thesis is set in the Minion typeface, designed in 1990 by Robert Slimbach for Adobe. The captions of figures and tables are set in the sans-serif Myriad, designed by Robert Slimbach and Carol Twombly, with lining figures. Mathematical symbols are from the MnSymbol LaTeXpackage. Email the author if you would like a copy of the source code.

Contents

List of Figures

List of Tables

Introduction: Fusion energy

At the heavy end of the atomic mass spectrum are the well-known fissionable elements: thorium, uranium, plutonium. Nuclear fission energy produces almost 6% of the world's energy today (13% of the electricity) and because of its low carbon footprint, is expected to remain an important part of the world energy mix throughout the 21st century.

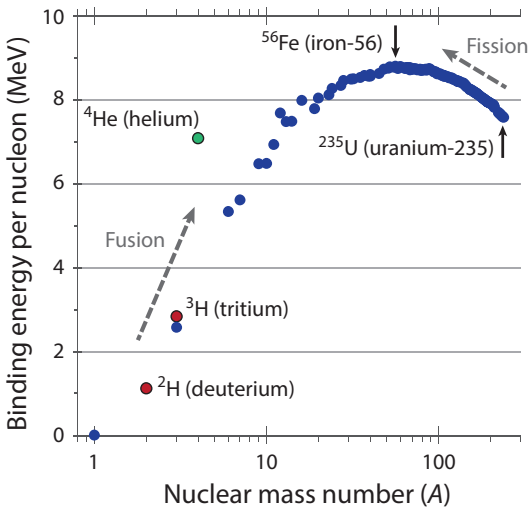

Figure i – Binding energy per nucleon vs. mass number for all naturally-occurring isotopes. Fusion-relevant isotopes are highlighted. Note logarithmic scale on the abscissa.

At the opposite end of the atomic mass spectrum are the very light elements: hydrogen, helium, lithium, and beryllium. These can also produce nuclear energy, but with the opposite process to uranium and plutonium: *fusion*, the joining together of light nuclei to produce heavier ones, with a portion of the mass being converted to kinetic energy. In Figure i, the atomic binding energy per nucleon is shown versus the atomic mass number A. The elements which can undergo fusion are at the far left.

The most promising reaction for terrestrial fusion energy fuses heavy isotopes of hydrogen, and is known as the deuterium–tritium (or D–T) fusion reaction:

$$ {}^{2}_{1}\mathrm{D} + {}^{3}_{1}\mathrm{T} \rightarrow {}^{4}_{2}\mathrm{He}\ (3.5\ \mathrm{MeV}) + {}^{1}_{0}\mathrm{n}\ (14.1\ \mathrm{MeV}) \qquad (1) $$

That is, deuterium combines with tritium to produce helium (an α particle), and a neutron, which carries most of the energy. This D–T reaction is the one being most actively pursued by the world fusion energy research program today. A discussion of the physics of the fusion reaction is not appropriate to include here; the reader is referred to the excellent book by Freidberg [2] for the details. In the remainder of this introduction, the future of humanity's energy use, and the prospects for fusion energy, are discussed.

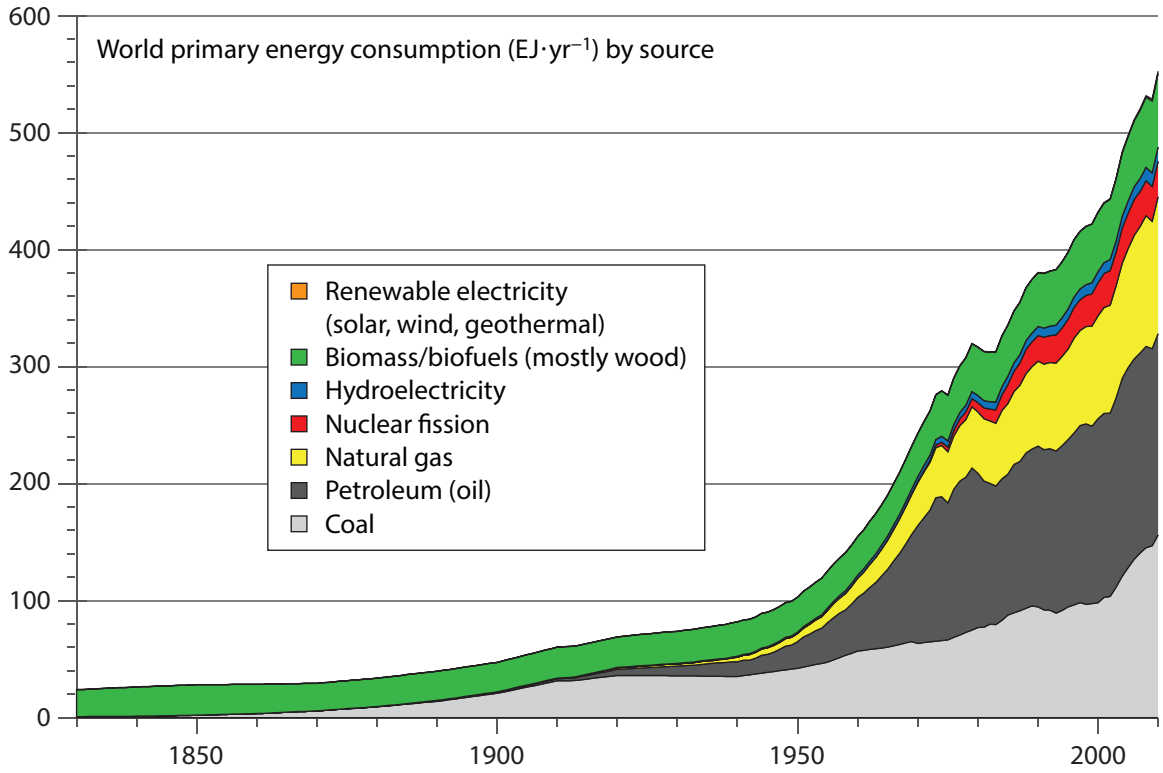

Figure ii – World primary energy use by source, 1830–2010. Data obtained from U.S. EIA [1]

Humanity's energy use

A history of the total primary energy consumption by humankind is shown in Figure ii. While growth in energy departed from an exponential curve after the oil shocks of the 1970s, it still continues to grow linearly at a high rate. It is expected that this growth in consumption will continue into the future: if it does not, severe economic dislocation could result.

Examining Figure iii, the "ascent of the rest of the world" over the past three decades can be seen. Energy consumption in North America and Europe is hardly changed from its value in 1980, and it actually *fell* in Eurasia after the collapse of the Soviet Union. But energy use has skyrocketed in Central and South America, the Middle East, Africa, and above all, Asia, dominated by the meteoric economic growth in China since the mid-1990s.

The path to fusion energy and the goal of this work

The tokamak is considered the world's leading candidate to become a fusion reactor [2, p. 308]. The tokamak is a magnetic-confinement device, which means it uses strong mag-

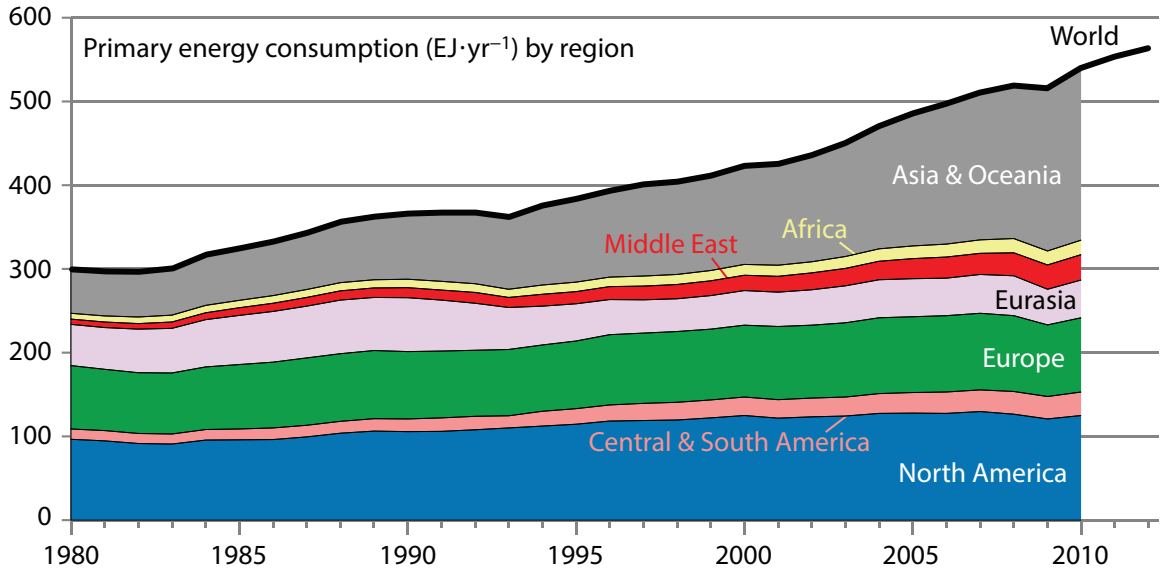

Figure iii – World primary energy use by region of the world, 1980–2010. Data obtained from U.S. EIA [1].

netic fields to *confine*, or hold in, a plasma.[1] Today, magnetic-confinement fusion is being actively pursued in most major industrialized countries.

The centerpiece of the world's research program is the ITER fusion reactor [3], currently under construction near the Cadarache nuclear research facility in the region of Provence–Alpes–Côte d'Azur in the south of France. ITER is expected to reach its first plasma in the early 2020s, and to achieve its goal of 500 MW of fusion energy late in that decade. After that, a demonstration fusion reactor which actually puts electricity onto the public grid, will be designed.[2]

However, the path to fusion energy is not a clear one. Several enormous scientific and engineering challenges stand in the path of achieving a reliable, economical tokamak fusion reactor. One of the largest of these challenges is the problem of dealing with off-normal and transient events [4]. Power plants work best when they are boring: operating at steady state for years at a time, putting inexpensive watts onto the grid. Today, tokamaks are plagued with instabilities known as *disruptions* which terminate the plasma discharge, and would be unacceptable in a fusion power reactor.

In this thesis, the problem of disruptions in tokamaks, and the proposed system by which these disruptions are ameliorated, are discussed. Then, an open question about these *disruption mitigation* systems is presented: the problem of radiation asymmetry in the thermal

[1] This is possible because at the temperatures required for the D–T fusion reaction, the electrons and ions of the deuterium and tritium, as well as all but very high-Z impurities, are fully stripped, and the electrically charged particles undergo spiral motion around the field lines.

[2] Such a facility is usually referred to as DEMO; this is not an initalism but rather is simply short for "demonstration fusion reactor".

quench. The remainder of the thesis discusses research that was conducted on the Alcator C-Mod tokamak at MIT to address this problem. Finally, the implications of the work for future reactors and for ITER are discussed.

References

[1] U.S. Energy Information Administration, "Total energy." Statistics on world primary energy consumption by country, region, and source (type of primary energy) obtained from EIA website at http://www.eia.gov/totalenergy/

[2] Freidberg, J. *Plasma Physics and Fusion Energy*. Cambridge University Press, 2007. ISBN 978-0521-85107-7.

[3] See ITER website, http://www.iter.org/

[4] "Research Needs for Magnetic Fusion Energy Sciences: Final Report of the Research Needs Workshop (ReNeW), Bethesda, Maryland, June 8–12, 2009." Weiser, P. (Ed.) Available online at http://burningplasma.org/renew.html. See Thrust 2 ("Control transient events in burning plasmas"), p. 243.

Chapter 1

Tokamaks and disruptions

A characteristic of tokamaks since the earliest experiments with these devices has been the sudden loss of confinement and subsequent termination of the plasma discharge [1]. This phenomenon was originally known as a "major disruption" to distinguish it from "minor" disruptions from which the plasma subsequently recovers. Today, these events are more commonly referred to simply as "disruptions". In this chapter, the various causes of disruptions, and their effects, are briefly described. Chapter 2 will then discuss the proposed schemes for mitigating these effects. The content in this chapter is not intended to be a comprehensive survey of the theory of plasma instabilities, but rather to give an operational overview of the causes of major disruptions in tokamaks. For a detailed discussion of the theory of magnetohydrodynamic (MHD) instabilities, refer to Chapter 12 of Freidberg [2].

1.1 Classes of disruptions

Originally, the sudden termination of the plasma current in a tokamak discharge was referred to as a "major disruption" or "the disruptive instability". Today, it is understood that disruptions have *many* causes [3]. In general, disruptions may be grouped into three "operational" classes: those caused by magnetohydrodynamic (MHD) instabilities,[1] those caused by impurity radiation, and those caused by a malfunction or failure of the control system or power supplies. The severity of each of these classes of disruptions, and the ability of systems to detect (and thus mitigate – the subject of Chapter 2) each specific type of disruption, are discussed in the following subsections.

1.1.1 Kink limit

The external kink limit was one of the earliest identified ideal MHD stability limits for toroidal confinement devices. It sets a limit on the amount of toroidal plasma current (and

[1] Within this category, the instabilities may be further classified as *pressure-driven* modes, which set limits on the plasma pressure, or *current-driven* modes, which set limits on the plasma current, and which can exist even in the limit of zero plasma pressure.

thus poloidal field strength) that can be carried by the plasma for a given strength of toroidal field. The limit is given for plasmas in the limited magnetic configuration (no poloidal X-point) by $q_{\text{edge}} > 2$, where q_{edge} is the magnetic safety factor at the plasma boundary. This quantity is equal to the number of toroidal transits that a field line on the last closed flux surface makes for every one poloidal transit. For plasmas without strong shaping (triangularity), and at high aspect ratio $A \equiv R/a$, where R and a are the plasma major and minor radius, respectively, the edge magnetic safety factor is approximated by the cylindrical safety factor q^*:

$$q \simeq q^* \equiv \frac{2\pi a^2 B_\phi}{\mu_0 R I_\text{p}} \left(\frac{1+\kappa^2}{2} \right) \tag{1.1}$$

where B_ϕ is the on-axis toroidal field strength [T], I_p is the plasma current [A], and the factor in round brackets is the correction for plasma elongation κ, the height-to-width ratio of the poloidal cross section.

For diverted plasmas, the edge safety factor is by definition infinity, since the field lines on the last closed flux surface become tangent to the poloidal null at the X-point. The safety factor is thus measured at the 95$^{\text{th}}$-percentile flux surface. That is, $\bar{\psi} \equiv (\psi - \psi_0) / (\psi_{\text{edge}} - \psi_0) = 0.95$, where ψ is the poloidal flux at that surface, and ψ_{edge} and ψ_0 are the poloidal flux values at the plasma edge and at the magnetic axis, respectively. Experiments have shown that the stability limit for diverted plasmas is set by $q_{95} > 2$, except when active feedback is used to stabilize the external $(2,1)$ kink mode [4].

Because the external kink stability limit[2] is an ideal MHD mode, with a very simple criterion for violation, this type of disruption is very rarely encountered in practice.[3] Typically, tokamak fusion reactor concepts are designed to have an edge safety factor which is well away from this stability limit, e.g. ARIES-AT [5] has $q_{95} \approx 3.7$.[4]

1.1.2 Beta limit

The beta of a plasma is defined as the ratio of its kinetic pressure p to the local magnetic pressure $B^2/2\mu_0$. The fusion power density S_f from a magnetic-confinement fusion reactor in the temperature range of interest to a reactor (10–30 keV) scales as $S_\text{f} \sim T^2 \cdot n_\text{D} n_\text{T} \sim (nT)^2 \sim p^2$. Thus, fusion power density from the entire reactor is maximized when volume-averaged plasma pressure is maximized: $S_\text{f} \sim \langle p \rangle^2$. Rewriting this in terms of the plasma beta:

[2] In practice, the kink limit is often referred to as the current limit or the q limit.

[3] One example of a kink-limit disruption is Alcator C-Mod shot 1120801032, where a power supply failure caused the plasma to become circular (lose its elongation) at a plasma current of 1.13 MA, which caused the kink limit to be violated and the plasma to immediately disrupt.

[4] The cylindrical safety factor q^* for ARIES-AT is actually 1.85 – less than the stability limit allows. The increase in q_{95} vs. q^* comes from the strong shaping (triangularity).

$$S_f \sim \beta^2 B^4 \tag{1.2}$$

where the left side is the "payoff" from a fusion reactor (fusion power density), and the magnetic field strength B on the right side of Equation 1.2 is the cost, since the strong magnetic fields in a tokamak are one of the most costly parts of such machines. Thus, the economic acceptability of a magnetic-confinement fusion reactor is largely determined by the achievable value of β, and much of controlled fusion research has been devoted to the pursuit of magnetic configurations that are stable at high values of β [2, p. 87].

The beta limit in a shaped, diverted tokamak is set by the MHD stability limit against high-spatial-frequency (high-m) kink-ballooning modes on the low-field (outboard) side of the plasma, and was stated in its current form in a computational study Troyon *et al.* [6], after a decade of experimental and theoretical investigations into the stability of shaped plasmas by various groups. The limit is given in terms of the so-called "normalized beta" $\beta_N \equiv \beta / \left(I_p / a B_\phi \right)$. The stability criterion is $\beta_N \lesssim 2.5$–3.5. This equation is not dimensionally consistent: it assumes that β is given in %, I_p in MA, a in m, and B in T. In dimensionally proper form, the Troyon stability limit is given by:

$$\beta \lesssim g \frac{\mu_0 I_p}{a B_\phi} \tag{1.3}$$

where β is given as a fraction (not a percentage), and g is a nondimensional constant which takes values from $(2.0 - 2.8) \times 10^{-2}$.

In practice, like the kink limit, the true beta limit is rarely reached in real experiments. In high-performance, long-pulse tokamak plasmas, other "soft" instabilities like neoclassical tearing modes, which do not cause a major disruption but rather reduce plasma confinement (which reduces plasma pressure and β), cause the achievable value of β to be lower than the ideal limit [7].

1.1.3 Resistive wall mode

The ideal MHD instabilities mentioned in Sections 1.1.1 and 1.1.2 are the "no-wall" stability limits, in which the plasma does not have any external conducting structures around it. The presence of a close-fitting perfectly conducting shell causes the stability limits to be increased because of image currents induced in the wall.[5]

Real tokamaks *do* have conducting walls around the plasma, but these walls are not perfectly conducting: they are the plasma-facing first wall components and surrounding vac-

[5] The stability limits are often derived mathematically for a plasma of minor radius a [m] in the presence of a perfectly-conducting wall at a radius b [m] from the plasma center; the no-wall value is then obtained by taking the limit as $b/a \to \infty$.

uum vessels, which have a nonzero resistivity. In the presence of a resistive wall, a plasma which is above the no-wall stability limit for either pressure or current, but which is below the perfectly-conducting wall stability limit[6] will instead grow on a resistive wall timescale $\tau_w = \mu_0 b d/\eta$, where b is the radius of the resistive wall from the plasma center [m], d is the thickness of the wall [m], and η is the wall material resistivity [Ω m]. For today's tokamaks, this is of the order of $\approx$ 1–10 ms; slow enough that active feedback using non-axisymmetric coils mounted in the wall is possible [8, 9]. Additionally, if the plasma (and thus the mode, and its associated magnetic fields) is moving relative to the wall, as is typically the case in ICRF-heated Alcator C-Mod plasmas [10], the resistive wall mode can be absolutely stabilized [11]. However, if a resistive wall mode gets large enough, eventually confinement will degrade to the point where other, faster instabilities take over, and a disruption occurs.

1.1.4 Locked mode

Under certain plasma conditions, typically at low density [12], resonant error fields caused by imperfections in the external toroidal and poloidal field coils can interact with magnetic islands in the plasma and cause a slowly-growing (resistive) instability to grow [13]. This mode is detectable by its magnetic signature ($m = 2$, $n = 1$ on Alcator C-Mod [14]), but also by the fact that the plasma core toroidal rotation velocity goes to zero due to magnetic braking by the interaction of the island and the external perturbation [14]. This "locking" of the perturbation to a particular toroidal location in the tokamak gives the locked mode its name. Like the resistive wall mode, the locked mode causes a disruption when it grows large enough to trigger some other, faster instability.

Because the root plasma perturbation in a locked mode is typically a slowly-growing neoclassical tearing mode (NTM) island [15], it can theoretically be stabilized by targeted application of electron cyclotron current drive (ECCD) in the island, although this is difficult once the mode has locked, because ECCD stabilization of NTMs requires driving current in the O-point of the island, and the island may lock with the O-point out of phase with the current-drive actuator. Schemes for preventing disruptions are discussed further in Section 2.3.

1.1.5 Radiative collapse

Impurities in a plasma cause energy loss by recombination and line radiation: in many circumstances, particularly on machines with high-Z plasma-facing walls, the energy loss is from line radiation is comparable to the ordinary energy loss by cross-field conduction [16, p. 262]. The energy loss due to line radiation is given in simplified form by:

[6] Plasmas which are above a perfectly-conducting wall stability limit will *always* disrupt immediately, regardless of the presence of a wall.

$$\varepsilon_{\text{rad}} = L_{\text{rad}}(T)\, n_e n_{\text{imp}} \tag{1.4}$$

where ε_{rad} is the power loss due to line radiation $[\text{W m}^{-3}]$, n_e and n_{imp} are the electron and impurity ion density, respectively $[\text{m}^{-3}]$, and $L_{\text{rad}}(T)$ is the temperature-dependent line radiation coefficient $[\text{W m}^3]$, which sums up the power from all atomic transitions from all the charge states of that impurity[7] that exist at a given temperature [17]. This line radiation coefficient increases at low temperature, but then decreases at higher temperatures as the impurity becomes fully ionized: this is the well-known process of "burnout" in a plasma, which must be accomplished in the early phases of a tokamak discharge in order to sustain a plasma [18].

It is in this temperature range where $\partial L_{\text{rad}}/\partial T < 0$ that radiative collapse is a possibility. At typical Alcator C-Mod core temperatures (1–6 keV), light impurities such as boron are burned out, but high-Z impurities such as molybdenum are not. Thermal instability results if a small downward perturbation in temperature results in a greater increase in power *lost* due to line radiation than the additional Ohmic heating *gained* by the fall in temperature. That is, the condition for thermal instability (radiative collapse) is:

$$\frac{\mathrm{d}L_{\text{rad}}}{\mathrm{d}T} n_e n_{\text{imp}} - \frac{\mathrm{d}\eta}{\mathrm{d}T} J^2 < 0 \tag{1.5}$$

where η is the Spitzer–Harm plasma resistivity ($\eta \sim T^{-3/2}$). It can be seen from Equation 1.5 that radiative collapse requires $\mathrm{d}L_{\text{rad}}/\mathrm{d}T < 0$, since $\mathrm{d}\eta/\mathrm{d}T < 0$. In today's high-performance tokamaks, and certainly in future devices like ITER, triggering an unplanned radiative collapse will require a sudden "injection" of impurities, for example, from a small flake of material falling off the wall. This scenario is described in Section 1.1.7. Further information about thermal instability and radiative collapse can be found in the review by Stacey [19].

1.1.6 Density limit

One of the longest-standing puzzles in magnetic-confinement fusion research has been the origin of the *density limit* in tokamaks. It was first proposed in the 1970s [20] that there was a maximum achievable plasma electron density in tokamaks $n_{\text{e, achievable}}\,[10^{19}\ \text{m}^{-3}] \approx B_\phi\,[\text{m}]/R\,[\text{m}]$, based on a survey of the densities attained in all tokamaks to date, although the scatter was large, and the Alcator A tokamak (at the time known as just Alcator) had achieved a density far above the proposed limit. Further effort in this line of research led eventually to the scaling law proposed by Greenwald *et al.* in 1988 [21]:

[7] L_{rad} can also be tabulated for each charge state individually, as for the helium, neon, and argon impurities shown in Figure 2-2.

$$n_{e,\max}\ \left[10^{20}\ \mathrm{m}^{-3}\right] \approx \frac{I_p}{\pi a^2}\ \left[\mathrm{MA\,m}^{-2}\right] \tag{1.6}$$

This scaling has proven robust, and today is usually referred to as the "Greenwald density limit" for tokamaks. However, it is still an open question what actually *causes* the disruption when the density limit is exceeded: it is thought that it is a radiative collapse of some sort [22], perhaps caused by a "radiative tearing mode" neoclassical island with a strong impurity-radiation term (see [23], [24], and Chapter 7 of this thesis), but there remain open questions about the effect of impurity radiation efficiency (L_{rad}) on this scaling (the Greenwald limit does not include any effect of varying impurity line radiation efficiency). In addition, the Greenwald density limit scaling cannot be put in a dimensionally consistent form – attempts to nondimensionalize it result in it no longer holding true [25].

Operationally, density-limit disruptions are in principle avoidable, because the limit is well-known, even if the physics underlying it are not completely understood. In practice, density-limit disruptions are usually caused by a loss of control of plasma electron density, because of fueling from the wall (outgassing) or the failure of a gas-injection (fueling) valve. It should be noted that at fixed safety factor q and toroidal magnetic field strength B_ϕ, the density limit decreases as R^{-1}, which sets a severe constraint on the allowable density in large devices like ITER and reactors. Thus, they are often designed to operate near the density limit, *e.g.* ITER $n/n_{GW} \approx 0.8$–0.85, and ARIES-AT $n/n_{GW} \approx 0.9$ [26], and the density limit may become one of the dominant causes of disruptions in such devices.

1.1.7 Injections (UFOs)

If a piece of material falls off of the wall of a tokamak or a heating antenna and into the plasma, it can drastically raise the electron density and impurity content of the plasma. A typical C-Mod plasma has an electron inventory of 2–4×10^{20} and has a mass of 1–2×10^{-6} kg (1–2 mg) A piece of molybdenum or tungsten no larger than 0.3 mm on a side (approximately the size of a broken-off piece of mechanical pencil lead) will have the same mass as the plasma, and significantly greater than the plasma in electron inventory. While a formal study of the causes of disruptions in Alcator C-Mod has not been conducted since that of Granetz in C-Mod's first few years of operation [27], a scan of the C-Mod logbook quickly reveals that these "injections" are the most common cause of disruptions on Alcator C-Mod. (See also Lipschultz [28] for a discussion of C-Mod disruptions caused by tungsten injections from a previously-melted divertor tile.)

Impurity injections are not actually the proximate cause of the disruption. When the impurities are injected into the plasma, it triggers either a density-limit disruption (Section 1.1.6), a radiative collapse (Section 1.1.5), or a current-driven MHD instability caused by the edge cooling changing the current profile. The process by which a solid piece of wall material is assimilated into the plasma is similar to what happens when a high-Z "killer" pellet is

injected into the plasma. These killer pellets are discussed further in Section 2.5.1.

In the United States, these events are usually referred to as "impurity injections"; in Europe and Japan they are often referred to as "UFOs" (unidentified flying objects) [29], especially when they can be seen on high-speed cameras slowly passing through the plasma and glowing as they ablate [30].

Disruptions caused by impurity injections are considered one of the most challenging categories for disruption prediction and mitigation systems, because the first indication that anything is happening is when the impurity hits the edge plasma and begins to ionize and glow. This may not be long enough for the disruption mitigation system to react and trigger the rapid shutdown system. Disruption mitigation and rapid shutdown systems are discussed in detail beginning in Chapter 2.

1.1.8 Vertical displacement events (VDEs)

It can be readily shown using a simple conducting-wire model of a tokamak plasma [2, p. 399] that any elongated plasma ($\kappa > 1$, where κ is the elongation, *i.e.* the height-to-width ratio of the plasma's poloidal cross section) is unstable to an ideal $n = 0$ axisymmetric vertical instability, in which the plasma moves vertically until it hits the surrounding plasma-facing components. The presence of a perfectly-conducting wall stabilizes this mode for finite values of κ, but as was discussed in Section 1.1.3, the finite conductivity of real vessel walls means that the mode is instead converted into a slowly-growing resistive wall mode. A close-fitting vessel wall and active feedback on the vertical stability coils means that tokamaks with aspect ratio $R_0/a \approx 3$, such as Alcator C-Mod and ITER, can typically maintain vertical control of plasmas up to an elongation of $\kappa \approx 1.8$ [2, p. 404–405].

Full-current VDEs are one of the few types of disruptions that can actually cause significant damage even to today's tokamaks, especially on JET, the current largest tokamak in the world [31]. Because the plasma contacts the wall when it is still carrying its full thermal and poloidal magnetic energy, this event tends to produce very large localized heat loads on divertor or wall components where the plasma "scrapes off" its edge. In addition, halo currents, which are poloidal currents flowing in vessel components due to the current in the edge of the plasma being shorted through material components, cause extremely large electromagnetic loads on the in-vessel components, vacuum vessel, and support structures.

During the ITER design review process that was undertaken in the late 2000s, a concern was raised about the ability of the superconducting poloidal field coils, which are outside the vacuum vessel, very far from the plasma, and have a limited allowable current slew rate, to maintain adequate vertical control of the plasma. Such is the worry about VDEs in large tokamaks that this concern led to the addition of normal-conducting (copper) in-vessel fast vertical control coils at a late stage of the design, at significant expense [32]. Fortunately, because the VDE occurs on the slow resistive wall time scale, and has a clear magnetic sig-

nature, they are reliably detectable by the plasma control system, allowing enough time to trigger the disruption mitigation/rapid shutdown system.

1.1.9 Other disruption classes

In the above subsections, the major causes of disruptions on tokamaks have been outlined. This list is not exhaustive. A fusion-grade plasma is an exquisite balance of forces, supported by a great variety of technological systems, and has a very high free energy available to drive instabilities. Many off-normal events can lead to a disruption, usually by the off-normal event causing the plasma to cross one of the well-understood stability limits: current, density, impurity radiation, vertical control, *etc.*

For example, if an internal transport barrier (ITB) collapses, the perturbation caused by the sudden outflow of energy can trigger a global MHD instability, which grows quickly and causes the plasma to disrupt [33]. Or, more mundanely, a poloidal field power supply can fail, causing a loss of vertical control of the plasma (a VDE) or a sudden drop in elongation which causes a kink-limit (q limit) disruption. The potential causes of disruptions are many, and it is only by systematic study of each and every disruption on a given machine (*e.g.* [3]) that they can all be classified with confidence. In the following section, the effects of unmitigated disruptions are discussed, followed by a brief discussion of the precursors that signal an oncoming disruption, and operational experience with disruptions.

1.2 Effects of disruptions

Because a disruption terminates the plasma discharge so suddenly, the stored energy in the plasma is rapidly dissipated into the vacuum vessel and plasma-facing material (PFM) surfaces. This includes the plasma's *thermal* energy $W_{\mathrm{th}} = (3/2)\langle p\rangle V$, where $\langle p\rangle$ is the volume-averaged plasma pressure and V is the plasma volume, as well as the *poloidal magnetic* energy $W_{\mathrm{pol}} = LI_{\mathrm{p}}^2/2$, where L is the inductance of the toroidal plasma and I_{p} is the toroidal plasma current. In today's tokamaks, there is more energy in the poloidal magnetic field than there is in the plasma pressure: $W_{\mathrm{pol}} > W_{\mathrm{th}}$.[8] The release of this stored energy in the $\approx$ ms timescale of a disruption has several effects on the machine, which are discussed in the following subsections.

[8] In Alcator C-Mod, a typical value of W_{th} might be 100 kJ in an H-mode plasma, with $W_{\mathrm{pol}} \approx 1$ MJ. The ratio of W_{th} to W_{pol} varies as the poloidal beta β_{pol}, and these two energies could be comparable in future high-beta reactors.

1.2.1 Divertor heat load

In the thermal quench of an unmitigated disruption on a diverted plasma, most of the plasma stored thermal energy W_{th} is transported by rapid cross-field conduction and convection from the core plasma to the edge, where it is then conducted along open magnetic field lines to material surfaces. The energy is deposited on a small area of the divertor: even though the heat load footprint broadens by a factor of ≈ 10 during a disruption [34], it can still be enough to ablate carbon surfaces [35] in today's machines. In addition, the heat load in an unmitigated disruption is expected to be well above the melt threshold for tungsten divertor components in ITER [36].

1.2.2 Halo and vessel currents

The loss of thermal energy causes the resistivity of the plasma to drastically increase, causing a sudden spike in loop voltage due to the plasma inductance. This induces toroidal currents in the surrounding plasma-facing components and vacuum vessel, which interact with the poloidal field to produce large $\vec{J} \times \vec{B}$ body forces on vessel components. Even more severe are the poloidal currents induced in the divertor structures and vessel components due to the shorting out of force-free plasma currents (parallel to magnetic field lines) as the plasma "scrapes off" on material structures during a VDE. These poloidal "halo" currents interact with the strong toroidal field to produce very large sideways forces on the vessel, especially because the halo currents are often toroidally peaked due to a $m = 1$, $n = 1$ "tilt" instability which can be produced during the current rampdown phase (current quench) of a disruption [37].

These electromagnetic forces produced by vessel currents during a disruption can be severe enough to cause machine damage on large tokamaks like JET [31], and are particularly severe during VDEs, because the plasma begins inducing poloidal halo currents in the vessel before it has a chance to begin resistively ramping down.

1.2.3 Runaway electrons

While runaway electrons are not the focus of this thesis, they are a very important consequence of disruptions, and mitigating their effect is a necessary part of any disruption mitigation system. (Disruption mitigation and rapid shutdown are introduced in Chapter 2). The drag force on an electron due to Coulomb collisions decreases as the electron gains kinetic energy; this is also the cause of the $T^{-3/2}$ inverse temperature dependence in the Spitzer–Harm plasma electrical resistivity equation. Thus, it is possible for electrons above a certain kinetic energy to "run away", reaching relativistic energies.[9] This effect was first

[9] The upper limit on their energy is set when the energy gained in each turn around the tokamak is equal to the energy lost due to bremsstrahlung and synchrotron radiation.

theorized by Dreicer in the early 1950s [38], as part of the then-classified fusion research being undertaken by the U.S. Atomic Energy Commission. The runaway electrons can then produce further runaways by a collisional avalanche process [39], leading to an exponential growth that can convert a significant fraction of the plasma current to runaway electrons with an energy of 30–60 MeV.

Runaways can be produced during plasma startup or low-density plasma operation, but this is theoretically avoidable through plasma control. Runaways following disruptions, however, are a concern for ITER, because the large loop voltages created during a disruption are unavoidable, and extended MHD modeling suggests that runaway confinement increases super-linearly with machine size [40]. Runaway electron beams carrying a current of order $\approx$ 100 kA are capable of causing significant damage to machine components [41], and are of large concern due to the possibility of $\approx$ 10 MA runaway beams in ITER [42]. Runaway electron mitigation schemes are briefly discussed in Section 2.9.

1.3 Disruption precursors

Many of the disruption classes discussed above have some technological failure as an ultimate cause, *e.g.* the failure of a poloidal field coil power supply, or a flake of material delaminating from the front of an ICRF antenna. But the proximate cause is usually the destabilization of some global (low toroidal and poloidal mode number) MHD mode, which grows exponentially until the core plasma loses its stored energy. These modes can often be detected by magnetic pickup coils or by other means, and are referred to as *disruption precursors* or *precursor oscillations*. Detecting these disruption precursors is an essential part of disruption prediction and mitigation, and the lack of such precursors is one reason why impurity injections are potentially one of the more difficult types of disruptions to detect and mitigate. Systems for detecting and mitigating disruptions are discussed further in Chapter 2.

1.4 Operational experience with disruptions

Typically, systematic efforts to avoid disruptions on today's experimental tokamaks are rare. This is the case for two reasons. First, disruptions do not usually cause any lasting damage to the current generation of machines. On small-major-radius machines like Alcator C-Mod, the vacuum vessel and internal components are built sufficiently robust to withstand an unmitigated full-performance disruption (B_ϕ = 9 T, I_p = 3 MA) [43]. On larger machines like JET, high-current VDEs can cause damage to the machine and impact operational schedules [31], but in this case, the machine is usually run in a careful manner, far from stability limits, when high-performance plasmas are being attempted.

The other, more important reason why there is not a strenuous effort to avoid disruptions on today's machines is because the goal of these devices is *research*: discovering new modes of plasma operation and techniques for producing fusion-grade plasmas that can be applied to the larger devices and reactors in the future. This necessarily requires exploring plasma regimes that have not been seen before, and running a tokamak in a novel way is a guarantee that plenty of discharges will end in disruptions.

With the design of ITER, which was the first machine where unmitigated disruptions had the potential to cause signficant damage and severely impact the operational schedule, there has been an increasing effort to systematically study the causes of disruptions and categorize them, with an eye toward developing prediction and mitigation systems for each class of disruption. One excellent early example of such a survey is that of Schüller [44], who describes several classes of disruptions and the early-onset signals (precursors) for each. Today, as will be described in greater detail in Chapter 2, it is recognized that developing reliable disruption detection and mitigation systems is a necessary step on the path to a tokamak fusion reactor [45].

It is important to note that the disruption categories presented here have been necessarily simplified. In reality, the lines get blurred, and strictly placing a disruption in one category or another becomes difficult. For example, one of the main causes of plasma terminations in recent long-pulse experiments on the Japanese Large Helical Device (a stellarator, but the principles here are applicable to tokamaks) was the following [46]: a flake of material (UFO) falls off of the wall and is assimilated by the plasma. The external heating systems are supplying enough heating power to prevent a radiative collapse *even with* this impurity injection, except that the sudden increase in plasma electron density causes a change in the electrical loading of the ICRF antennas. The antenna power reflection coefficient suddenly increases, and the heating system trips to avoid damage to the transmission network. At this new, lower level of heating power, the impurities are no longer burned out, and the plasma subsequently suffers a radiative collapse.

Or, for example, VDEs: Full-power VDEs are often caused by a power supply failure or the plasma undergoing a sudden vertical "jog" or change in internal inductance (due to, e.g. a sudden H-mode to L-mode transition, perhaps itself caused by an impurity injection) that takes it beyond the capability of the vertical control system. However, if the plasma disrupts for any other reason, the cold, resistive post-disruptive plasma becomes vertically unstable, and so in a sense, nearly *all* unmitigated disruptions become VDEs in their later stages. True VDEs are worse, though, because the plasma contacts material surfaces *before* it is cooled, and thus these types of disruptions produce the worst thermal and electromagnetic loads on vessel components.

1.5 Summary of disruptions in tokamaks

Some of the causes of major disruptions in tokamaks have been presented. Their effects on the machine have been described. In Chapter 2, the proposed schemes for detecting and mitigating the effects of disruptions will be presented, and the specific objective of this work—understanding the cause of the asymmetrical radiation during the thermal quench phase of massive gas injection rapid shutdowns—will be introduced.

References

[1] Kadomtsev, B.B. (1984). "Behaviour of disruptions in tokamaks." *Plasma Physics and Controlled Fusion* **26**(1A), 217–226. doi:10.1088/0741-3335/26/1A/320

[2] Freidberg, J. *Plasma Physics and Fusion Energy*, 1st ed. Cambridge University Press, hardcover version, 2007. ISBN 978-0-521-85107-7.

[3] de Vries, P.C. *et al.* (2011). "Survey of disruption causes at JET." *Nuclear Fusion* **51**(5), 053018 (12 pp). doi:10.1088/0029-5515/51/5/053018

[4] Piovesan, P. *et al.* (2013). "$q_{95} < 2$ operation via control of MHD stability in the DIII-D tokamak." Paper presented at the 40th European Physical Society Conference on Plasma Physics, Espoo, Finland, July 1–5, 2013. Paper Nº P2.146 (4 pp). Available online at http://ocs.ciemat.es/EPS2013PAP/pdf/P2.146.pdf

[5] Jardin, S.C. *et al.* (2006). "Physics basis for the advanced tokamak fusion power plant, ARIES-AT." *Fusion Engineering and Design* **80**(1–4), 25–62. doi:10.1016/j.fusengdes.2005.06.352

[6] Troyon, F. *et al.* (1988). "Beta limit in tokamaks: Experimental and computational status." *Plasma Physics and Controlled Fusion* **30**(11), 1597–1609. doi:10.1088/0741-3335/30/11/019

[7] Sauter, O. *et al.* (1997). "Beta limits in long-pulse tokamak discharges." *Physics of Plasmas* **4**(5), 1654–1664. doi:10.1063/1.872270

[8] Garofalo, A.M. *et al.* (2001). "Resistive wall mode dynamics and active feedback control in DIII-D." *Nuclear Fusion* **41**(9), 1171–1176. doi:10.1088/0029-5515/41/9/305

[9] Liu, Y. *et al.* (2009). "Progress in physics and control of the resistive wall mode in advanced tokamaks." *Physics of Plasmas* **16**(5), 056113 (12 pp). doi:10.1063/1.3123388

[10] Rice, J.E. *et al.* (1998). "Observations of central toroidal rotation in ICRF heated Alcator C-Mod plasmas." *Nuclear Fusion* **38**(1), 75–85. doi:10.1088/0029-5515/38/1/306

[11] Takechi, M. *et al.* (2007). "Identification of a low plasma-rotation threshold for stabilization of the resistive-wall mode." *Physical Review Letters* **98**(5), 055002 (4 pp). doi:10.1103/PhysRevLett.98.055002

[12] Scoville, J.T. *et al.* (1991). "Locked modes in DIII-D and a method for prevention of the low density mode." *Nuclear Fusion* **31**(5), 875–890. doi:10.1088/0029-5515/31/5/006

[13] Nave, M.F.F. and Wesson, J.A. (1990). "Mode locking in tokamaks." *Nuclear Fusion* **30**(12), 2575–2583. doi:10.1088/0029-5515/30/12/011

[14] Snipes, J.A. *et al.* (2002). "β limiting MHD activity and mode locking in Alcator C-Mod." *Plasma Physics and Controlled Fusion* **44**(3), 381–393. doi:10.1088/0741-3335/44/3/308

[15] La Haye, R.J. (2006). "Neoclassical tearing modes and their control." *Physics of Plasmas* **13**(5), 055501 (18 pp). doi:10.1063/1.2180747

[16] Hutchinson, I.H. *Principles of Plasma Diagnostics*, 2nd ed. Cambridge University Press, digitally printed paperback version, 2005.

[17] Tokar, M.Z. and Kelly, F.A. (2003). "The role of plasma–wall interactions in thermal instabilities at the tokamak edge." *Physics of Plasmas* **10**(11), 4378–4386. doi:10.1063/1.1613963

[18] Allen, S.L. *et al.* (1981). "The influence of the limiter on EUV emissions from light impurities in the Alcator A tokamak." *Nuclear Fusion* **21**(2), 251–255. doi:10.1088/0029-5515/21/2/012

[19] Stacey, W.M. (2007). "A survey of thermal instabilities in tokamak plasmas: Theory, comparison with experiment, and predictions for future devices." *Fusion Science and Technology* **52**(1), 29–67. Available online at http://www.ans.org/store/j_1485

[20] Murakami, M. *et al.* (1976). "Some observations on maximum densities in tokamak experiments." *Nuclear Fusion* **16**(2), 347–348. doi:10.1088/0029-5515/16/2/020

[21] Greenwald, M. *et al.* (1988). "A new look at density limits in tokamaks." *Nuclear Fusion* **28**(12), 2199–2207. doi:10.1088/0029-5515/28/12/009

[22] Suttrop, W. *et al.* (1997). "Tearing mode formation and radiative edge cooling prior to density limit disruptions in ASDEX upgrade." *Nuclear Fusion* **37**(1), 119–125. doi:10.1088/0029-5515/37/1/I09

[23] Gates, D.A. and Delgado-Aparicio, L. (2012). "Origin of tokamak density limit scalings." *Physical Review Letters* **108**(16), 165004 (4 pp). doi:10.1103/PhysRevLett.108.165004

[24] Gates, D.A. *et al.* (2013). "Physics of radiation-driven islands near the tokamak density limit." *Nuclear Fusion* **53**(6), 063008 (6 pp). doi:10.1088/0029-5515/53/6/063008

[25] Petty, C.C. *et al.* (2004). "Similarity in H-mode energy confinement: ν_* rather than $n/n_{\rm limit}$ should be kept fixed." *Plasma Physics and Controlled Fusion* **46**(5A), A207–A213. doi:10.1088/0741-3335/46/5A/022

[26] Najmabadi, F. *et al.* (2006). "The ARIES-AT advanced tokamak, advanced technology fusion power plant." *Fusion Engineering and Design* **80**(1–4), 3–23. doi:10.1016/j.fusengdes.2005.11.003

[27] Granetz, R. (1996). "Disruptivity in Alcator C-Mod." ITER Technical Report N$^{\underline{o}}$ D/PC/MHD EG. Referenced in Yoshino, R. *et al.* (1998). "Characterization of disruption phenomenology in ITER." Paper presented at the 17$^{\rm th}$ IAEA Fusion Energy Conference, Yokohama, Japan, October 19–24, 1998. Paper ITERP1/14. Available online at http://www-pub.iaea.org/MTCD/publications/PDF/csp_001c/pdf/itp1_14.pdf

[28] Lipschultz, B. *et al.* (2012). "Divertor tungsten tile melting and its effect on core plasma performance." *Nuclear Fusion* **52**(12), 123002 (9 pp). doi:10.1088/0029-5515/52/12/123002

[29] Winter, J. and Gebauer, G. (1999). "Dust in magnetic confinement fusion devices and its impact on plasma operation." *Journal of Nuclear Materials* **266–269**, 228–233. doi:10.1016/S0022-3115(98)00526-1

[30] Goodall, D.H.J. (1982). "High speed cine film studies of plasma behaviour and plasma surface interactions in tokamaks." *Journal of Nuclear Materials* **111–112**, 11–22. doi:10.1016/0022-3115(82)90174-X

[31] "Modelling magnetic forces during asymmetric vertical displacement events in JET." *Fusion Engineering and Design* **47**(4), 389–402. doi:10.1016/S0920-3796(99)00098-8

[32] Martin, A. *et al.* (2013). "Design evolution and integration of the ITER in-vessel components." *Fusion Engineering and Design*, in press, corrected proof. doi:10.1016/j.fusengdes.2013.01.004

[33] Riccardo, V. *et al.* (2003). "Disruptions and disruption mitigation." *Plasma Physics and Controlled Fusion* **45**(12A), A269–A284. doi:10.1088/0741-3335/45/12A/018

[34] Arnoux, G. *et al.* (2009). "Heat loads on plasma facing components during disruptions on JET." *Nuclear Fusion* **49**(8), 085038 (8 pp). doi:10.1088/0029-5515/49/8/085038

[35] Whyte, D.G. *et al.* (2003). "Disruption mitigation with high-pressure noble gas injection." *Journal of Nuclear Materials* **313–316**, 1239–1246. doi:10.1016/S0022-3115(02)01525-8

[36] Sugihara, M. *et al.* (2007). "Disruption scenarios, their mitigation and operation window in ITER." *Nuclear Fusion* **47**(4), 337–352. doi:10.1088/0029-5515/47/4/012

[37] Riccardo, V. *et al.* (2000). "Parametric analysis of asymmetric vertical displacement events at JET." *Nuclear Fusion* **42**(1), 29–40. doi:10.1088/0741-3335/42/1/304

[38] Dreicer, H. (1959). "Electron and ion runaway in a fully ionized gas. I." *Physical Review* **115**(2), 238–249. doi:10.1103/PhysRev.115.238

[39] Rosenbluth, M.N. and Putvinski, S.V. (1997). "Theory for avalanche of runaway electrons in tokamaks." *Nuclear Fusion* **37**(10), 1355–1362. doi:10.1088/0029-5515/37/10/I03

[40] Izzo, V.A. *et al.* (2011). "Runaway electron confinement modelling for rapid shutdown scenarios in DIII-D, Alcator C-Mod and ITER." *Nuclear Fusion* **51**(6), 063032 (10 pp). doi:10.1088/0029-5515/51/6/063032

[41] Nygren, R. *et al.* (1997). "Runaway electron damage to the Tore Supra Phase III outboard pump limiter." *Journal of Nuclear Materials* **241–243**, 522–527. doi:10.1016/S0022-3115(97)80092-X

[42] Putvinski, S. (2011). "Runaway electrons in tokamaks and their mitigation in ITER." Presentation at the 12th IAEA Technical Meeting on Energetic Particles in Magnetic Confinement Systems, Austin, TX, USA, September 7–10, 2011. Available online at http://w3fusion.ph.utexas.edu/ifs/iaeaep/talks/s11-i11-putvinski-sergei-ep-talk.pdf

[43] Irby, J. *et al.* (2007). "Alcator C-Mod design, engineering, and disruption research." *Fusion Science and Technology* **51**(3), 460–475. Available online at http://www.ans.org/pubs/journals/fst/a_1433

[44] Schüller, F.C. (1995). "Disruptions in tokamaks." *Plasma Physics and Controlled Fusion* **37**(11A), A135–A162. doi:10.1088/0741-3335/37/11A/009.

[45] "Research Needs for Magnetic Fusion Energy Sciences: Final Report of the Research Needs Workshop (ReNeW), Bethesda, Maryland, June 8–12, 2009." Weiser, P. (Ed.) Available online at http://burningplasma.org/renew.html. See Thrust 2 ("Control transient events in burning plasmas"), p. 243.

[46] Mutoh, T. *et al.* (2013). "Steady state operation of MW heating power using ICH and ECH in LHD." Presentation at the 7th IAEA Technical Meeting on Steady State Operation of Fusion Devices, Aix-en-Provence, France, May 14–17, 2013.

THIS PAGE INTENTIONALLY LEFT BLANK

Chapter 2

Disruption mitigation, rapid shutdown, and its limitations

As discussed in Chapter 1, unmitigated disruptions have the potential to cause damage to even present-generation tokamaks. At reactor scale, a full-current unmitigated disruption will almost certainly cause localized melting of metallic plasma-facing components, impacting reactor availibility. It is thus natural to seek methods of avoiding disruptions, or, if this is not possible, of reducing—that is, mitigating—their impact.

2.1 Overview of a disruption mitigation system

The strategy behind a disruption avoidance/mitigation system is shown in the flowchart in Figure 2-1. In a reactor, the disruption avoidance/mitigation system (DMS) must be completely integrated with the plasma control system (PCS), which in turn will be a part of the larger reactor control system (RCS).

Essentially, the PCS must constantly be answering the question "is the plasma in an off-normal state?". If the answer is *yes*, then the PCS's off-normal event handling routine must answer the question "Can the plasma be returned to its nominal (normal) state using the available actuators?". These actuators include heating, current drive, central solenoid, poloidal field coils, and non-axisymmetric coils, fuel mixture, radiative impurities in the divertor, *etc.* [1]. If the answer to this second question is *no*, the implication is that the plasma is about to disrupt.

In this case, the goal is to mitigate the "natural" (unmitigated) disruption by preempting it with a benign *rapid shutdown*, which dissipates the plasma stored energy in a way which is less harmful (ideally *not harmful at all*) to the machine than an unmitigated disruption.

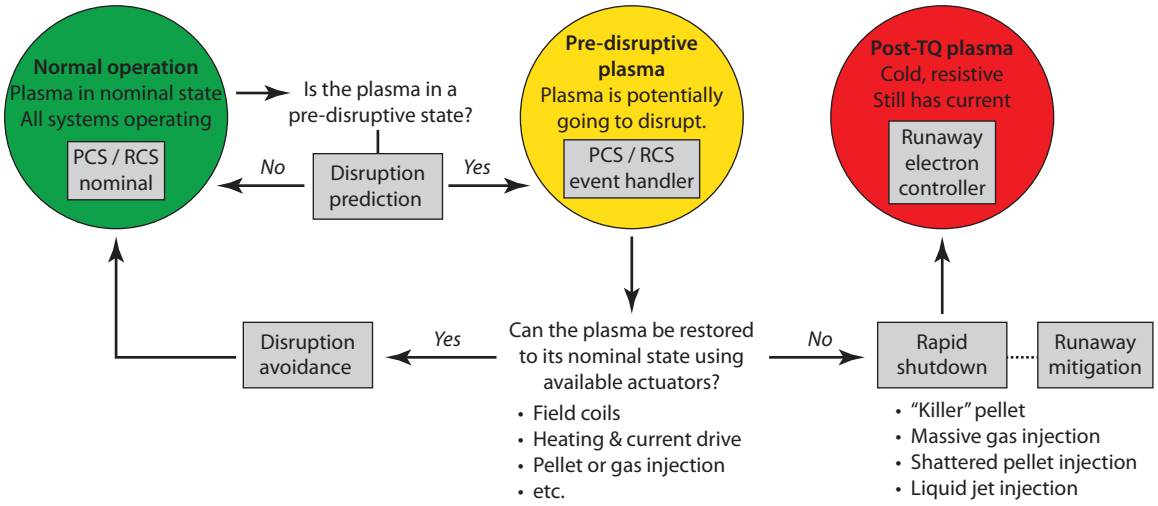

Figure 2-1 – Conceptual flowchart of a disruption avoidance/mitigation system and its integration with the main plasma control system (PCS) / reactor control system (RCS). The system must be able to detect off-normal events and decide whether or not a disruption is inevitable (*disruption prediction*). If it is avoidable, the PCS/RCS should take appropriate action to restore the normal state. If a disruption is unavoidable, then the rapid shutdown system will terminate the plasma in a benign way. A separate runaway electron mitigation system may be required; this is discussed briefly in Section 2.9.

2.1.1 Integration with plasma control system

Control of machine functions is often divided into multiple levels, with each successively higher level being simpler, more robust, and having authority over the lower levels of control. At the bottom is ordinary machine and plasma control, which attempts to control the tokamak systems and plasma using the full suite of detectors, actuators, and digital controllers. In ITER, this is known as the Conventional Control system [2]. More generally, this level of control is known as the Plasma Control System (PCS), Digital Plasma Control System (DPCS), or Reactor Control System (RCS).

Overlaid over the PCS is a second level of machine protection (MP) interlocks. These are *independent* controllers, built to a higher level of robustness than the basic PCS, which "protect the investment" by shutting off power supplies if an overcurrent or arc condition is detected, etc. Typically, these systems are built using slower, highly tested components such as PLCs, rather than the fast PID controllers or real-time digital computers used in the base PCS level. Examples of machine protection control in Alcator C-Mod include fault detectors in the ion cyclotron heating (ICH) heating system, and the "TF crowbar", which redirects the current in the toroidal field coils through a large shunt in case of a fault in the power supplies. These MP systems operate independently of the C-Mod PCS.

In ITER, the MP level of control is known as the Central Interlock System (CIS). The flow of authority is structured such that the PCS can always trigger an event (such as "shut down the plasma") in the MP system, but the MP system *never* relies on the PCS. In fact, total

failure of the PCS is usually specified as one of the conditions for the MP system to safely shut down the plasma and protect the machine.

Finally, at the highest level is the human and radiological safety system. In experimental tokamaks like Alcator C-Mod, this includes door interlocks, oxygen level sensors, etc. In ITER, this level of control, known as the Central Safety System (CSS), also includes all radiological protection, such as tritium leak detection [3]. The ITER CSS has been certified to the stringent requirements of the IEC 61513 nuclear power plant instrumentation standard [4].

2.2 Disruption detection/prediction

The first step in avoiding or mitigating a disruption is detecting that one is likely going to happen in the first place – *i.e.*, detecting that the plasma is in a "pre-disruptive" state. However, as discussed in Section 1.1, there are several classes of disruptions; prospects for detecting each of them vary depending on the class.

In general, the easiest disruption precursors to detect are those that are present on magnetic probes (Rogowski coils, flux loops, etc.). For example, the kink limit in a limited plasma requires only knowing the edge safety factor q, which is solely a function of the plasma current profile, plasma shape, toroidal field, and can be reliably calculated in real time using algorithms such as rtEFIT. Locked modes, in which a resistive wall mode MHD perturbation interacts with toroidal asymmetries in the boundary conditions (toroidal field, vessel components, etc.) causing a slowly-growing instability that is locked to a particular toroidal phase, are also relatively easy to detect. Toroidal arrays of magnetic pickup coils can give a real-time signal of $\cos(n\phi + \delta)$ perturbations, typically $n = 1$ and $n = 2$. For example, there are poloidal arrays of 26 magnetic pickup coils at each of four toroidal locations in Alcator C-Mod [5], allowing estimates of locked-mode amplitude for $n = 1$ and $n = 2$. Typically, the alarm criterion for locked-mode amplitude is set based on experience with previous disruptions; see, *e.g.* Reux *et al.* [6] where the alarm is set at a locked-mode amplitude of 2 mT during JET flat-tops.

Real-time prediction of beta limit disruptions is typically more difficult, since the kink–ballooning stability limit that sets the β limit in tokamaks depends on detailed radial profiles of pressure and rotation [7, Section 4]. Using a neural network trained on a large number of diagnostic inputs, Wróblewski *et al.* [8] were able to predict approximately 90% of beta-limit and locked-mode disruptions on DIII-D, with a false alarm rate of approximately 10%.

Also using a neural network approach, Pautasso *et al.* [9] were able to detect 85% of disruptions (with a 1% false positive rate) on the ASDEX Upgrade tokamak, using a training set of 99 previous disruptive plasma discharges. In this case, the disruption detector[1] was

[1] The rapid shutdown system was only triggered by the locked mode disruption detector, not the general

actually connected to a "killer" pellet system for rapid shutdown (see Section 2.5). They note that the disruptions which were missed (not recognized by the disruption predictor) were typically "because of impurity events (UFOs), or had been poorly represented in the training database, [e.g.] impurity accumulation or disruption after a locked-mode phase in ITB experiments." Such "training" is, however, problematic for ITER-class devices, since it may not be possible to build up a database of unimitigated disruptions without causing punitive damage to the machine. Therefore the development of physics-based disruption detection techniques [10] remains a key goal.

On Alcator C-Mod, the only off-normal detection used in routine PCS operation is a hard X-ray detector intended to detect "runaway discharges", in which a large fraction of the plasma current is carried by runaway electrons. This "runaway detector" triggers a controlled ramp-down of the plasma current, but is not connected to a rapid shutdown system.

2.3 Disruption avoidance

Once it has been detected that the plasma is in a pre-disruptive state, the ideal response would be to use the available actuators to restore the plasma to its nominal operating state. To date, however, the only classes of disruptions for which avoidance has been experimentally demonstrated[2] are radiative islands produced in density-limit disruptions on the FTU tokamak [11]. In this work, Esposito *et al.* injected electron-cyclotron resonance heating (ECRH) power into the O-point of a $(2,1)$ radiative island after a density increase due to Mo pellet injection, and found that in some cases, the island could be reduced in size and the disruption avoided or delayed.

Stabilization of neoclassical tearing modes (NTMs) using ECRH power has been proven on several tokamaks, including DIII-D [12], JT-60U [13], and ASDEX Upgrade [14]. It should be noted that these tearing modes are relatively "easy" to stabilize, as they grow on the NTM timescale, which can be a significant fraction of a second (compared to ideal MHD modes, which grow on a microsecond timescale). In addition, while NTMs degrade confinement and thus absolute plasma performance, they are not inherently disruptive: they usually grow and then saturate without causing a major disruption of the plasma.

For ITER and reactors, it is anticipated that disruption avoidance will be used for many disruption classes, including VDEs, density limit, radiative collapse, and beta limit disruptions [15, p. 53]. The intention is to predict the plasma state on the basis of diagnostic inputs and an *a priori* plasma state model, rather than simply inferring the likelihood of disrup-

neural network disruption predictor.

[2] One could consider the ordinary plasma control system as constantly avoiding density limit, kink limit, and VDE disruptions, and thus these have been experimentally demonstrated as well. However, because avoiding these operating limits is part of ordinary plasma control, these classes of disruption are generally not included in "disruption avoidance" research.

tion based on a database of previous disruptions.[3] As Wesley [16] notes, however, work to date has "mostly focused on mitigation", with the very important prediction and avoidance capabilities as yet undeveloped.

2.4 Disruption mitigation

If the disruption cannot be avoided through the use of available actuators (ECRH, etc.), then one turns to the available options for *mitigating* the inevitable disruption. This term is often used synonymously with *rapid shutdown* (see Section 2.5), but may actually include other techniques for mitigating the impact of the disruption on the machine, such as applying ECRH heating after the thermal quench in order to delay the onset of the current quench and decrease the plasma loop resistance during the CQ [14]. Disruption mitigation (including detection, avoidance, and rapid shutdown) is an *extremely* high priority research topic for ITER, as ITER is the first tokamak where an unmitigated major disruption can potentially cause damage significantly in excess of any tokamak to date [16, 17]. It may not be feasible to avoid *all* damage to ITER internal components from disruptions, but it is vital to make sure that this damage is less severe, so that physics operations are not unduly impacted.

2.5 Rapid shutdown

If an upcoming disruption has been determined to be unavoidable, the plasma is terminated in what is known as a *rapid shutdown*. The goal is to rapidly dissipate the stored energy density of the plasma (thermal and poloidal magnetic) in a benign way. Due to the large stored energy per unit wall area $[\mathrm{J\,m^{-2}}]$ on reactor-class devices like ITER, this means that the energy must be deposited over a large fraction of the plasma-facing first wall: if it were deposited in the divertor, it would melt (this is discussed further in Section 2.8.4). Because there is no way to ensure uniform *conduction* of heat from the plasma core to the entire first wall, this is accomplished through *radiation*. Thus, rapid shutdown is often known as *radiative shutdown* of a plasma.

It should be noted that the goal on today's tokamak experiments is to perform rapid shutdown in a way that the next pulse is a success – *i.e.* not a non-sustained discharge (NSD) or "fizzle". On ITER and reactors, the primary goal will be more modest: to simply prevent damage to the machine ("investment").

In the late 1980s and early 1990s, there was some investigation of using the ordinary inductive current drive system to rapidly terminate the plasma current; this was known as "rapid current rampdown" or "fast current rampdown", and was originally developed with the goal

[3] In today's tokamaks, that database is usually held implicitly, in the brains of the operators in the control room; on a few tokamaks it is a neural network in a computer, as discussed in Section 2.2.

of operating a tokamak in an alternating current (ac) fashion [18, 19]. This technique is reliant on the Ohmic current drive system being able to produce large (negative) loop voltages, and is not under active investigation today.

2.5.1 Killer pellets and high-pressure gas jets

The first proposal to use cryogenic D–T pellets to fuel a fusion reactor was published by Spitzer in a classified 1954 Project Matterhorn report [20] on the practical (engineering) considerations in making a stellarator into a useful power source. Some form of core fueling, whether it be pellet injection, gas puffing, molecular cluster injection, or liquid-drop injection, was considered a necessary technology for a fusion reactor. An actual working cryogenic hydrogen pellet injector was first developed at the UKAEA Culham laboratory in the 1960s [21]. In 1975, the first experimental tests of ablation rate were made [22], finding that the pellet ablation rate was higher than expected based on a simple theory of a shielding neutral gas layer. By 1978, pellet fueling was considered the "most promising" technique for tokamak fueling [23], due to its low specific energy consumption (*i.e.*, per injected fuel particle) and ability to deposit fuel atoms deep into the core of a reactor-grade plasma.

At the same time, researchers were already thinking about the possible application of pellets for rapid shutdown. At the First ANS Topical Meeting on the Technology of Controlled Nuclear Fusion [24] in 1974, two researchers from the Japanese Atomic Energy Research Institute (JAERI) proposed [25] using pellets of higher-Z material (rather than D–T fuel pellets) in order to radiatively shut down a tokamak. These high-Z pellets later became known as "killer" pellets, for obvious reasons.

In the United States, development of pellet injectors mainly proceeded at the Oak Ridge National Laboratory under a group led by Stanley L. Milora. The first injection of pellets into a tokamak was conducted at Oak Ridge's ORMAK device [26], but with an addition of only 1% to the particle inventory of the plasma. An improved pellet injector [27] was deployed on the ISX-A tokamak [28], with density increases of up to 30% obtained after pellet injection without inducing a disruption. Finally, a greatly improved fast-opening magnetically-driven gas valve [29] was developed at Oak Ridge in the 1980s for use on pellet-injection guns.

In the 1990s, ITER proceeded to its Engineering Design Activity (EDA) phase, in which the parties developed the design (at the time, with a major radius of over 8 m) and considered many of the practical engineering issues which would have to be overcome in order to build and operate ITER. The first demonstrations of using "killer" pellets for radiative rapid shutdown of a tokamak were published at this time: first, on the Japanese tokamak JT-60U at Naka [30], followed by the German ASDEX Upgrade at Garching [31], and then on the American DIII-D at General Atomics in San Diego [32]. Meanwhile, the ITER team was adopting the "killer" pellet radiative rapid shutdown concept as part of their design; at one point, it was suggested that ITER use "killer" pellets for shutdown of *all* plasmas, even those that were not about to disrupt on their own [33].

Just around this time, however, the problem of runaway electrons in killer pellet injection (KPI) shutdowns became apparent [34]. This issue is discussed further in Section 2.9; it is sufficient to note here that runaway electrons are suppressed as electron density increases. A typical killer pellet contains approximately 1–5 × 10^{20} neon atoms [31, 32], and the electrons on these atoms are not all assimiliated by the plasma, which means that the plasma electron density does not rise very much during a killer pellet rapid shutdown. Of late, there has been much investigation [35, 36] on the DIII-D tokamak into using larger pellets of deuterium (D_2) and bouncing them off of a steel plate before directing them into the plasma. The small pieces of these "shattered pellets" are more readily absorbed by the plasma than traditional killer pellets are.

The idea of using *gas jets* for radiative rapid shutdown of a tokamak was developed, using the Oak Ridge gas valves originally designed for pellet injectors [37], on the DIII-D tokamak [38]. Thus was born the concept of *massive gas injection* (MGI) rapid shutdown.[4] The idea of using a fast gas valve for rapid shutdown was also suggested by a team on the German tokamak TEXTOR [39], but this experiment used small puffs of helium that barely exceeded the tokamak density limit, and could not properly be described as "massive" gas injection. In a series of experiments on DIII-D in 2001–2005, Whyte *et al.* showed [40, 41] that MGI led to improved conversion of plasma stored energy to radiation compared to KPI, as well as suppression of runaway electrons. Today, MGI is the leading candidate for radiative rapid shutdown of ITER and reactors.

2.5.2 Gas species injected

Noble gases (or hydrogen isotopes) are always used for MGI in order to avoid adsorption or chemical reaction with the plasma-facing first wall. This narrows down the choice of possible gases to the following: hydrogen (H_2), deuterium (D_2), helium, neon, argon, krypton, or xenon. (Radon is not considered for obvious reasons.)

In Figure 2-2(a), the line radiation coefficient L_{rad} is plotted for every relevant charge state of argon, neon, and helium. Radiated power density is calculated as $P_{rad} = L_{rad} n_e n_{cs}$, where n_e and n_{cs} are the electron and impurity charge state density, respectively. In an MGI rapid shutdown, the total free electron inventory is dominated by electrons stripped from impurities: $n_e \approx \sum n_{cs} Z_{cs}$, where Z_{cs} is the charge of that charge state. Thus in Figure 2-2(b), $L_{rad} \cdot Z_{cs}$ is plotted versus electron temperature for each charge state, in order to give a better indication of the true contribution to line radiation.

It can be seen from Figure 2-2 that the expected radiation is roughly 10–30 times higher for argon or neon than for helium. Thus, one would desire to use higher-Z noble gases for MGI rapid shutdown. However, this must be balanced against the delivery time of the gas: the heavier higher-Z gases have a lower speed of sound. The slower the travel time of the

[4] The concept was sometimes referred to as "HiPGI", for high-pressure gas injection. The standard term today, however, is MGI.

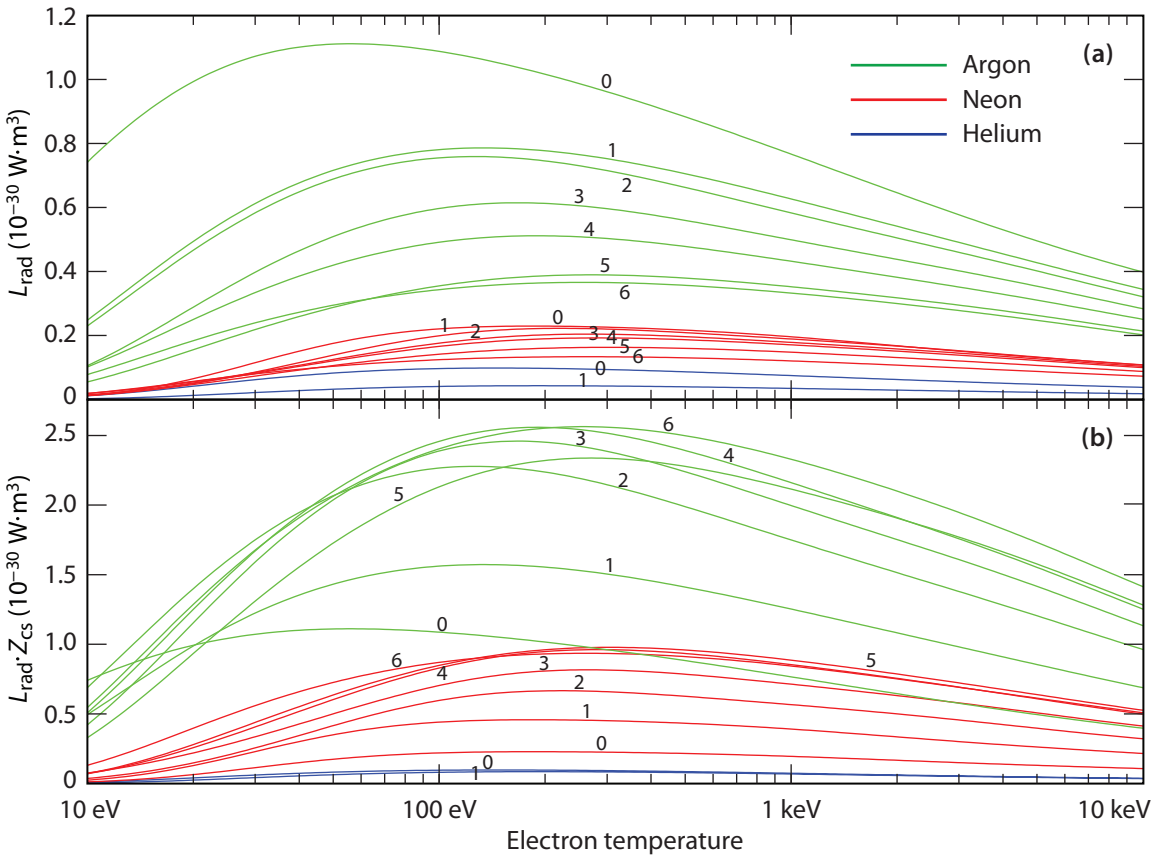

Figure 2-2 – **(a)** The line radiation coefficient L_{rad} is plotted for the each charge state of helium and the first six of charge states of argon and neon (these are the charge states present during a typical MGI rapid shutdown); **(b)** Each charge state's $L_{\mathrm{rad}} \cdot Z_{\mathrm{cs}}$, in order to account for the increased number of free electrons available when higher charge states are present. It can be seen that argon has more than an order of magnitude higher radiation than helium in the temperature range of 100 eV–1 keV. Each charge state is labeled; 0 refers to the neutral.

gas from the valve to the edge of the plasma, the more stringent the requirements on the notification time before a disruption that the disruption detection/prediction system (see Section 2.2) must give.

It was found in an experiment done on Alcator C-Mod [42] that *mixtures* of gases gave the best results. A small percentage of argon could be mixed with helium, and the mixed gas would have a sound speed nearly as high as that of pure helium. However, the small entrained fraction of argon would dominate the line radiation once the impurity gas was injected into the plasma. Based on the results of this experiment, rapid shutdown experiments on Alcator C-Mod are now typically carried out with a mixture of 15% Ar and 85% He. Experiments were also carried out on the TEXTOR tokamak with mixtures of gases; it was found there that an effective mixture was 15% argon in deuterium [43, 44].

Because argon-40 (which comprises 99.6% of natural argon) can, however, capture a neutron to become radioactive ^{41}Ar, it is anticipated that the ITER MGI rapid shutdown system will use either neon, or a mixture of neon with helium or deuterium.

2.6 Anatomy of a gas jet rapid shutdown

So far, we have discussed the idea of rapid shutdown in the abstract. Figure 2-3 shows several time series of actual plasma parameters during a massive gas jet rapid shutdown on Alcator C-Mod. The exact sequence of events that occurs during a gas jet rapid shutdown is still a matter of scientific debate (indeed, the purpose of this thesis is to answer some of these questions), but some things are generally accepted. The rapid shutdown begins when a signal is sent by the disruption mitigation system to the gas injector valve, located some meters away from the plasma edge. This valve opens rapidly[5] and the gas begins to travel down the pipe toward the plasma.

After a delay set by the transit time of the shock flow, which travels at three times the speed of sound for that gas [42], the impurity gas arrives at the plasma edge. The jet only penetrates the edge of the plasma; it does not penetrate to the core even in small tokamaks like C-Mod, and certainly will not in ITER. Originally, it was thought that the jet would penetrate the plasma to the point where the ram pressure of the jet was equal to the kinetic pressure of the plasma [40]; and thus a jet pressure of $\approx$ 100 kPa might be sufficient to allow penetration to the core of ITER. It was later found that the jet did not penetrate deeply into the C-Mod plasma [45]; the exact cause of shallow penetration is still under investigation at this time.

The arrival of the impurity gas jet at the edge of the plasma marks the beginning of the **pre-thermal quench** (pre-TQ) phase of the rapid shutdown. This can be seen in Figure 2-3(d) as the increase in radiation seen by a photodiode looking directly at the mouth of the gas jet. During this phase, the injected impurities rapidly ionize in the hot plasma, and begin

[5] The Oak Ridge–built valve used on C-Mod opens in less than 1 ms [29].

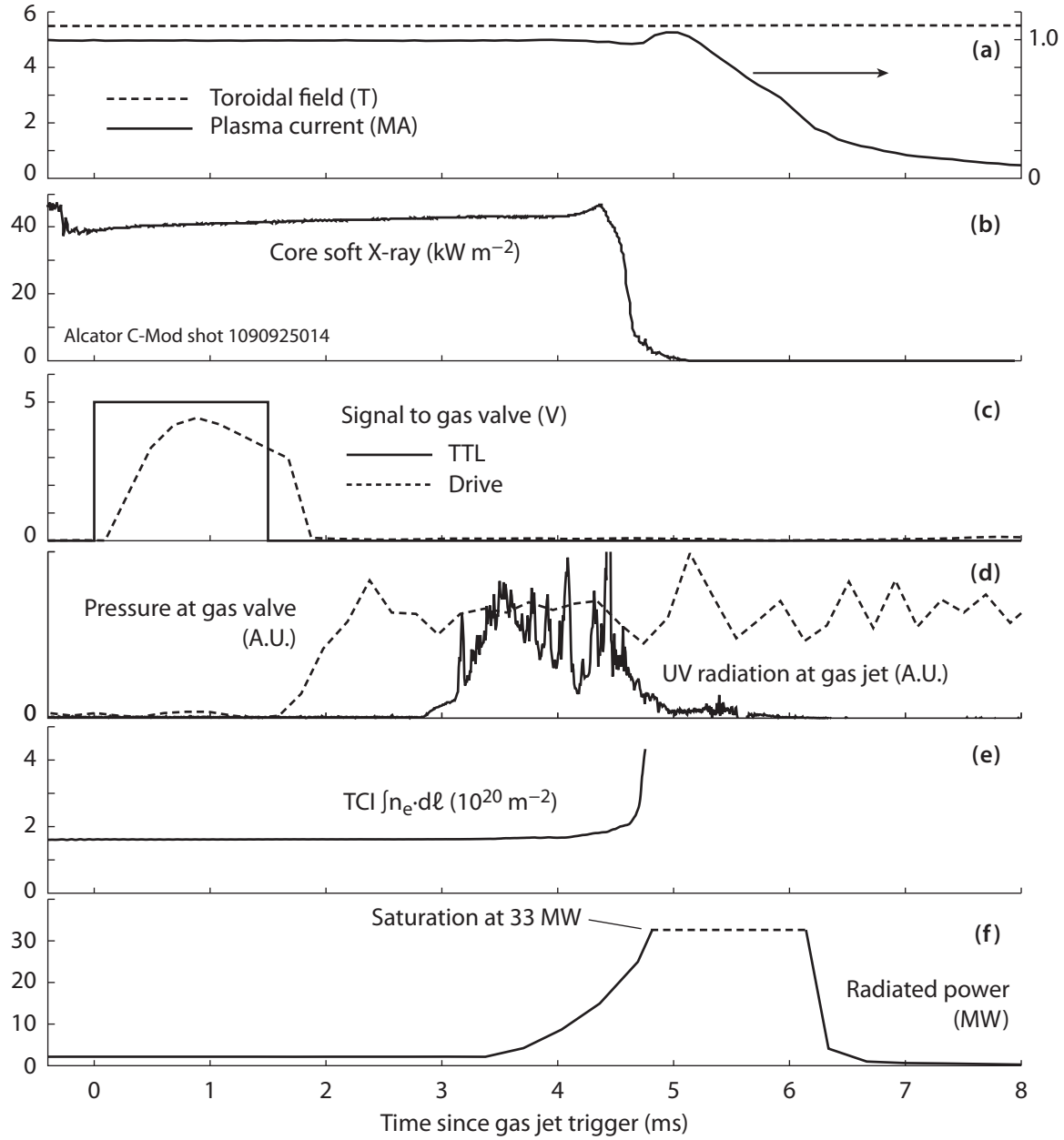

Figure 2-3 – Example traces of time series during massive gas injection rapid shutdown. From top: **(a)** Toroidal magnetic field, which remains essentially unchanged during the rapid shutdown sequence, and plasma current, which starts at its pre-disruptive value of 1.0 MA and resistively ramps down over a time scale of milliseconds; **(b)** Soft X-ray emissions from the core of the plasma, which act as a proxy for the core temperature (there is little SXR emission below ≈ 0.5 keV); **(c)** The logic signal and actual drive voltage to the gas injector valve; **(d)** Signal from a pressure transducer located just downstream of the gas injector valve, and radiation measured by a photodiode looking near the gas injector valve – the presence of a signal on this diode represents the arrival of the gas at the plasma edge; **(e)** Line-integrated plasma density as measured by two-color interferometry; and **(f)** Radiated power as measured by a foil bolometer. Note that slow time resolution of this bolometer prevents a true resolution of th radiated power during the fast thermal quench near 4.5 ms.

emitting line radiation at a levels that can approach several hundred megawatts per cubic meter of plasma. This rapidly cools the edge plasma wherever impurities are present. As the injected impurities are transported further in, an inward-moving *cooling front* is observed [46].

When this cooling front reaches a critical surface (thought to be the $q = 2$ surface; see [47] and Chapter 6 of this thesis), global (low-n) MHD modes are destabilized, and the **thermal quench** (TQ) phase of the rapid shutdown begins. This is manifested by a rapid drop in the core plasma temperature (see Figure 2-3(b) for a core soft X-ray signal as a proxy for core plasma temperature) and the reduction to essentially zero of the plasma stored energy. The TQ event also mixes the injected impurities throughout the core of the plasma, causing the spike in electron density seen in Figure 2-3(e). The plasma then undergoes a current rearrangement in which the peaked Ohmic current profile rearranges to a flat current profile [48], causing a "hump" (slight increase) in plasma current due to conservation of magnetic flux LI. This can be seen in Figure 2-3(a) at 5 ms.

At this point, the plasma is entirely cold, with a temperature set by a balance between Ohmic heating and line radiation: for typical injected impurities used in rapid shutdown, this is in the range of 2–6 eV [40]. The **current quench** (CQ) phase of the rapid shutdown then proceeds, in which the plasma resistively ramps down on its L/R timescale (L and R being the plasma inductance and loop resistance, respectively). During this time, the plasma control system attempts to maintain vertical control of the plasma. On Alcator C-Mod, the vertical control system is unable to control the plasma during this phase, but during MGI rapid shutdown, the plasma resistively ramps down in less time than it takes to drift vertically into the wall. Thus, it is valid to assume that the plasma resistively decays "in place" with only a few centimeters of vertical movement [45].

2.7 Unsolved problems for disruption mitigation and rapid shutdown

The scenario outlined in Section 2.6 can be considered the *ideal* version of how an MGI rapid shutdown will proceed. In reality, there are several open questions or problems with the technique, including:

- How early can the disruption be detected? How much warning time will be available?
- How close can the fast-opening gas valve be placed to the plasma, especially in a nuclear machine such as ITER or a fusion reactor? Is this valve compatible with neutron damage? Can it be maintained?
- How much gas can be injected before the thermal quench begins? Is this enough to cause the reduction in halo and vessel currents (versus an unmitigated disruption)

that MGI rapid shutdown is intended to cause?

- Can the torus pumping systems (cryopumps, turbopumps, and other vacuum-handling systems) handle the sudden influx of gas? On Alcator C-Mod, MGI rapid shutdowns can raise the torus pressure to a level of a few torr, up from its usual value of 10^{-8} torr (1 torr = 133.3 Pa).

But most pertinent for this work is the following open question: how *evenly* can the plasma stored energy be radiated onto the plasma-facing first wall? This issue is introduced in Section 2.8, and is the subject of the rest of this thesis.

2.8 Radiation asymmetry

Since the goal of massive gas injection is to benignly radiate the stored energy of the plasma over the entire surface of the plasma-facing wall, it is important that this radiation be *uniform*. After all, if all the energy were radiated onto a small portion of the wall, then MGI would be just as harmful to the device as an unmitigated disruption. Thus the uniformity, or *symmetry*, of the radiation during a gas jet rapid shutdown is a key figure of merit for the technique.

In this section, we will consider the radiation field inside the tokamak (Sections 2.8.1 and 2.8.2), and then relate that to the expected wall heating (Section 2.8.3). We will then discuss the practical measures of radiation asymmetry in use in experiments: asymmetry factors and peaking factors.

2.8.1 Total irradiance

The spectral radiance $L_{e\lambda}$ due to line radiation at some point inside the tokamak is a function of location, direction, wavelength, and time:

$$L_{e\lambda}\left(R, \phi, Z, \Omega, \lambda; t\right) = \frac{\mathrm{d}^3\Phi}{\mathrm{d}A\ \mathrm{d}\Omega\ \mathrm{d}\lambda} \tag{2.1}$$

where $L_{e\lambda}$ is the (triply-differential) spectral radiance $[\mathrm{W\,m^{-2}\,sr^{-1}\,m^{-1}}]$, (R, ϕ, Z) are the usual cylindrical coordinates, Ω is the direction of radiation through the point (expressed as a solid angle), λ is the wavelength $[\mathrm{m}]$, Φ is the radiant flux $[\mathrm{W}]$, $\mathrm{d}A$ is a differential unit of area $[\mathrm{m^2}]$, $\mathrm{d}\Omega$ is a differential unit of solid angle $[\mathrm{sr}]$, and $\mathrm{d}\lambda$ is a differential unit of wavelength $[\mathrm{m}]$.

For wall heating, the quantity of interest is the total irradiance E_e $[\mathrm{W\,m^{-2}}]$. This is the integral of the spectral radiance, integrated over the half-sphere at the wall ($\mathrm{d}\Omega = \sin\theta\,\mathrm{d}\theta\,\mathrm{d}\phi$),

and integrated over all wavelengths:

$$E_e = \int_0^\infty d\lambda \int_0^{2\pi} d\phi \int_0^{\pi/2} L_{e\lambda} \sin\theta \, d\theta \tag{2.2}$$

Ideally, one would like to know this quantity at every point on the wall, in order to calculate the wall heating due to radiation flux, and thus the risk of wall melting during a rapid shutdown. Measuring this quantity in an experiment would require a large number of 2π foil bolometers (that is, bolometers that view nearly an entire half-sphere) at many locations on the tokamak vessel wall. In practice, this is not possible due to cost, limited wall space, and the slow time response of foil bolometers (typically hundreds of milliseconds) [49].

2.8.2 Time integration of irradiance: radiant exposure

If we integrate the total irradiance in time, the result is the *radiant exposure*, H_e:

$$H_e = \int E_e \, dt \tag{2.3}$$

The units of H_e are energy per unit area $[\mathrm{J\,m^{-2}}]$. Because of their slow time constant, foil bolometers typically are used to measure the radiant exposure at a given point on the wall during a disruption, rather than the time-dependent irradiance.

2.8.3 Wall heating

Consider an infinite semi-plane of wall material, which is heated at its surface by radiation impinging on the wall, with irradiance E_e $[\mathrm{W\,m^{-2}}]$. (The definition of E_e is discussed in Section 2.8.1.) A diagram of the situation is shown in Figure 2-4.

Conduction of heat in the wall is assumed to be linear (that is, Fourier's law $\vec{q} = -k\nabla T$ holds), and thus the flow of heat in the wall is given by the one-dimensional heat equation:

$$\frac{\partial T}{\partial t} = \frac{k}{\rho C_p} \frac{\partial^2 T}{\partial x^2} \tag{2.4}$$

where T is the temperature in the wall material $[\mathrm{K}]$, k is the thermal conductivity of the wall material $\left[\mathrm{W\,m^{-1}\,K^{-1}}\right]$, ρ is the density of the wall material $[\mathrm{kg\,m^{-3}}]$, C_p is the heat capacity of the wall material $\left[\mathrm{J\,kg^{-1}\,K^{-1}}\right]$, and x and t are the space $[\mathrm{m}]$ and time $[\mathrm{s}]$ coordinates, respectively. The wall material is assumed to occupy the semi-infinite space $x > 0$, where x is the depth into the material. In fusion reactors and ITER, the thickness of the actively cooled plasma-facing materials is millimeters to centimeters, which is effectively infinite

for the timescales (milliseconds) considered for the thermal quench of disruptions. If a very short pulse of heat H_e [J m^{-2}] is applied to the surface, the resulting temperature distribution in the semi-infinite material is given by:

$$T(x,t) = T_0 + \frac{H_e}{\sqrt{\pi\alpha t}\,\rho C_p} \exp\left(-\frac{x^2}{4\alpha t}\right) \tag{2.5}$$

where $\alpha = k/\rho C_p$ is the thermal diffusivity [m^2 s^{-1}] and T_0 is the temperature of the wall material before the heat pulse is applied. It can be verified that this is the correct solution by showing the energy in the wall material $\int_0^\infty \rho C_p (T - T_0)\,dx = H_e$ is equal to the applied energy, *i.e.* the radiant exposure H_e.

The condition for the solution given in Equation 2.5 to be valid is that the heat pulse must be of short duration compared to the time constant of the material $\tau = d^2/4\alpha$ where d is the distance over which the heat is deposited into the material of interest, and α is the thermal diffusivity.

In this case, for a fixed wall material (fixed k, ρ, and C_p), for very short heat pulses, the peak temperature rise at the surface will be approximately given by:

$$\lim_{t\to 0} (T(x,t) - T_0)|_{x=0} = \frac{1}{\sqrt{\pi k \rho C_p}} \frac{H_e}{\sqrt{t}} \propto \frac{H_e}{\sqrt{t}} \tag{2.6}$$

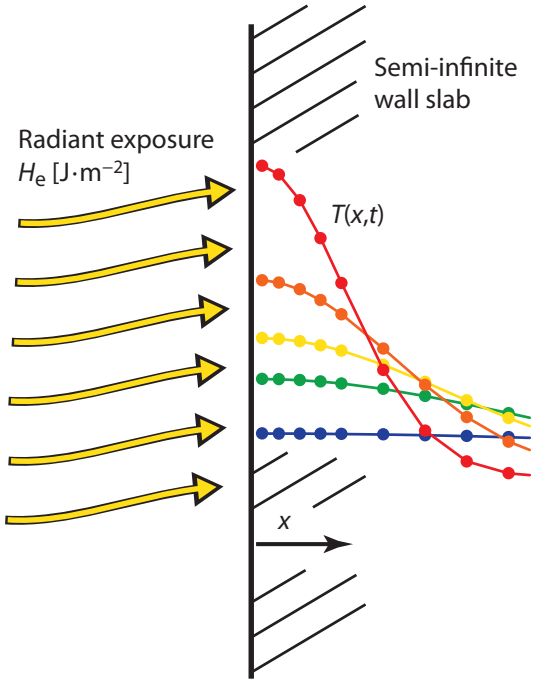

Figure 2-4 – One-dimensional wall-heating schematic assuming delta-function (pulse) wall heating waveform in time.

That is, the temperature rise is proportional to the deposited energy (radiant exposure), and inversely proportional to the square root of the energy pulse duration. If the starting temperature of the wall material, radiant exposure, heat pulse duration, and the properties of the wall material are all known, it is possible to calculate whether the wall material will melt during the gas jet rapid shutdown.

2.8.4 Size scaling of TQ and CQ heat loads

As discussed in Section 2.8.3, the peak temperature rise on the wall is proportional to the radiant exposure H_e and inversely proportional to the square root of the heat pulse duration.

Assuming a separation of the sequence of events into a discrete thermal quench (TQ), in which the stored *thermal* energy of the plasma is radiated to the wall, and a current quench (CQ), in which the stored *poloidal magnetic* energy of the plasma is radiated to the wall, we can examine how the wall heating scales as the major radius of the tokamak is changed.

For constant plasma conditions (same plasma pressure and shape), the plasma stored thermal energy scales simply as the volume of the plasma, $W_{\text{th}} \sim R^3$, where R is the plasma major radius [m]. The surface area of the plasma-facing first wall scales as the square of the plasma major radius, $A_{\text{wall}} \sim R^2$. Thus, for a given plasma pressure profile, radiation asymmetry, temporal profile of the radiation, and radiated energy fraction, the radiant exposure H_{e} in the TQ will scale linearly with the machine size: $H_{\text{e}} \sim R$. Of course, in reality, the plasma in large machines like ITER is hotter and higher pressure than in smaller machines,[6] so this scaling is actually somewhat worse: $H_{\text{e}} \sim R^n$, where $n \gtrsim 1$.

The duration of the thermal quench is discussed in further detail in Section 2.8.5; it suffices for this argument to note that it is consistent with current experimental observations that the TQ duration *does not scale with machine size*, so that the stored thermal energy of the plasma is released in approximately the same amount of time on machines of all sizes. In this worst-case (non-)scaling of TQ duration, then, the wall temperature rise in the thermal quench is simply proportional to the machine major radius: about a factor of nine larger for ITER than for Alcator C-Mod!

In contrast, the duration of the current quench in rapid shutdowns is set by the $L/\mathfrak{R}$ time constant of the decaying plasma current. (Here $\mathfrak{R}$ represents the plasma loop resistance, as opposed to R, which is the plasma major radius.) The inductance is given for a circular toroid by $L = \mu_0 R \left[\ln\left(8R/a\right) - 2 + \ell_{\text{i}}\right]$, where R and a are the major and minor radius of the plasma, respectively, and ℓ_{i} is the internal inductance (0 for skin current, 0.25 for uniform current profile; typically $\ell_{\text{i}} \lesssim 0.5$). For constant plasma shape, then, $L \sim R$.

The temperature of the post-thermal-quench plasma is very tightly pinned to a value that is set by the injected impurity species; it is only logarithmically sensitive to the density of impurities [40]. For argon, this temperature is approximately 2 eV. In this case, the plasma resisitivity in the CQ is constant, and thus the loop resistance varies as $\mathfrak{R} \sim 2\pi R/\kappa\pi a^2 \sim R^{-1}$ at constant plasma shape. The duration of the CQ thus scales as the plasma cross-sectional area: $\tau_{\text{CQ}} \sim R^2$.

The plasma *poloidal magnetic* energy is equal to LI_{p}^2; recall that $L \sim R$ and the plasma current $I_{\text{p}} \sim R$ as well (at constant magnetic safety factor q and toroidal field strength B_ϕ); this means that poloidal magnetic energy scales as the plasma volume: $W_{\text{mag}} \sim R^3$, just like the plasma stored thermal energy. Thus, the radiant exposure H_{e} at the wall scales linearly with machine size: $H_{\text{e}} \sim R$.

[6] ITER IPB98(y,2) energy confinement scaling [50, Equation 20 in Section 6.3.1]: $\tau_{\text{E}} \sim I_{\text{p}} R^2 P^{-3/4}$, and $I_{\text{p}} \sim R$, $P \sim R^3$, so $\tau_{\text{E}} \sim R^{3/4}$, and so $\langle T \rangle \sim R^{3/4}$ at constant plasma electron density, toroidal field, and heating power density. Note that Alcator C-Mod has similar electron density and toroidal field as ITER, but C-Mod's heating power density $\left[\text{W m}^{-3}\right]$ is much larger, even when heating from fusion alphas is included on ITER.

The net effect is that for the CQ, the wall temperature rise expected is approximately independent of machine size, since $H_e/\sqrt{\tau_{CQ}} \sim R/\sqrt{R^2} \sim R^0$. The conclusion is that if the wall radiation during the current quench of rapid shutdowns does not melt the wall in current machines (and it does not), then it likely will not in larger machines like ITER or reactors. Thus, the main concern is with the wall heat loading (radiant exposure) during the thermal quench, and not the current quench.

2.8.5 The duration of the thermal quench

The duration of the thermal quench in unmitigated disruptions and in rapid shutdowns is subject to considerable uncertainty, both because of a vague definition of the TQ, as well as large variation in the measured data. In unmitigated disruptions, the thermal quench may proceed in two distinct phases: a first, in which some of the core plasma energy redistributes to the edge plasma, and then a second "fast drop" phase in which the remaining energy is lost to the plasma-facing first wall. A database of thermal quench durations was created for the ITER EDA [51, Figure 54], and a line was drawn through the data indicating that $\tau_{TQ} \sim a$; that is, the TQ duration scales with the plasma minor radius. But the data had wide scatter: the mean TQ duration on Alcator C (a = 0.16 m) was as long as that on JET (a = 0.96 m). Furthermore, a more detailed study [52] of unmitigated ITB-collapse and VDE disruptions on JET showed a huge variation in TQ duration, from 0.05 ms to 3 ms (a factor of 60). In Alcator C-Mod, the mean length of the initial radiation flash in unmitigated disruptions is 160 μs, but with large scatter, ranging from 40–520 μs [53].

Turning to rapid shutdown (mitigated disruptions), early scoping studies for ITER disruption mitigation [54] tended to assume that the TQ duration in ITER would be set by a simple power balance: how long it would take to radiate the stored energy away given an even distribution of injected impurities throughout the core plasma. At the time, the only rapid shutdown experiments that had been conducted were those using killer pellets; the technique of massive gas injection was only just then being developed on DIII-D. Since then, results from MGI experiments at tokamaks around the world have indicated what can be expected for the length of the thermal quench: DIII-D reports TQ durations of 1–2 ms [47, Figure 3] based on core electron cyclotron emission. JET reports pre-TQ durations of 4–10 ms and a TQ duration of approximately 2 ms [55, Figure 3], based on core soft X-ray emission. In Alcator C-Mod, the TQ length as defined by the initial radiation flash and the fall of core soft X-ray emission, was 140 ± 20 μs [53].

The work in this thesis suggests a scaling with machine size for the duration of the TQ in gas jet rapid shutdowns; this impacts the allowable radiation peaking factor (see Section 2.8.6). This scaling is discussed further in Section 9.1.2. In addition the implications of using a too-simple pre-TQ/TQ/CQ taxonomy for MGI rapid shutdown are discussed in Section 6.5.

2.8.6 Radiation peaking factor in the TQ

As is often the case, the naïve assumption in the case of gas jet rapid shutdown is the most optimistic: that the energy radiated in the TQ is completely symmetric, shining with equal brightness at every point on the plasma-facing first wall. In practice, this is not the case: the radiation is asymmetric. Experimental observations of radiation peaking are discussed further in Section 2.8.9. First, though, turning to engineering considerations, we will discuss *how* asymmetric the radiation can be in reactor-class devices without melting the wall.

The *allowable* radiant exposure at the wall can be calculated, given assumptions about the wall material (its thermal conductivity and heat capacity, melt temperature, etc.), the temperature of the wall prior to the thermal quench, and the duration of the thermal quench. Because the *total* amount of energy to be radiated is known, and the area of the wall is known, this means that the *average* radiant exposure over the entire wall is known. Thus, one can normalize the *maximum* radiant exposure (if wall melting or ablation is to be entirely avoided, only the *maximum* radiant exposure is significant) to the *average* radiant exposure over the entire wall. This quantity is referred to as a *peaking factor* (PF).

Various incarnations of this calculation have been carried out for ITER; the first published was that of Kuteev *et al.* [56]. This study considered the ITER design at that time (R_0 = 8.11 m, W_{th} = 1.27 GJ) and assumed a pellet of frozen noble gas (Ne, Ar, Kr, or Xe) would be injected. The authors calculated the duration of the thermal quench using a simple model in which the only terms in the plasma power balance are Ohmic heating and impurity radiation due to the injected pellet.[7] The authors found that the thermal quench would last approximately 10 ms, and that the beryllium plasma-facing wall would not melt.

A slightly more realistic treatment was given in Chapter 3 of the original ITER Physics Basis (IPB), published in a special issue of *Nuclear Fusion* in 1999 [51, Section 4.5.3.2]. In this work, the authors reviewed the data that had been collected on rapid shutdown experiments using "killer" pellets. Based on these data, which were largely based on slow time-resolution foil bolometers and divertor IR thermography, they assumed that the entire thermal and magnetic stored energy of the plasma were radiated on the time scale of the *entire* rapid shutdown, which for ITER, was calculated to be well over 10 ms. Under these conditions, and with a "modest" PF of less than 2.0, the authors concluded that radiation during rapid shutdowns would be "comfortably clear" of the wall melting threshold.

Over the subsequent eight years, ITER was redesigned to be smaller (R_0 = 6.2 m [57], $W_{th} \simeq$ 350 MJ [58]), and the technology of disruption mitigation and rapid shutdown was further developed on tokamaks around the world. The technique of using high-pressure gas jets instead of "killer" pellets for impurity injection for rapid shutdown was developed on the DIII-D tokamak during this time period [40].

[7] The justification for this is that the time scales of interest are much less than the (pre-disruptive) energy confinement time of the plasma.

These developments were incorporated into two documents which, for the first time, properly stated the risk of melting large areas of the ITER beryllium first wall *even in the case of a successful rapid shutdown*. These were Chapter 3 of the updated ITER physics basis (published as "Progress in the ITER Physics Basis", again in a special issue of *Nuclear Fusion*, in 2007 [59]), and an investigation by Sugihara *et al.* at the ITER Naka Joint Work Site [60].

In the updated IPB, the authors note that "elementary calculations show that the minimum deposition time for uniform radiation of the full W_{th} to a beryllium first-wall should be $\gtrsim 0.6$ ms if surface melting is to be avoided." This represented an important recognition that the TQ time scale was the important time scale for wall melting.

The most detailed study of the allowable PF for ITER was published in 2007 by Sugihara *et al.*. In this study, the authors simulated several types of mitigated and unmitigated disruptions (VDEs and high-beta disruptions), and calculated the expected heat load on the beryllium wall tiles and tungsten divertor modules due to direct plasma contact and due to radiation (in the case of mitigated disruptions). While they note that mitigating VDEs is realistic due to the long time scale of plasma vertical displacement in ITER (over 0.5 seconds), they also point out that extensive wall melting of beryllium tiles can occur if the radiation PF is over 2.0, at a TQ duration of 1.0 ms.

2.8.7 Allowable peaking factor in C-Mod and ITER

In the worst case for wall melting (which is the *best* case for divertor heat load mitigation!) the *average* energy radiated in the TQ is simply the total stored thermal energy of the plasma: $W_{rad} = W_{th}$. In this case, the radiant exposure $H_e = W_{th}/A_{wall}$, where A_{wall} is the wall area exposed to the radiation flux during the TQ. Then, using Equation 2.6, with the temperature set at the melt temperature of the material at the location of the peak radiant exposure:

$$\frac{1}{\sqrt{\pi k \rho C_p}} \frac{W_{th} \cdot PF}{A_{wall}\sqrt{\tau_{TQ}}} \leq T_{melt} - T_0$$

$$PF \leq \sqrt{\pi k \rho C_p}\sqrt{\tau_{TQ}} \cdot \frac{A_{wall}}{W_{th}} \cdot (T_{melt} - T_0) \tag{2.7}$$

The results for Alcator C-Mod and ITER are shown in Table 2-1. Compared to the more detailed one-dimensional heat transfer simulations conducted in [60], this simple calculation slightly overestimates the allowable PF. In reality, it will be necessary to have a TQ radiation peaking factor of less than approximately 2.0 to avoid melting of the beryllium wall.

In contrast, Alcator C-Mod suffers no such limitation, mainly because of the much lower ratio of plasma stored energy to wall area, and higher melt temperature of Alcator C-Mod's molybdenum alloy tiles compared to ITER's beryllium tiles. It should be noted that in this

Tokamak		Alcator C-Mod	ITER
Plasma-facing wall material		TZM (Mo alloy)	Beryllium
Thermal conductivity ($\mathrm{W\,m^{-1}\,K^{-1}}$)	k	80.4	92.1
Density ($\mathrm{kg\,m^{-3}}$)	ρ	1.022×10^4	1.848×10^3
Heat capacity ($\mathrm{J\,kg^{-1}\,K^{-1}}$)	C_p	372	3026
Melt temperature (K)	T_melt	2820	1551
Pre-TQ temperature (K)	T_0	≈ 1000	590 [60]
TQ duration (s)	τ_TQ	3×10^{-4}	1.0×10^{-3}
Plasma-facing wall area	A_wall	6.7 [61]	700
Plasma thermal energy (J)	W_th	1.5×10^5	3.5×10^8
Avg. radiant exposure ($\mathrm{J\,m^{-2}}$)	H_e	2.2×10^4	5.0×10^5
Allowable peaking factor	PF	44	2.4

Table 2-1 – Comparison of representative wall conditions in Alcator C-Mod and ITER. Properties for molybdenum alloy TZM at 2000 K and beryllium at 1000 K from Karditsas & Baptiste [62]. TQ duration for ITER is that assumed by Sugihara *et al.* [60]; TQ duration is typical for gas jet rapid shutdowns in Alcator C-Mod. Average radiant exposure is calculated for uniform radiation over entire plasma-facing first wall surface.

calculation, the Alcator C-Mod wall was assumed to start the disruption at 1000 K: this is a representative temperature of a divertor or limiter tile on C-Mod, and overestimates the temperature of inner wall tiles. Thus, the above calculation is pessimistic (conservative) for C-Mod.

2.8.8 Measurements of the peaking factor

In Sections 2.8.6 and 2.8.7, it was noted that the *allowable* PF for ITER can be calculated through elementary considerations. But what will the PF actually *be* on ITER? The typical way in which questions of this type are answered is to do experiments on today's tokamaks, and determine the way in which the results scale to a reactor-class tokamak like ITER. However, because the radiation during the thermal quench varies in time (it is not a constant power through the entire TQ), and it is impossible to cover the entire wall with radiation detectors (bolometers or photodiodes), we must define proxies that can actually be measured in experiments.

The time-averaged radiation peaking factor PF can be defined as the highest value of the *time integral* of the normal radiation power flux witnessed at each wall location, divided by the time integral of the average outward normal radiation power flux over the entire wall:

$$\overline{\mathrm{PF}} = \frac{\left[\int Q_{\mathrm{rad}}\,\mathrm{d}t\right]_{\mathrm{peak}}}{\int \langle Q_{\mathrm{rad}}\rangle\,\mathrm{d}t} = \frac{H_{\mathrm{e}}|_{\mathrm{peak}}}{\langle H_{\mathrm{e}}\rangle} \tag{2.8}$$

where Q_{rad} is the incident radiation power flux, integrated over all radiation wavelengths, at the wall, and the angle brackets denote spatial averaging over the plasma-facing wall surface. Note that if all stored thermal energy is radiated, $\int \langle Q_{\mathrm{rad}}\rangle\,\mathrm{d}t = W_{\mathrm{th}}/A_{\mathrm{wall}}$. The limits of (time) integration are usually taken to be the thermal quench (TQ) phase of the mitigated disruption, because as was discussed in Section 2.8.4, the TQ radiation is more important for wall melting in reactor-class devices than the radiation in the CQ. It will, however, be important in future studies to consider the radiant heating through the beginning of the current quench, as the highest instantaneous radiation rates are expected at this time (see Section 5.2.7 for discussion of why this is not observed on AXUV diodes), and the wall will have already been preheated by the TQ radiation.

The radiation field at the wall can, in principle, be different at every toroidal and poloidal location. As with many quantities which vary in toroidal and poloidal angle, one can represent the quantity as a Fourier expansion in sinusoids.

If one averages the radiation over poloidal angle θ, one can define a (time-averaged) *toroidal* peaking factor:

$$\overline{\mathrm{TPF}} = \frac{\left[\int\int Q_{\mathrm{rad}}\,\mathrm{d}t\,\mathrm{d}\theta\right]_{\mathrm{peak}}}{\int\int \langle Q_{\mathrm{rad}}\rangle\,\mathrm{d}t\,\mathrm{d}\theta} \tag{2.9}$$

Calculating the quantity $\overline{\mathrm{TPF}}$ given in Equation 2.9 would require measuring the radiation intensity at every toroidal location. If measurements are instead made at only discrete toroidal locations, the calculated TPF will constitute a lower limit on the true TPF.

2.8.9 Previous observations of radiation asymmetry

The first observations of radiation asymmetry through the thermal quench on Alcator C-Mod were made by Reinke *et al.* [63], who investigated the spatial pattern of radiation during a single MGI rapid shutdown,[8] using four 22-channel AXUV diode arrays. (Details of AXUV diode hardware are discussed further in Chapter 3.) It was observed that the instantaneous brightness ratio of opposite-facing view chords with equal tangency radius and vertical coordinate ranged from 0.4–4.0. However, for *this particular shutdown*, the disruption-integrated radiation asymmetry on these two opposite-facing chords was less than 25%.

Poloidal radiation asymmetry during MGI rapid shutdowns was investigated on the JET

[8] Alcator C-Mod shot 1071220025.

tokamak (with the Mark II HD divertor configuration, operated 2006–2009) by Huber *et al.* [64] using several poloidal fans of foil bolometers with approximately 1 ms time resolution [65] at a single toroidal location. This was built upon by Lehnen *et al.* [55], who also investigated the *toroidal* radiation asymmetry using a pair of fast-framing visible-light camera. The authors calculate an upper limit on the TPF of approximately 5.0 during the TQ, and a poloidal peaking factor of approximately 2.0, well above the limit for which the ITER wall would melt. However, it is important to note that these peaking factors are calculated based on the brightnesses seen by different lines of sight (pixels) on the camera view; this is an extremely pessimistic assessment of the peaking factor *at the plasma-facing wall*.

The rationale behind the hardware used for this thesis is discussed in Chapter 3. It is important to note, however, that there have been no previous observations of toroidal radiation asymmetry in MGI rapid shutdowns using dedicated, toroidally-separated photodiodes.

2.9 Runaway electrons in rapid shutdown

The theory behind runaway electrons was introduced in Section 1.2.3. Creation of runaways is also a problem in rapid shutdowns. Indeed, the post-TQ plasma in a rapid shutdown is colder than the post-TQ plasma in an unmitigated disruption, and has a commensurately higher electrical resistance and thus higher loop voltage for a given pre-disruption plasma current. As was discussed in Section 2.5.1, the presence of runaway electrons in KPI rapid shutdown was one of the motivations for creating the MGI technique. However, runaway electrons can still be created on some tokamaks after massive gas injection. For example, runaway electrons carrying up to 30% the original plasma current were seen after argon injection in TEXTOR [43]. Runaway electrons can be produced after massive gas injection in DIII-D [36] by reducing the amount of injected impurities; these runaway beams are then controlled by the PCS [66] as part of a runaway mitigation scheme.

More ominously for ITER, extended MHD simulations indicate [67] that runaway confinement increases super-linearly with machine size, such that no runaways would be expected after MGI in C-Mod, runaways are reasonably well confined after MGI in DIII-D—these two predictions are borne out in experiments—and runaways would be *extremely* well confined in ITER. It may be possible for a significant fraction of the 15 MA plasma current in a full-performance ITER discharge to be converted into relativistic runaways. Thus, understanding the physics of runaway confinement during MGI rapid shutdown, and ensuring that significant populations of runaway electrons are not created or confined, will be essential for a reliable disruption mitigation system in ITER or a reactor.

2.10 Halo and vessel currents in rapid shutdown

While MGI is proven to reduce halo currents compared to unmitigated disruptions [55], electromagnetic forces can still be a problem in larger machines and at higher toroidal magnetic field strengths. Because the post-TQ plasma is so cold in MGI rapid shutdowns compared to unmitigated disruptions, the L/R timescale over which the current ramps down in the CQ is very short. This causes a large toroidal electric field (loop voltage) to be generated, and a commensurately large toroidal vessel current to be induced. Thus is it is actually possible to have *too short* of a CQ time. In ITER, the goal is to have a CQ time of 50–150 ms [68]; shorter than 40 ms means that electromagnetic loads on the vessel will be unacceptable.

2.11 Motivation for this work

While there are many open challenges to making a reliable disruption mitigation system for a tokamak fusion reactor, this work focuses on radiation asymmetry in the thermal quench: what causes it, and what can be done about it. The world's first multi-gas-jet massive gas injection system was installed on the Alcator C-Mod tokamak; and dedicated diagnostics were built to study the radiation pattern during the TQ of gas jet rapid shutdowns; this is described in Chapter 3. The experimental program is described in Chapter 4. The experimental observations are presented in Chapter 5, and the remaining chapters contain the interpretation of the data. Finally, the work is summarized and the implications for ITER and reactors are discussed in Chapter 9.

References

[1] Snipes, J.A. *et al.* (2012). "Actuator and diagnostic requirements of the ITER Plasma Control System." *Fusion Engineering and Design* **87**(12), 1900–1906. doi:10.1016/j.fusengdes.2012.04.002

[2] ITER Plant Control Design Handbook, version 6.1 (11 Mar 2011). Available online at http://static.iter.org/codac/pcdh/PCDH_v6_1.pdf

[3] Scibile, L. *et al.* (2009). "An overview of the ITER interlock and safety systems." In *Proceedings of the 12th International Conference on Accelerator and Large Experimental Physics Control Systems*, Kobe, Japan, October 12–16, 2009. Paper WEC005, pp. 403–405. Available online at http://accelconf.web.cern.ch/accelconf/icalepcs2009/papers/wec005.pdf

[4] "Nuclear power plants—Instrumentation and control important to safety—General requirements for systems." IEC standard 61513, edition 2.0, August 25, 2011.

[5] Granetz, R.S. *et al.* (1990). "Magnetic diagnostics in Alcator C-MOD." *Review of Scientific Instruments* **61**(10), 2967–2969. doi:10.1063/1.1141741

[6] Reux, C. *et al.* (2013). "Use of the disruption mitigation valve in closed loop for routine prediction at JET." *Fusion Engineering and Design*, article in press (corrected proof). doi:10.1016/j.fusengdes.2012.12.026

[7] Taylor, T.S. (1997). "Physics of advanced tokamaks." *Plasma Physics and Controlled Fusion* **39**(12B), B47–B73. doi:10.1088/0741-3335/39/12B/005

[8] Wróblewski, D. *et al.* (1997). "Tokamak disruption alarm based on a neural network model of the high-β limit." *Nuclear Fusion* **37**(6), 725–741. doi:10.1088/0029-5515/37/6/I02

[9] Pautasso, G. *et al.* (2001). "Prediction and mitigation of disruptions in ASDEX Upgrade." *Journal of Nuclear Materials* **290–293**, 1045–1051. doi:10.1016/S0022-3115(00)00546-8

[10] Humphreys, D.A. *et al.* (2007). "Development of ITER-relevant plasma control solutions at DIII-D." *Nuclear Fusion* **47**(8), 943–951. doi:10.1088/0029-5515/47/8/028

[11] Esposito, B. *et al.* (2008). "Disruption avoidance in the Frascati Tokamak Upgrade by means of magnetohydrodynamic mode stabilization using electron-cyclotron-resonance heating." *Physical Review Letters* **100**(4), 045006 (4 pp). doi:10.1103/PhysRevLett.100.045006

[12] Humphreys, D.A. *et al.* (2006). "Active control for stabilization of neoclassical tearing modes." *Physics of Plasmas* **13**(5), 056113 (9 pp). doi:10.1063/1.2173606

[13] Isayama, A. *et al.* (2003). "Achievement of high fusion triple product, steady-state sustainment and real-time NTM stabilization in high-β_p ELMy H-mode discharges in JT-60U." *Nuclear Fusion* **43**(10), 1272–1278. doi:10.1088/0029-5515/43/10/031

[14] Esposito, B. *et al.* (2009). "Disruption control on FTU and ASDEX Upgrade with ECRH." *Nuclear Fusion* **49**(6), 065014 (10 pp). doi:10.1088/0029-5515/49/6/065014

[15] "Research needs for magnetic fusion energy sciences." Report of the Research Needs Workshop (ReNeW), Bethesda, MD, USA, June 8–12, 2009. Available online at http://burningplasma.org/web/renew.html

[16] Wesley, J. (2010). "Disruption avoidance and mitigation challenges for ITER and beyond." Presentation at the 15th Workshop on MHD Stability Control and Joint U.S.–Japan Workshop, Madison, WI, USA, November 15–17, 2010. Available online at https://fusion.gat.com/conferences/mhd10/talks/Wesley.pdf

[17] Campbell, D.J. (2012). "The ITER research plan." Presentation given at the ITER Town Meeting at the 24th IAEA Fusion Energy Conference, San Diego, CA, USA, October 8–13, 2012. Available online at http://www.iter.org/doc/www/content/com/Lists/Stories/Attachments/1361/David2.pdf

[18] Shoucri, M.M. *et al.* (1990). "A study of the Tokamak de Varennes plasma during fast current ramp-down: Experiment and simulation results with the TSC code." *Nuclear Fusion* **30**(12), 2563–2573. doi:10.1088/0029-5515/30/12/010

[19] Mitarai, O. *et al.* (1993). "Experiments on the current rampdown phase in the STOR-M tokamak for AC operation." *Plasma Physics and Controlled Fusion* **35**(6), 711–722. doi:10.1088/0741-3335/35/6/005

[20] Spitzer, L. *et al.* (1954). "Problems of the stellarator as a useful power source." (278 pp). Project Matterhorn Report PM-S-14, later published as U.S. AEC Report NYO-6047. OSTI ID 4294054.

[21] Taylor, A.F.D.S. (1969). "A solid hydrogen pellet launcher." *Journal of Physics E: Scientific Instruments* **2**(8), 696–700. doi:10.1088/0022-3735/2/8/323

[22] Jørgensen, L.W. *et al.* (1975). "Ablation of hydrogen pellets in hydrogen and helium plasmas." *Plasma Physics* **17**(6), 453–461. doi:10.1088/0032-1028/17/6/005

[23] Turnbull, R.J. (1978). "Review of pellet fueling." In *Proceedings of the Fusion Fueling Workshop*, held at Princeton University, Princeton, NJ, USA, November 1–3, 1977, pp. 86–89. DOE report number CONF-771129, OSTI ID 7018374. Available online at http://www.osti.gov/energycitations/product.biblio.jsp?osti_id=7018374

[24] Kulcinski, G.L. (1974). "Technology of controlled nuclear fusion: Report on the First Topical Meeting, held at San Diego, Calif., USA, 16–18 April 1974." *Nuclear Fusion* **14**(4), 561–567. doi:10.1088/0029-5515/14/4/013

[25] Yamato, H. & Ohta, M. (1974). "Ignition, fueling and shutdown of a D–T fusion plasma." In *Proceedings of the First Topical Meeting on the Technology of Controlled Nuclear Fusion*, April 16–18, 1974, pp. 123–124. Published by the American Nuclear Society, 1974.

[26] Foster, C.A. *et al.* (1977). "Solid hydrogen pellet injection into the ORMAK tokamak." *Nuclear Fusion* **17**(5), 1067–1075. doi:10.1088/0029-5515/17/5/017

[27] Milora, S.L. & Foster, C.A. (1979). "Pneumatic hydrogen pellet injection system for the ISX tokamak." *Review of Scientific Instruments* **50**(4), 482–487. doi:10.1063/1.1135856

[28] Milora, S.L. *et al.* (1979). "Hydrogen-pellet fueling experiments on the ISX-A tokamak." *Physical Review Letters* **42**(2), 97–101. doi:10.1103/PhysRevLett.42.97

[29] Milora, S.L. *et al.* (1986). "Fast-opening magnetic valve for high-pressure gas injection and applications to hydrogen pellet fueling systems." *Review of Scientific Instruments* **57**(9), 2356–2358. doi:10.1063/1.1138677

[30] Yoshino R. *et al.* (1997). "Fast plasma shutdown by killer pellet injection in JT-60U with reduced heat flux on the divertor plate and avoiding runaway electron generation." *Plasma Physics and Controlled Fusion* **39**(2), 313–332. doi:10.1088/0741-3335/39/2/008

[31] Pautasso, G. *et al.* (1996). "Use of impurity pellets to control energy dissipation during disruption." *Nuclear Fusion* **36**(10), 1291–1297. doi:10.1088/0029-5515/36/10/I02

[32] Evans, T.E. *et al.* (1997). "Measurements of non-axisymmetric halo currents with and without 'killer' pellets during disruptions in the DIII-D tokamak." *Journal of Nuclear Materials* **241–243**, 606-611. doi:10.1016/S0022-3115(97)80108-0

[33] Fisher, R.K. *et al.* (1997). "Alpha diagnostics using pellet charge exchange: Results on the Tokamak Fusion Test Reactor and prospects for ITER." *Review of Scientific Instruments* **68**(1), 336–339. doi:10.1063/1.1147863

[34] Rosenbluth, M.N. *et al.* (1997). "Liquid jets for fast plasma termination in tokamaks." *Nuclear Fusion* **37**(7), 955–966. doi:10.1088/0029-5515/37/7/I04

[35] Commaux, N. *et al.* (2010). "Demonstration of rapid shutdown using large shattered deuterium pellet injection in DIII-D." *Nuclear Fusion* **50**(11), 112001 (4 pp). doi:10.1088/0029-5515/50/11/112001

[36] Hollmann, E.M. *et al.* (2010). "Experiments in DIII-D toward achieving rapid shutdown with runaway electron suppression." *Physics of Plasmas* **17**(5), 056117 (8 pp). doi:10.1063/1.3309426

[37] Jernigan, T.C. *et al.* (2005). "Massive gas injection systems for disruption mitigation on the DIII-D tokamak." In *Fusion Engineering 2005, Proceedings of the 21st IEEE/NPSS Symposium on*, Knoxville, TN, USA, September 26–29, 2005. 3 pp. doi:FUSION.2005.252977

[38] Taylor, P.L. *et al.* (1999). "Disruption mitigation studies in DIII-D." *Physics of Plasmas* **6**(5), 1872–1879. doi:10.1063/1.873445

[39] Finken, K.H. *et al.* (2001). "Mitigation of disruptions by fast helium gas puffs." *Nuclear Fusion* **41**(11), 1651–1661. doi:10.1088/0029-5515/41/11/315

[40] Whyte, D.G. *et al.* (2002). "Mitigation of tokamak disruptions using high-pressure gas injection." *Physical Review Letters* **89**(5), 055001 (4 pp). doi:10.1103/PhysRevLett.89.055001

[41] Whyte, D.G. *et al.* (2003). "Disruption mitigation with high-pressure noble gas injection." *Journal of Nuclear Materials* **313–316**, 1239–1246. doi:10.1016/S0022-3115(02)01525-8

[42] Bakhtiari, M. *et al.* (2011). "Using mixed gases for massive gas injection disruption mitigation on Alcator C-Mod." *Nuclear Fusion* **51**(6), 063007 (9 pp). doi:10.1088/0029-5515/51/6/063007

[43] Bozhenkov, S.A. *et al.* (2008). "Generation and suppression of runaway electrons in disruption mitigation experiments in TEXTOR." *Plasma Physics and Controlled Fusion* **50**(10), 105007 (18 pp). doi:10.1088/0741-3335/50/10/105007

[44] Bozhenkov, S.A. *et al.* (2011). "Fuelling efficiency of massive gas injection in TEXTOR: mass scaling and importance of flow dynamics." *Nuclear Fusion* **51**(8), 083033 (10 pp). doi:10.1088/0029-5515/51/8/083033

[45] Granetz, R. *et al.* (2006). "Gas jet disruption mitigation studies on Alcator C-Mod." *Nuclear Fusion* **46**(12), 1001–1008. doi:10.1088/0029-5515/46/12/003

[46] Granetz, R.S. *et al.* (2007). "Gas jet disruption mitigation studies on Alcator C-Mod and DIII-D." *Nuclear Fusion* **47**(9), 1086–1091. doi:10.1088/0029-5515/47/9/003

[47] Hollmann, E.M. *et al.* (2007). "Observation of q-profile dependence in noble gas injection radiative shutdown times in DIII-D." *Physics of Plasmas* **14**(1), 012502 (8 pp). doi:10.1063/1.2408404

[48] Hutchinson, I.H. (1976). "Magnetic probe investigation of the disruptive instability in tokamak LT-3." *Physical Review Letters* **37**(6), 338–341. doi:10.1103/PhysRevLett.37.338

[49] Thornton, A.J. *et al.* (2012). "Characterization of disruption mitigation via massive gas injection in MAST." *Plasma Physics and Controlled Fusion* **54**(12), 125007 (14 pp). doi:10.1088/0741-3335/54/12/125007

[50] ITER Physics Basis, Chapter 2: Plasma confinement and transport. Authors: ITER Physics Expert Group on Confinement and Transport and ITER Physics Expert Group on Confinement Modelling and Database (M. Wakatani, chair). Published in *Nuclear Fusion* **39**(12), December 1999, pp. 2175–2249. doi:10.1088/0029-5515/39/12/302.

[51] ITER Physics Basis, Chapter 3: MHD stability, operational limits and disruptions. Authors: ITER Physics Expert Group on Disruptions, Plasma Control, and MHD (S. Mirnov & J. Wesley, chairs). Published in *Nuclear Fusion* **39**(12), December 1999, pp. 2251–2389. doi:10.1088/0029-5515/39/12/303

[52] Riccardo, V. *et al.* (2005). "Timescale and magnitude of plasma thermal energy loss before and during disruptions in JET." *Nuclear Fusion* **45**(11), 1427–1438. doi:10.1088/0029-5515/45/11/025

[53] Data collected by G.M. Olynyk. Presented by B. Lipschultz at ITPA SOL/Divertor Workshop, La Jolla, CA, USA, October 15, 2012. Unpublished otherwise.

[54] Putvinski, S. *et al.* (1997). "Halo current, runaway electrons and disruption mitigation in ITER." *Plasma Physics and Controlled Fusion* **39**(12B), B157–B171. doi:10.1088/0741-3335/39/12B/013

[55] Lehnen, M. *et al.* (2011). "Disruption mitigation by massive gas injection in JET." *Nuclear Fusion* **51**(12), 123010 (12 pp). doi:10.1088/0029-5515/51/12/123010

[56] Kuteev, B.V. *et al.* (1995). "Emergency discharge quench or rampdown by a noble gas pellet." *Nuclear Fusion* **35**(10), 1167–1172. doi:10.1088/0029-5515/35/10/I02

[57] Kessel, C.E. *et al.* (2009). "Development of ITER 15 MA ELMy H-mode inductive scenario." *Nuclear Fusion* **49**(8), 085034 (19 pp). doi:10.1088/0029-5515/49/8/085034

[58] Pitts, R.A. *et al.* (2011). "Physics basis and design of the ITER plasma-facing components." *Journal of Nuclear Materials* **415**(1, Suppl. 1), S957–S964. doi:10.1016/j.jnucmat.2011.01.114

[59] Hender, T.C. *et al.* (2007). "Progress in the ITER physics basis, Chapter 3: MHD stability, operational limits and disruptions." *Nuclear Fusion* **47**(6), S128–S202. doi:10.1088/0029-5515/47/6/S03

[60] Sugihara, M. *et al.* (2007). "Disruption scenarios, their mitigation and operation window in ITER." *Nuclear Fusion* **47**(4), 337–352. doi:10.1088/0029-5515/47/4/012

[61] LaBombard, B. *et al.* (1991). "Design of limiter/divertor first-wall components for Alcator C-Mod." In *Fusion Engineering 1991, Proceedings of the 14th IEEE/NPSS Symposium on*, San Diego, CA, USA, Sep. 30–Oct. 3, 1991, vol. 1, pp. 31–36. doi:10.1109/FUSION.1991.218832

[62] Karditsas, P.J. & Baptiste, M.-J. (1995). "Thermal and structural properties of fusion related materials." UKAEA Report UKAEA-FUS-294. doi:10068/692915

[63] Reinke, M.L. *et al.* (2008). "Toroidally resolved radiation dynamics during a gas jet mitigated disruption on Alcator C-Mod." *Nuclear Fusion* **48**(12), 125004 (7 pp). doi:10.1088/0029-5515/48/12/125004

[64] Huber, A. *et al.* (2011). "Radiation loads onto plasma-facing components of JET during transient events – Experimental results and implications for ITER." *Journal of Nuclear Materials* **415**(1), Suppl. 1, S821–S827. doi:10.1016/j.jnucmat.2010.10.061

[65] Huber, A. *et al.* (2007). "Upgraded bolometer system on JET for improved radiation measurements." *Fusion Engineering and Design* **82**(5–14), 1327–1334. doi:10.1016/j.fusengdes.2007.03.027

[66] Eidetis, N.W. *et al.* (2012). "Control of post-disruption runaway electron beams in DIII-D." *Physics of Plasmas* **19**(5), 056109 (9 pp). doi:10.1063/1.3695000

[67] Izzo, V.A. *et al*. (2011). "Runaway electron confinement modelling for rapid shutdown scenarios in DIII-D, Alcator C-Mod and ITER." *Nuclear Fusion* **51**(6), 063032 (10 pp). doi:10.1088/0029-5515/51/6/063032

[68] Putvinski, S. *et al*. (2011). "Disruption mitigation in ITER." Presentation given at the 2011 International Sherwood Fusion Theory Conference, Austin, TX, USA, May 2–4, 2011. Available online at http://ptolemy.ph.utexas.edu/Talks/PutvinskiS.pdf

Chapter 3

Hardware and diagnostics on the Alcator C-Mod tokamak

In Chapters 1–2, the challenge of mitigating major disruptions on tokamaks was discussed. In this chapter, the hardware and diagnostics on the Alcator C-Mod tokamak are described, with an emphasis on how they were used for the experiments described in the subsequent chapters.

3.1 Alcator C-Mod

Alcator C-Mod [1], usually referred to in day-to-day operations as "C-Mod", is a compact, high-field tokamak located at the Plasma Science and Fusion Center (PSFC) at MIT. C-Mod is the third in the Alcator series of tokamaks at the PSFC, after Alcator A (1973–1979) and Alcator C (1978–1987). In operation since 1992, it has the highest plasma pressure, magnetic field, and heating power density of any tokamak in existence today. The main parameters of the Alcator C-Mod plasma are described in Table 3-1.

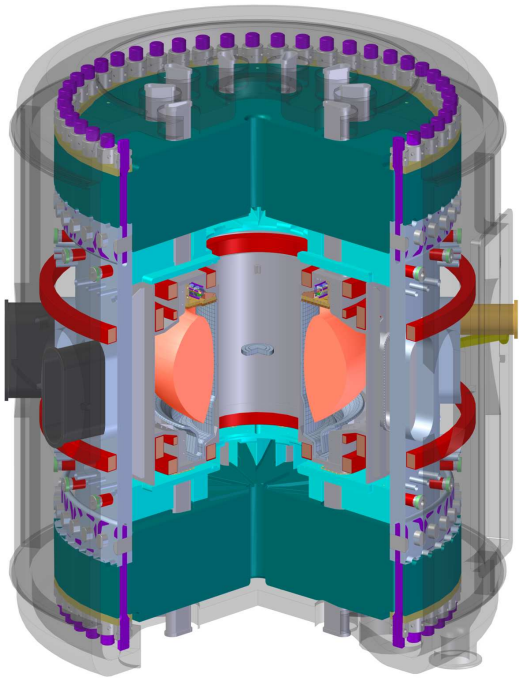

Figure 3-1 – Cutaway rendering of Alcator C-Mod, showing vacuum vessel, ports, magnets, and plasma. Plasma major radius is 0.67 m.

Rapid shutdown experiments have been conducted on Alcator C-Mod since 2005. The data used for this thesis were the result of experiments conducted in February–September 2012, as part of the 2012 C-Mod run campaign. Further details are given in Chapter 4.

Param.	Description	Achievable values	Standard value
R	Major radius [m]	0.6–0.75	0.67
a	Minor radius [m]	0.15–0.22	0.22
κ	Plasma elongation	0.98–1.62	1.6
—	Magnetic configuration	USN, LSN, BDN	LSN
δ_{U}	Plasma triangularity (upper)	0–0.7	0.34
δ_{L}	Plasma triangularity (lower)	0.2–0.8	0.52
B_ϕ	On-axis toroidal field [T]	3.0–8.0	5.4
I_{p}	Plasma current [MA]	0.25–2.0	1.0
$\bar{n}_{\mathrm{e}}$	Volume-averaged electron density [10^{20} m^{-3}]	0.3–5.0	1.5
P_Ω	Ohmic heating power [MW]	0.2–3.0 [2]	1.2
P_{ICRF}	Auxiliary (ICRF) heating power [MW]	0–6	0–6
V	Plasma volume [m^3]	0.6–0.9	0.90
W_{th}	Stored thermal energy [kJ]	20–250	50–150
A_{wall}	Plasma-facing wall area [m^2]	—	6.7

Table 3-1 – Principal parameters of Alcator C-Mod plasma and machine. Standard values are those used for the so-called "fiducial" C-Mod plasmas, which can be produced with high reliability and are thus ideal target plasmas for MGI rapid shutdown experiments. The auxiliary (ICRF) heating system has 8 MW power at the source; the maximum power *absorbed* in the plasma is ≈ 6 MW.

3.1.1 Base magnetics

The "base" magnetics system in C-Mod consists of four poloidal arrays of 26 pickup coils for measuring the time-derivative of the poloidal magnetic field B_θ, three Rogowski coils to measure plasma current, and 27 flux loops (some full flux loops and some "virtual" ones created from electronically combining partial flux loops). A full description of the base magnetic diagnostics in Alcator C-Mod is given in Granetz *et al.* [3].

These magnetic diagnostics are used for control of the plasma shape and location, and have been used in the past for real-time detection of locked modes and VDEs for active mitigation purposes [4]. However, they are digitized at only 10 kHz, which is not fast enough to resolve the exponentially growing $n = 1$ mode in the pre-TQ of MGI rapid shutdowns. Thus, the fast magnetics system (Mirnov coils) are used instead. These coils are described in Section 3.4.

3.1.2 Control system

The plasma control system (PCS) on Alcator C-Mod is a real-time digital computer which is emulating an older "hybrid" analog/digital control system. The control system takes 64 inputs from the plasma and multiplies by a matrix to generate 16 linearized observers for the 16 physical quantities under the control of the PCS. Proportional/ integral/derivative (PID) control is then used to drive 16 outputs, which are multiplied by "controller matrices" to drive the actual power supplies and fueling gas valves. The observer matrices, PID control coefficients, and controller matrices are all stepwise time-dependent, and are modified according to the phase of the discharge (this was the role of the digital portion of the earlier "hybrid" analog/digital control system). A full description of the C-Mod PCS is given by Stillerman *et al.* [5].

Because the control system is completely digital, it is feasible to consider implementing real-time, active disruption detection, prediction, and mitigation systems as described in Section 2.1.1, although with two exceptions,[1] this has not been done to date.

3.2 The massive gas injector system

The massive gas injection (MGI) system on Alcator C-Mod consists of two fast gas valves, connected by a simple length of stainless steel tubing to the plasma edge. They are located at B- and F-ports, as shown in panel (a) of Figure 3-2. Photographs of the injectors are shown in Figure 3-3. Each gas injector uses a 300 mℓ plenum filled to 7 MPa with noble gas, typically

[1] To wit: an $n = 1$ locked-mode detector which was only used for a graduate student's thesis work on August 30, 2007, and then deactivated [4], and a real-time VDE detector which was connected to the MGI rapid shutdown system (see Miniproposal 449 in Table 4-1) and used on a single run day.

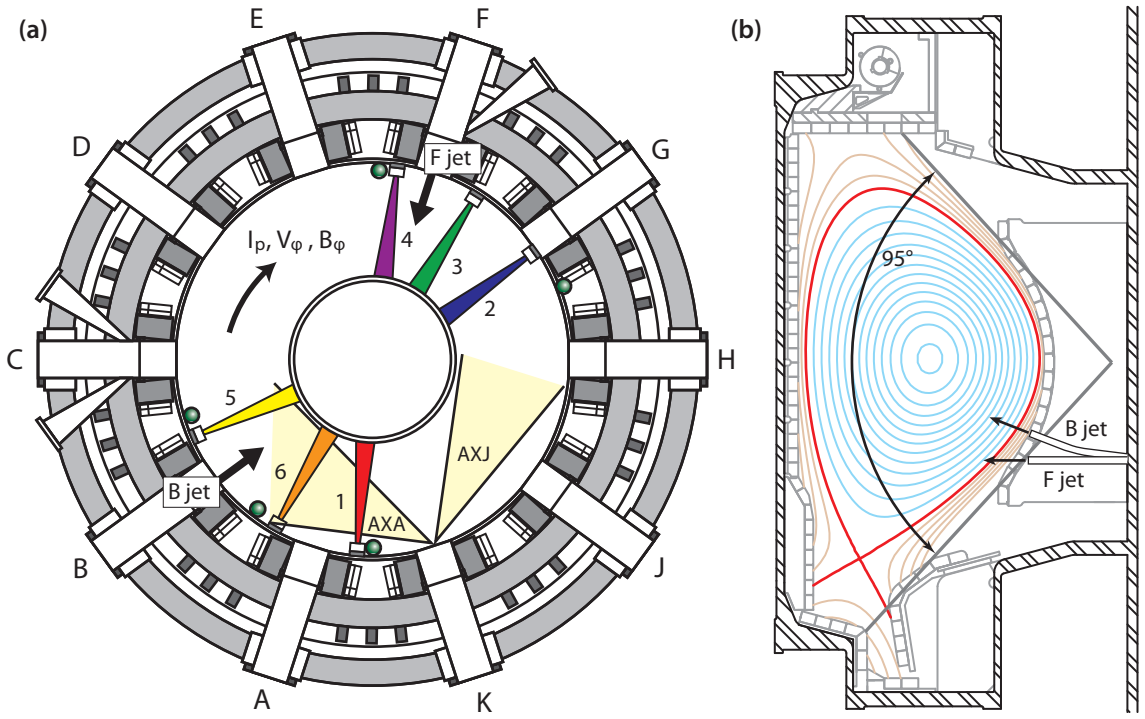

Figure 3-2 – Layout of equipment and diagnostics used for MGI rapid shutdown experiments. **(a)** Top view of Alcator C-Mod showing Alcator C-Mod ports, wall-mounted photodiodes and gas jets, as well as fast magnetic pickup coils (green circles). **(b)** View area of wall-mounted photodiodes and poloidal position of gas injectors.

a mixture of 15% argon, 85% helium, which gives an optimum balance between gas delivery time and MGI radiation efficiency [6].

As can be seen in panel (b) of Figure 3-2, the two gas injectors have a slightly different poloidal profile. This is due to the visible-light camera (WIDE2) at F-port, which would have been blocked had the F-jet bent up to point at the magnetic axis like the B-jet. The straight F-jet and the visible-light camera can be seen in the photograph in panel (b) of Figure 3-3.

The fast gas valves, which open in less than 1 ms, were supplied by the Oak Ridge National Laboratory and are described in detail in [7] and [8]. The two gas valves used were not identical: they were different generations of the Oak Ridge fast gas valve design. It is suspected that this, as well as the slightly different poloidal profile of the two jets, led to differing performance of the two-jet MGI rapid shutdown when one was fired before the other. This is discussed further in Section 6.3.5.

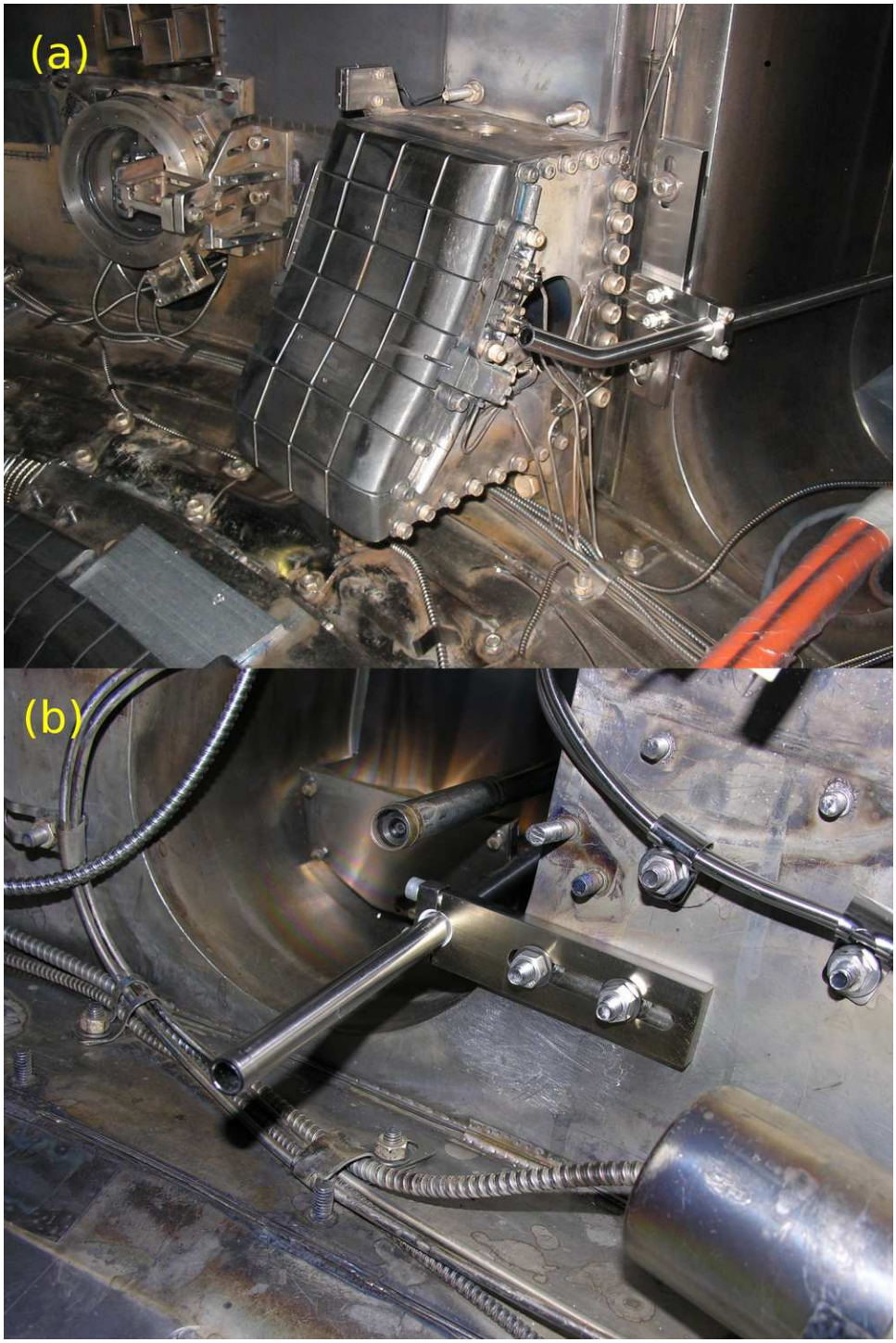

Figure 3-3 – Photographs of massive gas injection system in Alcator C-Mod. **(a)** B-jet; **(b)** F-jet. The poloidal profile of the F-jet was required to be different than the B-jet to avoid blocking the visible-light camera seen in panel (b).

3.3 Disruption bolometry

A toroidal array of six wall-mounted photodiodes was installed in order to diagnose the toroidal radiation asymmetry in MGI rapid shutdowns. The toroidal location of each photodiode is shown in panel (a) of Figure 3-2. The location of the photodiodes was constrained by available wall space (mainly by limiters and ICRF heating antennas). Each diode sampled the incident irradiance in a "slice" which was narrowly collimated in the toroidal direction, as shown in panel (a) of Figure 3-2, but which viewed the entire poloidal cross-section, as shown in panel (b).

The peak value of integrated radiation from this array is used as a proxy for the true toroidal peaking factor (TPF), and thus the calculated TPF is a lower bound on the true TPF. If the radiation pattern varies smoothly (has a low-n character), then the true TPF will be closer to the measured TPF than if the radiation pattern is strongly toroidally peaked. This issue is discussed further in Section 6.4.

This array of wall-mounted photodiodes is known as the "DMBolo" system, for "disruption mitigation bolometry". Additional photos of the assembly and calibration of the photodiodes can be seen in Appendix E.

3.3.1 AXUV diodes and electrical design

The photodiodes used in this series of experiments are Opto-Diode IRD AXUV20A Absolute eXtreme UltraViolet silicon photodiodes [9]. These diodes are each mounted in a optically blackened 304L stainless-steel box on the outer wall of the Alcator C-Mod vacuum vessel at the midplane.

The diodes were amplified by a transimpedance amplifier (schematic of the standard Alcator C-Mod Eurocard-format transimpedance amplifier board is given in Appendix F) with a gain of 1×10^3 V A^{-1}, which allowed a bandwidth of over 1 MHz at the amplifier board. Digitization was performed at 250 kHz by a D-tAcq DT196 16-bit ADC, and the data was stored in the Alcator C-Mod MDSplus data system. The manufacturer's drawing of the AXUV20A photodiode is reproduced in Appendix F.

Using photodiodes for diagnosing radiated power instead of foil bolometry has the advantage of a fast time response (approaching 1 MHz for the AXUV20A diodes used), which allows the radiated power to be resolved through the different phases of an MGI rapid shutdown on Alcator C-Mod. Foil bolometers are too slow for this. One disadvantage is that the diodes are not sensitive to low-energy neutral particles (created by charge-exchange processes in the edge plasma), which may be a significant energy loss channel during gas jet rapid shutdowns [10]. Nevertheless, diode-based measurements of radiated power *asymmetry* are still useful, under the assumption that the ratio of radiation to total (radiation + CX neutral) power loss is roughly constant at each toroidal location.

3.3.2 Diode boxes

The photodiodes were mounted in optically-blackened 304L stainless steel boxes on the outer wall of the C-Mod vacuum vessel. The optical blackening was an oxidation process performed according to the military standard MIL-C-13924. A schematic of the diode box can be seen in Figure 3-4, showing the mechanical construction of the diode boxes. They were attached to the C-Mod vessel wall by welded studs. The electrical signal was carried from the diode box to the vacuum feed-through connection by a fully coaxial signal path using Microtech CO-1-30 Teflon coaxial cable (which is very close in dimensions to the military cable standard RG/174A, allowing the use of electronic components designed for that cable specification). The coaxial cable was shielded from plasma exposure inside Penflex SL-SS-002 1/8 inch flexible stainless steel instrumentation tubing.

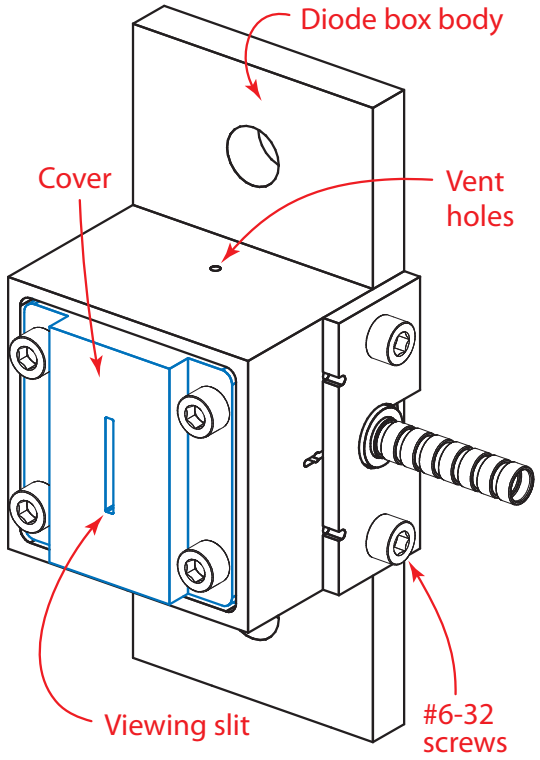

Figure 3-4 – Mechanical overview of diode boxes. Molybdenum aperture disc is mounted behind cover plate.

3.3.3 Optical pinhole

The photodiodes observe the plasma unfiltered through a 100 μm pinhole, which was sized so that the diodes stay within their linear range up to a plasma emissivity of 4 GW m^{-3}. The pinhole aperture disc was a Lenox Laser HP-3/8-DISC-MLY-100 molybdenum disc. A micrograph of the pinhole can be seen in Photo 1 of Appendix E.

In Figures 3-5 and 3-6, the attenuation of high-energy photons in this molybdenum foil is shown. It can be seen that the foils effectively shield the non-viewing area of the photodiode from all photons and X-rays that would be present in the tokamak (up to ≈ 5 keV).

3.3.4 Spectral sensitivity and calibration procedure

The toroidal and poloidal extent of the photodiode view were verified using a laser on a benchtop, pointing at the photodiode from a known angle. A photo of this calibration procedure can be seen in Photo 3 of Appendix E.

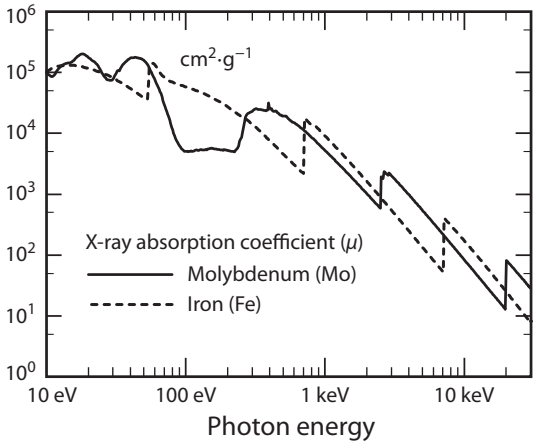

Figure 3-5 – Attenuation coefficient of X-rays in iron and molybdenum (normalized to density).

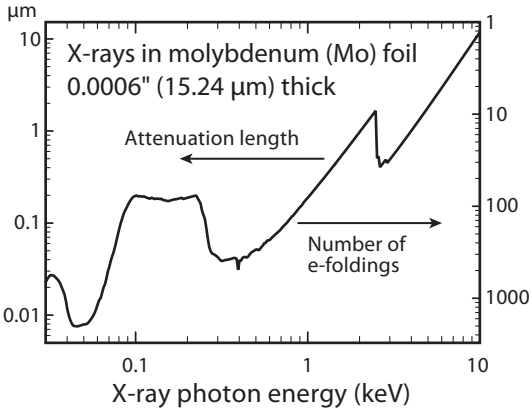

Figure 3-6 – Attenuation of X-rays in 15.24 μm (0.0006″) thick molybdenum foil. X-rays up to a photon energy of 5 keV are essentially completely stopped.

The photodiodes were then absolutely calibrated (for a spectrum created by a flattop plasma with typical C-Mod impurities) by comparison to a wide-viewing (2π) foil bolometer (see Section 3.5) using a separate amplifier with 500 times higher gain, which allows the diodes to resolve the radiated power during quiescent plasmas. The absolute calibration is thus valid for the UV to soft X-ray region, since this is the dominant photon energy released during flat-top plasmas on Alcator C-Mod (when $T_e \gtrsim 1$ keV).

The published responsivity curve of the AXUV photodiodes is shown in Figure 3-7. In Section 5.2.7, the effect of this wavelength-dependent responsivity on the radiated power measurements and the energy balance in MGI rapid shutdowns is discussed.

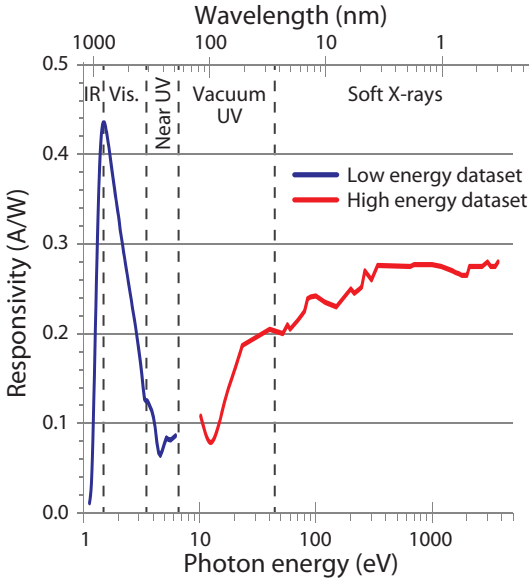

Figure 3-7 – Published responsivity curve $[\mathrm{A\,W^{-1}}]$ of AXUV photodiodes. Note the approximately 3-fold decrease in responsivity between high-energy X-rays and the near UV region.

3.4 Fast magnetics

The fast magnetics (Mirnov coil) system on Alcator C-Mod measures the time derivative of the poloidal field ($\dot{B}_\theta$) at high time resolution (digitized at 2.5 MHz). There are 72 coils, in toroidally- and poloidally-separated sets, although not all coils are digitized. Most of the pickup coils are located in the C-Mod limiters, although several of the coils are located on "stalks" or "booms" on the vessel wall in order to more adequately resolve low-n MHD activity. These are the coils that were used to diagnose the $n = 1$ mode

Coil name	ϕ	Z [m]	r [m]
BP_AB_TOP	349.8°	0.098	0.259
BP_BC_TOP	300.1°	0.098	0.261
BP_EF_TOP	190.4°	0.108	0.263
BP_KA_TOP	15.2°	0.098	0.259
BP06_GHK	128.1°	0.077	0.277

Table 3-2 – Fast $\dot{B}_\theta$ pickup coils (Mirnov coils) used for fitting growth rate and phase of low-n MHD modes in the pre-TQ phase of MGI rapid shutdowns. Z refers to the distance that the coil is above the midplane, r refers to the coil's distance from the nominal position of the plasma center at $R = 0.673$ m.

present in MGI rapid shutdowns.

In Table 3-2, the five Mirnov coils used for diagnosis of the $n = 1$ mode in MGI rapid shutdown experiments are listed. Their locations are shown in panel (a) of Figure 3-2 as the green circles on the vessel wall. The circle which is set slightly farther back than the others is BP06_GHK, which is a limiter-mounted coil (not on a boom on the vessel wall). A description of the fast magnetics system in Alcator C-Mod is given by Snipes *et al.* [11].

3.5 Foil bolometry

For absolute calibration of the AXUV photodiodes, as well as measurement of the total (time-integrated) radiated power during unmitigated disruptions and rapid shutdowns, Alcator C-Mod's wide-viewing ("2π") foil bolometer was used. This uses an optically blackened gold foil connected to an ac Wheatstone bridge in order to measure the irradiance at the wall with a flat spectral response across all photon wavelengths. The foil bolometer is also sensitive to charge-exchange neutral particles. A full description of the foil bolometry system is given in Section IV of [12].

3.6 Other photodiodes

In addition to the dedicated toroidal array of wall-mounted photodiodes, Alcator C-Mod has tangentially-viewing arrays of AXUV photodiodes at the midplane, located at K-port and viewing clockwise ("AXA", since it views toward A-port) and counter-clockwise ("AXJ", viewing toward J-port). The use of these photodiode arrays for diagnosing the radiated power evolution during MGI rapid shutdowns is described in [13].

3.7 Soft X-ray tomography

The X-ray tomography system on Alcator C-Mod consists of five linear photodiode arrays, with 38 detectors each, with three viewing the core plasma and two at higher spatial resolution viewing the edge. The core-viewing arrays view the plasma through a slit aperture and through a 38 μm beryllium filter, ensuring that only X-rays are seen (transmission is 50% at a photon energy of 2 keV). These core arrays are used for diagnosing the poloidal mode number (m number) of the brightness feature in the early thermal quench of MGI rapid shutdowns; see Section 6.8.

A single chord (chord 18 of SXR array 3) is typically used in MGI rapid shutdown studies as a proxy measure of core temperature, since the density rises high enough that the usual measures of core temperature (electron cyclotron emission) are cut off, and the background light is too high for Thomson scattering measurements.

A full description of the soft X-ray tomography system is given by Granetz *et al.* [14].

3.8 Electron cyclotron emission

Electron temperature profiles were diagnosed at high time resolution using a 32-channel radiometer-based second-harmonic X-mode ECE spectrometer fielded on Alcator C-Mod by the University of Texas Fusion Research Center.[2] The ECE radiometer covers the frequency range from 234–306 GHz, designed to cover the outboard half of the plasma if the standard on-axis toroidal field value of 5.4 T is used. In this case, the core channels go into cutoff at a plasma electron density of $\approx 5.9 \times 10^{20}$ m^{-3}, which means that the system does not function after the early phases of the thermal quench in an MGI rapid shutdown, as the injected impurities are assimilated and ionized, raising the electron density to 10^{21} m^{-3} or more. A full description of the system is given by Heard *et al.* [15].

3.9 X-ray crystal spectrometry

Alcator C-Mod is equipped with a five-channel, high-resolution X-ray spectrometer (in the von Hamos geometry), which views the plasma toroidally and has a wavelength range of 0.28–0.4 nm. By observing the broadening and Doppler shift in the emission lines from the Rydberg series of helium-like argon (+16 charge state) and hydrogen-like argon (+17 charge state), the impurity ion temperature and velocity can be determined. For these experiments, this system was used only to measure the toroidal rotation velocity of the argon impurity in

[2] Thus, the system is known as the "FRCECE" system, to distinguish it from the various MIT-designed grating polychromator ECE spectrometers.

the pre-disruptive target plasma, which was assumed to be equal to the rotational velocity of the main plasma ion (deuterium).

This system is physically located at K-port in Alcator C-Mod, and is referred to as HiReX-Jr, where HiReX means "High-resolution X-ray spectrometer".[3] A full description of the HiReX-Jr system is given in Rice *et al.* [16].

3.10 Two-color interferometry

Line-integrated density measurements are obtained from the ten vertical chords of the Alcator C-Mod two-color interferometer (TCI) system. This system takes advantage of the different responses of lasers at different wavelengths to plasma density fluctuations and machine vibrations in order to remove the effect of machine vibrations from the density measurement. It uses a CO_2 laser at 10.6 μm wavelength running coaxially with a He-Ne laser at a wavelength of 0.63 μm. A full description of the TCI system is given by Irby *et al.* [17].

3.11 Thomson scattering

Profiles of electron temperature and density are measured on Alcator C-Mod with the Thomson scattering (TS) system. Two Nd-doped yttrium–aluminum–garnet (Nd:YAG) lasers are fired at a 30 Hz repetition rate each, allowing profile data at 60 Hz, or in a "burst" mode where the two lasers are fired close in time to each other, with a pair of profiles every 1/30 s. The lasers are fired from above the machine, through a top port and out through a slot in the divertor. The scattered light is collected by optics looking horizontally from G-port. A full description of the C-Mod TS system is given by Hughes *et al.* [18].

3.12 Auxiliary heating

Besides the Ohmic heating from the plasma current itself, which is substantial on Alcator C-Mod (up to 3 MW [2], with a more typical value being ≈ 1 MW), the machine is equipped with radio-frequency heating at two different frequencies: up to approximately 6 MW absorbed power in the ion cyclotron range of frequencies (ICRF) at ≈ 80 MHz, and up to 1 MW of lower hybrid heating (LHH) and current drive (LHCD) at 4.6 GHz. For the experiments presented here, only the ICRF system was used for auxiliary heating, in its standard hydrogen-minority heating regime. 80 MHz corresponds to the on-axis resonance of the

[3] HiReX-Jr is a retronym created for this system after its successor, the **s**patially **r**esolved HiReX-SR was fielded.

hydrogen minority ion species at a toroidal field of 5.4 T. At 5.6 T, the resonance layer moves outward slightly.

The ICRF fast wave is coupled to the plasma through three flux-coupling antennas: two-strap antennas at each of D-port and E-port run in dipole phasing [19], and a rotated (field-aligned) four-strap antenna at J-port [20]. ICRF heating was used to increase the stored energy of the target plasmas for MGI rapid shutdown experiments.

3.13 Summary of hardware and diagnostics

In this chapter, the characteristics of the Alcator C-Mod tokamak were described, as well as the capabilities of the hardware and diagnostic systems which are used for massive gas injection rapid shutdown studies. In Chapter 4, the program of experimental studies which was carried out for this work is described. The results are then presented in Chapter 5.

References

[1] Marmar, E. *et al.* (2009). "Overview of the Alcator C-Mod research program." *Nuclear Fusion* **49**(10), 104014 (10 pp). doi:10.1088/0029-5515/49/10/104014

[2] Fairfax, S.A. (1993). "Start-up and early results from Alcator C-MOD." *Fusion Engineering 1993, Proceedings of the 15th IEEE/NPSS Symposium on.* Hyannis, MA, USA, October 11–15, 1993. Vol. 2, pp. 812–817. doi:10.1109/FUSION.1993.518449

[3] Granetz, R.S. *et al.* (1990). "Magnetic diagnostics in Alcator C-MOD." *Review of Scientific Instruments* **61**(10), 2967–2969. doi:10.1063/1.1141741

[4] Angelini, S.M. "Disruption mitigation and real-time detection of locked modes." S.M. thesis, Massachusetts Institute of Technology, 2008. doi:1721.1/44766

[5] Stillerman, J.A. *et al.* (2006). "Digital real-time plasma control system for Alcator C-Mod." *Fusion Engineering and Design* **81**(15–17), 1905–1910. doi:10.1016/j.fusengdes.2006.04.054

[6] Bakhtiari, M. *et al.* (2011). "Using mixed gases for massive gas injection disruption mitigation on Alcator C-Mod." *Nuclear Fusion* **51**(6), 063007 (9 pp). doi:10.1088/0029-5515/51/6/063007

[7] Granetz, R.S. *et al.* (2006). "Gas jet disruption mitigation studies on Alcator C-Mod." *Nuclear Fusion* **46**(12), 1001–1008. doi:10.1088/0029-5515/46/12/003

[8] Milora, S.L. *et al.* (1986). "Fast-opening magnetic valve for high-pressure gas injection and applications to hydrogen pellet fueling systems." *Review of Scientific Instruments* **57**(9), 2356–2358. doi:10.1063/1.1138677

[9] Opto-Diode Corporation (a member of the ITW Photonics Group). "IRD UV Photodiodes – Operating Principles & Applications". PDF available online at http://www.optodiode.com/library.html

[10] Gray, D.S. *et al.* (2004). "Time resolved radiated power during tokamak disruptions and spectral averaging of AXUV photodiode response in DIII-D." *Review of Scientific Instruments* **75**(2), 376–381. doi:10.1063/1.1642745

[11] Snipes, J.A. *et al.* (2005). "Active and fast particle driven Alfvén eigenmodes in Alcator C-Mod." *Physics of Plasmas* **12**(5), 056102 (8 pp). doi:10.1063/1.1865012

[12] Reinke, M.L. & Hutchinson, I.H. (2008). "Two dimensional radiated power diagnostics on Alcator C-Mod." *Review of Scientific Instruments* **79**(10), 10F306 (4 pp). doi:10.1063/1.2965018

[13] Reinke, M.L. *et al.* (2008). "Toroidally resolved radiation dynamics during a gas jet mitigated disruption on Alcator C-Mod." *Nuclear Fusion* **48**(12), 125004 (7 pp). doi:10.1088/0029-5515/48/12/125004

[14] Granetz, R. *et al.* (1990). "The X-ray imaging diagnostics of Alcator C-MOD." MIT PSFC Tech Report Nº PSFC/JA-91-2, November 1990. Available online at http://www.psfc.mit.edu/library1/catalog/reports/1990/91ja/91ja002/91ja002_full.pdf

[15] Heard, J.W. *et al.* (1999). "High resolution electron cyclotron emission temperature profile and fluctuation diagnostic for Alcator C-Mod." *Review of Scientific Instruments* **70**(1), 1011–1013. doi:10.1063/1.1149368

[16] Rice, J.E. *et al.* (1995). "Observations of Alcator C-Mod plasmas from a five chord high energy resolution X-ray spectrometer array." *Review of Scientific Instruments* **66**(1), 752–754. doi:10.1063/1.1146279

[17] Irby, J.H. *et al.* (1988). "Two-color interferometer system for Alcator C-MOD." *Review of Scientific Instruments* **59**(8), 1568–1570. doi:10.1063/1.1140199

[18] Hughes, J.W. *et al.* (2003). "Thomson scattering upgrades on Alcator C-Mod." *Review of Scientific Instruments* **74**(3), 1667–1670 doi:10.1063/1.1532764

[19] Golovato, S.N. *et al.* (1995). "ICRF heating in the Alcator C-Mod tokamak." Presented at the 5th Topical Conference on Radio Frequency Power in Plasmas, Palm Springs, CA, USA, May 17–19, 1995. Published in *AIP Conference Proceedings* **355**, 23–30. doi:10.1063/1.49586

[20] Wukitch, S.J. *et al*. (2013). "Characterization and performance of a field aligned ion cyclotron range of frequency antenna in Alcator C-Mod." *Physics of Plasmas* **20**(5), 056117. doi:10.1063/1.4803882

Chapter 4

Experimental program

In this chapter, the experimental runs of Alcator C-Mod used for massive gas injection rapid shutdown experiments are described, and tables are presented which list the shots and target plasma parameters used for the various scans. The experimental observations and interpretation are presented in the subsequent chapters. The two Alcator C-Mod miniproposals for MGI rapid shutdown experiments in the 2012 run campaign are reproduced in Appendix C.

Table 4-1 is a listing of every experimental run day on Alcator C-Mod dedicated (or partially dedicated) to MGI rapid shutdown experiments. Most of the data presented in Chapter 5 of this thesis was collected in 2012 (the four run days with G.M. Olynyk listed as session leader in Table 4-1). They are sorted by date; the first instance of each miniproposal is hyperlinked to the text of miniproposal on the Alcator C-Mod facility information website.

Date	MP	Session leader	Description
2005-06-03	424	R.S. Granetz	First MGI rapid shutdown on Alcator C-Mod.
2005-07-21	424	R.S. Granetz	Only one shutdown – TF scanner failed. First observation of $n = 1$ magnetic mode in pre-TQ using Mirnov coils.
2005-07-22	424	R.S. Granetz	Tested MGI with argon and neon
2005-08-11	424	R.S. Granetz	Half day (9 shots). Measured halo currents with MGI rapid shutdown
2005-08-25	424	R.S. Granetz	Half day (12 shots). Tested MGI with krypton.
2006-03-08	439	R.S. Granetz	Testing scaling of pre-TQ length with q_{95}. MP written by V.A. Izzo.
2006-04-14	449	R.S. Granetz	Real-time mitigation of VDEs with MGI.
2006-06-22	450	R.S. Granetz	First use of mixed gases for MGI rapid shutdown. MP written by M. Bakhtiari.
2006-07-06	449	R.S. Granetz	Gas jet didn't function today – no shutdowns.

Table continues on next page…

…Table continues from previous page

Date	MP	Session leader	Description
2007-12-20	450	R.S. Granetz	Further testing of gas mixtures for MGI, and first attempt to seed fast electrons using lower hybrid.
2009-09-24	567	M.L. Reinke	Investigation of the spatial dynamics of pre-TQ and TQ radiation using AXUV diodes. Only four good shutdowns.
2009-09-25	567	M.L. Reinke	Continuation of previous day's run. Investigation of spatial dynamics of pre-TQ/TQ radiation.
2010-09-08	604	R.S. Granetz	Attempt to create runaway electrons with MGI into LHCD plasma.
2010-11-03	604	R.S. Granetz	Continuation of MP 604. Only two shutdowns and no sign of runaway electrons.
2012-02-02	675	G.M. Olynyk	Initial operation with two gas jets; scan of gas jet stagger time with 1 MW ICRF-heated L-mode target plasmas, normal field, LSN diverted configuration
2012-06-04	675	G.M. Olynyk	Gas jet tests only (no plasma).
2012-06-22	675	G.M. Olynyk	Scan of stagger time and comparison to unmitigated VDEs.
2012-08-02	714	G.M. Olynyk	Single-jet MGI rapid shutdown. Scans of κ, q_{95}.
2012-09-11	675	G.M. Olynyk	Scan of stagger time into high-power I-mode target plasmas. Scan of stored thermal energy W_{th} with single jet.

Table 4-1 – Overview of Alcator C-Mod run days dedicated, or partially dedicated, to rapid shutdown and/or disruption mitigation experiments.

4.1 Scans of gas jet stagger time

After "shaking down" the gas jet hardware by test-firing into the tokamak with no plasma in it, MGI rapid shutdowns were conducted with two gas jets. The timing of the two jets was first confirmed by firing each individually into a fiducial 1.0 MA target plasma, and the time when the pre-TQ began, as indicated by impurity light first appearing on photodiodes, was noted. The relative timing between the gas jet triggers could then be adjusted so that the gas *arrived at the plasma* with a relative delay t_{stag}, where $t_{stag} < 0$ means that the gas from the

Shot number	$\bar{n}_e$ (10^{20} m^{-3})	W_{th} (kJ)	t_{stag} (ms)
1120202006	1.55	52	F only
1120202015	1.61	43	−1.81
1120202023	1.58	50	−1.56
1120202014	1.56	48	−1.31
1120202013	1.56	48	−0.81
1120202021	1.56	49	−0.81
1120202010	1.58	52	−0.31
1120202011	1.55	45	−0.31
1120202012	1.56	48	−0.31
1120202016	1.59	46	+0.19
1120202020	1.58	51	+0.19
1120202017	1.57	48	+0.79
1120202022	1.59	48	+0.94
1120202018	1.57	52	+1.29
1120202019	—	50	+1.79
1120202004	1.56	50	B only
1120202009	1.56	47	B only

Table 4-2 – Shot numbers and target plasma parameters for the "L-mode t_{stag} scan" dataset. All shots in this dataset were from run 1120202 (February 2, 2012), and were in the normal ($-\phi$) magnetic field direction and lower single null magnetic configuration, and were L-mode with 1 MW ICRF auxiliary heating. Stored thermal energy W_{th} ranged from 43–52 kJ in these target plasmas. The line-averaged electron density $\bar{n}_e$ was measured by two-color interferometry (see Section 3.10). The TCI system failed on shot 1120202019.

F-jet arrived at the plasma first.

Scans were then conducted of t_{stag} for two-jet MGI rapid shutdown of two different target plasmas. The first, on February 2, 2012, was a 1 MW ICRF-heated L-mode target plasma, with stored energy 43–52 kJ. The shots used in the final "L-mode t_{stag} scan" database are listed in Table 4-2.

The second target plasma was a 3.6 MW ICRF-heated I-mode plasma (with the toroidal field in the $+\phi$ "reverse-field" direction). The shots listed in Table 4-3 were taken on September 11, 2012. Stored thermal energy in these target plasmas ranged from 120–130 kJ. (In any case, absolute stored thermal energy does not appear to impact MGI shutdown performance; see Section 5.2.4.) There is a more limited dataset of two-jet shutdowns of these high-power plasmas, due to machine performance problems during the 2012-09-11 run.

Shot number	$\bar{n}_e$ (10^{20} m^{-3})	W_{th} (kJ)	t_{stag} (ms)
1120911010	1.17	128	F only
1120911013	1.15	127	−0.69
1120911014	1.11	128	−0.19
1120911021	1.13	124	+0.01
1120911019	1.13	121	+0.31
1120911016	1.15	124	+0.81
1120911018	1.11	122	+1.31
1120911008	1.19	121	B only

Table 4-3 – Shot numbers and target plasma parameters for the "I-mode t_{stag} scan" dataset. All shots in this dataset were from run 1120911 (September 11, 2012), and were in the reverse ($+\phi$) magnetic field direction and lower single null magnetic configuration, and were I-mode with 3.6 MW ICRF auxiliary heating. Stored thermal energy W_{th} ranged from 120–130 kJ in these target plasmas. The line-averaged electron density $\bar{n}_e$ was measured by two-color interferometry (see Section 3.10).

4.2 Scan of plasma stored energy

On September 11, 2012, single-jet MGI rapid shutdown experiments were conducted with target plasmas of varying stored thermal energy W_{th}. The stored thermal energy was controlled by varying the amount of auxiliary (ICRF) heating, and taking advantage of the natural variability of stored energy in high-power Alcator C-Mod shots due to impurity contamination. One shot from the June 22, 2012 run was used for the lowest stored-energy datapoint. The shots used in the "W_{th} scan" dataset are listed in Table 4-4.

4.3 Scans of plasma elongation

On August 2, 2012, single-jet MGI rapid shutdowns were conducted for target plasmas in the inner-wall limited magnetic configuration, with a varying elongation κ. The plasma current was kept constant, in order to keep the poloidal magnetic field energy available to the disruption ($W_{pol} = L\, I_p^2/2$) approximately constant from shutdown to shutdown. Because the safety factor varies with plasma elongation κ at constant plasma current, the toroidal field B_ϕ was varied in order to keep the safety factor approximately constant as κ varied. The shots used in this "κ scan" dataset are listed in Table 4-5. Flux surface reconstructions from EFIT [1] for two plasmas from this dataset (at κ = 1.1 and 1.5), just before the time at which the rapid shutdown system was triggered, are shown in Figure 4-1. There were two MGI rapid shutdowns for each elongation, in order to build statistical confidence in the results.

Shot number	$\bar{n}_e$ (10^{20} m^{-3})	P_{aux} (MW)	W_{th} (kJ)	Notes
1120622007	1.55	1.0	64	Forward field; L-mode; note higher density than other shots in scan
1120911006	1.12	3.5	89	Reverse field; ICRF tripping in and out; probably L-mode
1120911003	1.01	3.0	97	Reverse field; probably L-mode
1120911005	1.08	4.0	107	Reverse field; ICRF tripping in and out; probably L-mode
1120911004	1.06	3.5	111	Reverse field; probably L-mode
1120911007	1.07	3.5	113	Reverse field; unclear if L- or I-mode
1120911008	1.19	3.5	121	Reverse field; good ICRF; I-mode

Table 4-4 – Shot numbers and target plasma parameters for the "W_{th} scan" dataset. All shots in this dataset were lower single null magnetic configuration. The line-averaged electron density $\bar{n}_e$ was measured by two-color interferometry. Plasma stored energy calculated by EFIT [1].

Shot number	κ	B_ϕ (T)	$\bar{n}_e$ (10^{20} m^{-3})	W_{th} (kJ)	q
1120802010	1.0	6.9	1.37	31	3.45
1120802018	1.0	6.9	1.50	39	3.45
1120802009	1.1	6.3	1.44	32	3.57
1120802017	1.1	6.3	1.59	32	3.60
1120802006	1.3	5.2	1.46	30	3.59
1120802015	1.3	5.2	1.69	29	3.67
1120802007	1.5	4.3	1.60	24	3.77
1120802016	1.5	4.3	1.55	24	3.70
1120802008	1.6	4.0	1.59	23	3.79
1120802026	1.6	4.1	1.59	25	3.85

Table 4-5 – Shot numbers and target plasma parameters for the "κ scan" dataset. All shots in this dataset were from run 1120802 (August 2, 2012), and were in the normal ($-\phi$) field direction and inner-wall limited magnetic configuration. All shots were L-mode, with Ohmic heating only (no auxiliary heating). Stored thermal energy W_{th} ranged from 23–40 kJ in these target plasmas. The line-averaged electron density $\bar{n}_e$ was measured by two-color interferometry.

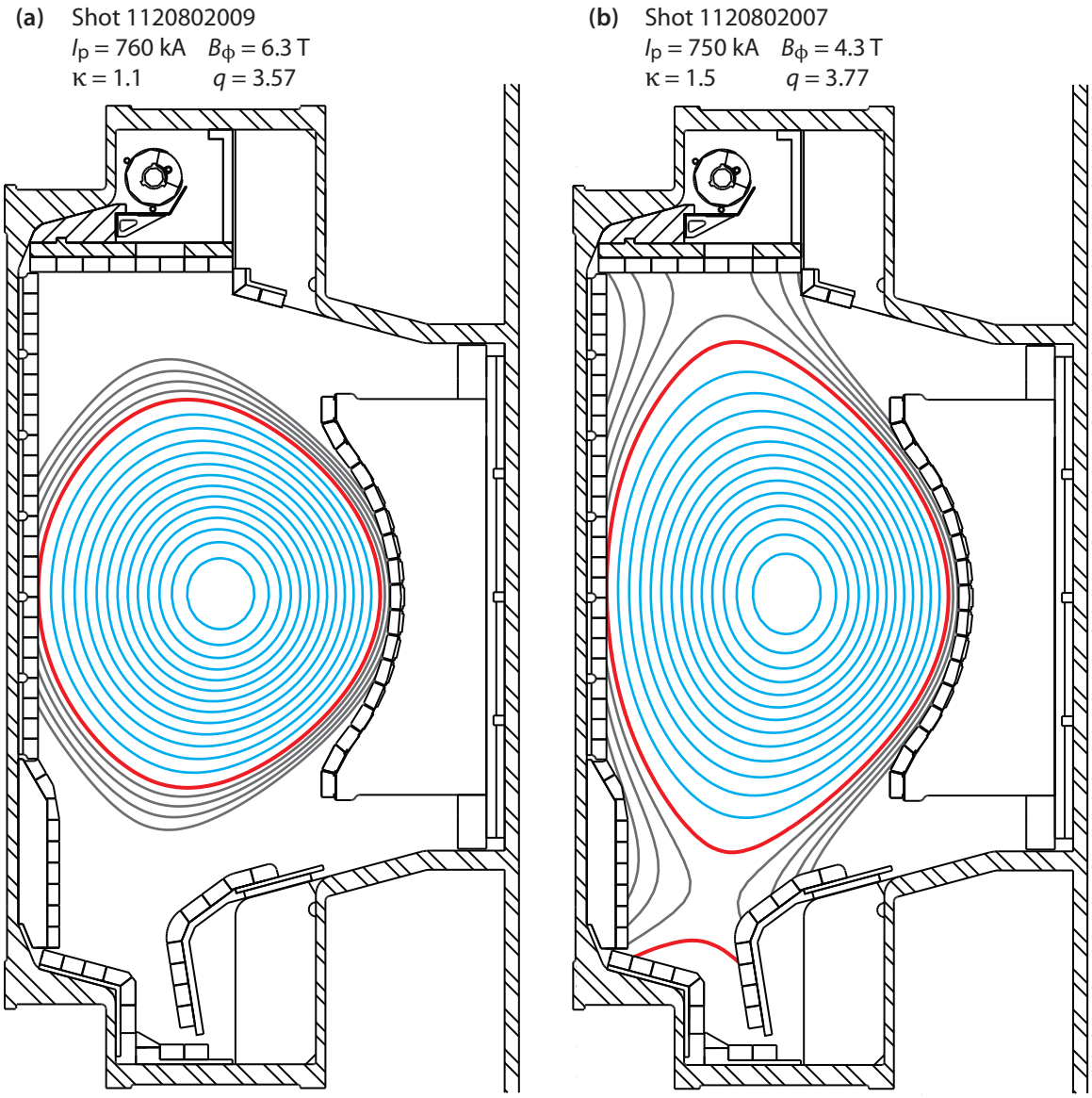

Figure 4-1 – Plasma flux surface reconstruction (EFIT) in **(a)** low-elongation ($\kappa = 1.1$) and **(b)** high-elongation ($\kappa = 1.5$) inner-wall limited plasmas from August 2, 2012.

Shot number	q^*	q_{95}	B_ϕ (T)	$\bar{n}_e$ (10^{20} m^{-3})	W_{th} kJ
1120802011	3.4	3.46	4.08	1.40	22
1120802020	3.4	3.50	4.08	1.50	26
1120802012	4.2	4.28	5.03	1.59	28
1120802021	4.2	4.26	5.03	1.56	25
1120802013	5.0	5.03	5.96	1.57	29
1120802023	5.0	4.93	5.96	1.61	24
1120802014	5.9	5.58	6.89	1.56	22
1120802024	5.9	5.56	6.90	1.58	20

Table 4-6 – Shot numbers and target plasma parameters for the "q_{95} scan" dataset. All shots in this dataset were from run 1120802 (August 2, 2012), and were in the normal ($-\phi$) field direction and inner-wall limited magnetic configuration. All shots were L-mode, with Ohmic heating only (no auxiliary heating). Stored thermal energy W_{th} ranged from 20–30 kJ in these target plasmas. The line-averaged electron density $\bar{n}_e$ was measured by two-color interferometry.

4.4 Scans of magnetic safety factor

The final dataset used in this thesis is a set of single-jet MGI rapid shutdowns of lower-single-null diverted plasmas, in which the magnetic safety factor at the 95th percentile flux surface (q_{95}) was varied by changing the toroidal field. As was done for the elongation scan, the plasma current was kept constant, in order to keep the poloidal magnetic field energy available to the disruption approximately constant from shutdown to shutdown. Four different safety factors were studied in the scan, with two rapid shutdowns of a plasma at each safety factor, for a total of eight shutdowns, summarized in Table 4-6. The cylindrical safety factor q^* is given by:

$$q^* \equiv \frac{2\pi a^2 B_\phi}{\mu_0 R I_p}\left(\frac{1+\kappa^2}{2}\right) \tag{4.1}$$

where a and R is the plasma minor and major radius [m] respectively, B_ϕ is the toroidal field [T], I_p is the plasma current [A], and κ is the dimensionless plasma elongation.

4.5 Summary of experimental program

Massive gas injection (MGI) rapid shutdown experiments have been conducted on Alcator C-Mod since 2005, investigating the effectiveness of various noble gases for MGI, the use

of mixed gases, the confinement of runaway electrons during the thermal quench and current quench of MGI rapid shutdowns, and the spatial distribution (in the poloidal plane) of the radiation in the pre-TQ and TQ. In 2012, the first two-gas-jet MGI rapid shutdown experiments in the world were conducted on Alcator C-Mod. In addition, single-jet rapid shutdowns were conducted on a variety of plasmas in order to determine the effect of various target plasma parameters on rapid shutdown figures of merit such as radiation peaking factor.

In Chapter 5, the observations from these rapid shutdown experiments are presented. Then, in Chapters 6, 7, and 8, the results are interpreted and the theory of low-n magnetohydrodynamic modes controlling the radiation asymmetry in the thermal quench is presented. Conclusions are drawn and the implications are summarized in Chapter 9.

References

[1] Lao, L.L. *et al*. (1985). "Reconstruction of current profile parameters and plasma shapes in tokamaks." *Nuclear Fusion* **25**(11), 1611–1622. doi:10.1088/0029-5515/25/11/007

Chapter 5

Experimental observations

This chapter presents the observations from the massive gas injection rapid shutdown experiments that were outlined in Chapter 4. First, in Section 5.1, the plasma emissivity measurements from the toroidally distributed "DMBolo" array of wall-mounted photodiodes are discussed. The observations of radiation asymmetry in rapid shutdowns are presented in Section 5.2. In Section 5.3, observations from fast magnetic pickup coils are presented, and their significance is discussed. The correlations between and the causes of these observations will be discussed in Chapter 6.

5.1 Plasma emissivity in rapid shutdowns

A time series of the inferred plasma emissivity in the poloidal slice of plasma at each of the six DMBolo diodes through a typical massive gas jet rapid shutdown is shown in Figure 5-1. Several features are evident in the figure. At early times in the rapid shutdown sequence, during the pre-TQ phase before $t = 4.3$ ms since the gas jet trigger , there is more light emitted in the plasma at the diodes which are toroidally near the injector location. This is consistent with the gas spreading toroidally from the gas jet at a speed of about 650 $\mathrm{m\,s^{-1}}$, as previously reported [1]. However, about 4.35 ms after the trigger was sent to the gas jet, the emissivity traces begin to change. There is a jump in the emissivity at all locations in the plasma up to approximately 0.1 $\mathrm{GW\,m^{-3}}$. The emissivity measured by the photodiodes then plateaus for approximately 0.15 ms, while soft X-ray emission increases. This indicates that the total radiation has increased due to the introduction of impurities, but the core plasma remains hot.

Then, approximately 4.55 ms after the gas jet trigger, the thermal quench (TQ) begins. The emissivity rises rapidly at all locations, but quickly decreases 0.1 ms later on the detectors toroidally opposite from the gas jet (blue, green, and purple in Figure 5-1). During this phase, the radiation is clearly toroidally "peaked" near the gas jet location. However, the emissivity feature then moves toroidally, passing in front of the other three detectors in sequence: purple (#4) at 4.7 ms, green (#3) at 4.75 ms, and blue (#2) at 4.8–4.9 ms. Simultaneously, the emissivity falls to $\approx$ 0.1 $\mathrm{GW\,m^{-3}}$ at the toroidal locations near the gas jet (red, orange,

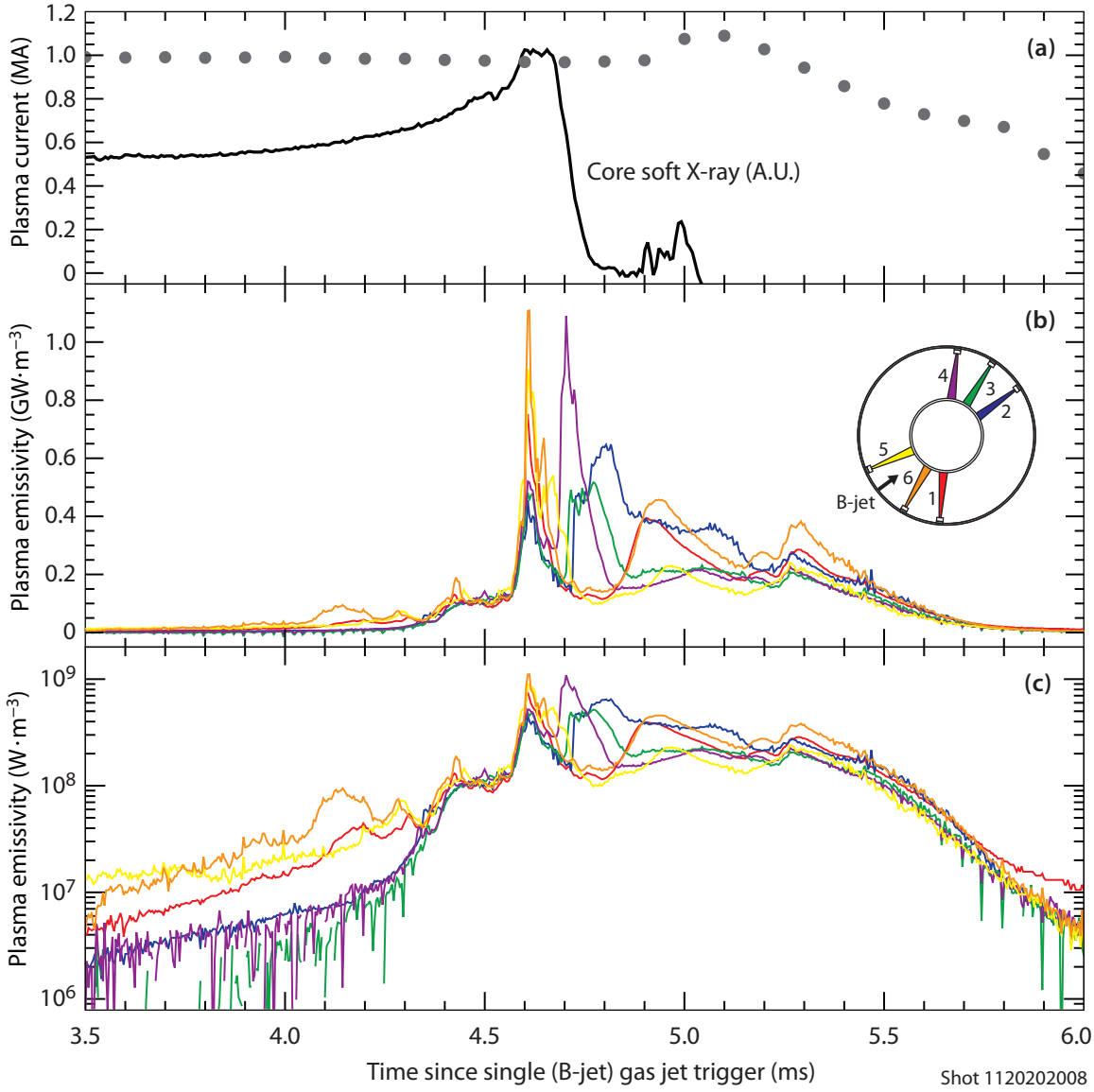

Figure 5-1 – **(a)** Plasma current (measured by a Rogowski coil at 10 kHz) and core soft X-ray emission from a chord through the center of the plasma; **(b)** Inferred plasma emissivity from photodiodes at six toroidal locations through the entire rapid shutdown sequence in C-Mod shot 1120202008; **(c)** Plasma emissivity on logarithmic scale. This shutdown used a single gas jet, at the location shown in the inset (marked "B-jet"). Photodiode locations are represented by colors, at toroidal locations shown in the inset.

yellow). The thermal quench ends at approximately 4.8 ms, as indicated by the core soft X-ray emission having fallen to near zero. It can be observed in Figure 5-1 that there appears to be a toroidal emissivity feature rotating past each diode in turn duing the TQ – as will be discussed further, this is typical of many gas jet rapid shutdowns, and has important implications for the radiation asymmetry.

At this point, at $t \approx 4.9$ ms, the plasma current profile begins to flatten, causing an increase in the plasma current due to conservation of LI [2]. This rapid flattening of the radial current profile (in approximately 0.2 ms, as can be seen in Figure 5-1) is permitted due to the high resistivity of the plasma, and indicates that the plasma is now very cold (< 10 eV). By the traditional definition, the current quench begins at 5.1 ms, *i.e.* when the maximum plasma current is observed and after which the current monotonically decays. As discussed in Section 3.3.1, the silicon photodiodes used in this work have a greatly reduced sensitivity in the visible and near UV compared to the soft X-ray range of wavelengths; this means that the apparent radiated power during the current quench, when the plasma is cold and emitting at longer wavelengths, is, according to the AXUV diodes, lower than that in the thermal quench. This issue is discussed further in Section 5.2.7. The emissivity feature continues to be toroidally asymmetrical during this current rearrangement (CR) period.

Finally, the resistive current quench (CQ) occurs from the current peak at 5.1 ms until the complete termination of the plasma. During this phase, there are typically small asymmetries in this time. A rotating feature may be evident, but is not always present. The radiation falls to essentially zero on the photodiodes before the CQ actually ends, as the plasma can no longer produce significant radiation through Ohmic heating ($\sim J^2$).

The average emissivity from all working wall-mounted photodiodes is shown for 18 single-gas-jet rapid shutdowns (using the B-jet) in Figure 5-2. The target plasmas were all of the lower-single-null diverted magnetic configuration, but had widely varying plasma parameters (stored energy, toroidal field, plasma current, etc.). In addition, the gas jet parameters were not identical on all these shots. Thus, the radiated energy varies widely. However, there are certain features in common to the emissivity profile in all of these rapid shutdowns: a slowly-rising emissivity during the pre-TQ phase, followed by a bright flash of light in the TQ and current-rearrangement (CR) phases, followed by a decaying temporal profile in the early part of the CQ.

It can be observed that there is sometimes an apparent double flash of light (as in shot 1120202009, Figure 5-2(c)) or a triple flash of light (shot 1120622007, Figure 5-2(d)) during the TQ/CR phase. This is essentially an artifact of the limited toroidal coverage by photodiodes – the apparent drop in average emissivity in between the "bumps" in the emissivity time series is due to the radiation feature moving into a region of the tokamak that does not have any coverage by photodiodes. This issue is discussed futher in Section 6.4.

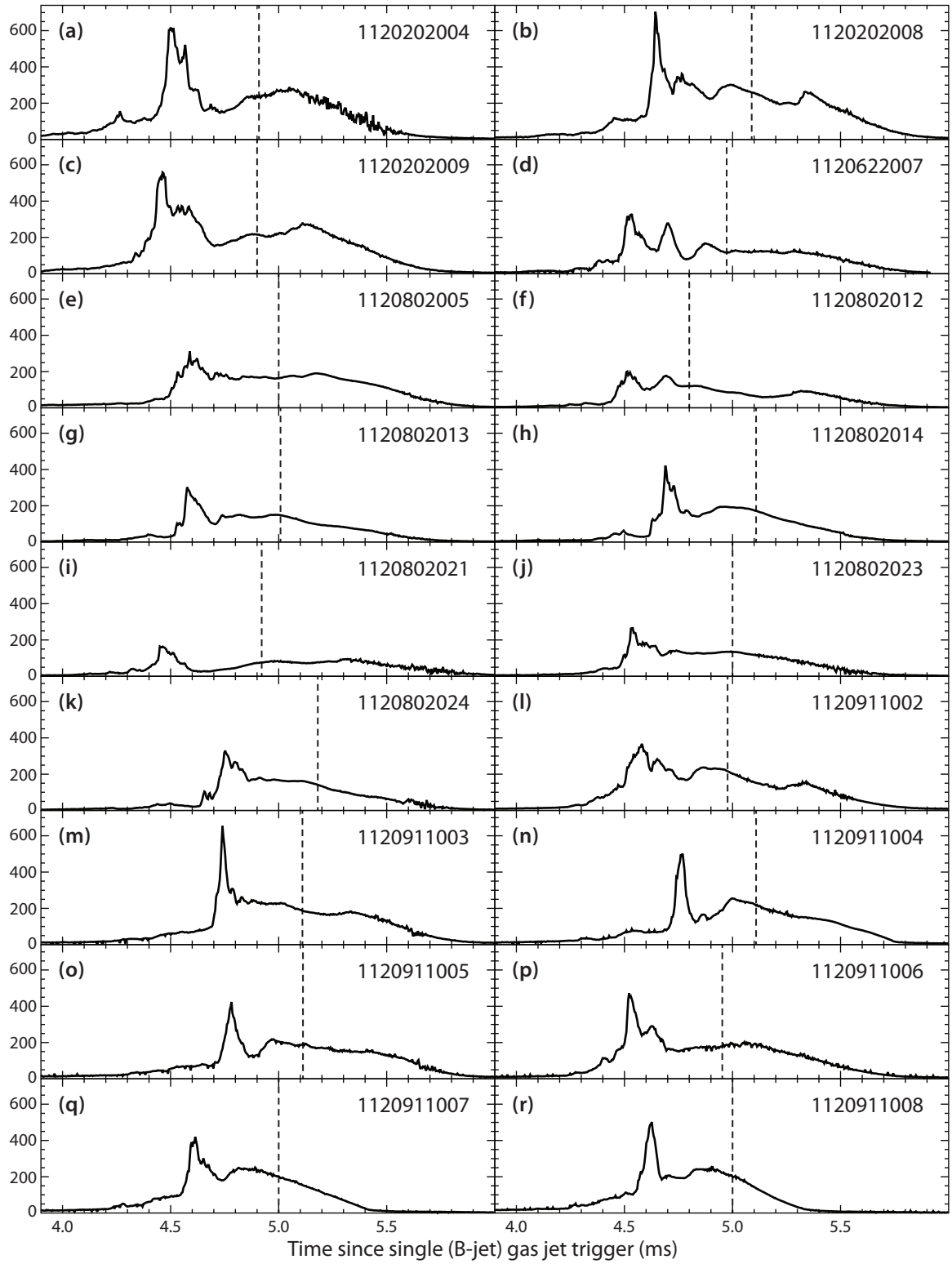

Figure 5-2 – Average plasma emissivity as diagnosed by AXUV photodiodes from 18 single-jet (B-jet) MGI rapid shutdowns. The vertical dashed lines mark the time of the start of the current quench for each rapid shutdown, defined as the peak in the measured toroidal plasma current.

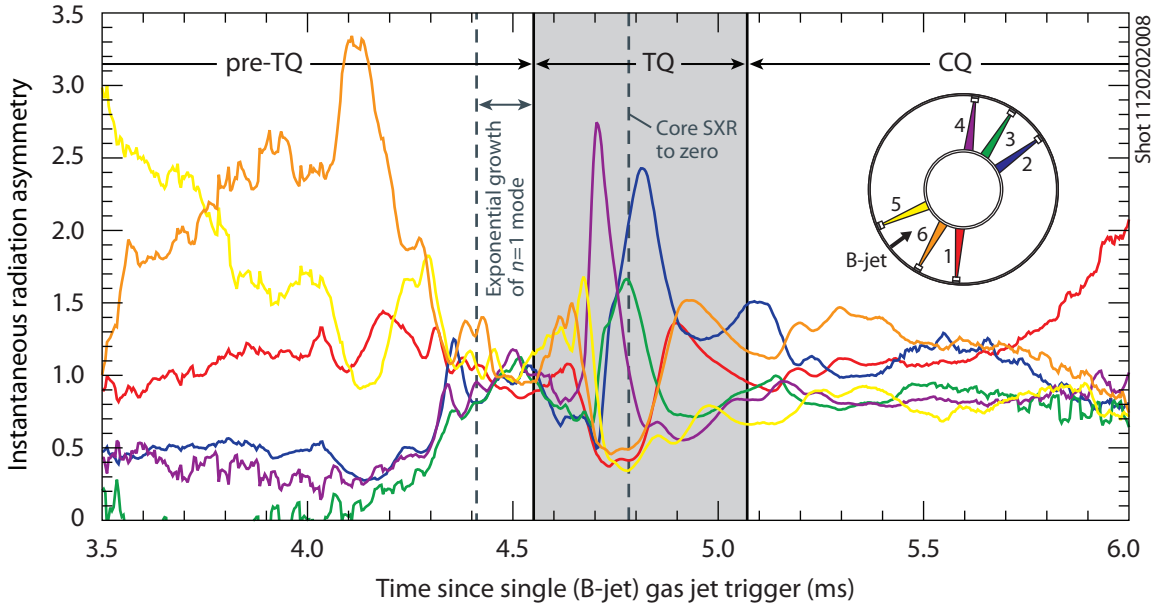

Figure 5-3 – Asymmetry factor (each value normalized to average) for the six diodes shown in Figure 5-3. Thermal quench is indicated by shaded area. Diode #3 (green) falls below zero in the pre-TQ due to a slight baseline drift.

5.2 Radiation asymmetry

In Figure 5-3, the *asymmetry factor* for each diode (each value, divided by the average of the six) is plotted. Normalizing the signal to the average emission allows one to examine the spatial distribution while the absolute emission varies by 10× or more. Several features are evident in the plot. The first is that the pre-thermal quench (pre-TQ) phase is highly asymmetric. This is typical of all single-gas-jet rapid shutdowns. The peaking factor can be as high as 3–5 in this phase. It should be noted, however, that the pre-TQ accounts for a small fraction of the eventual radiated energy on C-Mod gas jet rapid shutdowns; typically, less than 20% of the disruption-integrated radiated energy W_{rad} is radiated during the pre-TQ. This is consistent with the thermal energy available in the periphery of the plasma. During this phase, the radiation asymmetry is determined by gas spreading from the single gas jet, and thus it is not surprising that the radiation is highly asymmetric and peaked near the gas jet location.

Just before the onset of the thermal quench, during the time when an $n = 1$ MHD mode is growing exponentially (marked with a broken line in Figure 5-3; this will be discussed further in Chapter 6), the peaking factor is very low – *i.e.* the plasma radiates very evenly. Again, this is typical of single gas-jet rapid shutdowns. Then, at 4.55 ms, the thermal quench begins. The most obvious feature on the asymmetry plot during the TQ phase is that there is a rotating brightness feature, which moves in the $-\phi$ (clockwise) direction past the purple (#4), green (#3), blue (#2), red (#1), and then orange (#6) diodes in turn. The toroidal location of each diode can be seen in the inset of Figure 5-3.

Finally, as the thermal quench ends, the current rearranges itself internally and the total current increases slightly. In this phase, the peaking factor is more modest, and finally, as the current decays during the CQ phase, the peaking factor is typically very small; less than 1.5. As the brightness measured on all channels decays to low levels, a slight error in baseline subtraction causes the apparent peaking factor on one channel (#1, in red) to increase.

In Section 5.2.1, the problem of defining the limits of time integration when calculating peaking factors is briefly discussed. Then, in the following subsections (5.2.2, 5.2.4, 5.2.5, and 5.2.6), the observations of radiation peaking factor vs. various target plasma parameters of interest are presented.

5.2.1 Defining the limits of time integration

As discussed in Section 2.8.6, the peaking factor is defined as the maximum value of radiant exposure, divided by the average value over the entire plasma-facing first wall. Radiant exposure is the time integral of total irradiance at the wall, but one must decide what limits to integrate over in order to calculate a value of radiant exposure. One wishes to bracket the thermal quench, as this is the phase that will lead to the greatest potential for wall melting in ITER (see Section 2.8.4). The beginning of the TQ is easy to define. The break between the pre-TQ and TQ phases of a rapid shutdown is always marked by two things: the saturation of an $n = 1$ MHD mode, and a sudden sharp rise (break in slope) of plasma emissivity as measured by AXUV diodes.

However, the end of the TQ is more ambiguous. As discussed in Section 2.6, the "traditional" definition of the end of the TQ (and start of the CQ) is when the plasma current reaches its peak. This has the advantage of being a convenient marker, which can be easily read from the plasma current Rogowski coil. On Alcator C-Mod MGI rapid shutdowns, however, the core plasma is cold well *before* the measured plasma current peaks. This can be seen in Figure 5-1(a), where the core soft X-ray signal has decayed to near zero approximately 4.8 ms after the gas jet trigger, but the plasma current does not peak until more than 200 μs later.

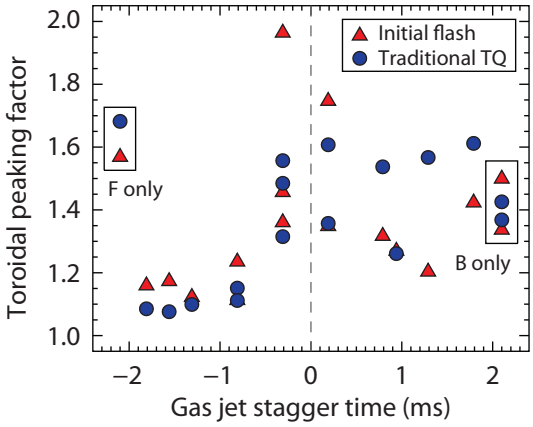

Figure 5-4 – Toroidal peaking factor in the TQ vs. gas jet stagger time for 1 MW ICRF-heated L-mode target plasmas. Negative stagger times mean that the gas from the F-jet arrived first. Red triangles: initial TQ flash only; blue circles: traditional TQ. All target plasmas in this dataset were lower-single-null diverted plasmas with $q_{95} \approx 3.45$, elongation $\kappa \approx 1.59$.

It is, however, always observed that there is an *initial bright flash of light* seen on the photodiodes, which coincides with the fall of the core soft X-ray signal to zero. Thus, we define two possible ends to the TQ. In the first,

referred to as **initial TQ flash only**, the end of the TQ is when the initial bright flash on the photodiodes has subsided, and the core soft X-ray signal has decayed down to noise. These observations indicate that the core plasma has decreased in temperature to $\lesssim 100$ eV or less, *i.e.* that the injected impurities have removed a large fraction of the plasma's stored thermal energy by radiation to the wall. It should be noted that in this case, the end of the TQ does not correspond to the beginning of the CQ: there is an intermittent phase which is referred to as the *current-rearrangement* (CR) phase. This is discussed further in Section 6.5. In the second definition, referred to as **traditional TQ**, the TQ ends as the CQ begins, at the time when the plasma current signal reaches its peak. These names are used throughout this work when labeling figures.

5.2.2 Peaking factor vs. stagger time

The naïve assumption about massive gas jet rapid shutdown would be that all gas jets should be fired at the exact same time[1] in order to optimize the radiation distribution, but this turns out not to be the case. The toroidal peaking factor (TPF) is shown in Figure 5-4 versus the gas jet stagger time t_{stag} (defined in Section 4.1), for 1 MW ICRF-heated L-mode plasmas. The C-Mod plasmas used for this dataset are listed in Section 4.1. At the far left and right are shown representative data for single gas-jet shots (F-jet only or B-jet only).

Several features are identifiable in the figure. First, examining the data during the initial TQ flash only (red triangles), one can see that the highest peaking factors are obtained when the gas jets are nearly synchronized. The peaking factor is lower for asynchronous injection. Single gas-jet injections also have higher radiation asymmetry than the asynchronous two-jet injections, however, asymmetry in these cases is not as high as for the synchronous two-jet injections. In all cases, however, the peaking factor is moderate: less than 2.0, not high enough to cause melting even in ITER.

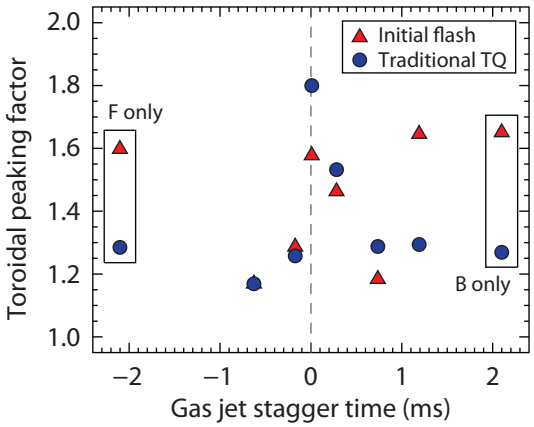

Figure 5-5 – Toroidal peaking factor vs. gas jet stagger time for 3.6 MW ICRF-heated I-mode target plasmas. Negative stagger times mean that the gas from the F-jet arrived first. Red triangles: initial TQ flash only; blue circles: traditional TQ.

In addition, the data are not symmetric about a stagger time of zero (synchronous injection). Lower peaking factors are obtained with the gas from the F-jet arriving at the plasma first. This indicates that the differences in hardware between the two gas jets (see Section 3.2 for more details) are important in setting the radiation behavior of two-jet rapid

[1] Or, more accurately: fired at times such that the gas *arrives at the plasma* at the exact same time. If all the gas jet hardware were identical, this would mean firing all the jets at the same time, but this is not the case on C-Mod; see Section 3.2.

shutdowns. It has been observed on other tokamaks [3] and in extended MHD simulations [4] that varying the poloidal location of the injector can change the impurity assimilation, although in those cases, the two injectors were at the low-field side and the high-field side of the plasma, respectively. On Alcator C-Mod, the two injectors are both on the low-field side. Thus, differences in gas jet hardware may be more important than the poloidal location of the injectors in explaining the +/− asymmetry in Figure 5-4.

In Figure 5-5, the peaking factor for several MGI rapid shutdowns of high-power ICRF-heated I-mode [5] target plasmas is shown vs. gas jet stagger time. Again, we observe higher peaking factors for the nearly-synchronous two-jet injections and the single-jet injections, with the lowest peaking factors obtained for slightly asynchronous two-jet injections (≈ 1.0 ms in either direction). Additionally, the same asymmetry between the two jets is seen in Figure 5-5 as in Figure 5-4. There is a large scatter in the calculated toroidal radiation peaking factor for the single-jet MGI rapid shutdowns, as well as for the two-jet shutdowns in which the gas from the B-jet arrived first. However, the peaking factor is consistently low for the two-jet shutdowns in which the gas from the F-jet arrived first. This observation holds true for two-jet MGI rapid shutdowns of five L-mode plasmas and two I-mode plasmas, which gives some statistical confidence in the observation.

5.2.3 Peaking factor in the pre-TQ

The above observations of peaking factor were for the thermal quench phase. In Figure 5-6, the toroidal peaking factor during the pre-thermal quench phase is plotted against the gas jet stagger time for two-jet MGI rapid shutdowns. It can be seen that the peaking factor is lowest for the synchronous two-jet shutdowns. This is consistent with the radiation asymmetry during this phase as being set by gas spreading from the discrete injectors.

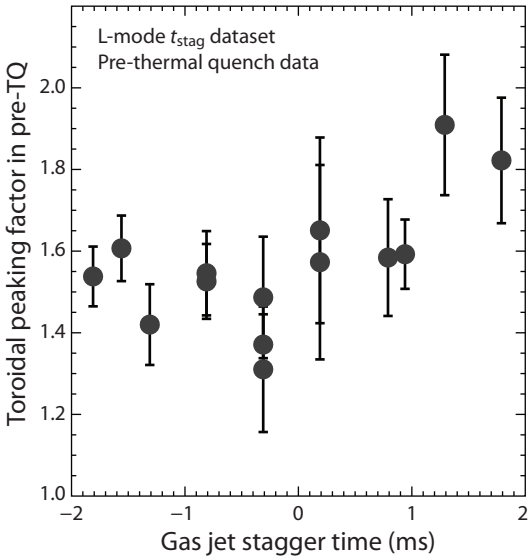

Figure 5-6 – Toroidal peaking factor in the pre-TQ phase versus gas jet stagger time for two-jet MGI rapid shutdowns of 1 MW ICRF-heated L-mode target plasmas.

5.2.4 Peaking factor vs. plasma stored energy

As discussed in Section 4.2, MGI rapid shutdowns were conducted into lower single-null plasmas with varying stored thermal energy. The toroidal peaking factor in the thermal quench was calculated for both definitions of the TQ, and the observations are reported in Figure 5-7.

The most important thing to note is that there is no obvious trend in toroidal peaking factor with plasma stored energy. The highest peaking factors were obtained for the lowest stored energy ($W_{th} \approx 64$ kJ), but there are not enough data to determine if this is a reproducible effect. In addition, peaking factors are again modest in this dataset: usually below 2.0, and only in one case just above 2.0. It is thus concluded that plasma stored energy is not a dominant effect in setting the toroidal radiation peaking factor in MGI rapid shutdowns. It is noted that plasma stored energy also does not correlate to other figures of merit for rapid shutdown, such as pre-TQ duration [6, Figure 6] (which instead correlates to plasma magnetic safety factor [7]), indicating that the plasma stored energy (proportional to the plasma pressure) is not a dominant parameter in determining the dynamics of the rapid shutdown.

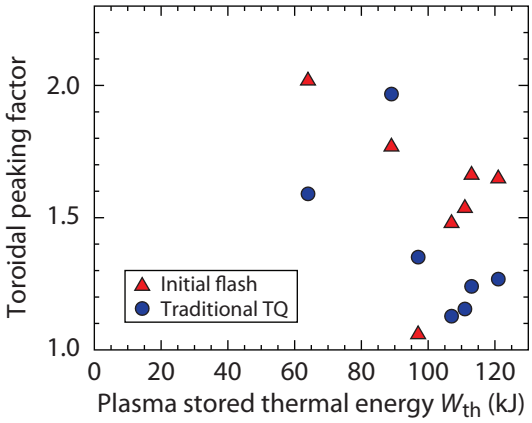

Figure 5-7 – Toroidal peaking factor vs. plasma stored energy for lower single-null auxiliary-heated target plasmas. Red triangles: initial TQ flash only; blue circles: traditional TQ. No trend is discernible.

5.2.5 Peaking factor vs. elongation

As discussed in Section 4.3, a scan was conducted of plasma elongation in the inner-wall limited magnetic configuration. MGI rapid shutdowns were conducted using a single gas jet (B-jet) into these target plasmas. The toroidal peaking factor in the TQ is plotted vs. target plasma elongation κ in Figure 5-8. In addition, in order to estimate statistical confidence in the results at each elongation, the standard deviation of the TPF was calculated from the four data points at each elongation (two for each definition of the TQ). The one- and two-sigma confidence intervals are then shown in grey and yellow, respectively, in Figure 5-8.

It can be seen that while the statistics are poor, the peaking factor over the entire traditional TQ (from the start of the radiation flash to the start of the CQ) tends to be lower for the higher-elongation target plasmas. The scatter is larger, and there is no definite trend, for the peaking factor in the initial TQ flash only.

5.2.6 Peaking factor vs. magnetic safety factor

Finally, as discussed in Section 4.4, a scan was conducted of plasma magnetic safety factor in the lower single null diverted magnetic configuration. MGI rapid shutdowns were conducted using the single gas jet (B-jet). The toroidal radiation peaking factor in the TQ is

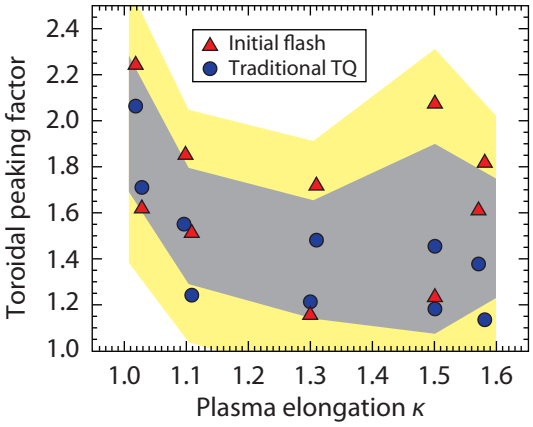

Figure 5-8 – Toroidal peaking factor vs. plasma elongation in the inner-wall limited plasma configuration. Red triangles: initial TQ flash only; blue circles: traditional TQ. Grey and yellow shaded regions represent estimated one- and two-sigma confidence intervals at each elongation.

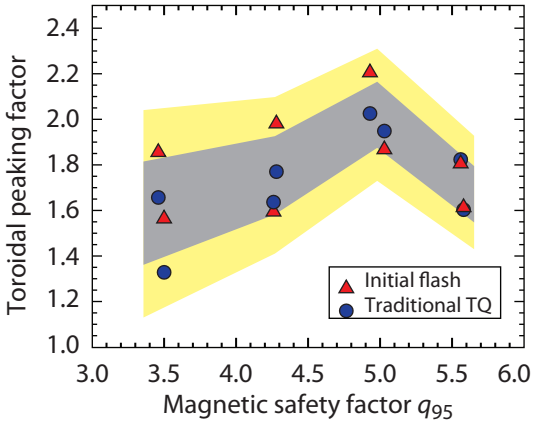

Figure 5-9 – Toroidal peaking factor in the thermal quench vs. plasma magnetic safety factor in the lower single-null magnetic configuration. Red triangles: initial TQ flash only; blue circles: traditional TQ. The error ranges are estimated from the standard deviation of *all* TPFs (initial flash and traditional TQ) at a given magnetic safety factor. Grey and yellow bars are one- and two-sigma errors, respectively, estimated from all four TPFs (initial TQ flash *and* traditional TQ) at each safety factor.

plotted vs. the target plasma magnetic safety factor q_{95} in Figure 5-9.

The statistics again are limited, with only eight rapid shutdowns in the dataset (two at each safety factor). However, it can be seen that the peaking factor has a maximum at a safety factor q_{95} near 5, declining for higher and lower values of q_{95}. This is favorable for ITER, which has a safety factor of $q_{95} \approx 3$ in its baseline inductive scenario.

5.2.7 Energy balance in TQ and CQ using AXUV diodes

A typical Alcator C-Mod H-mode discharge will have a plasma stored thermal energy W_{th} of 80–150 kJ, and a poloidal magnetic field energy W_{mag} of 800–1600 kJ. The thermal energy for a constant plasma shape (ε, κ, δ) varies as $W_{\text{th}} \sim \langle p \rangle \cdot R^3$, where $\langle p \rangle$ is volume-averaged plasma pressure and R major radius. The stored poloidal magnetic field energy $W_{\text{mag}} = LI_{\text{p}}^2/2$, where $L \sim \mu_0 R$ is the plasma ring inductance, and I_{p} is plasma current. Thus:

$$\frac{W_{\text{th}}}{W_{\text{mag}}} \sim \frac{\langle p \rangle R^3}{RI_{\text{p}}^2} = \frac{\langle p \rangle R^2}{I_{\text{p}}^2} \tag{5.1}$$

Noting that the poloidal field $B_\theta \simeq \mu_0 I_{\text{p}}/2\pi a$ for a circular plasma, Equation 5.1 can be rewritten as:

$$\frac{W_{\text{th}}}{W_{\text{mag}}} \sim \frac{\langle p \rangle R^2}{B_\theta^2 \varepsilon^2 R^2} \sim \beta_\theta \tag{5.2}$$

where β_θ is the poloidal beta, $\beta_\theta \equiv 2\mu_0 \langle p \rangle / B_\theta^2$. Thus, the ratio of thermal to magnetic stored energy in the plasma scales as the plasma poloidal beta, and low-beta machines like Alcator C-Mod ($\beta_\theta \approx 0.3$) have most of the energy accessible during a disruption or rapid shutdown stored in the poloidal magnetic field created by the plasma current, not in the plasma pressure.

With this in mind, examine the plasma emissivity traces seen in panel (b) of Figure 5-1. The plasma emissivity is very low after the start of the current quench, despite the radiated energy being approximately an order of magnitude higher in the CQ. This is true in general of diode emissivity traces for MGI rapid shutdowns[2]. In Figure 5-10 the plasma stored energy (magnetic and thermal) is shown versus time through the rapid shutdown sequence. This plasma had a stored thermal energy of 50 kJ (from EFIT) before the rapid shutdown, and a plasma current of 1.0 MA, corresponding to a poloidal magnetic field energy of approximately 750 kJ (15 times higher than the thermal energy!)

[2] This can be seen on other tokamaks as well: see e.g. Figure 3 of [7]; P_{rad} is essentially zero after the peak in the current which marks the start of the CQ. JET used a foil bolometer with slow time resolution for radiated power measurements (see Figure 3 of [6]), however, even in this case, it can be seen that the apparent radiated energy in the pre-TQ and TQ are equal or greater to the radiated energy during the CQ.

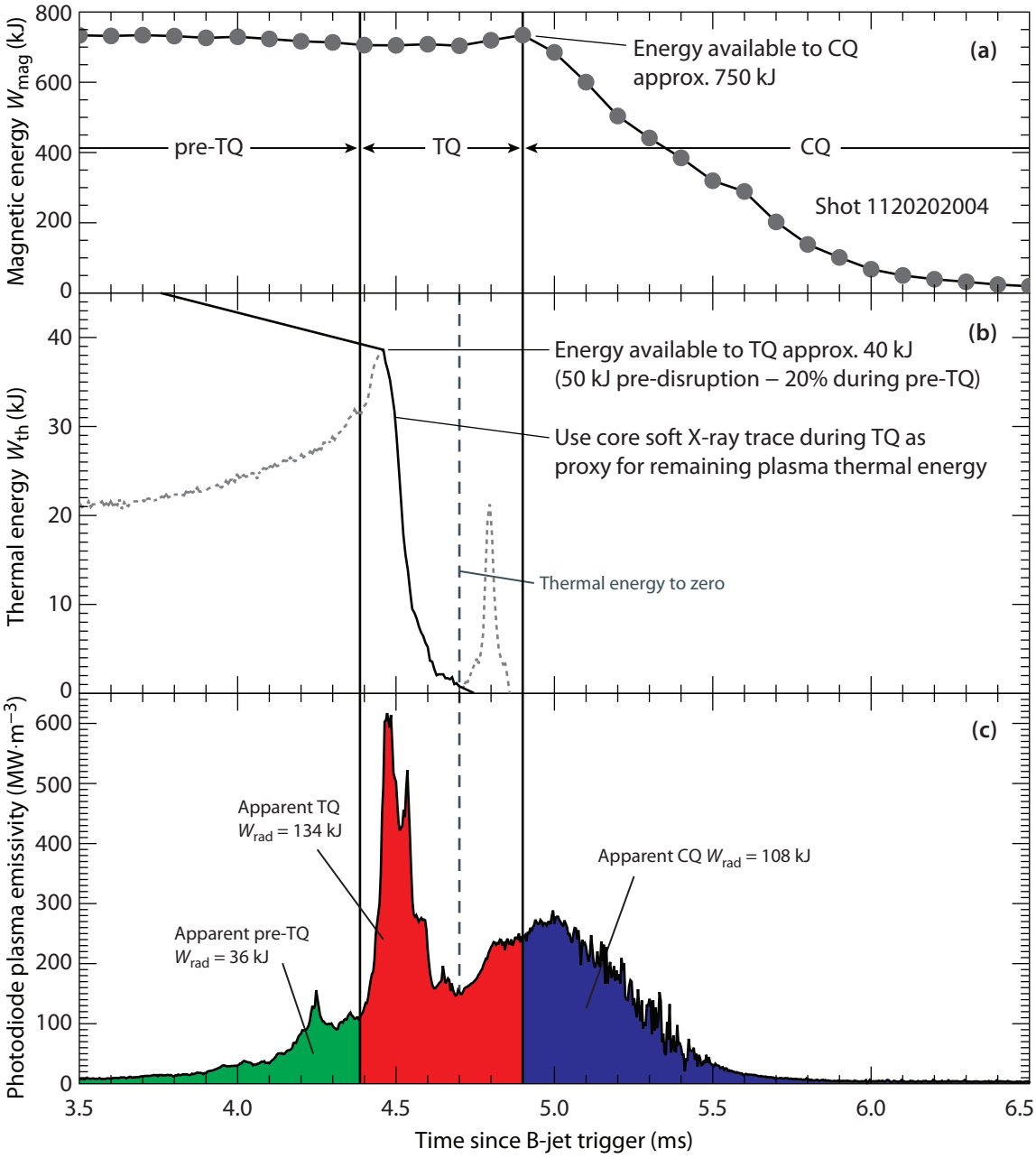

Figure 5-10 – **(a)** Estimated plasma magnetic and **(b)** thermal energy as inferred from plasma current, edge cooling from ECE radiometry, and core cooling from core soft X-ray emission; **(c)** Average plasma emissivity inferred from photodiodes, for single (B-jet) rapid shutdown of Alcator C-Mod shot 1120202004. The thermal energy curve shown is based on a decline from 50 kJ to 40 kJ through the pre-TQ, and then a decline to near zero following the core soft X-ray emission curve.

In comparison, the apparent radiated energy from the photodiodes is 36 kJ in the pre-TQ, and using the traditional definition of the TQ, 134 kJ in the TQ and 108 kJ in the CQ. Even ascribing all radiation after the core thermal crash and initial flash of radiant power to the CQ, the TQ still has an apparent radiation of 92 kJ and the CQ, only 150 kJ.

The diodes are calibrated using the flat-top of highly impure plasmas (seeded with argon and nitrogen) at temperatures above 1 keV, which produces a mostly soft X-ray spectrum (see Section 3.3.4). Examining Figure 3-7, it can be seen that the diode responsivity is flat in the soft X-region, with a trough (reduced sensitivity) in the UV (and especially near-UV) region. Thus, as the plasma cools during the TQ, the effective diode responsivity to the outcoming radiation will decrease, meaning that the diodes will underestimate the radiated energy later in the disruption (especially in the current quench). This trough, however, is not that deep: according to the published responsivity curve, the diode responsivity is only a factor of approximately 2.5 lower at its lowest point in the near UV region compared to the diode responsivity to soft X-rays.

There are thus two conclusions that can be drawn from the apparent energy imbalance in MGI rapid shutdowns. First, there must be some poloidal magnetic field energy radiated before the thermal quench is over. There simply is not enough stored thermal energy to account for the radiated power during the TQ. (Recall, the diodes can only *underestimate* the radiated power during the disruption sequence.) Certainly, the power being radiated during the phase between the end of the core soft X-ray crash and the peak in the measured plasma current must be coming from poloidal magnetic field energy, since the plasma thermal energy is already gone by that point.

The second conclusion is that the published diode responsivity curves must be incorrect. That is, the trough in the responsivity curve must be deeper than the published data. This could not be verified on the diodes used for these experiments, since producing photons through the entire energy range covered by Figure 3-7 requires access to a synchrotron light source, but it is supported by the experience of other experimentalists who work with AXUV diodes on DIII-D and Alcator C-Mod [8].

For the purposes of this thesis, the unknown diode responsivity curves complicate the interpretation of the measurements, but do not invalidate it, for two reasons. First, the diode responsivity may differ from the published data, but it did not change through the experimental campaign. The diodes were absolutely calibrated using a UV LabSphere (URS-600) calibrated photosource before the experiments, and again after, with a decrease of only 2% in photocurrent.

Secondly, because the concern with MGI rapid shutdown is mainly with toroidal peaking factors, and not with absolute radiated power (this is already assumed to be equal to W_{th}/τ_{TQ}). There is however a simple argument for why toroidal radiation asymmetry as measured by diodes approximates true toroidal radiation asymmetry: because the radiation *spectrum* will be toroidally symmetric, even if the *power* is not. For the peaking factor calculated by photodiodes to differ significantly from the true toroidal peaking factor, there would

have to be a significant toroidal variation in the spectrum of the radiation. The radiation is produced by recombination of impurity electrons. Recombination rates are dependent on density, which means that charge state densities could be different at different toroidal locations, but the *temperature* will equilibrate very quickly:

$$\vec{q} = -\kappa \nabla T_e \tag{5.3}$$

where κ is the Spitzer thermal conductivity $\kappa = \kappa_0 T_e^{5/2}$ [$m^{-1} s^{-1}$], and $\kappa_0 = 2000$ W m^{-1} $eV^{-7/2}$. At 100 eV (late in the thermal quench), then, $\kappa \approx 1.25 \times 10^{27}$ $m^{-1} s^{-1}$, and the toroidal temperature equilibration time $\tau \approx 2n(\pi R)^2/\kappa \approx 4$ μs $\ll \tau_{TQ}$. While kinetic modifications to the Spitzer thermal conductivity may produce slight toroidal temperature asymmetries, it can be assured that large differences ($gtrsim$100 eV) are not possible, and thus the radiation spectrum will be the same on each side of the tokamak.

Thus, it is concluded that the apparent discrepancy in the radiated power between the TQ and CQ phases are likely caused mainly by a combination of an incorrect diode responsivity curve, and a "blending" of the phases: some of the poloidal magnetic field energy is radiated in the thermal quench, especially in its later phases. This would be an interesting area of further theoretical investigation: for example, some of the poloidal magnetic field energy from the region outside the plasma, but inside the vacuum vessel, may be converted into thermal energy and radiated during the thermal quench. However, the values of radiated power asymmetry calculated from photodiode observations are still trustworthy.

5.3 Magnetic oscillations in rapid shutdowns

Up to now, the toroidal peaking factor integrated through the thermal quench for MGI rapid shutdown of various target plasmas has been discussed. This section will present the other important piece of data that was obtained during the experiments: poloidal magnetic field fluctuations. The fast magnetics pickup coils were described in Section 3.4; it is reiterated here that they measure the rate of change of the magnetic field (dB/dt), are mounted on stalks on the outboard (low-field) side of the plasma, and have a bandwidth of over 100 kHz. (The coils are digitized at a rate of 2.5 MHz.)

A typical signal from one of the fast magnetics pickup coils through a two-jet MGI rapid shutdown is plotted in Figure 5-11. Several features are apparent. In the pre-thermal quench phase, there is a growing perturbed poloidal magnetic field, whose amplitude reaches a peak near the time when the thermal quench begins. This mode is actually growing even before approximately 4.3 ms, but it cannot be seen on the scale of Figure 5-11. During the thermal quench, there are large magnetic fluctuations, but these pale in comparison to the magnetic fluctuations during the phase between the end of the thermal quench and the beginning of the current quench: the fluctuations during this period are so large that they saturate the

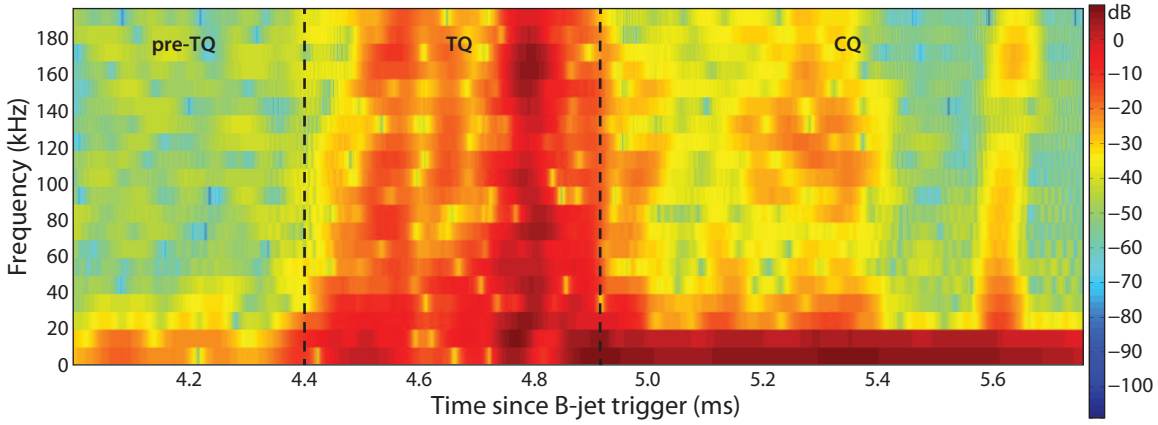

Figure 5-12 – Spectrogram of magnetic fluctuations ($\mathrm{d}B/\mathrm{d}t$) as measured by Mirnov coil BP_BC_TOP through MGI rapid shutdown of Alcator C-Mod shot 1120202004. Power in each frequency in arbitrary units. The dashed lines mark the start of the TQ and CQ, respectively. Note that the magnetic pickup coils saturate during the later phase of the TQ, approximately from 4.7 to 4.9 ms after the gas jet trigger.

magnetic pickup coils (the amplifiers on the coils have a range of +/− 5 V, corresponding to approximately 2.4×10^3 T s^{-1}. Finally, during the current quench phase, the magnetic fluctuations are again resolvable, with a constant positive baseline on the $\mathrm{d}B/\mathrm{d}t$ signal caused by the exponentially decaying plasma current.

A spectrogram (short-time Fourier transform) of the same magnetic fluctuation data is shown in Figure 5-12. The Mirnov coils are digitized at 2.5 MHz, corresponding to a Nyquist frequency of 1.25 MHz; the data in Figure 5-12 are shown only up to 200 kHz as that is the maximum frequency range of interest for the low-n MHD modes being investigated here.

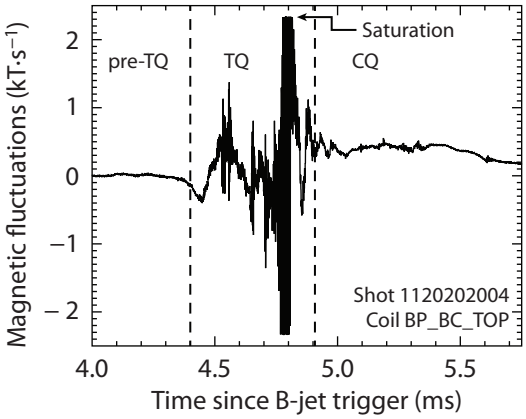

Figure 5-11 – Magnetic fluctuations ($\mathrm{d}B/\mathrm{d}t$) as measured by Mirnov coil BP_BC_TOP through MGI rapid shutdown of Alcator C-Mod shot 1120202004. See Table 3-2 for list of locations of magnetic coils.

There are 72 Mirnov coils in total in Alcator C-Mod, although most of them are closely-spaced coils within the limiter structures, and at any given time, only a subset of them are digitized. The nine coils used in this study were listed in Table 3-2. In the following section, it will be discussed how these coils were used to resolve the amplitude and phase of low-n MHD modes, and how this relates to the toroidal radiation peaking factor observations reported earlier in the chapter.

5.4 Magnetic mode growth rate in the pre-TQ

A typical procedure for identifying coherent electromagnetic fluctuation modes in a tokamak is the following: First, plot a spectrogram of the fluctuations (time on the x-axis, frequency on the y-axis) as measured by Mirnov coils in order to identify coherent modes, and the frequency at which those modes exist. Then, filter the data digitally in order to increase the signal-to-noise level. Finally, using the cross-correlation between poloidally and toroidally separated pickup coils, or a more sophisticated procedure like SparSpec [9], the spatial frequency (or mode number) in the toroidal and poloidal direction is identified.

However, this procedure fails when applied to the magnetic fluctuations in MGI rapid shutdowns on Alcator C-Mod, because there are simply not enough oscillation periods to unambiguously identify the mode. Particularly in the pre-TQ phase, when the mode is exponentially growing, there might be one or two oscillations on each coil before the mode saturates and the TQ begins. This is in contrast to a typical MHD mode (such as a toroidal Alfvén eigenmode) which might have an oscillation frequency of $\approx$ 10 kHz and exist for 0.1 s, meaning there are $\approx$ 1000 oscillations of the mode present on the magnetic pickup coils. Furthermore, the growth rate γ $[\mathrm{s}^{-1}]$ of the mode is comparable to the rotation rate ω $[\mathrm{s}^{-1}]$, which again renders the techniques usually used on steady-state oscillations ineffective.

Instead, the procedure is simple: Assume the poloidal magnetic field perturbation from the mode is of the form:

$$\tilde{B}_\theta = B_0 \exp(\gamma t) \cos(n\phi - \omega t - \delta_0) \tag{5.4}$$

where B_0 is the amplitude of the perturbed magnetic field at the start of exponential growth, γ is the magnetic field growth rate $[\mathrm{s}^{-1}]$ ($\tau = \gamma^{-1}$ is then the magnetic field "growth time", in $[\mathrm{s}]$), n is the toroidal mode number of the perturbation, ω is its toroidal rotation rate $[\mathrm{rad\,s}^{-1}]$, and δ_0 is simply an initial phase at the start of exponential growth, defined at $t = 0$.

However, the perturbed poloidal magnetic field itself is not measured, but rather its time derivative. Taking the derivative of Equation 5.4:

$$\dot{B}_\theta = B_0 \left[\gamma \exp(\gamma t) \cos(n\phi - \omega t - \delta_0) + \omega \exp(\gamma t) \sin(n\phi - \omega t - \delta_0)\right] \tag{5.5}$$

$$\dot{B}_\theta = B_0 \left[\gamma \cos(n\phi - \omega t - \delta_0) + \omega \sin(n\phi - \omega t - \delta_0)\right] \exp(\gamma t) \tag{5.6}$$

where $\dot{B}_\theta$ is the time derivative of the *perturbed* magnetic field. Defining $\delta_\mathrm{t} \equiv \delta_0 + \omega t$ and $B_{0\mathrm{t}} \equiv B_0 \exp(\gamma t)$, Equation 5.6 becomes:

$$\dot{B}_\theta = B_{0t}\left[\gamma\cos\left(n\phi - \delta_t\right) + \omega\sin\left(n\phi - \delta_t\right)\right] \tag{5.7}$$

which is what the $\dot{B}$ mode appears as at *at each point in time*. Equation 5.7 can then finally be rewritten as follows:

$$\dot{B}_\theta\left(\phi; t\right) = B\cos\left(n\phi - \delta\right) \tag{5.8}$$

where B is simply the apparent amplitude of the $\dot{B}$ mode, and δ is the apparent phase of the $\dot{B}$ mode. Comparing Equation 5.8 to Equation 5.7, it is easily seen that $\delta = \delta_t + \tan^{-1}\left(\omega/\gamma\right)$, and $B = B_{0t}\sqrt{\gamma^2 + \omega^2}$. That is, *if* the actual perturbed poloidal magnetic field is exponentially growing (or shrinking) and rotating at *constant* growth and rotation rates, then the apparent $(\dot{B}_\theta)$ mode growth and rotation rates will be the same as the true (B_θ) mode growth and rotation rates. The true B_θ mode amplitude can be easily obtained from the apparent $\dot{B}_\theta$ mode amplitude by simply dividing by $\sqrt{\gamma^2 + \omega^2}$, and the true mode phase is obtained by subtracting the phase shift $\tan^{-1}\left(\omega/\gamma\right)$ of the apparent mode.

The actual growth and rotation rates γ and ω are then obtained for experimental data as follows: at every time point, fit an $n = 1$ (or $n = 2$) $\dot{B}$ mode to the available Mirnov coils using a least-squares minimization. In Figure 5-13, the results of this procedure for an actual two-jet MGI rapid shutdown (C-Mod plasma 1120202004) are shown. It can be seen that the mode grows with an e-folding time of approximately 76 μs, with approximately 250 μs elapsing between the observed start of exponential growth and the time when the mode saturates and the thermal quench begins (see Section 5.4.1 for further discussion of this timing).

In Section 5.4.1, the timing of the exponential growth of the $n = 1$ mode relative to the other phases of the disruption is discussed. Then, in Sections 5.4.2 and 5.4.3, experimental observations of the growth rate of this $n = 1$ mode in the pre-TQ for various target plasmas are presented.

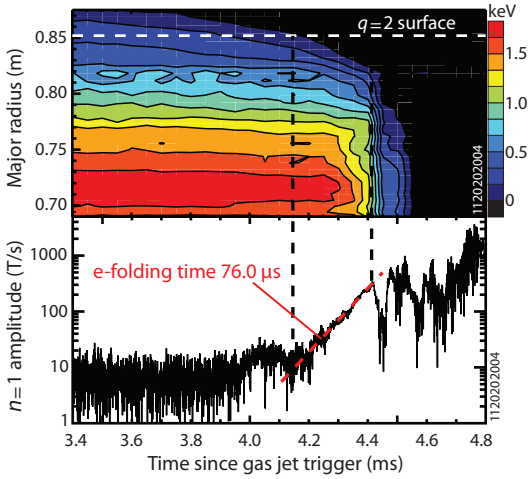

Figure 5-14 – **(a)** Second-harmonic X-mode ECE radiometry of plasma electron temperature; and **(b)** Amplitude of $n = 1$ MHD mode through the sequence of MGI rapid shutdown of Alcator C-Mod plasma 1120202004. It can be seen that the thermal quench event, marked by the sudden crash of core temperature (and mixing of impurities into the core, eventually causing cutoff of the ECE signal) begins just as the $n = 1$ mode reaches its peak amplitude.

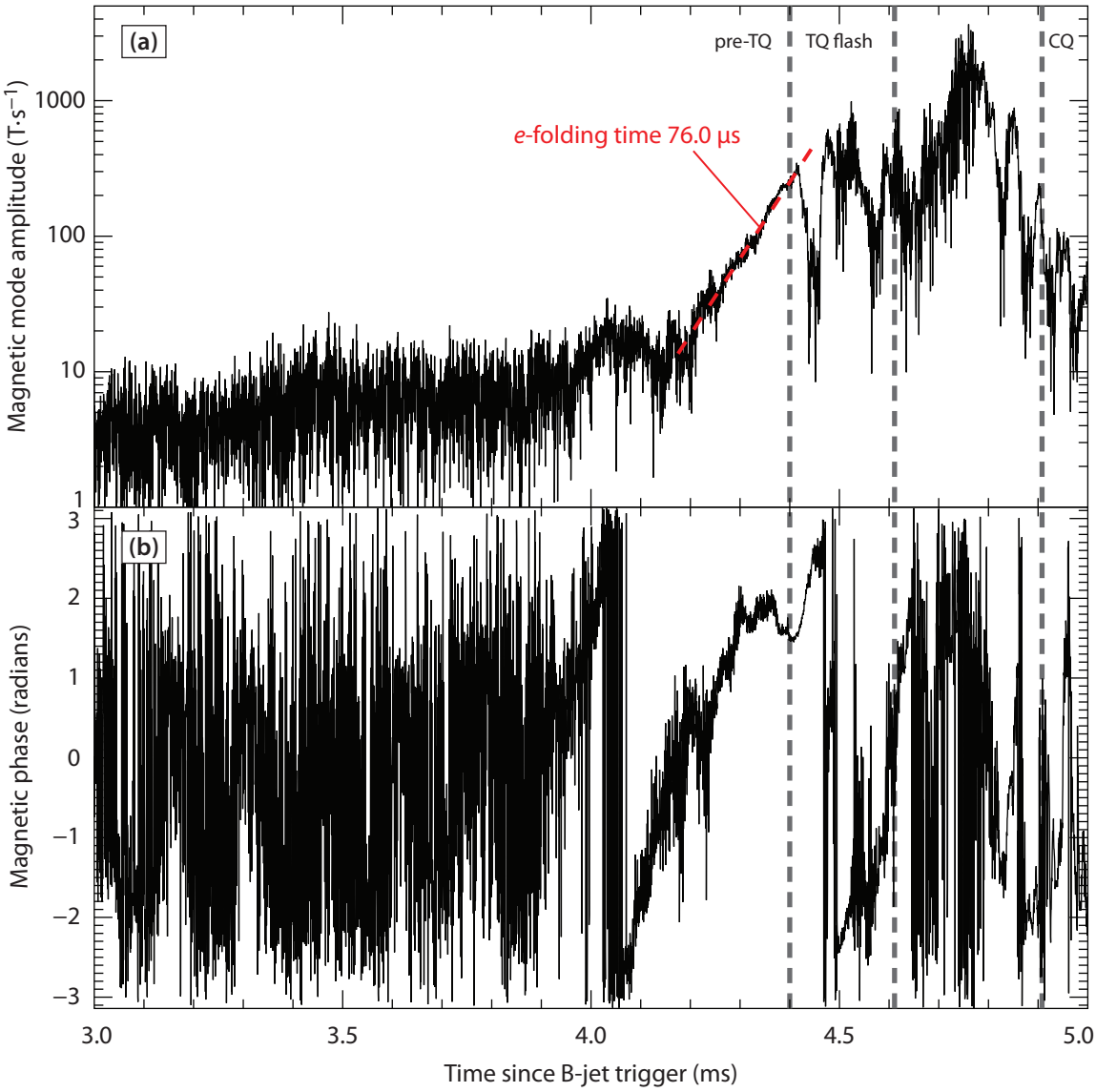

Figure 5-13 – Results of magnetic $n = 1$ mode fitting procedure in pre-TQ of MGI rapid shutdown of Alcator C-Mod shot 1120202004. **(a)** *Amplitude*. The mode is growing with an e-folding time of 76 μs, or a growth rate of 1.3×10^4 s^{-1}. **(b)** *Phase*. The mode is rotating in the counter-clockwise ($+\phi$) direction during the growth phase. Ordinarily, the phase of the mode is unresolvable during the thermal quench.

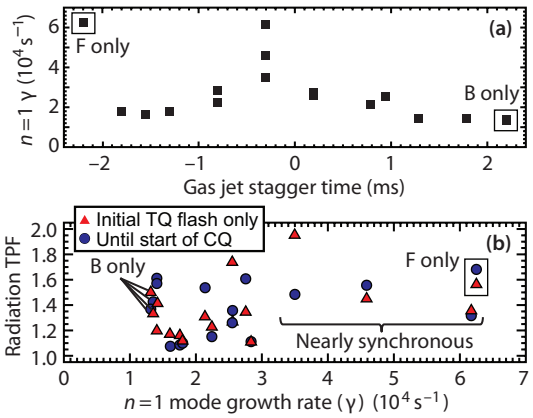

Figure 5-15 – **(a)** Growth rate of $n = 1$ magnetic mode in pre-TQ vs. gas jet stagger time for MGI rapid shutdown of identical L-mode target plasmas; **(b)** Toroidal radiation peaking factor for both definitions of the TQ versus $n = 1$ magnetic mode growth rate for the same dataset.

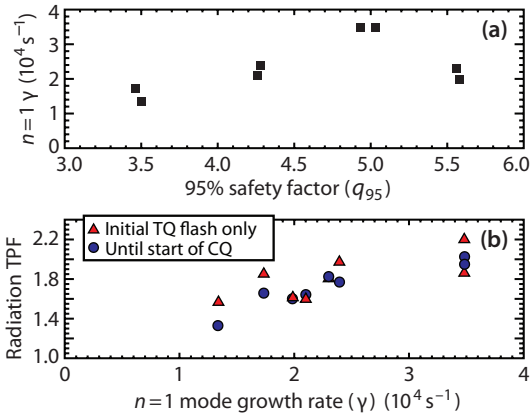

Figure 5-16 – **(a)** $n = 1$ magnetic mode growth rate vs. plasma magnetic safety factor for the q-scan dataset; **(b)** Toroidal radiation peaking factor for both definitions of the TQ versus $n = 1$ magnetic mode growth rate for the same q_{95} dataset.

5.4.1 Timing of exponential growth relative to thermal quench

In every MGI rapid shutdown, the $n = 1$ mode exponentially grows in the pre-TQ phase. Furthermore, it saturates at the exact time that the plasma brightness jumps, marking the start of the thermal quench event. Figure 5-14 shows the amplitude of the $n = 1$ mode in the pre-TQ phase of MGI rapid shutdown of C-Mod shot 1120202004, as well as a profile of plasma electron temperature as measured by second-harmonic X-mode ECE radiometry.

It can be seen that the mode begins growing approximately when the cooling front has reached the $q = 2$ surface (although this is difficult to resolve, since the $q = 2$ surface is so close to the plasma edge on a typical Alcator C-Mod shot). More importantly, the onset of the TQ corresponds to the time when the $n = 1$ mode stops growing. Typically, the magnetic mode amplitude either saturates at this point (levels off), or its apparent amplitude shrinks. This is because the mode being fit is the apparent ($\dot{B}$) mode, not the true magnetic mode itself; recall that the $\dot{B}$ amplitude is the true mode amplitude multiplied by the scaling factor $\sqrt{\gamma^2 + \omega^2}$; thus when the mode stops growing, $\gamma \to 0$ and thus the apparent ($\dot{B}$) mode amplitude decreases.

5.4.2 Magnetic growth rate vs. gas jet stagger time

The growth rate of the $n = 1$ mode in the pre-TQ was calculated using the procedure outlined in Section 5.4 for each of the two-gas-jet MGI rapid shutdowns in the "L-mode t_{stag} dataset. The results are shown in panels (a) and (b) of Figure 5-15.

It can be seen that the fastest pre-TQ $n = 1$ growth rates are also obtained for these "nearly synchronous" two-jet shutdowns. Recall that the the highest toroidal peaking factors were also obtained for these "nearly synchronous" two-jet shutdowns; see Figure 5-4. This is observable in panel (b), where the radiation peaking factor is plotted against the $n = 1$ growth rate. The "nearly synchronous" shutdowns cluster away from the asynchronous-injection shutdowns.

5.4.3 Magnetic growth rate vs. magnetic safety factor

In panel (a) of Figure 5-16, it can be clearly seen that the growth rate of the $n = 1$ magnetic mode in the pre-TQ depends on magnetic safety factor, although not in a monotonic fashion. The fastest growth rates are obtained near a safety factor of $q_{95} \approx 5$, while the growth rate is lower for safety factors higher or lower than this. The radiation asymmetry is plotted against the $n = 1$ mode growth rate in panel (b), showing a clear increasing trend between the radiation asymmetry and the MHD mode growth rate. This is in contrast to results presented in the past for radiation asymmetry in single-jet rapid shutdowns as measured by opposite-facing diode arrays [10].

5.5 Comparison of DMBolo and AXA/AXJ asymmetries

In addition to the toroidal array of six photodiodes, one can determine a radiation asymmetry using the opposite-facing "AXA" and "AXJ" arrays (see Section 3.6). Integrating the radiated power in a similar fashion as for the ordinary photodiode arrays, one can then define an "asymmetry factor" AF:

$$\mathrm{AF} \equiv \frac{W_{\mathrm{AXA}} - W_{\mathrm{AXJ}}}{W_{\mathrm{AXA}} + W_{\mathrm{AXJ}}} \tag{5.9}$$

where W_{AXA} and W_{AXJ} are simply the time-integrated radiated power as seen by chords on the AXA and AXJ arrays, respectively. In Figure 5-17, this quantity AF is plotted against gas jet stagger time for the "L-mode t_{stag}" dataset. (See Figure 5-4 for the TPF as calculated by the toroidal DMBolo array of photodiodes versus t_{stag} for this dataset.)

Finally, in Figure 5-18, the peaking factor from the six wall-mounted DMBolo photodiodes is compared to the AXA/AXJ asymmetry factor. It can be seen that the peaking factor as calculated by the wall-mounted photodiodes generally increases as the AXA/AXJ asymmetry factor increases (in either direction), although there is a large scatter, likely due to the different toroidal coverage of the two diagnostic sets.

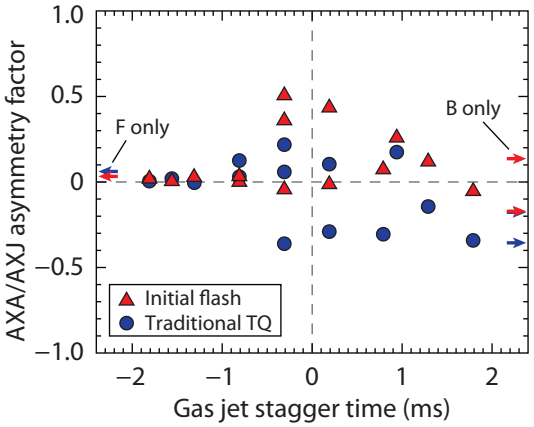

Figure 5-17 – Asymmetry factor calculated from opposite-facing diode arrays (AXA/AXJ) in the thermal quench vs. gas jet stagger time for the "L-mode t_{stag}" dataset. Red triangles: initial TQ flash only; blue circles: traditional TQ.

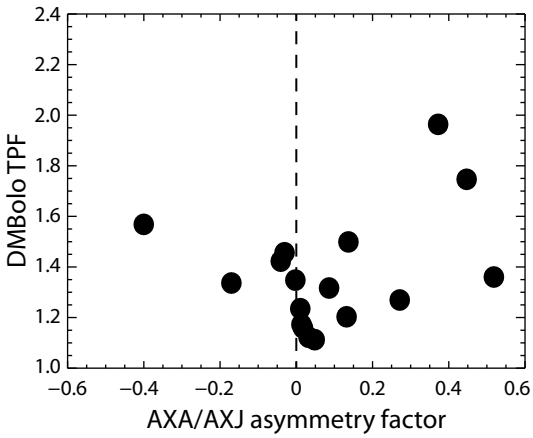

Figure 5-18 – Comparison of the AXA/AXJ asymmetry factor (defined in Equation 5.9) with the toroidal peaking factor calculated from the DMBolo wall-mounted photodiode array for the "L-mode t_{stag} dataset.

5.6 Summary of experimental observations

In this chapter, we have presented observations of toroidal radiation peaking in MGI rapid shutdowns of various Alcator C-Mod target plasmas. While the naïve assumption would be that the radiation would be most symmetric (lowest) peaking factor for two-jet MGI rapid shutdowns with synchronous (or nearly synchronous) injection, this is not the case. In fact, those shutdowns have the *worst* radiation asymmetry. Furthermore, it appears that the radiation asymmetry can be affected by changing the plasma magnetic safety factor (*i.e.* the toroidal field; the plasma current was kept constant in this dataset), although not in a monotonic fashion. The radiation asymmetry had only a weak trend with plasma elongation for inner-wall limited plasmas, and changing the plasma stored energy had no effect on the symmetry of the radiation during the TQ. Finally, the growth rate of an $n = 1$ magnetic mode in the pre-TQ phase correlates with the radiation asymmetry: the shutdowns with the highest asymmetry had the fastest growth rate of the $n = 1$ mode.

In Chapter 6, we will discover how the presence of a rotating single-peaked radiation mode sets the TQ-integrated radiation asymmetry, and the relation of this rotating radiation mode to the observed exponentially-growing $n = 1$ magnetic mode in the pre-TQ. Then, in Chapter 7, we will discuss the theory of radiative tearing modes (RTMs), and explore how the observed exponentially-growing $n = 1$ mode is likely one of these RTMs. In Chapter 8, we will briefly compare and contrast the results of extended MHD simulations of an Alcator C-Mod MGI rapid shutdown to the experimental results. Finally, in Chapter 9, we will summarize the results obtained and make suggestions for future work.

References

[1] Reinke, M.L. *et al.* (2008). "Toroidally resolved radiation dynamics during a gas jet mitigated disruption on Alcator C-Mod." *Nuclear Fusion* **48**(12), 125004 (7 pp). doi:10.1088/0029-5515/48/12/125004

[2] Hutchinson, I.H. (1976). "Magnetic probe investigation of the disruptive instability in tokamak LT-3." *Physical Review Letters* **37**(6), 338–341. doi:10.1103/PhysRevLett.37.338

[3] Pautasso, G. *et al.* (2011). "Massive gas injection from the high field side of ASDEX Upgrade." Contributed paper at the 38th European Physical Society Conference on Plasma Physics, Strasbourg, France, June 27–July 1, 2011. Paper P4.108. Available online at http://ocs.ciemat.es/EPS2011PAP/pdf/P4.108.pdf

[4] Izzo, V.A. (2013). "Impurity mixing and radiation asymmetry in massive gas injection simulations of DIII-D." *Physics of Plasmas* **20**(5), 056107 (8 pp). doi:110.1063/1.4803896

[5] Whyte, D.G. *et al.* (2010). "I-mode: An H-mode energy confinement regime with L-mode particle transport in Alcator C-Mod." *Nuclear Fusion* **50**(10), 105005 (11 pp). doi:10.1088/0029-5515/50/10/105005

[6] Lehnen, M. *et al.* (2011). "Disruption mitigation by massive gas injection in JET." *Nuclear Fusion* **51**(12), 123010 (12 pp). doi:10.1088/0029-5515/51/12/123010

[7] Hollmann, E.M. *et al.* (2007). "Observation of q-profile dependence in noble gas injection radiative shutdown times in DIII-D." *Physics of Plasmas* **14**(1), 012502 (8 pp). doi:10.1063/1.2408404

[8] E.M. Hollmann and (separately) M.L. Reinke, personal communication, 2012.

[9] Klein, A. *et al.* (2008). "A sparsity-based method for the analysis of magnetic fluctuations in unevenly-spaced Mirnov coils." *Plasma Physics and Controlled Fusion* **50**(12), 125005 (17 pp). doi:10.1088/0741-3335/50/12/125005

[10] Olynyk, G.M. *et al.* (2011). "Radiation asymmetry in gas jet mitigated disruptions on Alcator C-Mod." Presented at the 53rd Annual Meeting of the APS Division of Plasma Physics, Salt Lake City, UT, USA November 14–18, 2011. Poster UP9.00014. Available online at http://www.psfc.mit.edu/research/alcator/pubs/APS/APS2011/Olynyk_APS_poster.pdf

Chapter 6

The role of low-n MHD modes in the thermal quench

The importance of radiation symmetry in the thermal quench of massive gas injection rapid shutdowns was discussed in Chapter 2. Observations of asymmetry (as measured by the *toroidal peaking factor*, TPF, were presented in Chapter 5). This chapter will introduce the concept of low-n MHD modes in the thermal quench as controlling the radiation asymmetry, and discuss how their rotation creates the observed scatter seen in peaking factors when nominally identical target plasmas are shut down.

6.1 Evidence for a rotating brightness feature

In Figure 6-1, the plasma brightness as seen by the toroidally opposite-looking AXA and AXJ photodiode arrays (see Figure 3-2) are plotted for rapid shutdowns of two identical target plasmas (I_p = 1.0 MA, B_t = 5.5 T, P_{ICRF} = 2.0 MW). Recall from Section 3.6 that the AXA array looks toroidally toward the B-jet injector, and the AXJ array looks away from it.[1] The difference between the two, although this was not recognized at the time of publication of these results, is that in the shutdown with a high degree of toroidal symmetry (Figure 6-1(a)), the brightness feature starts on the AXA array, and then appears on AXJ, and *then appears on AXA again*. On the highly peaked shutdown (Figure 6-1(b)), in contrast, the radiation feature essentially stays in front of the AXA array until ≈ 1.5 ms after the gas hits the plasma.

The installation of the toroidal array of wall-mounted photodiodes allows for a more effective diagnosis of the rotating feature. Figure 6-2 shows important time traces through the single gas jet (B-jet) rapid shutdown of Alcator C-Mod plasma 1120202008, a lower-single-null diverted plasma at 5.5 T, 1.0 MA with 1 MW of auxiliary (ICRF) heating. Examining the inset in panel (b), it can be seen that there is a brightness feature which rotates clockwise (as viewed from the top, *i.e.* the $-\phi$ direction) around the machine, going through one complete rotation with the peak at diode #6 (the orange line) appearing at approximately 4.65 ms and again at 4.95 ms. This time delay indicates that the brightness feature is rotating at

[1] At the time of the experiments presented in Figure 6-1, the F-jet had not yet been installed.

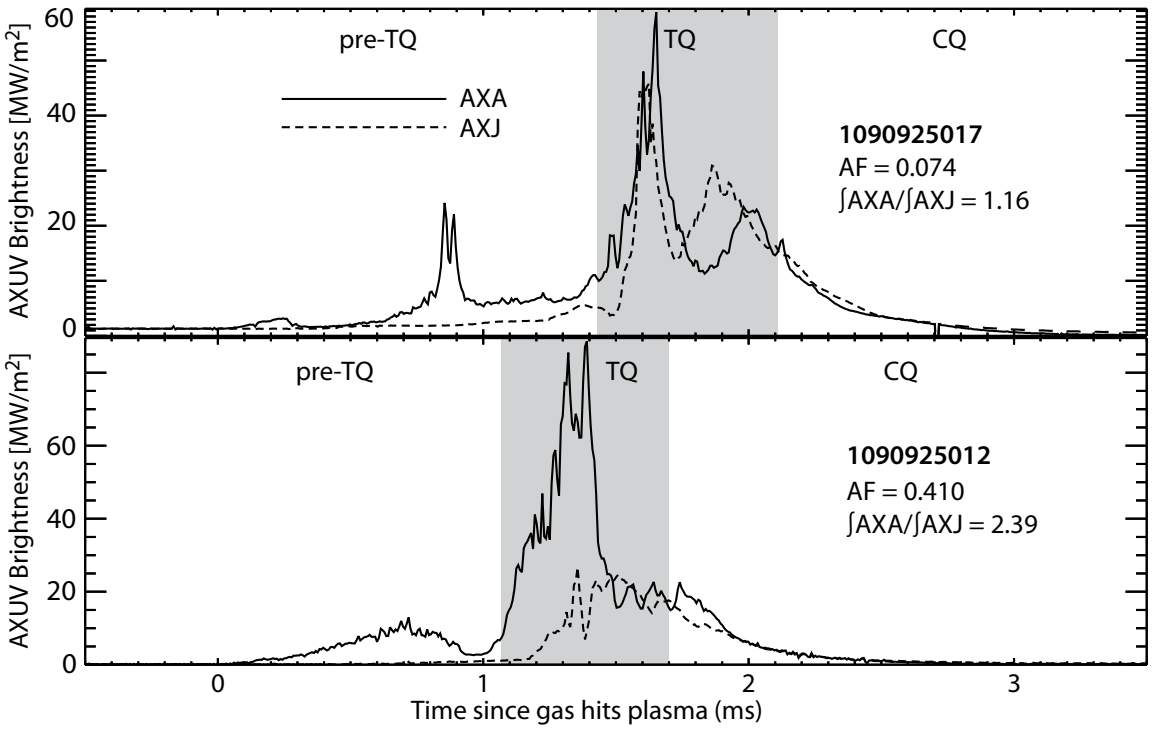

Figure 6-1 – In these two rapid shutdowns from 2009, opposite-viewing photodiode arrays (AXA and AXJ) see very different radiation asymmetries for globally identical target plasmas. **(a)** Shot 1090925017, with a radiation asymmetry factor $\mathrm{AF} = 0.074$ (denoted as symmetric); **(b)** Shot 1090925012, with a radiation asymmetry factor $\mathrm{AF} = 0.410$ (denoted as asymmetric).

approximately 3.3 kHz in this MGI rapid shutdown; in Section 6.2 a more accurate procedure involving cross-correlation of the photodiode channels is described.

It can also be seen in panel (c) of Figure 6-2 that there is an apparent "double hump" in the instantaneous toroidal peaking factor, just as there was in the AXA/AXJ data presented in Figure 6-1. This is an artifact of the limited toroidal coverage by the photodiode array: if there were a denser toroidal array of photodiodes, then the apparent peaking factor would be even lower throughout the entire thermal quench. This issue is discussed further in Section 6.4.

The following observations have been made:

- The toroidal radiation asymmetry in single-gas jet MGI rapid shutdowns varies widely even for identical target plasmas;
- There is a rotating brightness feature observed in the thermal quench of *some* rapid shutdowns; and
- There is an exponentially-growing $n = 1$ magnetic mode in the pre-TQ phase of the MGI rapid shutdown; the thermal quench begins, as identified by the sudden increase in radiation, when this mode saturates.

It is thus hypothesized that these observations are related: the $n = 1$ mode which is present during the pre-TQ is a radiative tearing mode which produces a magnetic island. This island grows, saturates, and then couples to a related $n = 1$ mode, which causes the energy to be preferentially transported out of the core to the radiative edge at one particular phase of the mode. The mode then appears as a brightness feature on wall-mounted photodiodes, which then either rotates during the thermal quench, or locks to a particular toroidal location. This implies two conclusions regarding the observed variation in toroidal radiation peaking factor

i. If the radiation mode rotates quickly during the TQ, then the time-integrated toroidal peaking factor will be lower. If it rotates much more than one time during the TQ, the TPF should be essentially unity.

ii. If the radiation mode does not rotate (that is, it "locks"), then the toroidal peaking factor should be large. However, because of limited toroidal coverage by photodiodes in these experiments, the *apparent* toroidal peaking factor may have a large scatter, because the mode can lock at a varying phase relative to the location of the diodes.

These predictions are compared to experiment in the following sections. In Section 6.2, the procedure by which the rotation rate is determined from the cross-correlation is presented. Then, in Section 6.3 evidence is presented to show that these two predictions are indeed observed in the experiments, supporting the original *ansatz*.

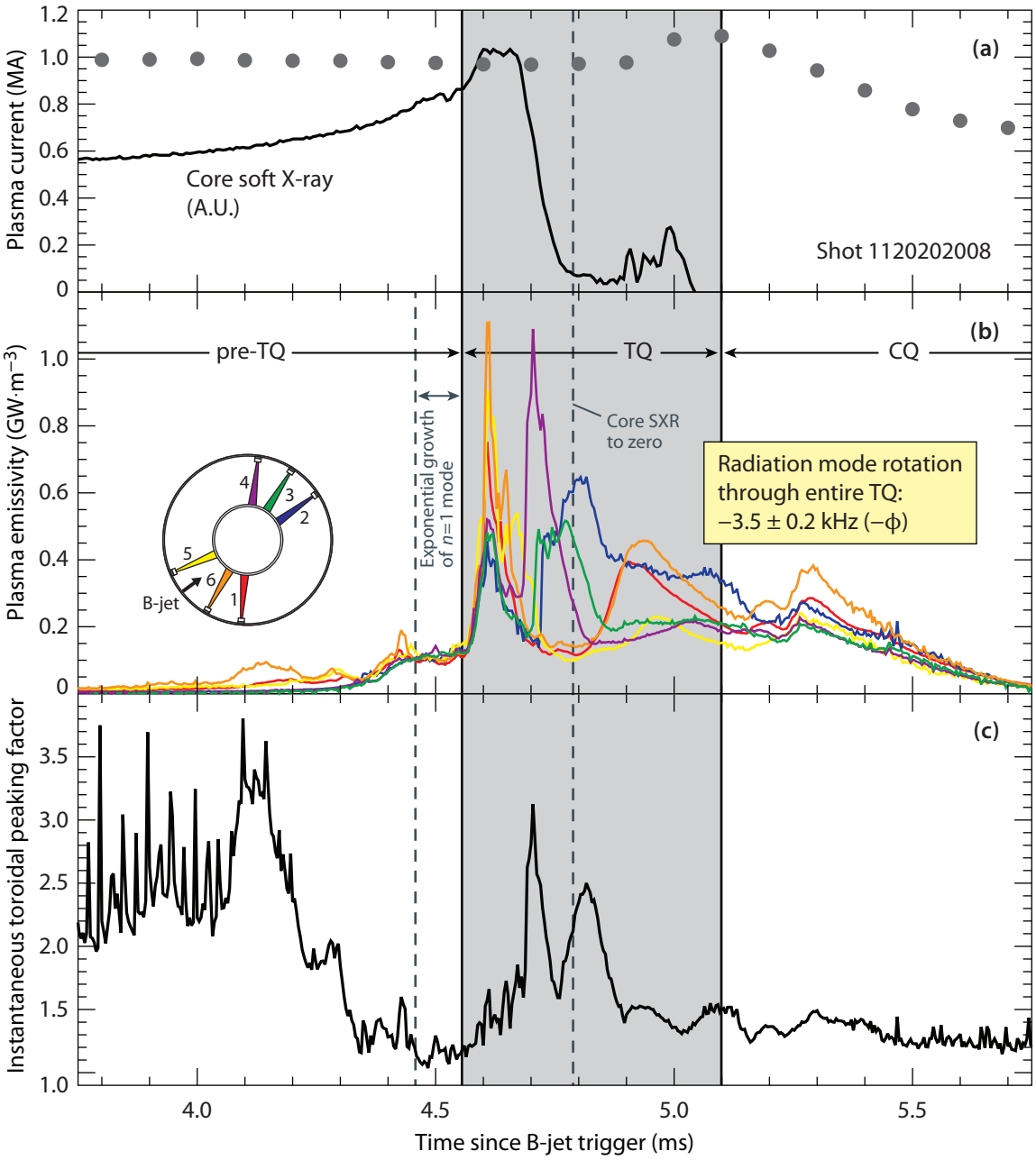

Figure 6-2 – **(a)** Plasma current and core soft X-ray brightness; **(b)** Plasma emissivity in front of each of six wall-mounted photodiodes; **(c)** Instantaneous peaking factor (the maximum of the emissivity on each of the six diodes, divided by the average) for single-jet rapid shutdown of C-Mod plasma 1120202008.

6.2 Cross-correlation of photodiodes

In Figure 6-2, there was a clear rotating brightness feature in the thermal quench. However, in order to accurately determine its rotation rate, as well as to determine if there is a rotating mode in shutdowns where the plasma brightness signals are much noisier than this one, a procedure was developed by which the various wall-mounted photodiodes were cross-correlated with each other and the peaks in the cross-correlation determined. The entire procedure is plotted for the thermal quench of MGI rapid shutdown of C-Mod shot 1120202008 in Figure 6-3. (Note that this is the same shutdown for which the time traces were plotted in Figure 6-2.)

The procedure is as follows: first, the plasma brightness time series for each wall-mounted photodiode is loaded into memory. These time series are denoted by $\varepsilon_i[t]$, where i runs from 1 to 6 (the number of wall-mounted diodes). The argument of the function (time t) is given in square brackets because it is discrete (digitization frequency of 250 kHz). The interval for the cross-correlation analysis is chosen to be the same time period as for which the peaking factor is calculated. This ensures a reliable comparison between different shutdowns, in which the thermal quench might start and end at different times, or if the brightness feature rotation decreases later in the shutdown sequence (as indeed, it frequently does: see Section 6.7).

A vector of "lag" or "delay" is then generated with $2N-1$ integers, where N is the number of time points in the data interval. They range from $-(N-1)$ to $(N-1)$. Then, for each lag L, the cross-correlation P_{ij} between ε_i and ε_j is given by:

$$P_{ij}(L) = \begin{cases} \dfrac{\sum_{k=0}^{N-L-1} \left(\varepsilon_i[t_{k+L}] - \bar{\varepsilon}_i\right)\left(\varepsilon_j[t_k] - \bar{\varepsilon}_j\right)}{\bar{P}} & L < 0 \\ \dfrac{\sum_{k=0}^{N-L-1} \left(\varepsilon_i[t_k] - \bar{\varepsilon}_i\right)\left(\varepsilon_j[t_{k+L}] - \bar{\varepsilon}_j\right)}{\bar{P}} & L > 0 \end{cases} \tag{6.1}$$

where $\varepsilon_i[t_{k+L}]$ is the brightness of photodiode i at time index $k+L$, $\bar{\varepsilon}_\alpha$ is the mean of the time series ε_α, and the denominator term $\bar{P}$ is defined as:

$$\bar{P} \equiv \sqrt{\left[\sum_{k=0}^{N-1} \left(\varepsilon_i[t_k] - \bar{\varepsilon}_i\right)^2\right]\left[\sum_{k=0}^{N-1} \left(\varepsilon_j[t_k] - \bar{\varepsilon}_j\right)^2\right]} \tag{6.2}$$

that is, for the cross-correlation, each time series has its mean subtracted and is normalized to its own standard deviation. Then, if two time series are identical at some lag L, their cross-correlation will be unity; if they are completely uncorrelated, their cross-correlation will be zero. If $i = j$, then the cross-correlation becomes an *autocorrelation*, which identifies the

similarity of a signal to a time-delayed version of itself.

The small plots in Figure 6-3 show this cross-correlation for each pair of photodiodes vs. the time lag $L \cdot \Delta t$, where Δt is the time delay between successive time points in the data (4 μs for the photodiode data). For each diode pair, the toroidal separation between those diodes is then plotted versus the lag value at which the cross-correlation is maximized. That is, $\Delta\phi_{ij} = \phi_j - \phi_i$ is plotted versus $\arg\max\left(P_{ij}\left(L\right)\right) \times \Delta t$.[2] A linear fit then gives the rotation rate of the brightness feature, with an error estimate. This can be seen in the large frame in the bottom-left of Figure 6-3.

The computer code used to do the brightness cross-correlation is reproduced in Appendix D. In the following subsections, the results of this cross-correlation analysis is shown to explain the observed scatter in radiation peaking factor seen with one- and two-jet MGI rapid shutdowns.

6.3 Rotation and toroidal peaking factor

The cross-correlation analysis was conducted on all the MGI rapid shutdowns from the 2012 dataset, and the results are presented here for one- and two-jet shutdowns. Because the thermal quench can last a slightly different amount of time in each rapid shutdown (for single-jet shutdowns, the duration of the initial TQ flash $\bar{\tau}_{TQ}$ = 405 μs, with a standard deviation of 34 μs), the results are normalized to the length of the thermal quench. Thus, the results are presented versus $f \cdot \tau_{TQ}$, where f is the frequency of rotation of the brightness feature, and τ_{TQ} is the duration of the initial TQ flash. This quantity is equal to the number of rotations the brightness feature makes during the thermal quench.

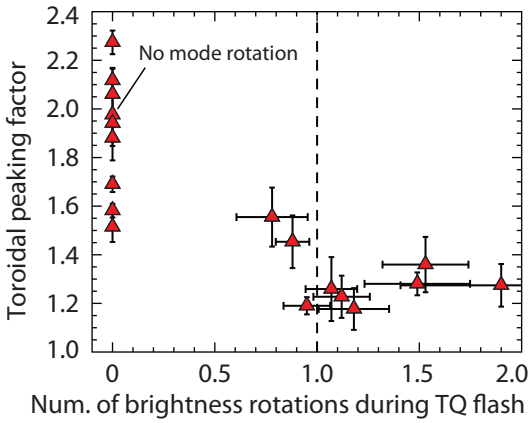

Figure 6-4 – Toroidal peaking factor vs. the number of toroidal rotations $f\tau$ that the $n = 1$ mode transits during the initial TQ flash of every B-jet single-jet MGI rapid shutdown on Alcator C-Mod.

6.3.1 Mode rotation in single-jet rapid shutdowns

The rotation rate of the brightness feature was analyzed for every MGI rapid shutdown using the B-jet. (There were significantly more single-jet MGI rapid shutdowns available for

[2] The arg max ( ) function stands for "argument of the maximum", and refers to the x-axis value corresponding to the maximum y-axis value. For example, $\arg\max\left(4 - x^2\right) = 0$, not 4.

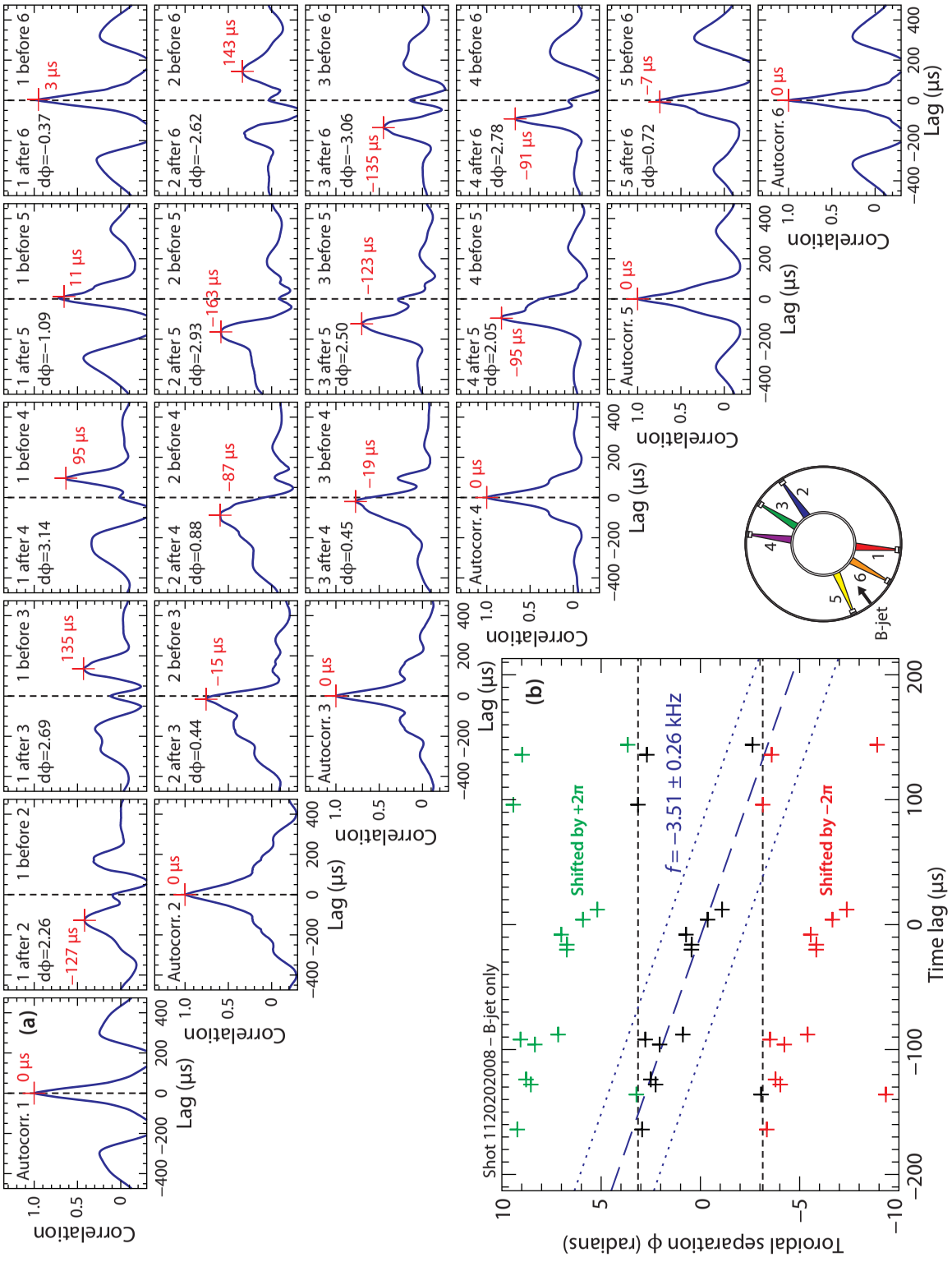

Figure 6-3 – (*Rotated figure.*) Cross-correlation analysis of photodiodes to determine radiation mode rotation velocity. See text for details.

the B-jet than the F-jet.) These shutdowns had widely varying target plasmas: clockwise or counter-clockwise toroidal field and plasma current direction, varying magnetic safety factor, and even some inner-wall limited plasmas.

In Figure 6-4, the toroidal peaking factor is shown versus $f\tau_{TQ}$ (the number of rotations that the $n = 1$ mode makes during the initial TQ flash), for this entire dataset. It can be seen, first of all, that the highest peaking factors are obtained when the brightness feature does not rotate. If there is any rotation of the brightness feature at all, the peaking factor does not go over approximately 1.6, compared to peaking factors of up to 2.3 obtained when the mode "locks" (does not rotate). If the mode rotates more than once during the TQ ($f\tau_{TQ} > 1$), the peaking factor is even lower: less than 1.4.

Second, the scatter in the radiation peaking factor for the shutdowns with a "locked" brightness is much larger than the scatter for the rotating-mode shutdowns. This is discussed further in Section 6.4.

6.3.2 Mode rotation in two-jet rapid shutdowns

It was observed (see Section 5.2.2) that of the two-jet MGI rapid shutdowns, the toroidal peaking factor was worst when the two jets were fired in such a way that the gas arrived at the plasma nearly synchronously (the "nearly synchronous" shots discussed in Section 5.2.2). In Figure 6-5, the toroidal peaking factor and the mode rotation rate $\omega\tau_{TQ}$ (again, multiplied by the length of the thermal quench, so that $\omega\tau_{TQ} = 2\pi$ means that the mode rotated once during the TQ) are plotted versus the gas jet stagger time for two-jet rapid shutdowns of identical 1 MW ICRF-heated L-mode plasmas.

Two features are evident from Figure 6-5. First, examining the red points (the initial TQ flash only) in panel (a), it can be seen that the highest peaking factors are obtained for the "nearly synchronous" shutdowns, with $t_{stag} \approx 0$. Second, it is obvious that the two gas jets are not behaving identically: the shutdowns where the F-jet was fired first ($t_{stag} < 0$) have reliably low radiation asymmetry. (These differences are discussed further in Section 6.3.5.)

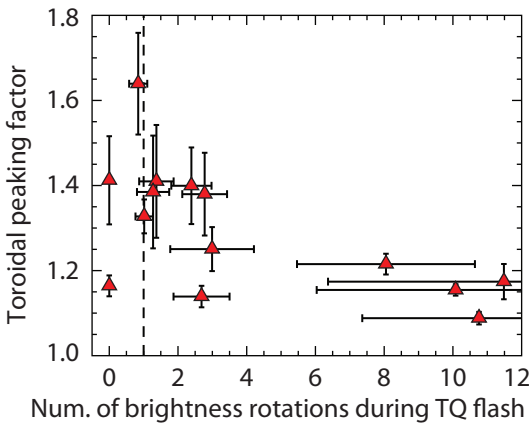

Figure 6-6 – Toroidal peaking factor vs. the number of toroidal rotations $f\tau$ that the $n = 1$ mode transits during the initial TQ flash for two-jet MGI.

The lower panel plots the rotation rate versus the gas jet stagger time. Again, firing the F-jet reliably produces high mode rotation: higher than that seen in any of the single-jet shutdowns. In addition, it can be seen that one of the B-jet first shutdowns ($t_{stag} \approx +0.95$ ms)

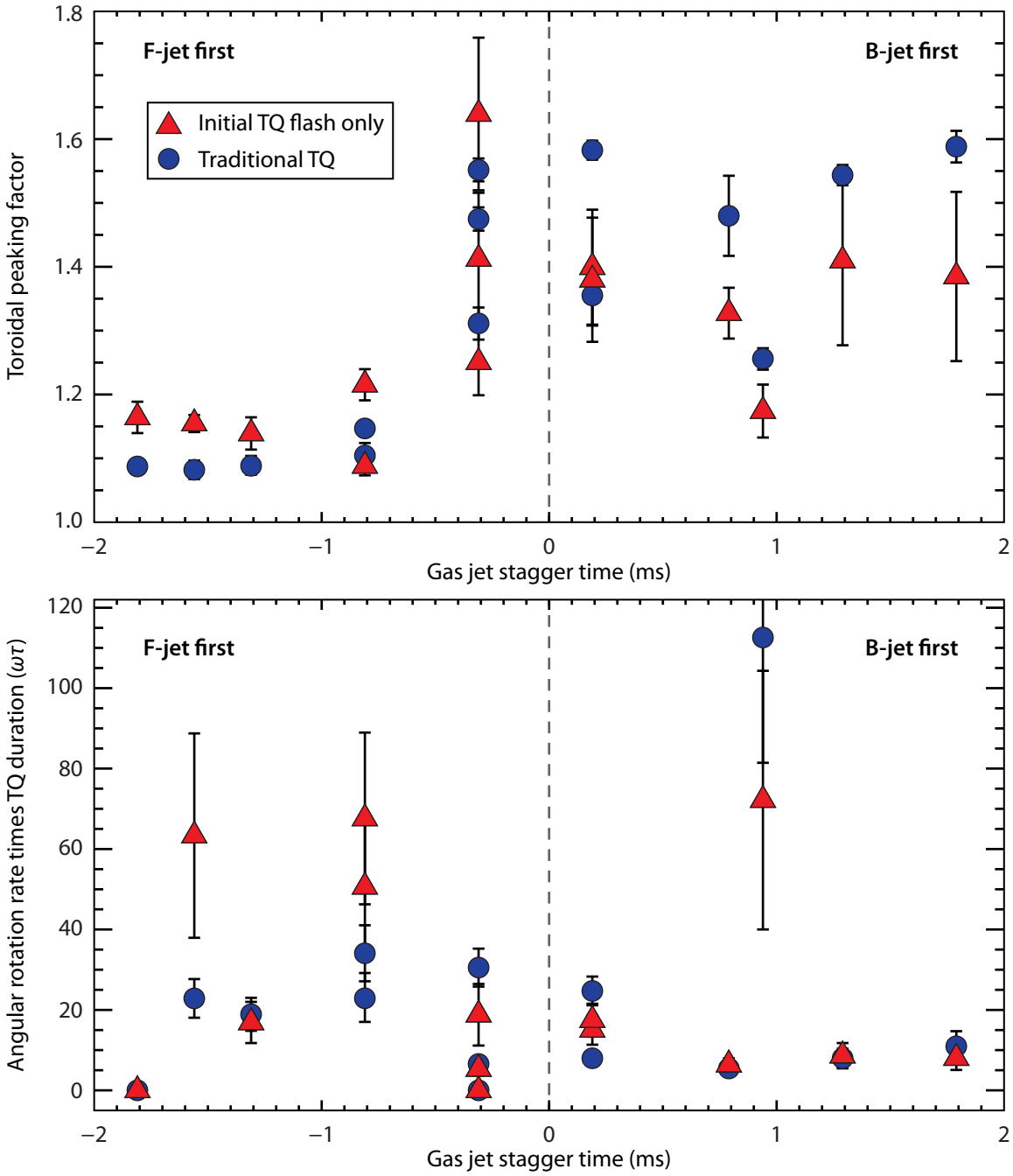

Figure 6-5 – **(a)** Toroidal peaking factor; and **(b)** The number of toroidal rotations $f\tau$ that the $n = 1$ mode transits during the initial TQ flash, versus the gas jet stagger time for the dataset of two gas jet MGI rapid shutdowns of L-mode plasmas.

has a high rate of mode rotation *and* a low radiation asymmetry, indicating that the mode rotation has the same effect for the two-jet shutdowns as it does for the single-jet shutdowns.

This effect is more readily seen when the toroidal radiation peaking factor is plotted versus the number of brightness rotations during the TQ flash ($f\,\tau_{TQ}$) for the two-jet shutdowns. This is shown in Figure 6-6. Again, the highest asymmetries are obtained when the mode rotates less than once during the TQ, and if the mode rotates quickly, the radiation is reliably symmetric.

This observation is linked to the counter-intuitive result that the peaking factor during the thermal quench is *worst* for the two-jet MGI rapid shutdowns where the two jets are nearly synchronous: the $n = 1$ MHD mode which causes the energy transport out of the core during the TQ does not rotate during the TQ on these shots. This effect can be seen in the two-jet MGI rapid shutdown of C-Mod shot 1120202020 ($t_{stag} \approx +0.19$ ms), plotted in Figure 6-7.

Essentially, the mode is stationary during the TQ flash, and the instantaneous peaking factor is as high as 3.0 during this phase, although the integrated toroidal peaking factor through the initial TQ flash is only 1.75. Toward the end of the initial TQ flash, and into the current-flattening phase, the mode indeed starts rotating, at 2.51 ± 0.04 kHz in the counter-clockwise ($+\phi$) direction. This causes the toroidal peaking factor integrated through the entire "traditional" TQ to be lower: approximately 1.6.

This effect can also be seen on another "nearly synchronous" two-jet MGI rapid shutdown, this time for a 3.6 MW ICRF-heated I-mode target plasma, shot 1120911021, shown in Figure 6-8. In this case, however, there is no evidence that the mode ever starts rotating: it sits fixed in position through the entire TQ and even into the CQ. This leads to a high radiation asymmetry for both definitions of the TQ: approximately 1.6 through the initial TQ flash only, and even higher, approximately 1.8, through the entire traditional TQ.[3]

6.3.3 Mode rotation and magnetic safety factor

It can be seen in Figure 6-9 that only a single shutdown of the eight used for the magnetic safety factor scan had a rotating radiation mode: this was shot 1120802020, which also had the lowest toroidal peaking factor of any of the shots in this scan. This is consistent with the mode rotation primarily setting the radiation asymmetry, although there could be an additional effect, dependent on magnetic safety factor, modifying the radiation asymmetry *even for those shutdowns without a rotating mode*.

[3] Recall that radiation peaking above 2.0–2.5 in the TQ could be a problem for wall melting on ITER. Even the highest values of peaking factor observed for the two-jet shots (1.6–1.8) probably would not melt the ITER wall.

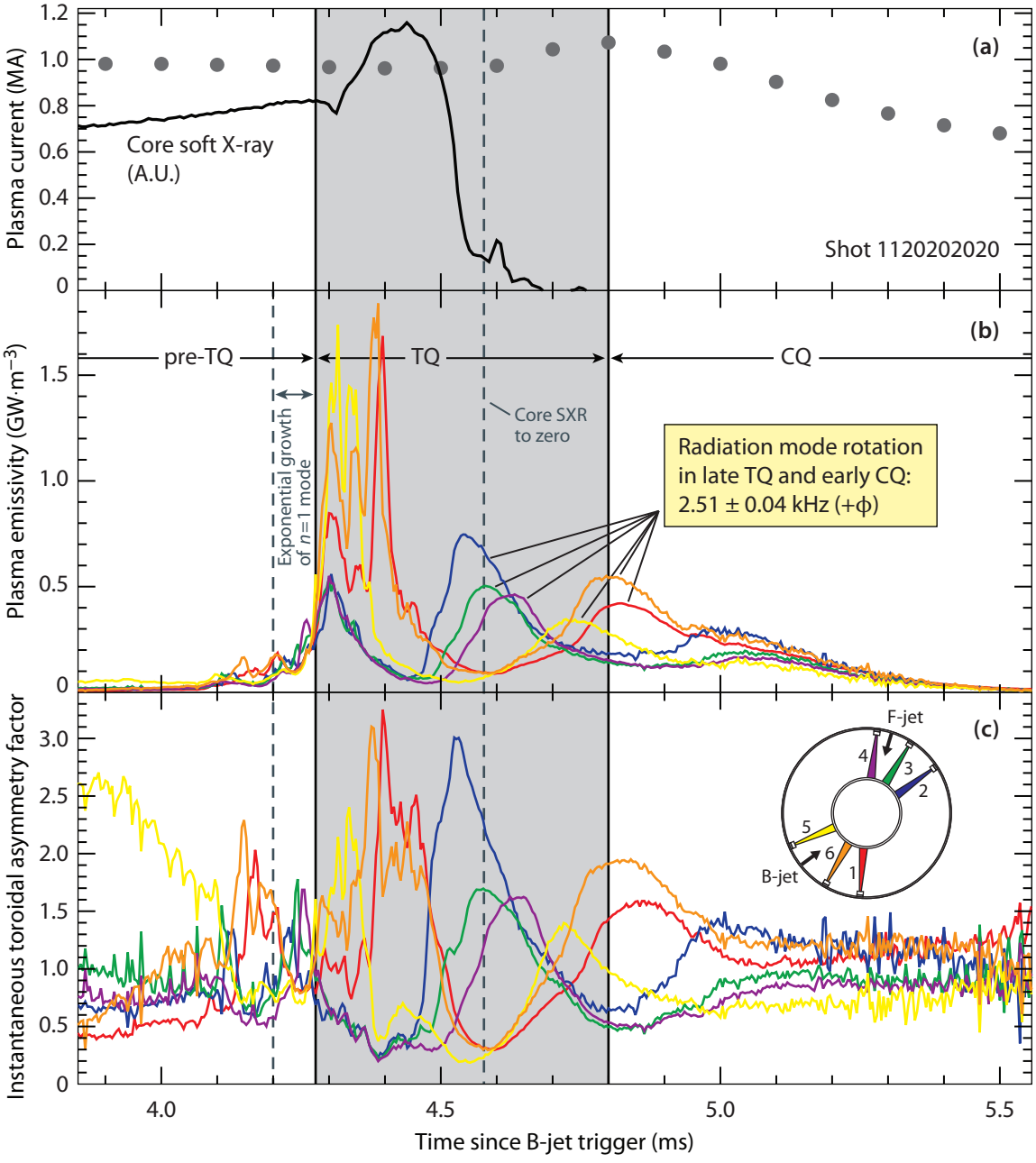

Figure 6-7 – Timeline of two-jet MGI rapid shutdown of Alcator C-Mod shot 1120202020. A rotating brightness feature is evident.

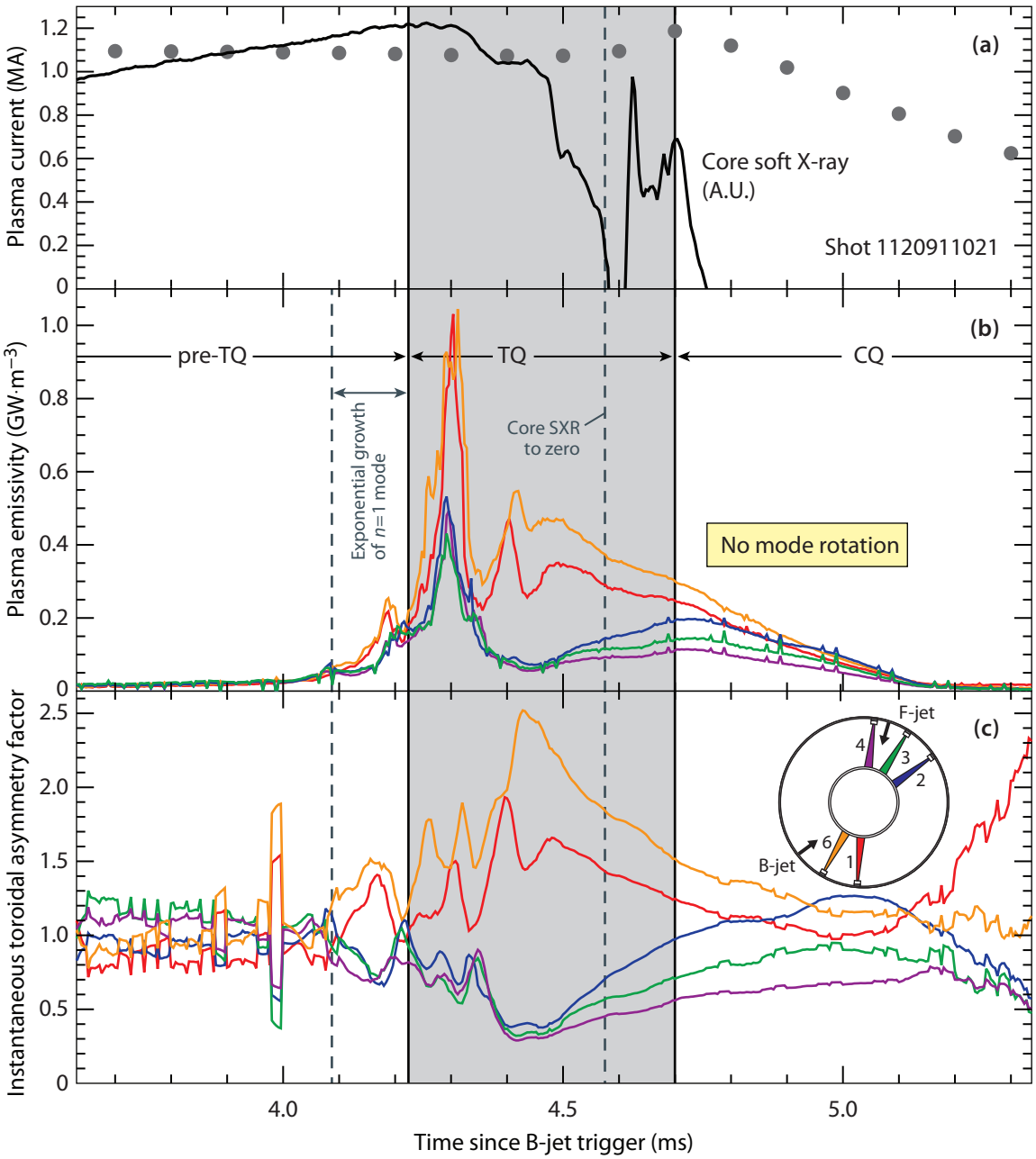

Figure 6-8 – Timeline of nearly synchronous two-jet MGI rapid shutdown of Alcator C-Mod shot 1120911021. A five-point moving average smooth has been applied to the asymmetry data in (c) because of noise in the pre-TQ and late CQ.

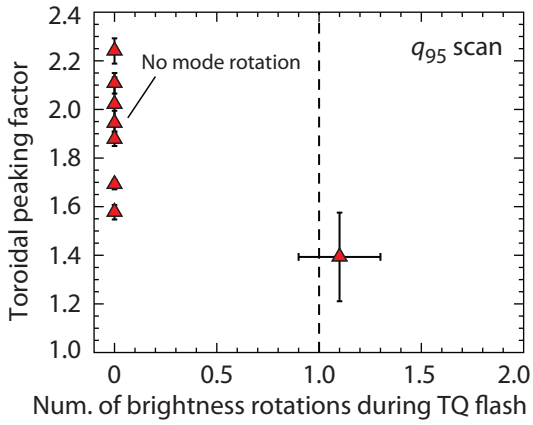

Figure 6-9 – Toroidal peaking factor vs. the number of toroidal rotations $f\tau$ that the $n = 1$ mode transits during the initial TQ flash for the shots used in the q_{95} scan. See Figure 5-9 for observations of toroidal peaking factor versus safety factor.

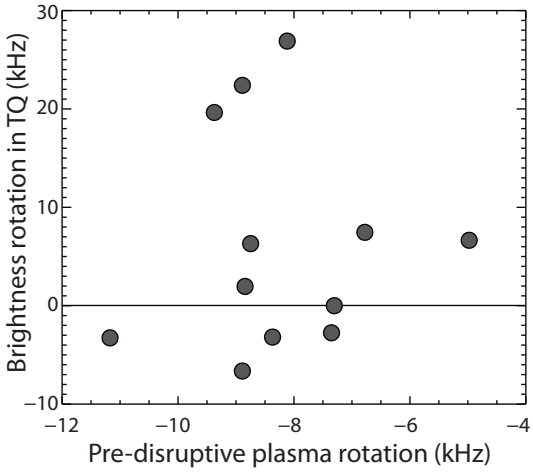

Figure 6-10 – The rotation rate of the brightness feature in two-jet MGI rapid shutdowns plotted against the pre-disruptive plasma rotation rate as measured by X-ray crystal spectrometry. Negative values of rotation mean rotation in the $-\phi$ (clockwise) direction.

6.3.4 Rotation rate vs. intrinsic plasma rotation rate

It might be hypothesized that the rotation of the mode is simply the pre-disruption (intrinsic) plasma rotation. However, this is not the case. In Figure 6-10, the rotation rate of the brightness feature is plotted against the pre-disruptive rotation rate as measured by a single-chord X-ray crystal spectrometer (see Section 3.9). It can be seen that there is no correlation, indicating that the radiation mode is rotating independently of the pre-disruptive plasma rotation.

Additionally, this is consistent with a different line of reasoning: when the gas jet is fired, approximately 10–30% of the injected impurities are assimilated into the plasma, which increases the mass of the rotating plasma by approximately an order of magnitude. Thus, even if the pre-disruptive plasma were rotating at ≈ 8 kHz, conservation of angular momentum would require that it be rotating at less than 1 kHz after absorbing the impurities. The observed brightness modes here are rotating much faster than that; often faster than even the pre-disruptive plasma rotation, and quite often in the wrong direction,[4] *i.e.* in the opposite direction from the target plasma's rotation. Thus, the brightness feature cannot simply be a "lump" of injected impurities being convected around the machine by intrinsic plasma rotation.

[4] Shots 1120802011 and 1120802020 were identical target plasmas and both shut down using the B-jet; however, shot 011 had no mode rotation during the initial TQ flash and a rotation of +2.62 ± 0.33 kHz in the later part of the TQ. Shot 020 had a mode rotation of −3.99 ± 0.48 kHz in the initial TQ flash, slowing to −2.13 ± 0.13 kHz in the later part of the TQ. These two rapid shutdowns were nominally identical, and yet the brightness feature rotated in the opposite direction.

6.3.5 Differences between the two gas jets

It is important to note that the two gas jets are not identical. The valve hardware is different (although a flow orifice was applied to the B-jet in order to make their flow rates the same). These differences are discussed further in Section 3.2. Their poloidal position is also different, although not greatly. However, the peaking factor obtained from firing each of the two gas jets first is not the same indicating that the hardware differences may play a role in setting the radiation asymmetry in two-jet MGI rapid shutdowns.

However, in Figure 6-11, the toroidal peaking factor and radiation mode rotation rate are plotted for single-jet MGI rapid shutdowns with both the B-jet and the F-jet. (There are many more single-jet shutdowns with the B-jet than with the F-jet in the data set.) It can be seen that the behavior of the two individual gas jets is qualitatively similar for toroidal peaking factor; however, there is one single-jet shutdown producing a very rapid mode rotation with the F-jet (four rotations during the TQ), and none with the B-jet.

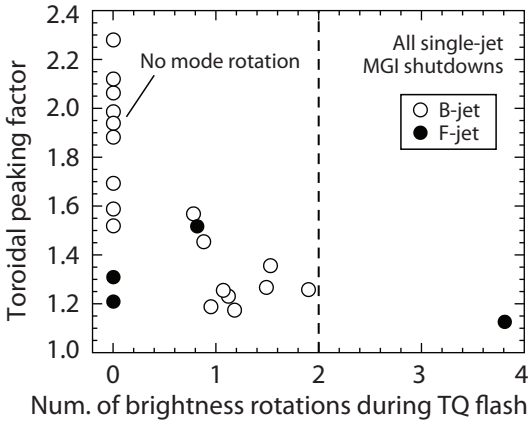

Figure 6-11 – The toroidal radiation peaking factor is plotted vs. the number of rotations of the brightness feature during the TQ for all single-jet MGI rapid shutdowns. Open circles: B-jet; closed circles: F-jet.

6.4 Limitations of toroidal coverage by photodiodes

It has been discussed how there is a wide scatter in the toroidal peaking factor for the shutdowns in which the brightness feature is not observed to rotate (*i.e.*, it "locks"). This could be an artifact of the limited coverage of the plasma by the photodiodes. In Figure 6-12, this is shown for a simple representative "locked" brightness feature with a true toroidal peaking factor of 2.4, and two different phases. The actual location of the wall-mounted photodiodes are shown by vertical lines. In this case, the estimated TPF

In fact, in the limit of a narrow, locked (non-rotating) brightness feature, the diodes could miss the peak entirely: it could fall in the region between the diodes, and the TPF could be very high. In practice, however, the brightness peak has a large toroidal extent: see Section 6.7. If the mode is rotating, this issue is not present, because the brightness feature will rotate past each diode in turn.

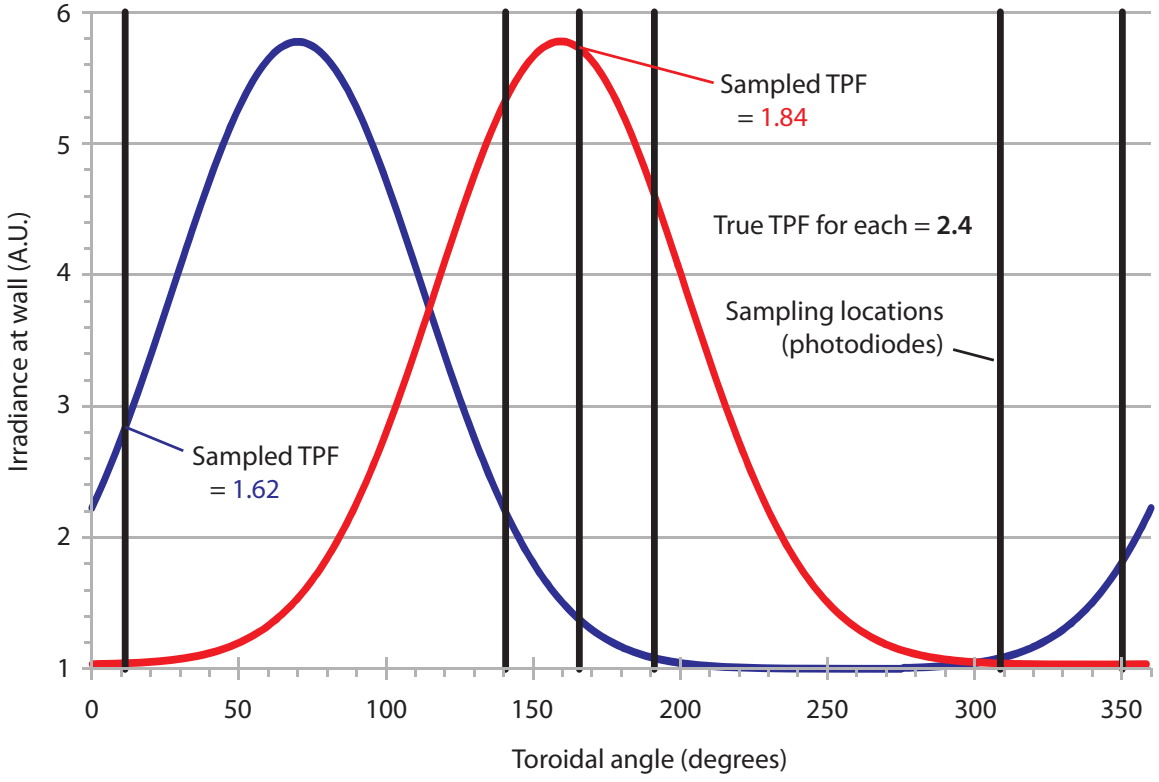

Figure 6-12 – Having only a discrete number of photodiodes on the wall, in two clusters of three, means that they are not fully sampling the plasma brightness profile. In this figure, two possible phases of a "locked" brightness feature with a torodial peaking factor of 2.4 are shown, in blue and red, respectively. The actual locations of the wall-mounted DMBolo photodiodes are shown as vertical lines. The calculated TPF is 1.62 (blue) and 1.84 (red) from the average of six photodiodes.

6.5 A new taxonomy of the phases of a rapid shutdown

There are two "traditional" phases of an unmitigated major disruption in a tokamak, recognized since very early in controlled fusion research:

- **Thermal quench:** The plasma loses nearly its entire stored thermal energy and cools, and then;
- **Current quench:** The plasma current ramps down from its peak.

With the advent of gas jet rapid shutdown, an additional phase before the other two is added:

- **Pre-thermal quench:** The impurity gas has reached the plasma and is cooling the edge, but the sudden loss of core thermal energy that marks the thermal quench has not yet begun.

Throughout this work, there has been discussion of the confusion caused by the vague definition of the end of the thermal quench. The end of the thermal quench is usually defined by the core soft X-ray signal falling to the noise floor (indicating that the core plasma is cold); the start of the current quench is usually marked by the peak of the measured plasma current (indicating that the current has fully rearranged itself to a flat profile).

However, these events are not simultaneous: the core plasma is cold *before* the measured plasma current reaches its peak. This causes confusion, not just on Alcator C-Mod, but on JET [1], where Lehnen *et al.* state "Previously, we defined the start of the CQ to be at the maximum current during the current spike. The end of the TQ can be assumed to coincide with this time …", and then spend three paragraphs discussing the uncertainty that this causes in the measured values of the radiated power P_{rad} when attempting to calculate the total radiated power during MGI rapid shutdowns on JET.

Thus, it is proposed to divide an MGI rapid shutdown into *four* phases, as shown in Figure 6-13. The pre-thermal quench (pre-TQ) phase uses the standard definition: the edge of the plasma is cooling, but the TQ has not yet begun. The start of the thermal quench (TQ) is defined by the saturation of the $n = 1$ magnetic mode, which is simultaneous with the sharp rise in plasma brightness that marks the start of the large-scale MHD transport of energy out of the hot core to the radiative mantle. The *end* of the TQ is marked by the fall of the core soft X-ray signal to near the noise floor, as well as a fall in core plasma brightness (although this "trough" is often not well defined).

Once the TQ is over, but before the current quench (CQ) begins, there is an interim phase referred to as the *current rearrangement* (CR) phase. During this phase of the rapid shutdown, the plasma current profile is flattening [2], causing an increase in plasma current due

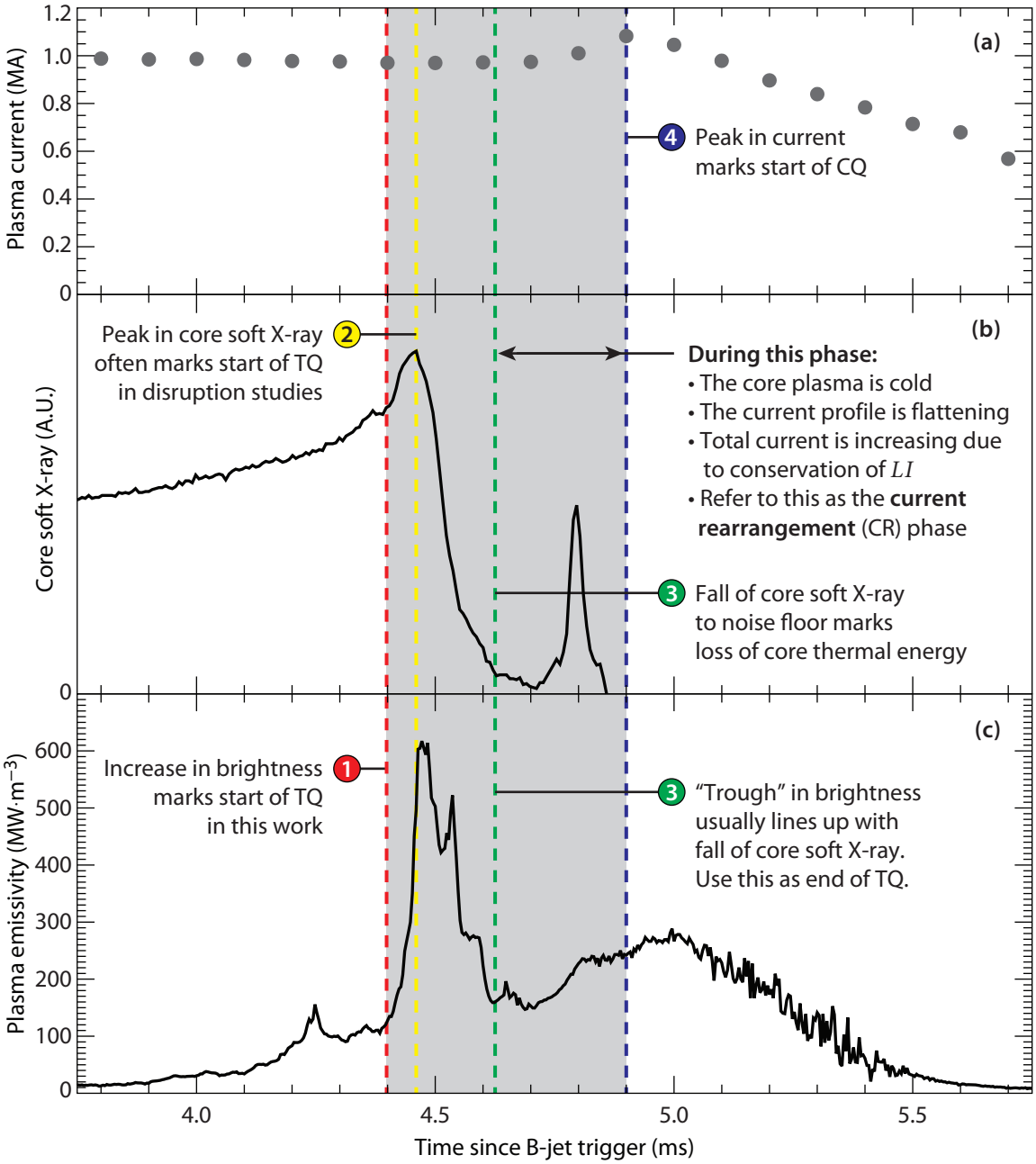

Figure 6-13 – **(a)** Plasma current; **(b)** Core soft X-ray emission; and **(c)** Average plasma emissivity from wall-mounted photodiodes for a typical single gas jet MGI rapid shutdown on Alcator C-Mod. Overlaid are the different markers usually used for subdividing the rapid shutdown into pre-TQ, TQ, and CQ phases, as well as the proposed "current rearrangement" (CR) phase in between the TQ and CQ phases.

to conservation of magnetic flux LI. There is large-amplitude noise on Mirnov coils during this phase; see Figures 5-11 and 5-12. It should be noted that if LI_p is truly conserved, then the poloidal magnetic energy of the plasma increases during this phase, since $W_{pol} \sim LI_p \cdot I_p$, and I_p increases. This energy must be coming from somewhere, for example from the poloidal field energy outside the plasma but inside the vacuum vessel. This issue was also discussed in Section 5.2.7. Finally, the end of the CR phase, and the start of the CQ, is defined by the peak in the measured plasma current. During the CQ, the plasma resistively ramps down on its characteristic L/R timescale.

6.6 Magnetic growth rate and radiation peaking factor

Observations were presented in Section 5.4 of the growth rate of the $n = 1$ magnetic mode in the pre-TQ phase, and its correlation to the radiation asymmetry in the thermal quench. In Figure 6-14, the rotation rate of the brightness feature in the thermal quench (for both positive and negative rotations) is plotted versus the growth rate of the $n = 1$ mode in the pre-TQ. While it was not possible to resolve the amplitude and phase of the $n = 1$ magnetics mode in the thermal quench due to noise on the Mirnov coils, it can be seen in Figure 6-14 that the shutdowns with a "locked" brightness feature (rotation $\approx$ zero) had the fastest-growing (highest growth rate) $n = 1$ magnetics mode in the pre-TQ, although there is significant overlap and the distinction is not entirely clear. This is consistent with the typical stabilization of MHD modes by rotation: it would be expected that the rotating modes grow more slowly.

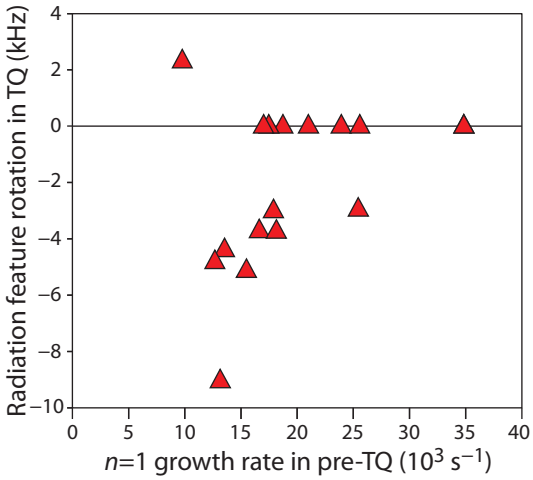

Figure 6-14 – The rotation of the $n = 1$ brightness feature in the TQ versus the growth rate of the $n = 1$ magnetic mode in the pre-TQ. It can be seen that the "locked" brightness features have the highest growth rates of the $n = 1$ magnetic mode in the pre-TQ. (These are the shots with the highest toroidal peaking factors.)

6.7 Toroidal extent of the brightness feature

Because the brightness feature often rotates past the photodiodes, the width of the feature in the time domain can be multiplied by the rotation rate to get a width of the feature in toroidal angle. Typically, these widths (expressed as a full width at half maximum, FWHM) are 60°–120° in the initial TQ flash. Often, during the current-rearrangement phase and

later, the brightness feature gets wider. Such a case is presented in Figure 6-15, for single-jet MGI rapid shutdown of C-Mod shot 1120202008. The peaks get wider in time through the CR phase of the shutdown, and since the rotation rate is constant, this means that the brightness feature is increasing in toroidal extent. A best fit indicates that the FWHM of the brightness feature increases in real width by 8.4 km s^{-1}, or 4.2 km s^{-1} in each direction.

6.8 Poloidal structure of the brightness feature

It is known that the MHD mode in the pre-TQ typically starts growing when the cooling front reaches the $q = 2$ surface; see Figure 5-14 or the discussion in Section III of [3]. This suggests that the exponentially-growing $n = 1$ mode observed in Alcator C-Mod MGI rapid shutdowns is, in fact, an $m = 2$, $n = 1$ helical mode. The nature of this exponentially-growing mode is discussed further in Chapter 7.

While the Mirnov coils on Alcator C-Mod do not allow diagnosis of the poloidal structure of the magnetic perturbation associated with the exponentially growing mode, the soft X-ray tomography system (see Section 3.7) can be used to observe the radiation pattern in the early phase of the disruption, when the plasma is still hot enough to produce radiation that can pass the beryllium filter on the soft X-ray detectors ($\gtrsim 2\ keV$). Temporal profiles of the emission from each of two detectors for single-jet MGI rapid shutdown of C-Mod shot 1090925012 are plotted in Figure 6-16. It can be seen that while the vertical-viewing array (looking down at the plasma) sees only a single bright spot, the horizontal-viewing array sees two, indicating that the emission has a poloidal profile with two peaks in it. It should be noted that this shutdown had a high toroidal radiation asymmetry and no detectable mode rotation; see panel (b) of Figure 6-1.

6.9 Rotating MHD modes in the current quench

A rotating magnetic mode has been observed in the current quench phase of unmitigated disruptions on Alcator C-Mod [4], JT-60U [5], and JET [6]. This mode typically rotates in the counter-current direction on C-Mod, although it has been observed to rotate in both directions on JET. This rotating mode causes a peaking in the halo currents. The peak value of halo current divided by its average value, like the radiation peaking studied in this work, is typically referred to as a "toroidal peaking factor" (TPF) in this context.

It is then natural to ask if this rotating mode that creates a halo current asymmetry in the CQ is the same rotating mode as that which creates the *radiation* asymmetry in the TQ. There are no experimental observations of halo current rotation on Alcator C-Mod in MGI rapid shutdowns: the Rogowski coils used for the experiments presented in [4] were removed before any MGI experiments were conducted.

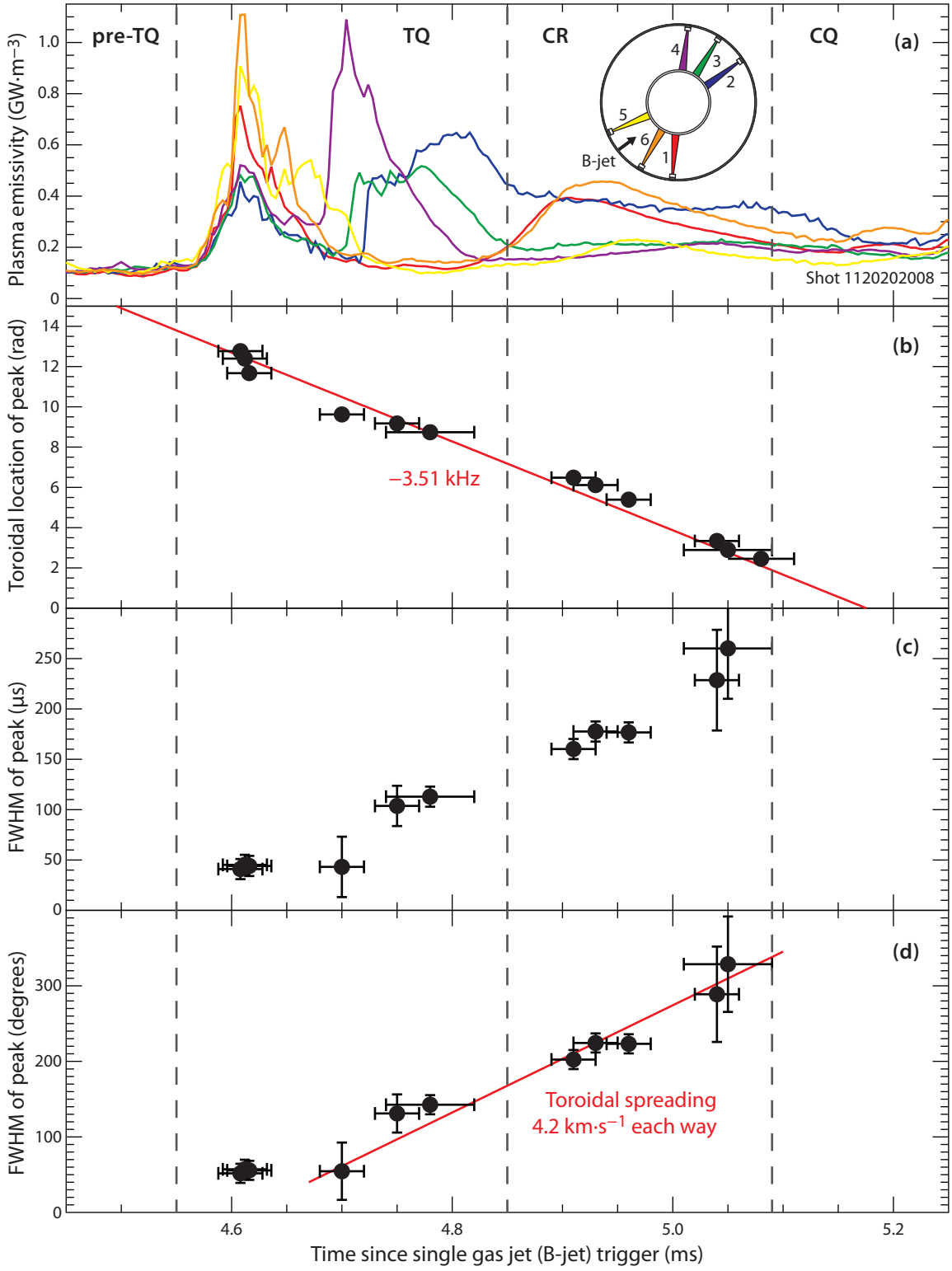

Figure 6-15 – **(a)** Plasma brightness as measured by wall-mounted photodiodes; **(b)** Toroidal location of each peak with best fit rotation rate (as determined by cross-correlation analysis); **(c)** Full width at half-maximum of each peak in time domain; **(d)** Full width at half-maximum of each peak in toroidal angle, with fit indicating the rate at which the brightness feature gets wider.

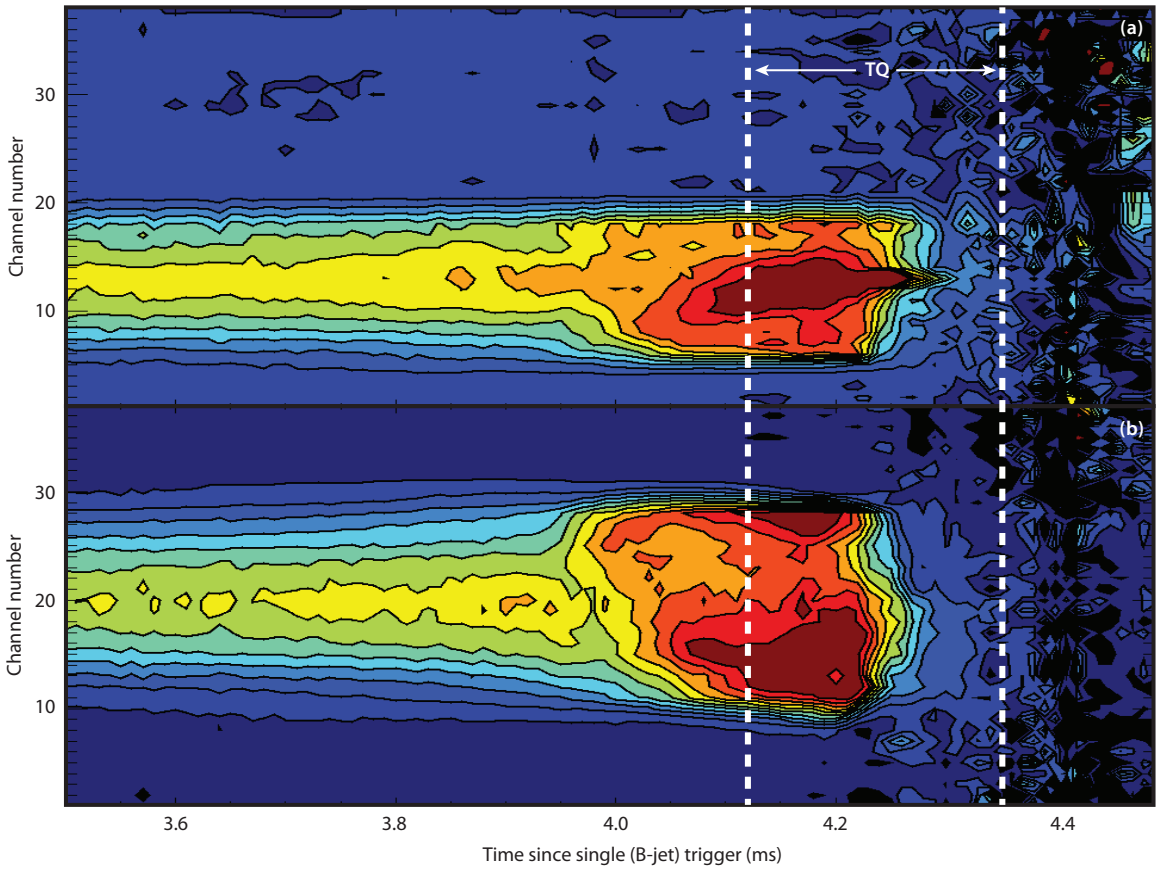

Figure 6-16 – Soft X-ray profiles (arbitrary units) from **(a)** vertical and **(b)** horizontal arrays for single-jet MGI rapid shutdown of C-Mod shot 1090925012, indicating emission from an $m = 2$-like poloidal structure.

However, it is noted that very different processes are involved in the two phenomena: in the TQ radiation asymmetry feature, it is bulk MHD flow convecting heat out of the hot plasma core into the radiative edge. In contrast, in the current quench, the halo current peaking is thought to be created by a rotating (1,1) "plasma tilt" mode in which the cold, resistive plasma is essentially wobbling like the last phase of a spinning coin on a table. Where the plasma contacts the vessel, current is shorted through the divertor and vessel structures, creating the measured halo current peaking. It is, however, suggested that it would be fruitful to conduct MGI rapid shutdown experiments on a machine equipped with *both* a toroidal array of photodiodes *and* a toroidal array of "halo Rogowskis" capable of measuring halo current peaking, in order to definitively establish or rule out a link between the two rotating modes.

6.10 Conclusions on the $n = 1$ mode

Evidence has been presented to show that the toroidal radiation peaking factor in the thermal quench of MGI rapid shutdowns is largely set by the rotation rate of a ubiquitous brightness feature: if the bright spot rotates more than once during the initial TQ flash, then the shutdown will have a low asymmetry; if it locks or does not rotate once during the TQ, then the asymmetry will be higher. This feature does not rotate at the same rate, or even in the same direction, as the pre-disruptive (intrinsic) plasma rotation. It is proposed that this brightness feature is caused by a magnetohydrodynamic perturbation, likely of $m = 2$, $n = 1$ helical structure, convecting heat from the hot core of the plasma to the radiative edge. It should be noted that this theory is also supported by extended MHD simulations done in 2012 by Izzo [7]. This mode is initially created during the pre-TQ phase and then saturates at the time the TQ begins.

In Chapter 7, the theory of radiative tearing modes (RTMs) are discussed, and it is proposed that the exponentially growing $n = 1$ mode observed in the pre-TQ of MGI rapid shutdowns is such an RTM. Then, in Chapter 8, the observations are compared to the output of a simulation of an MGI rapid shutdown on Alcator C-Mod using the extended MHD code NIMROD.

References

[1] Lehnen, M. *et al.* (2011). "Disruption mitigation by massive gas injection in JET." *Nuclear Fusion* **51**(12), 123010 (12 pp). doi:10.1088/0029-5515/51/12/123010

[2] Hutchinson, I.H. (1976). "Magnetic probe investigation of the disruptive instability in tokamak LT-3." *Physical Review Letters* **37**(6), 338–341. doi:10.1103/PhysRevLett.37.338

[3] Hollmann, E.M. *et al.* (2007). "Observation of q-profile dependence in noble gas injection radiative shutdown times in DIII-D." *Physics of Plasmas* **14**(1), 012502 (8 pp). doi:10.1063/1.2408404

[4] Granetz, R.S. *et al.* (1996). "Disruptions and halo currents in Alcator C-Mod." *Nuclear Fusion* **36**(5), 545–556. doi:10.1088/0029-5515/36/5/I02

[5] Neyatani, Y. *et al.* (1999). "Characteristics of halo currents in JT-60U." *Nuclear Fusion* **39**(4), 559–567. doi:10.1088/0029-5515/39/4/312

[6] Garasimov, S.N. *et al.* (2012). "The rotation of plasma current asymmetries during disruptions in JET." In *Proceedings of the 39th European Physical Society Conference on Plasma Physics*, Stockholm, Sweden, July 2–6, 2012. Paper P5.074. Available online at http://ocs.ciemat.es/epsicpp2012pap/pdf/P5.074.pdf

[7] Izzo, V.A. (2013). "Impurity mixing and radiation asymmetry in massive gas injection simulations of DIII-D." *Physics of Plasmas* **20**(5), 056107 (8 pp). doi:10.1063/1.4803896

THIS PAGE INTENTIONALLY LEFT BLANK

Chapter 7

Radiative tearing modes

In Chapters 5 and 6, it was shown that there is an exponentially-growing $n = 1$ mode present in the pre-thermal quench phase of MGI rapid shutdowns on Alcator C-Mod. This mode grows with an e-folding time of approximately 20–150 μs, which is too slow to be an ideal MHD mode. In this chapter, the theory of *radiative tearing modes* is presented, and the predictions of the theory are compared to the experimental observations.

7.1 The features of radiative tearing modes

The class of instabilities which are stable in the limit of zero plasma electrical resistivity (infinite plasma electrical *conductivity*), but which become unstable in the presence of nonzero plasma resistivity, are known as *resistive* modes [1]. One particular class of resistive instabilities are known as *tearing modes*. The energy driving a tearing mode comes from gradients in the magnetic field direction; creating the magnetic island requires reconnection (and thus a non-zero plasma resistivity). The degree to which the magnetic field direction changes spatially is measured in a tokamak by the magnetic shear, which is the normalized derivative of the magnetic safety factor q with respect to minor radius r. These modes were first identified in the seminal 1963 paper by Furth [2], and extended over the following decades to include the effects of "missing" bootstrap current, impurity accumulation, and radiative power loss inside the island.

In the equation which describes the evolution of the size of a magnetic island in a tokamak, if the term involving impurity radiation inside the island is dominant, then the instability is known as a "radiative tearing mode" (RTM). In Section 7.2, the magnitude of each of the terms during the pre-TQ phase of an MGI rapid shutdown is calculated, and it is shown that the radiation-drive term dominates. In this case, based on the expectations of tearing mode theory, the $m = 2$, $n = 1$ mode present in the pre-TQ phase of MGI rapid shutdowns mode would be a radiative tearing mode. However, the predicted growth rate is too large to describe the experimentally observed growth rate: some reasons for this discrepancy are discussed in Section 7.2.3.

7.2 Expected growth rate

The complete nondimensionalized equation describing the growth rate of a resistive island in a toroidal plasma, including plasma resisitivity, neoclassical effects, radiation, and impurity accumulation, is given here, adapted from Delgado-Aparicio *et al.* [3]. It is typically known as the extended or modified Rutherford model:

$$\frac{\mathrm{d}\hat{w}}{\mathrm{d}\hat{t}} = \Delta' + C_1\left(\frac{\hat{w}}{\hat{w}^2 + \hat{w}_\chi^2}\right) + C_2\left(\frac{\hat{w}}{\hat{w}^2 + \hat{w}_\chi^2} - \frac{\hat{w}_\Pi^2}{\hat{w}^3}\right) + C_3\hat{w} + \frac{C_4}{\hat{w}} \tag{7.1}$$

where $\hat{w} \equiv w/r_\mathrm{s}$ is the nondimensionalized island width, w is the island width $[\mathrm{m}]$, and r_s is the minor radius of the rational surface at which the island grows. The nondimensionalized time $\hat{t} \equiv t/\tau_\mathrm{R}$ is equal to the actual time t $[\mathrm{s}]$ normalized to the resistive time scale $\tau_\mathrm{R} \equiv 1.22a^2/(\eta/\mu_0)$, based on the minor radius of the plasma.

The five terms on the right side of Equation 7.1 represent the various driving forces in the growth of a tearing mode. The first is the "classical" tearing mode stability term first derived by Furth *et al.* [2] for straight cylindrical plasmas:

$$\Delta' \equiv \lim_{\delta_\mathrm{r}\to 0}\left[\frac{r}{\psi}\frac{\mathrm{d}\psi}{\mathrm{d}r}\right]_{r=r_\mathrm{s}-\delta_\mathrm{r}}^{r=r_\mathrm{s}+\delta_\mathrm{r}} \tag{7.2}$$

where r is the minor radius coordinate $[\mathrm{m}]$ and ψ is the poloidal magnetic flux $\left[\mathrm{Wb}\cdot\mathrm{rad}^{-1}\right]$. This term is positive (destabilized) if the gradient of the plasma current profile is too steep. The second term constitutes the stabilizing effects of toroidal geometry, $C_1 \equiv 6D_\mathrm{R}$, where D_R is a complicated function of plasma shape and magnetic field profiles, first derived by Glasser *et al.* [4] and thus often known as the "Glasser, Greene, and Johnson term". For tokamak plasmas, $D_\mathrm{R} < 0$ and thus this term is stabilizing. At small island sizes, there is a threshold effect due to finite energy transport inside the island [3] which prevents this stabilization term from dominating; this effect manifests itself mathematically as the transport threshold island width w_χ. This threshold width is then normalized to the resonant surface radius: $\hat{w}_\chi \equiv w_\chi/r_\mathrm{s}$.

The third term is the "neoclassical drive": because of the flattening of the pressure profile inside a magnetic island, the local bootstrap current is suppressed, contributing to the growth of the island. Resistive islands for which this term is significant are generally known as *neoclassical tearing modes* [5]. The coefficient C_2 is proportional to the plasma poloidal beta and is thus worse (larger) for high-performance plasmas:

$$C_2 \equiv \sqrt{\frac{r_\mathrm{s}}{R}}\frac{L_\mathrm{q}}{L_\mathrm{p}}\beta_\theta \tag{7.3}$$

where R is the plasma major radius [m], and L_q and L_p are the magnetic safety factor and pressure gradient scale lengths, respectively: $L_X \equiv \left| X \left(\mathrm{d}X / \mathrm{d}r \right)^{-1} \right|$. In the round brackets for this term, one sees that the neoclassical drive is also subject to thresholds: the same transport threshold width $\hat{w}_\chi$ as for the toroidal stabilization term, as well as a polarization threshold width $\hat{w}_\Pi \equiv w_\Pi / r_s$, which arises due to ion polarization drift at low collisionality (*i.e.*, at small island width) [6].

The fourth term is the radiation drive, and if dominant, gives the radiative tearing mode its name. The coefficient is given by:

$$C_3 \equiv 3 \frac{r_s^2}{s} \frac{\tilde{\varepsilon}_{\mathrm{rad}}}{\chi_{\perp,\mathrm{eff}}^{\mathrm{island}} n_e \langle T_e \rangle} \tag{7.4}$$

where $s \equiv (r/q)\, \mathrm{d}q/dr$ is the magnetic shear at the resonant surface [dimensionless] and $\tilde{\varepsilon}_{\mathrm{rad}}$ is the net radiated power density in the island [$\mathrm{W\,m^{-3}}$]. Note that the *net* radiated power density is equal to the radiated power loss with the Ohmic heating subtracted: $\tilde{\varepsilon}_{\mathrm{rad}} \equiv \varepsilon_{\mathrm{rad}} - \eta J^2$, where $\varepsilon_{\mathrm{rad}}$ is the actual radiated power loss [$\mathrm{W\,m^{-3}}$], η is the plasma toroidal resistivity [$\Omega\,\mathrm{m}$], and J is the plasma current density [$\mathrm{A\,m^{-2}}$].

Turning back to Equation 7.4, $\chi_{\perp,\mathrm{eff}}^{\mathrm{island}}$ is the perpendicular thermal diffusivity into the island, n_e is the electron density [$\mathrm{m^{-3}}$], and $\langle T_e \rangle$ is the electron temperature (times Boltzmann's constant), spatially averaged over the island, in units of [J]. It is noted that if this term dominates, then Equation 7.1 predicts exponential growth for the island width ($\mathrm{d}w/\mathrm{d}t \sim C_3 w$).

Finally, the fifth term describes the effect of impurity accumulation (and thus an increase in the effective ion charge Z_{eff} when islands are small. The coefficient is approximately given by:

$$C_4 \approx 5.43 \left(\frac{2-s}{s} \right) \left(\frac{\tilde{Z}_{\mathrm{eff}}}{Z_{\mathrm{eff}}} \right) \tag{7.5}$$

where s is again the magnetic shear, and $\tilde{Z}_{\mathrm{eff}}$ is the change in Z_{eff} in the island relative the surrounding plasma. In Section 7.2.2 it will be discussed which of these terms are significant in MGI rapid shutdown experiments on Alcator C-Mod.

7.2.1 Island width and magnetic growth rates

It is important to note that Equation 7.1 gives the growth rate of the *island width* w. It is typical when studying NTMs in the flat-top of high-performance plasmas to directly measure the island width using electron cyclotron emission temperature profiles: the island flattens the temperature profile, and as the tearing mode rotates past the ECE radiometer in the lab-

oratory frame, one can simply pick off the width of the island from the temperature profile data [7].

However, in the case of the pre-TQ of MGI rapid shutdowns on Alcator C-Mod, the island grows *when the cooling front reaches the $q = 2$ surface*, and thus the width of the island cannot be resolved on the ECE radiometer. The magnitude of the perturbation is instead inferred from the perturbation that it makes in the poloidal magnetic field at the plasma boundary, as detected by external pickup coils. It is known, however, that for magnetic islands in toroidal geometry, the island width $w \sim \sqrt{\tilde{B}_r}$ [8], where $\tilde{B}_r$ is the perturbation to the radial magnetic field at the island. For rapidly-growing ($\gamma \gtrsim 10^3$ s^{-1}) modes, the vessel wall can be assumed to be a perfect conductor. Then, neglecting the perturbed current outside the island, the perturbed *poloidal* magnetic field at the radius of the pickup coils is given by [8]:

$$\tilde{B}_\theta\left(r_c\right) = \tilde{B}_r\left(r_s\right)\left(\frac{r_s}{r_c}\right)^{m+1}\frac{1+\left(\frac{r_c}{r_w}\right)^{2m}}{1-\left(\frac{r_s}{r_w}\right)^{2m}} \tag{7.6}$$

where $\tilde{B}_\theta\left(r_c\right)$ is the perturbed poloidal magnetic field at the radius of the pickup coils r_c; $\tilde{B}_r\left(r_s\right)$ is the perturbed radial magnetic field at the island (resonant surface) radius r_s; r_w is the radius of the conducting wall, and m is the poloidal mode number of the island, likely $m = 2$ in the case of the radiative island in the pre-TQ of MGI rapid shutdown on Alcator C-Mod (see Section 6.8). For a typical resonant surface ($q = 2$ surface) radius on Alcator C-Mod, evaluating Equation 7.6 gives $\tilde{B}_r\left(r_s\right) \simeq 2.2\tilde{B}_\theta\left(r_c\right)$. Thus, the island width $w \sim \sqrt{\tilde{B}_\theta\left(r_c\right)}$. In the case of an exponentially growing magnetic mode with a measured growth rate γ_B, the growth rate of the island width will be half: $\gamma_w = \gamma_B/2$. Also, since the energy in the magnetic perturbation scales as $E \sim \tilde{B}_\theta^2$, the growth rate of energy in the magnetic perturbation will scale as $\gamma_E = 2\gamma_B$.

7.2.2 Dominant terms in MGI rapid shutdown

In the case of Alcator C-Mod plasmas undergoing MGI, an estimate of the magnitude of each of the terms in Equation 7.1 can be made. The classical tearing mode stability term plus the toroidal stabilization term is negative (stable), and of order unity in the flat-top of a quiescent plasma [7, Figure 8(a)]. However, the cooling itself will be expected to alter the current profile, and therefore, this term may change. This cannot be dealt with by this simple application of the theory, and therefore, in Chapter 8, computer simulation using an extended MHD code will be used to properly treat the coupled radiation and current drive terms for the instability. The other terms can be evaluated using the example of the single-jet MGI rapid shutdown of Alcator C-Mod shot 1120202008. The relevant quantities are listed in Table 7-1.

The electron temperature was estimated from second-harmonic X-mode electron cyclotron

Symbol	Quantity (unit)	Value
R	Plasma major radius (m)	0.68 ± 0.02
a	Plasma minor radius (m)	0.22 ± 0.02
r_s	Minor radius of resonant surface (m)	0.18 ± 0.02
s	Magnetic shear (dimensionless)	0.52 ± 0.10
L_q	Magnetic safety factor gradient scale length (m)	0.35 ± 0.07
L_p	Pressure gradient scale length (m)	≈ 0.029 m
β_θ	Plasma poloidal beta at resonant surface	$\approx 4.5\%$
η	Plasma resistivity at resonant surface (Ω m)	$(5.5 \pm 2.5) \times 10^{-6}$
ε_{rad}	Radiated power density in island (W m^{-3})	$(1.56 \pm 0.10) \times 10^{8}$
J	Plasma current density at resonant surface (A m^{-2})	2.18×10^{6}
ηJ^2	Ohmic heating density (W m^{-3})	2.61×10^{7}
$\tilde{\varepsilon}_{rad}$	Net power density in island (W m^{-3})	$(1.3 \pm 0.1) \times 10^{8}$
$\chi_{\perp,eff}^{island}$	Effective perpendicular thermal diffusivity (m^2 s^{-1})	0.5
n_e	Electron density at resonant surface (m^{-3})	$(1.4 \pm 0.5) \times 10^{20}$
$\langle T_e \rangle$	Electron temperature (eV)	57 ± 20
	Electron temperature (J)	$(9.1 \pm 3.2) \times 10^{-18}$
Z_{eff}	Plasma effective charge state	Assumed 2.0
$\tilde{Z}_{eff}$	Change in Z_{eff} in radiative island	Assumed 3.0
γ_w	Growth rate of island width (s^{-1}) for RTM	$(2.8 \pm 2.1) \times 10^{6}$
γ_B	Growth rate of magnetic perturbation (s^{-1})	$(5.7 \pm 4.3) \times 10^{6}$

Table 7-1 – Evaluated quantities in $n = 1$ exponential growth phase of MGI rapid shutdown of Alcator C-Mod shot 1120202008.

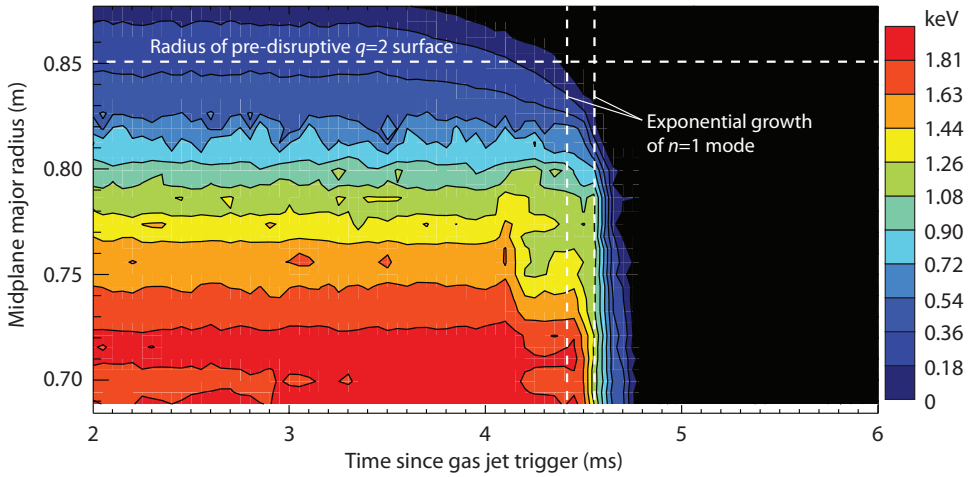

Figure 7-1 – Electron temperature profile through the pre-TQ of shot 1120202008 as measured by second harmonic X-mode ECE radiometry.

emission (ECE) radiometry (see Section 3.8). A contour plot of the ECE temperature through the rapid shutdown sequence can be seen in Figure 7-1. The interpolated temperature at the pre-disruptive location of the $q = 2$ magnetic surface can be seen in Figure 7-2. The assumed effective perpendicular thermal diffusivity in the island is typical of the core plasma in Alcator C-Mod [9].

The radiated power density ε_{rad} was estimated for the time of exponential $n = 1$ growth by taking the total radiated power at the time of exponential growth (4.42–4.55 ms after the gas jet trigger) from the wall-mounted photodiodes ($P_{rad} \approx 107 \pm 5$ MW) and assuming it all comes from the boundary plasma between the flux surface 5 cm (1/4 of the plasma minor radius) radially inward from the $q = 2$ surface, and the last closed flux surface (a volume of 0.68 m^3). This gives a radiated power density of $\varepsilon_{rad} \approx (1.56 \pm 0.10) \times 10^8$ W m^{-3}. The net power density is then the radiated power density subtract the Ohmic heating power ηJ^2.

For the purposes of the neoclassical drive (the C_2 term), the pre-disruptive pressure (and thus β_θ) and pressure gradient scale length were used. Finally, it was assumed that $Z_{eff} = 2$ and $\tilde{Z}_{eff}$ (the increase in Z_{eff} in

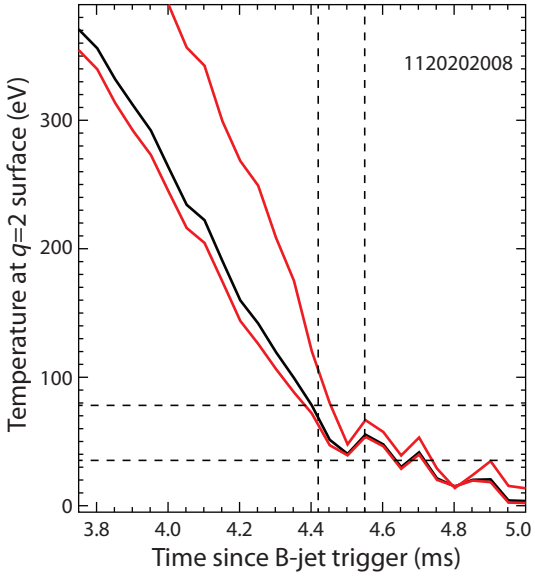

Figure 7-2 – Electron temperature at $q = 2$ surface as measured by 2nd-harmonic X-mode ECE radiometry. *Black line*: the temperature at the $q = 2$ surface, as interpolated from the adjacent two channels (*red lines*). Vertical dashed limes represent the start and end of exponential growth of the $n = 1$ mode; the horizontal dashed lines represent the uncertainty interval for the electron temperature (57 ± 20 eV).

the radiative island relative to the surrounding plasma) was 3.

The result is that the neoclassical term (C_2 term) has a value of approximately 0.28, the radiative term (C_3 term) has a value of approximately 3.8×10^4 and the impurity accumulation term (C_4 term) attains a value of approximately 23. That is, for the exponential growth of an $n = 1$ mode in the pre-TQ phase of an MGI rapid shutdown, it is expected that the radiation-drive term in the extended Rutherford model of a magnetic island is totally dominant. That is, the "radiative tearing mode" (RTM) model applies in this case.

Under this assumption, in which the C_3 term dominates in Equation 7.1—that is, the mode is a radiative tearing mode (RTM)—then the growth rate can be calculated. Taking only that term, Equation 7.1 simplifies to $\mathrm{d}\hat{w}/\,\mathrm{d}\hat{t} \simeq C_3\hat{w}$. Expanding each of the nondimensional variables ($\hat{w}$, $\hat{t}$, C_3) gives:

$$\frac{\tau_R}{r_s}\frac{\mathrm{d}w}{\mathrm{d}t} = \left(3\,\frac{r_s^2}{s}\,\frac{\tilde{\varepsilon}_{rad}}{\chi_{\perp,eff}^{island}\,n_e\,\langle T_e\rangle}\right)\frac{w}{r_s} \tag{7.7}$$

Noting that $\tau_R \equiv 1.22a^2/(\eta/\mu_0)$, and simplifying terms, Equation 7.7 can be written as an equation of pure exponential growth of the island width:

$$\frac{\mathrm{d}w}{\mathrm{d}t} = \left[\frac{2.46}{s}\left(\frac{r_s}{a}\right)^2\frac{\eta\,\tilde{\varepsilon}_{rad}}{\mu_0\,\chi_{\perp,eff}^{island}\,n_e\,\langle T_e\rangle}\right]w \tag{7.8}$$

where the term in square brackets in Equation 7.8 is the growth rate of the island width γ_w [s^{-1}]. Recall that the growth rate of the poloidal magnetic field as measured by Mirnov coils is then twice this rate ($\gamma_B = 2\gamma_w$), and the growth rate of the energy in the magnetic island is $\gamma_E = 4\gamma_w$.

7.2.3 Comparison with experimental observations

Evaluating the growth rate given by Equation 7.8 for the exponential growth phase of the $n = 1$ mode in the pre-TQ of the MGI rapid shutdown of Alcator C-Mod shot 1120202008 gives a value of $\gamma_B \approx 5.66 \times 10^6$ s^{-1}. This corresponds to a growth *time* of only 177 ns, or roughly 340 times faster than the actual observed growth time of 60.1 μs. This growth time is nearly as small as the ideal MHD time scale for Alcator C-Mod ($\tau_A = a/v_A \approx 31$ ns). Therefore, the identification of the growing $n = 1$ mode as a radiative tearing mode, as described by the simplified Rutherford model (Equation 7.8), is uncertain. The island growth *is* exponential, which is consistent with experimental observations, but the growth rate is highly overestimated. The shortcomings of the analytic Rutherford model here further motivates assessment of the MHD activity during MGI rapid shutdowns using a more complex and complete numerical treatment, as will be discussed in Chapter 8. Typically, the Rutherford model for resistive islands is more commonly applied to plasmas with much lower levels of

impurities (*e.g.* density-limit disruptions [10]).

The calculated growth rate (the square brackets in Equation 7.8) varies as $\gamma_B \sim \eta/T_e$, and thus is highly sensitive to the local electron temperature. The plasma resistivity (Spitzer–Harm) varies inversely with the 3/2 power of temperature: $\eta \sim T_e^{-3/2}$. Thus the overall growth rate varies as $\gamma_B \sim T_e^{-5/2}$, and a factor of two error in plasma temperature would lead to a nearly 6-fold error in the calculated growth rate. However, this still cannot account for the numerical discrepancy between the calculated and observed mode growth rates.

Thus, it is likely that the main reason why the growth rate of the mode is overpredicted is simply because the extended Rutherford model of radiative nonlinear tearing modes [11] is derived only for *modest* radiative power loads. The theory assumes that the island is radiating power, which is being restored from the surrounding plasma by cross-field conduction. The pressure gradient produced by the power "sink" in the island produces the additional (radiative) term in the growth rate equation (Equation 7.1). The radiated power densities assumed here ($\gtrsim 100$ MW m^{-3}) are very large, even when compared to highly radiative stationary plasmas (≈ 1 MW m^{-3}).

Despite the quantitative failure of the Rutherford model, it is important to note that the theory does predict that impurity radiation can lead to exponentially-growing MHD islands. An examination of the RTM growth model (Equation 7.7) indicates that if a $\chi_\perp$ value from the quiescent plasmas is used, then the normalized growth rate is set by the ratio of the energy confinement time ($\simeq r_s^2/\chi_\perp$) to the characteristic timescale for the radiation to remove the edge plasma's thermal energy ($\simeq \tilde{\varepsilon}_{rad}/n_e T_e$). Using the global energy confinement time ($\approx$ 50 ms) in Alcator C-Mod flat-top plasmas, and the observed edge cooling time scale (≈ 0.5 ms), this ratio is approximately 100. Thus, the model predicts that the mode will grow approximately 100 times faster than the resistive time scale of the plasma.

However, it is likely that such a large ratio violates the physical reasoning underlying the Rutherford model. The island cannot grow 100 times faster than the local current redistribution timescale. It is suggestive that the resistive time scale τ_R takes a value of ≈ 1 ms for the measured temperatures over the edge region where the cooling is taking place. This is of the same order of magnitude as the duration of the pre-TQ phase of the MGI rapid shutdown.

Therefore, it is concluded that while the growing $n = 1$ mode is suggestive of radiation-driven MHD, the RTM label cannot be directly assigned to it. However, the analytic model's failure in the extreme conditions of an MGI rapid shutdown is unsurprising, and does not preclude the importance of resistive MHD in the sequence of events during the shutdown.

7.3 Scaling of growth rate to larger machines

If the mode which triggers the onset of the thermal quench is indeed a magnetic island caused by a tearing mode, then this island may also be the feature which is rotating and

causing the bulk MHD flow of heat from the hot plasma core to the radiative edge, producing the observed brightness feature. In this case, given that the rotation rate of the mode appears to control the radiation asymmetry during the thermal quench (see Chapter 6), it is of interest how the rotation rate of the mode scales to larger machines.

This problem has not been thoroughly investigated theoretically, but two papers suggest a direction forward. Mikhailovskii *et al.* [12] calculate the "natural" rotation frequency of a saturated magnetic island in a tokamak, concluding that for constant plasma conditions, the rotation frequency $\omega \sim R^{-2}$. However, it is not certain that the conditions of this theory are valid in the highly perturbing, non-stationary thermal quench. In a theoretical study of rotating magnetic islands in tokamaks, Smolyakov *et al.* [13] note that the perpendicular (radial) MHD velocity produced by the mode is proportional to its rotation rate: $v_\perp \sim \omega$, so if the duration of the thermal quench is set by the time it takes to convect heat from the core to edge ($\tau_{TQ} \sim a/v_\perp$), then this indicates that $\omega\tau_{TQ}$—proportional to the number of times the mode rotates during the TQ—is independent of machine size. This issue is discussed further in Section 9.1.2.

Finally, it should be noted that Smolyakov *et al.* studied modes which were not growing any more: they were saturated, rotating magnetic islands. Extended MHD modeling of the thermal quench has suggested [14] that the energy transport begins while the mode is still exponentially growing, although this is not observed in the magnetic signals on Alcator C-Mod presented here. In this case, the MHD transport will depend on both the mode growth rate and its rotation rate (which could be zero), rather than just on the rotation rate. This suggests further avenues for future theoretical investigation.

7.4 Conclusions on the radiative tearing mode

The theory of the radiative tearing mode (RTM) was presented. The growth rate of the $n = 1$ mode in the pre-TQ phase of MGI rapid shutdowns was calculated from the extended Rutherford model, and it was shown that the theory overpredicts the growth rate of the mode compared to the experimental observations. The reasons for the failure of the model were discussed.

In the next chapter, some lessons from extended MHD computer modeling of MGI rapid shutdown on Alcator C-Mod will be discussed, and the output of the computer model compared to the experimental observations and the analytic theory presented in this chapter. Finally, in Chapter 9, the conclusions and implications of the work will be presented.

References

[1] Fitzpatrick, R. "Linear tearing mode theory." University of Texas at Austin class notes for PHY 380L: Plasma Physics. Available online at http://farside.ph.utexas.edu/teaching/plasma/plasma.html

[2] Furth, H.P. *et al.* (1963). "Finite-resistivity instabilities of a sheet pinch." *Physics of Fluids* **6**(4), 459–484. doi:10.1063/1.1706761

[3] Delgado-Aparicio, L. *et al.* (2011). "Impurity transport experiments and effects on MHD in the National Spherical Torus Experiment (NSTX)." *Nuclear Fusion* 51(8), 083047 (12 pp). doi:10.1088/0029-5515/51/8/083047

[4] Glasser, A.H. *et al.* (1975). "Resistive instabilities in general toroidal plasma configurations." *Physics of Fluids* **18**(7), 875–888. doi:10.1063/1.861224

[5] Buttery, R.J. *et al.* (2000). "Neoclassical tearing modes." *Plasma Physics and Controlled Fusion* **42**, Suppl., B61–B73. doi:10.1088/0741-3335/42/12B/306

[6] Wilson, H.R. *et al.* (1996). "Threshold for neoclassical magnetic islands in a low collision frequency tokamak." *Physics of Plasmas* **3**(1), 248–265. doi:10.1063/1.871830

[7] Chang, Z. *et al.* (1998). "Neoclassical tearing modes in Tokamak Fusion Test Reactor experiments: I. Measurements of magnetic islands and Δ'." *Physics of Plasmas* **5**(4), 1076–1084. doi:10.1063/1.872627

[8] Salzedas, F. *et al.* (2002). "Exponentially growing tearing modes in Rijnhuizen Tokamak Project plasmas." *Physical Review Letters* **88**(7), 075002 (4 pp). doi:10.1103/PhysRevLett.88.075002

[9] Luis Delgado-Aparicio, personal communication, April 2013.

[10] Suttrop, W. *et al.* (1997). "Tearing mode formation and radiative edge cooling prior to density limit disruptions in ASDEX Upgrade." *Nuclear Fusion* **37**(1), 119–125. doi:10.1088/0029-5515/37/1/I09

[11] Rutherford, P.H. (1985). "Resistive instabilities in tokamaks." Princeton Plasma Physics Laboratory Report No. PPPL-2277. 36 pp. Available online at http://www.osti.gov/bridge/servlets/purl/5086595-qWS7L8/

[12] Mikhailovskii, A.B. *et al.* (2000). "An approach to calculation of magnetic island rotation frequency." *Physics of Plasmas* **7**(6), 2530–2538 doi:10.1063/1.874093

[13] Smolyakov, A.I. *et al.* (1995). "Rotating nonlinear magnetic islands in a tokamak plasma." *Physics of Plasmas* **2**(5), 1581–1598. doi:10.1063/1.871308

[14] Izzo, V.A. (2013). "Impurity mixing and radiation asymmetry in massive gas injection simulations of DIII-D." *Physics of Plasmas* **20**(5), 056107 (8 pp). doi:10.1063/1.4803896

Chapter 8

Extended MHD simulation of rapid shutdown

It has been observed in MGI rapid shutdown experiments on Alcator C-Mod that there is an $n = 1$ magnetic mode which exponentially grows in the pre-thermal quench phase. When this mode reaches its peak amplitude, the thermal quench (TQ) begins. During the thermal quench, the radiation as measured by wall-mounted photodiodes is toroidally peaked, with the time-integrated peaking factor controlled by the rotation rate of the observed brightness feature. This suggests that the $n = 1$ MHD mode which grows exponentially during the pre-TQ remains in the TQ, and is the cause of the flow of energy from the hot plasma core to the radiative edge. In Chapter 7, the theory of radiative tearing modes (RTMs) was discussed, and it was shown that while they are a plausible candidate for the $n = 1$ mode present in the pre-TQ, the mode growth rate predicted by the Rutherford model of magnetic islands in a tokamak is larger than that observed in the experiments.

In this chapter, the results of a computer simulation of an MGI rapid shutdown on Alcator C-Mod are presented. Insight is gained into the nature of the MHD activity during a rapid shutdown, and the limitations of the computer model for simulating rapid shutdown are presented. Suggestions for future investigations are discussed.

8.1 The extended MHD code NIMROD

The NIMROD code [1] solves the time-dependent equations of extended MHD on a computational domain that consists of real-space finite elements in the poloidal plane, and Fourier components in the toroidal direction. The equations are solved for real time, *i.e.*, not for steady-state vibrating components. The initialism NIMROD stands for "**N**on-**I**deal **M**agnetohydrodynamics with **R**otation – **O**pen **D**iscussion" [2].

In general, "extended MHD" refers to plasma fluid models which solve for more quantities than those in Maxwell's equations plus the five fluid quantities solved for in the ideal MHD model (to wit: density ρ, vector velocity $\vec{v}$, and pressure p). The extended MHD model used in NIMROD consists of the resistive MHD equations, with included models for the electrical

resistivity η with Ohmic heating, anisotropic thermal conduction (different in the parallel and perpendicular directions to the magnetic field), viscous kinetic energy dissipation (viscous heating), particle diffusion, and numerical diffusion of magnetic divergence error (that is, $\nabla \cdot \vec{B} \neq 0$ due to numerical error, and this error is then numerically diffused with a diffusion coefficient $\kappa_{\text{div B}}$ throughout the domain. The complete set of equations solved by the base version of NIMROD, formulated in terms of steady-state and perturbed components, can be found in Equations (4a)–(4f) of [3].

NIMROD closes the MHD moment hierarchy with user-selectable "closures", including a Chew–Goldberger–Low anisotropic stress tensor [4], a fast electron pressure model, or, as was used in the simulation here, the KPRAD module implemented in NIMROD by V.A. Izzo of the UCSD Center for Energy Research [5]. KPRAD, which stands for "killer pellet radiation", is a set of cooling curves originally developed by Whyte *et al.* [6] based on ADAS atomic line spectra databases. The KPRAD model includes the line radiation coefficients (L_{rad}), and temperature-dependent atomic transition rates (ionization and recombination) for noble gases of interest to rapid shutdown on tokamaks. In 2005–2007, Izzo originally implemented the KPRAD model in NIMROD[1] in order to simulate MGI rapid shutdown on Alcator C-Mod and DIII-D adding quantities for the neutral plus every charge state of a user-selectable impurity (typically helium, neon, or argon). The impurities have their own density but do not have their own temperature or velocity: NIMROD only tracks a single bulk MHD fluid velocity $\vec{V}$, (the ion velocity), electron temperature T_{e} and a single ion temperature T_{i}, which is assumed to be the same for the main ion species and the impurities. In the "base" NIMROD model, the ion density is assumed to be the same as the electron density (by quasineutraity), but this is not true when the KPRAD closure is used (see below). The continuity equations solved when NIMROD is used with the KPRAD closure are as follows:

$$\rho \frac{\partial \vec{V}}{\partial t} = -\nabla p + \vec{J} \times \vec{B} + \nabla \cdot \left(\nu \rho \nabla \vec{V} \right) \tag{8.1}$$

$$\vec{E} + \vec{V} \times \vec{B} = \eta \vec{J} \tag{8.2}$$

$$n_{\text{e}} \frac{\partial T_{\text{e}}}{\partial t} = (\gamma - 1) \left(n_{\text{e}} T_{\text{e}} \nabla \cdot \vec{V} + \nabla \cdot \vec{q}_{\text{e}} - Q_{\text{loss}} \right) \tag{8.3}$$

$$\vec{q}_{\text{e}} = -n_{\text{e}} \left[\chi_{\parallel} \hat{b}\hat{b} + \chi_{\perp} \left(\overleftrightarrow{I} - \hat{b}\hat{b} \right) \right] \cdot \nabla T_{\text{e}} \tag{8.4}$$

$$\frac{\partial n_{\text{e}}}{\partial t} + n_{\text{e}} \nabla \cdot \vec{V} = \nabla \cdot \left(D \nabla n_{\text{e}} \right) + S_{\text{ion}} + S_{\text{rec}} \tag{8.5}$$

$$\frac{\partial n_{\text{i}}}{\partial t} + n_{\text{i}} \nabla \cdot \vec{V} = \nabla \cdot \left(D \nabla n_{\text{i}} \right) + S_{\text{ion}} + S_{\text{3-body}} \tag{8.6}$$

$$\frac{\partial n_{\text{z}}}{\partial t} + n_{\text{z}} \nabla \cdot \vec{V} = \nabla \cdot \left(D \nabla n_{\text{z}} \right) + S_{\text{ion}} + S_{\text{rec}} \tag{8.7}$$

[1] This implementation of "NIMROD plus KPRAD" was originally referred to as "NIMRAD", although today this name is not used. Simulations using NIMROD with the KPRAD closure are simply referred to as NIMROD simulations using the KPRAD closure.

where ρ is the mass density of the plasma $[\mathrm{kg\,m^{-3}}]$, $\vec{V}$ is the fluid velocity $[\mathrm{m\,s^{-1}}]$, p is the plasma pressure [Pa], $\vec{J}$ is the current density $[\mathrm{A\,m^{-2}}]$, $\vec{B}$ is the local magnetic field [T], ν is the kinematic viscosity $[\mathrm{m^2\,s^{-1}}]$, $\vec{E}$ is the electric field $[\mathrm{V\,m^{-1}}]$, η is the electrical resistivity $[\Omega\,\mathrm{m}]$, γ is the adiabatic constant, n_e, n_i, and n_z are the density of electrons, main ion species (deuterium), and impurity charge state z, respectively $[\mathrm{m^{-3}}]$, T_e is the electron temperature [J], $\vec{q}_e$ is the heat flux carried by electrons $[\mathrm{W\,m^{-2}}]$, $\hat{b}$ is the unit vector in the local magnetic field direction, and $\chi_\parallel$ and $\chi_\perp$ are respectively the parallel and perpendicular electron thermal diffusivities $[\mathrm{m^2\,s^{-1}}]$. Time is t [s], and the spatial gradient operator is ∇. Particle diffusion is given by the particle diffusivity D $[\mathrm{m^2\,s^{-1}}]$. The rates of ionization, 2-body recombination, and 3-body recombination $[\mathrm{m^{-3}\,s^{-1}}]$ are given by S_{ion}, S_{rec}, and $S_{\mathrm{3\text{-}body}}$, respectively.

Finally, the energy loss term Q_{loss} $[\mathrm{W\,m^{-3}}]$ includes line radiation and bremsstrahlung as calculated by KPRAD, ionization energy, and dilution (energy lost to heating up newly liberated electrons from impurities). Q_{loss} also includes the Ohmic heating density $\eta\vec{J}\cdot\vec{J}$. Viscous heating can be included in NIMROD, but was not included in the model that was run. In addition to these continuity equations, Maxwell's equations with numerical diffusion of magnetic field divergence error are used, as described in [3]. Refer to Section II of [5] for discussion of the subtleties of the numerical treatment of these continuity equations in NIMROD. In particular, in order to increase performance, the S_{ion} and S_{rec} in the continuity equation for the charge states (n_z) are not included in the NIMROD time advance; they are solved internally by the KPRAD module and used as a constant in the NIMROD advance.

8.2 NIMROD simulation of Alcator C-Mod rapid shutdown

The time-dependent simulation presented here was initialized with the EFIT-calculated equilibrium of Alcator C-Mod shot 1071220025 (from December 20, 2007). This was a standard, lower single null magnetic configuration, normal-field ($-\phi$ direction), I_p = 1.00 MA, B_ϕ = 5.4 T Alcator C-Mod discharge with 1 MW of ICRF auxiliary heating and W_{th} = 68 kJ of stored thermal energy. The EFIT equilibrium at t = 0.980 s was used for the simulation. This target plasma is essentially identical to that used for the lower-single-null discharges used for MGI rapid shutdown experiments on February 2, 2012 for which results have been presented throughout this thesis.

A flux-aligned poloidal grid consisting of 25 cells in the radial direction and 40 cells in the poloidal direction was used for this simulation, with finite element polynomial degree 4. In the toroidal direction, 11 Fourier modes were used: the axisymmetric n = 0 component, plus n = 1–10 perturbations. The simulation took approximately 32 hours of runtime on 55 nodes (8 processors per node) of the Loki compute cluster at the MIT Plasma Science and Fusion Center. The simulation presented here was run in April 2013.

8.3 Sequence of events in simulated MGI rapid shutdown

The simulation starts with an argon impurity being created just outside the last closed flux surface at $t = 0$. In this simulation, the impurities were deposited over the entire toroidal extent, as if there were an continuous toroidal array of gas injectors. In the poloidal plane, the impurities are deposited in a broad poloidal swath over nearly 180° of poloidal angle, although concentrated toward the outboard midplane. The neutral argon immediately begins diffusing inward across the field lines, ionizes, and begins to radiate power from the edge of the plasma.

In Figure 8-1, contours of electron temperature T_e [eV], radiated power density P_{rad} [W m^{-3}], and argon impurity density n_{imp} [m^{-3}] are plotted for nine time slices covering the entire TQ of the simulation. Note that the quantities shown in Figure 8-1 are only the $n = 0$ (axisymmetric) components of each: they do not show any of the toroidal asymmetries. (Toroidal asymmetries in P_{rad} and the poloidal MHD fluid flow velocity $|\vec{v}_{pol}|$ are shown in Figures 8-2 and 8-4, respectively.)

It can be seen from the second row of Figure 8-1 that in the simulation, essentially all the radiated power comes from the outboard (low-field) side of the plasma. Additionally, the peak radiated power density in the simulation is very large: almost 10 GW m^{-3}. This is not inconsistent with the experimental measurements presented in earlier chapters, as the plasma emissivity values measured by the wall-mounted photodiodes on Alcator C-Mod were sampling an *average* emissivity through the entire poloidal slice in front of the photodiode.

8.3.1 Toroidal and poloidal mode structure

The MHD activity is most easily visualized by examining Figure 8-3 for the poloidal plane (m number), and Figure 8-5 for the toroidal mode number (n). It can be seen in Figure 8-3 that as the cooling front moves in, MHD modes are destabilized on successive resonant surfaces. In the third subplot, corresponding to the peak amplitude of the $n = 2$ mode, one can see the poloidal velocity eigenfunction (axisymmetric $n = 0$ component only shown in this figure) has a complicated radial structure and exists at the $q = 2$, $q = 3/2$, and $q = 1$ surfaces. However, the first row of Figure 8-1 shows that these modes do not complete the transport of energy out of the core plasma: that is done later, by an $n = 1$ mode, approximately at $t = 1.40$–1.50 ms.

The true poloidal velocity (summed over all toroidal Fourier modes) is shown for four toroidal locations at the peak of the $n = 1$ amplitude in Figure 8-4. It can be seen that the poloidal velocity is peaked on the outboard (low-field) side of the plasma, at the $q = 2$, $q = 3/2$, and $q = 1$ surfaces. This corresponds to the resonant surfaces at which the $(m, n) = (2, 1)$, $(3, 2)$, and $(1, 1)$ modes exist (in the cylindrical approximation, which is not accurate for a shaped, diverted plasma like Alcator C-Mod's). This suggests that once the thermal quench begins,

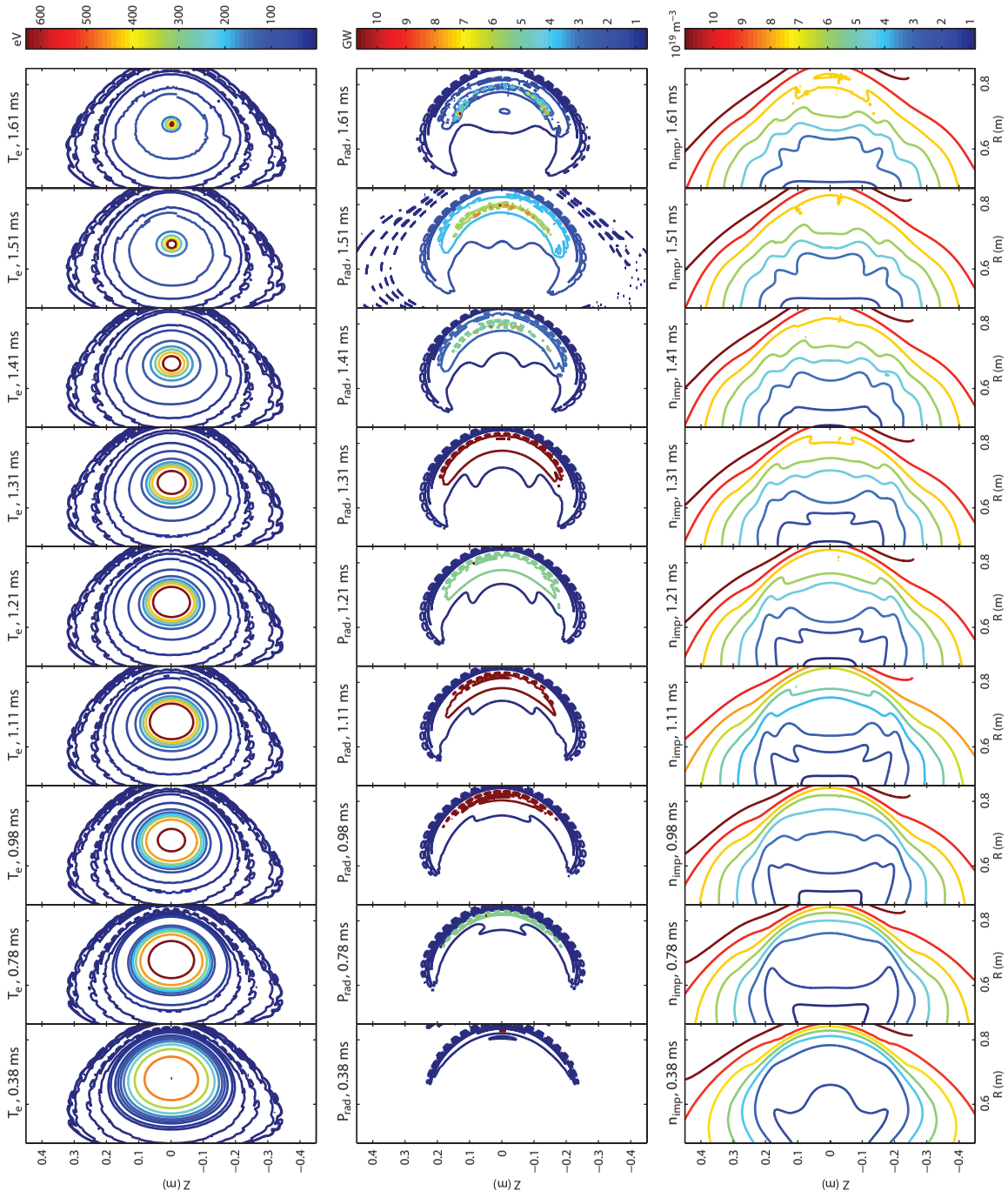

Figure 8-1 – (*Rotated figure.*) Contour plot of axisymmetric ($n = 0$) components of three quantities from NIMROD simulation of single-jet MGI rapid shutdown of Alcator C-Mod shot 1071220025. Top row: Electron temperature $[\mathrm{eV}]$; Middle row: Radiated power density $[\mathrm{GW\,m^{-3}}]$; Bottom row: density of argon impurities $[10^{19}\ \mathrm{m^{-3}}]$. Quantities are evaluated at times marked by vertical lines in Figure 8-5.

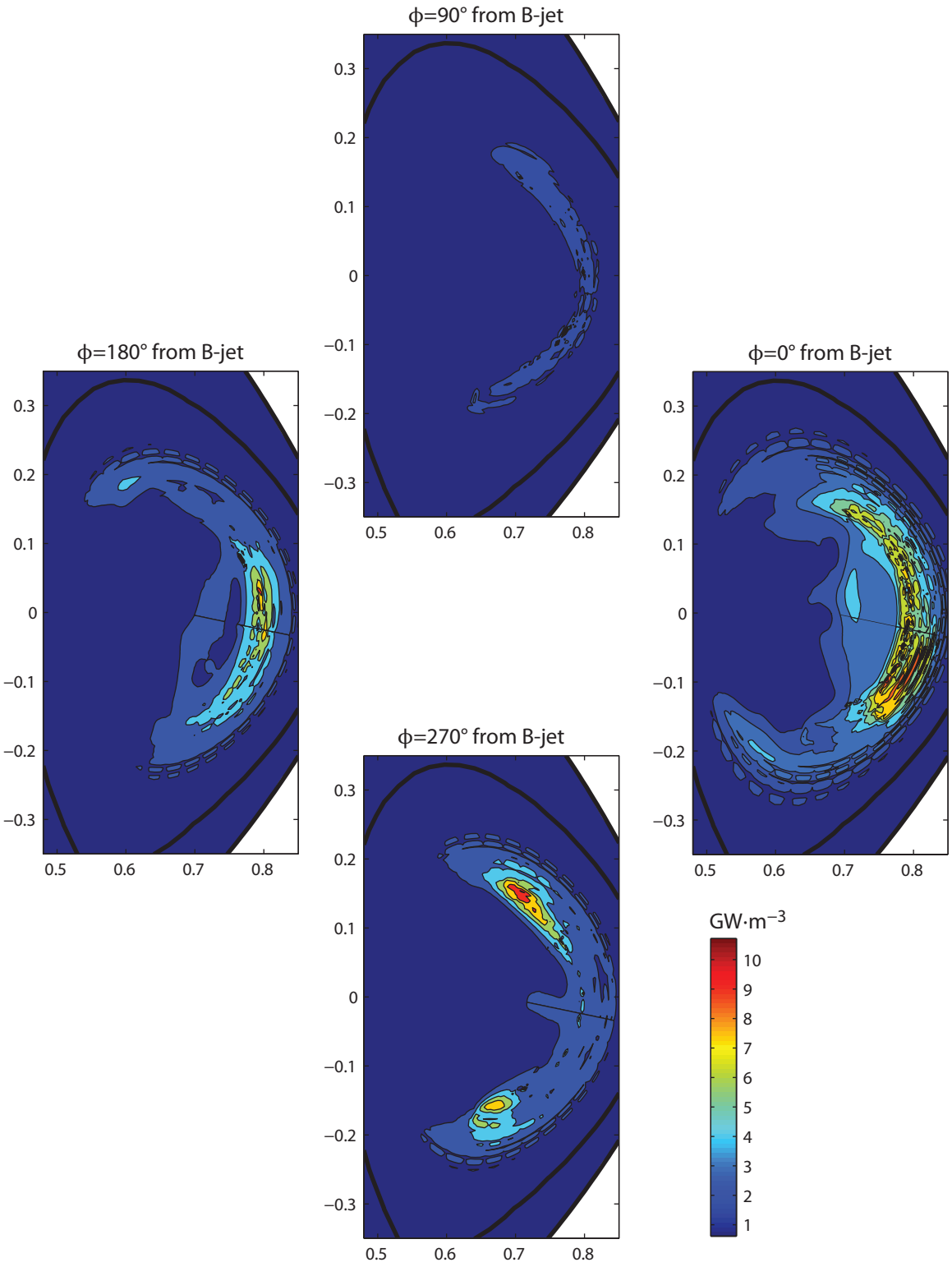

Figure 8-2 – Radiated power density (all toroidal Fourier modes included) due to impurities at four toroidal locations in NIMROD simulation of single-jet MGI rapid shutdown on Alcator C-Mod. Evaluated at $t = 1.51$ ms, at the peak amplitude of the $n = 1$ MHD activity (see Figure 8-5).

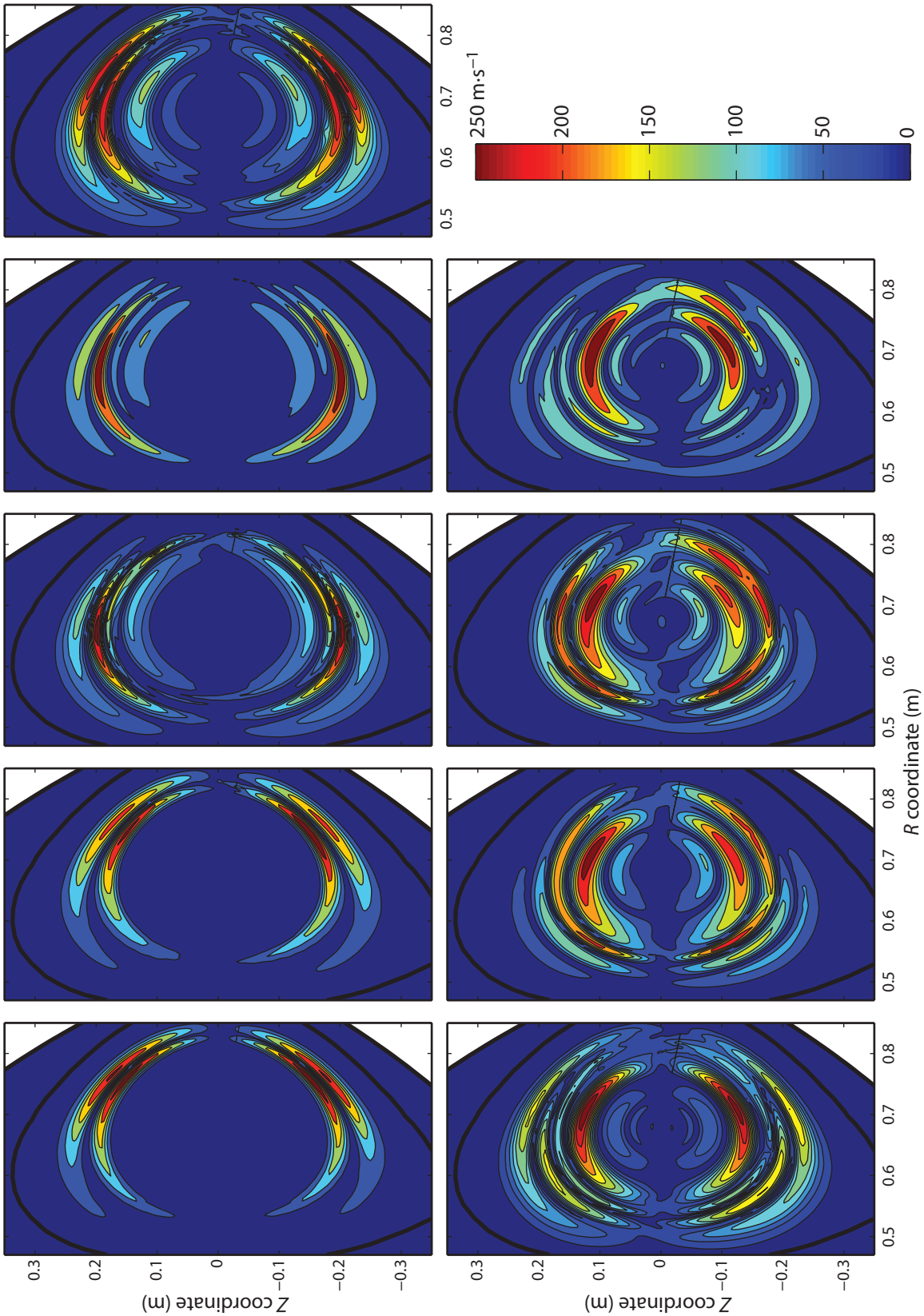

Figure 8-3 – Axisymmetric ($n = 0$) component of poloidal velocity due to MHD activity at nine time slices through NIMROD simulation of single-jet MGI rapid shutdown. The thick black line is the last closed flux surface of the pre-disruptive equilibrium. Quantities are evaluated at times marked by vertical lines in Figure 8-5.

there is significant coupling between core MHD modes, even between different toroidal mode numbers, and one should not expect to detect a "pure" $(2,1)$ mode during the thermal quench.

The energy in each toroidal mode is shown in Figure 8-5. The vertical lines correspond to the times at which the profiles in the various subplots in Figures 8-1 and 8-3 were evaluated. It can be clearly seen from panel (b) of Figure 8-5 that the initial mode destabilized is an $n = 2$ mode; it is only later that the $n = 1$ mode becomes dominant, once the cooling front has moved in to the $q = 1$ surface (in part by the impurity mixing created by the growing $(3,2)$ mode). This is unlike the experimental observations, in which the $n = 1$ mode is destabilized when the cooling front reaches the $q = 2$ surface, indicating that the "killer" mode is a $(2,1)$-like mode.

8.4 Comparison of simulations to analytic RTM theory

It was discussed how in the simulation, the thermal quench began with the MHD activity created when the cooling front penetrated to the $q = 3/2$ surface. This is in contrast to the experiment, where the thermal quench is triggered by $n = 1$ MHD activity when the cooling front reaches the $q = 2$ surface. However, the observed growth rates are consistent with experiments. In the simulation, the $n = 2$ mode grows exponentially with a magnetic field growth rate of $2.16 \times 10^4 \mathrm{s}^{-1}$, or an e-folding time of 46 μs.

The $n = 1$ mode, which grows slightly later, has a magnetic field growth rate of $\gamma_B = 1.12 \times 10^4\ \mathrm{s}^{-1}$, or an e-folding time of 89 μs. This is right in the middle of the experimentally observed $n = 1$ growth times, which ranged from approximately 20–150 μs.

8.4.1 Rotation and locking of modes in simulations

The most important difference between the NIMROD simulation and the observations is the rotation of the mode. In the simulations, the $n = 2$ and $n = 1$ modes remained locked to a particular toroidal phase, which led to a large toroidal radiation asymmetry (as shown in Figure 8-2). This is consistent with the experiment—in fact, the interpretation of the radiation asymmetry as being caused by toroidally asymmetric bulk MHD flow of hot core plasma to the cold, radiative edge was originally proposed by Izzo [7] based on NIMROD simulations—but does not include the important "lighthouse effect" in which the rotating mode causes the brightness feature to rotate around the tokamak.

The mode does not rotate in the simulations precisely *because* of the toroidally asymmetric injection of gas [7]: the "boundary condition" imposed by the radiative power loss caused by the injected impurities sets the phase of the mode. Thus, the NIMROD simulation cannot, at this point, give information about what is setting the rotation rate of the radiation mode

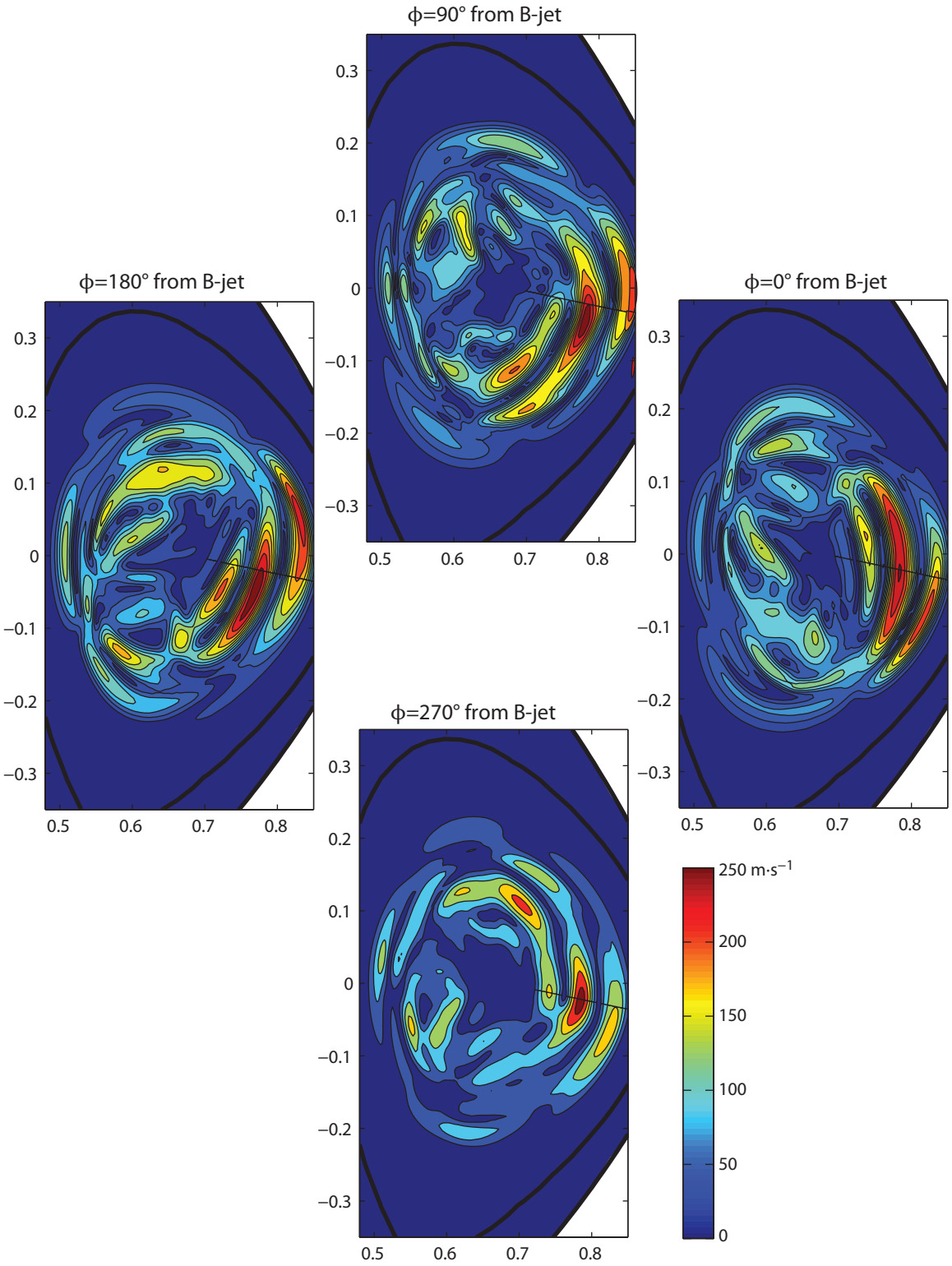

Figure 8-4 – Poloidal MHD bulk velocity (all toroidal Fourier modes included) at four toroidal locations in NIMROD simulation of single-jet MGI rapid shutdown of Alcator C-Mod. Evaluated at $t = 1.51$ ms, at the peak amplitude of the $n = 1$ MHD activity (see Figure 8-5). The thick black line is the last closed flux surface of the pre-disruptive equilibrium.

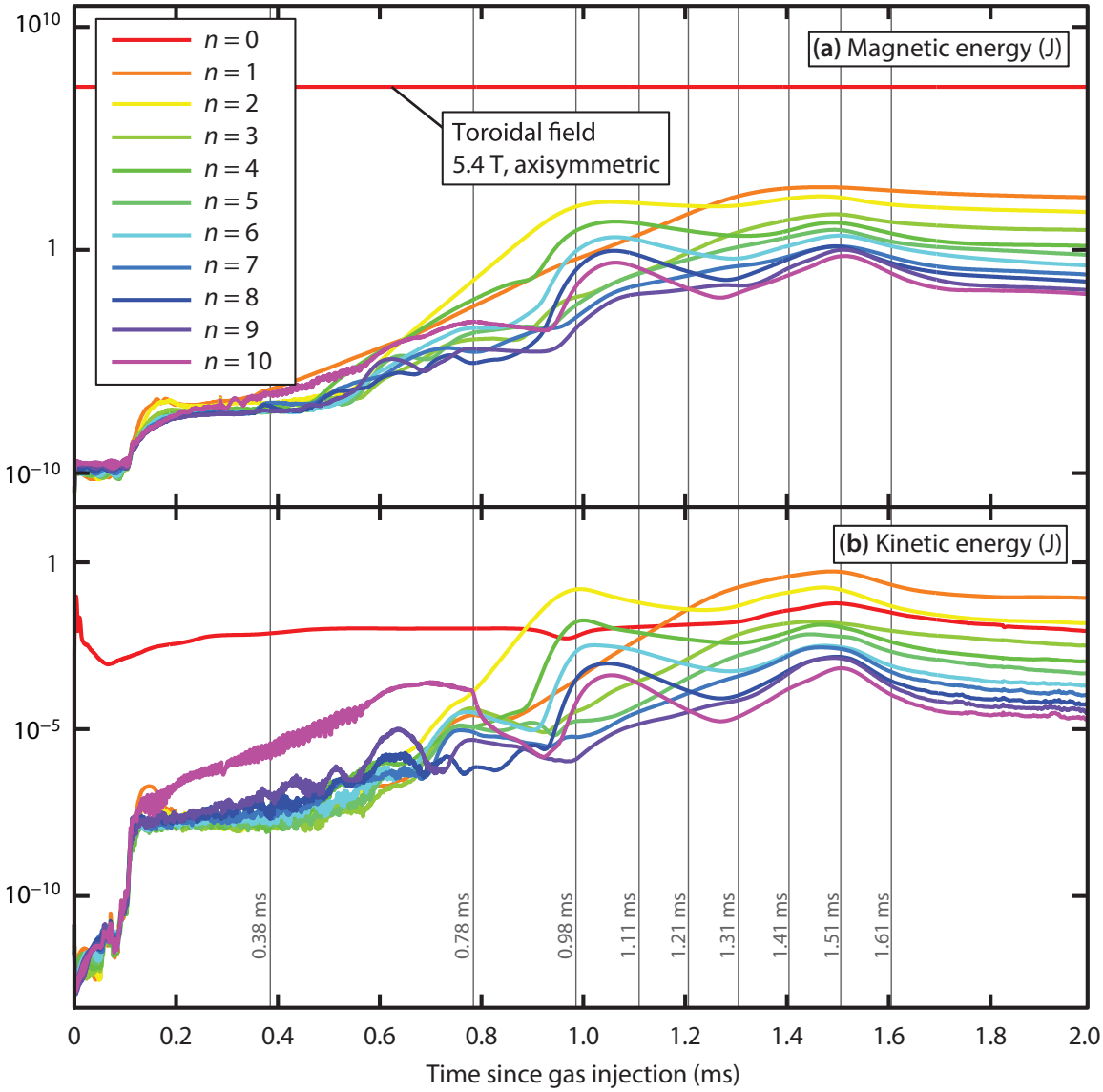

Figure 8-5 – The extended MHD code NIMROD outputs the magnetic and kinetic energy in each toroidal mode in the Fourier expansion. Note the large range of the data (logarithmic y-axis). Vertical lines indicate the times at which the contour plots in Figures 8-1 and 8-3 were evaluated.

in the experiments, nor give insight into what that rotation rate might be in larger machines like ITER.

8.5 Conclusions on extended MHD simulations

A time-dependent extended MHD simulation of a single gas jet MGI rapid shutdown on Alcator C-Mod was conducted using the NIMROD code with the KPRAD closure. The simulation is shown to produce a toroidally peaked radiation profile in the thermal quench because of the toroidally varying pattern of fluid flow produced by an $n = 1$ MHD mode. This is consistent with the experimental observations presented in this thesis.

Another insight gained from the simulation to guide the interpretation of the experimental observations is that the separate MHD "modes" are highly coupled in a shaped, diverted plasma like Alcator C-Mod. While the thermal quench might be *triggered* by a mode which exists at the $q = 2$ resonant surface, one should not expect that this mode remains "pure" through the thermal quench. There will be poloidal flows around the $q = 3/2$ and $q = 1$ surfaces as well. Furthermore, the large-amplitude non-axisymmetric magnetic perturbations cause the magnetic field to become stochastic (destroy the magnetic surfaces), which will cause rapid transport of the core thermal energy even in the absence of bulk MHD flow.

In the next, final chapter of this thesis, the transport implications of stochastic magnetic fields and bulk MHD flow during the thermal quench are discussed. The experimental observations and their interpretation by analytic theory and extended MHD computer simulation are discussed. Finally, the implications of the observations and theory for rapid shutdown and disruption mitigation on future tokamaks are presented, and a simulation of the ITER wall is conducted.

References

[1] Sovinec, C.R. *et al.* (2003). "NIMROD: A computational laboratory for studying nonlinear fusion magnetohydrodynamics." *Physics of Plasmas* **10**(5), 1727–1732. doi:10.1063/1.1560920

[2] NIMROD Team home page. https://nimrodteam.org/

[3] Sovinec, C.R. *et al.* (2004). "Nonlinear magnetohydrodynamics simulation using high-order finite elements." *Journal of Computational Physics* **195**(1), 355–386. doi:10.1016/j.jcp.2003.10.004

[4] Glasser, A.H. *et al.* (1999). "The NIMROD code: a new approach to numerical plasma physics." *Plasma Physics and Controlled Fusion* **41**(3A), A747–A755. doi:10.1088/0741-3335/41/3A/067

[5] Izzo, V.A. *et al*. (2008). "Magnetohydrodynamic simulations of massive gas injection into Alcator C-Mod and DIII-D plasmas." *Physics of Plasmas* **15**(5), 056109 (9 pp). doi:10.1063/1.2841526

[6] Whyte, D.G. *et al*., in *Proceedings of the 24th European Conference on Controlled Fusion and Plasma Physics, Berchtesgaden, 1997* (European Physical Society, Petit-Lancy, 1997), Vol. **21A**, p. 1137.

[7] Izzo, V.A. (2013). "Impurity mixing and radiation asymmetry in massive gas injection simulations of DIII-D." *Physics of Plasmas* **20**(5), 056107 (8 pp). doi:10.1063/1.4803896

Chapter 9

Conclusions and implications

It has been shown that the radiation asymmetry in the thermal quench of gas jet rapid shutdowns on Alcator C-Mod is caused by a toroidally localized brightness feature, which sometimes rotates. When the rotation rate is large enough that the brightness feature rotates more than once around the torus during the thermal quench, then the time-integrated radiation asymmetry is low; when the mode rotates slowly, or does not rotate at all (locks), then the radiation asymmetry is higher. When the brightness feature is locked, the measured radiation asymmetry using a toroidal array of wall-mounted photodiodes has a large variance from shutdown to shutdown, even with identical target plasmas, because of limited toroidal coverage by the diagnostics.

In this chapter, the implications of this work for future machines (ITER and reactors) is discussed, and avenues of future research are suggested.

9.1 Implications for ITER and reactors

The port allocations for the ITER disruption mitigation system have already been decided [1]: a portion of each of three equally-spaced upper ports for "thermal mitigation", *i.e.*, rapid shutdown. (To wit: these ports are #02, #08, and #14 at $\phi = 30°$, 150°, and 270° respectively.) In addition, a portion of equatorial port #08 has been allocated for runaway electron suppression. Thus, it is now imperative to ensure that the ITER rapid shutdown system can reliably and safely radiate the stored thermal energy of a full-performance ITER plasma without large toroidal peaking.

The toroidal asymmetry during the pre-TQ phase is reduced when multiple gas jets are used, because the radiation during this phase is produced simply by the impurities spreading from the injector location. Thus, the goal of reducing localized wall preheating *during the pre-TQ* supports having three gas injectors on ITER. In addition, redundancy is necessary in order to ensure reliability of the rapid shutdown system: because the beryllium wall in ITER can only withstand $\lesssim 10$ unmitigated, full-performance upward VDEs before the wall is removed from service [2, Section 4.2.1], the disruption mitigation system is "mission-critical" and thus there must be redundancy in all parts of the system.

ITER uses beryllium on the first wall outside the divertor because at the time of its design (the Engineering Design Activity in 1992–1998), the ITER parties had little experience with high-Z wall materials such as tungsten or molybdenum. Thus, only carbon (CFC) and beryllium were considered seriously for the bulk of the plasma-facing first wall [3]. Off-normal events were not the main consideration when choosing a wall material, but rather the compatibility of the first wall with routine high-performance plasmas [4]. CFC was eventually eliminated because of concerns about tritium co-deposition, leaving beryllium as the "compromise" candidate. As was discussed in Section 2.8.6, it was assumed at the time that the timescale of rapid shutdown would be very long ($\approx$ 10 ms or longer), and thus wall melting would not be a possibility. It was only much later, after ITER was redesigned to be smaller, that the problem of wall melting *even in the case of a successfully mitigated disruption*, let alone the case of an unmitigated VDE, was fully studied [2].

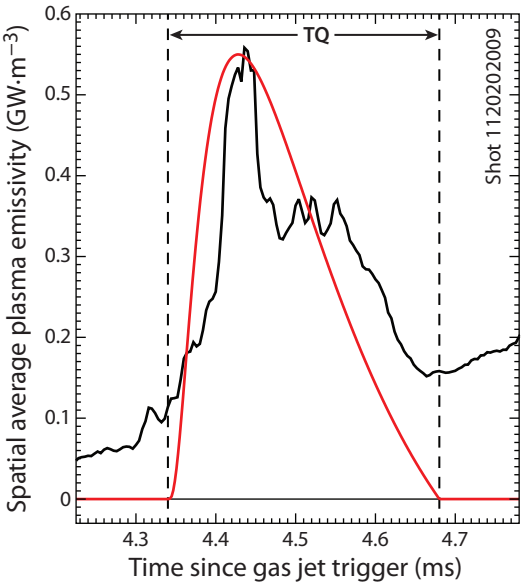

Figure 9-1 – Plasma brightness as measured by photodiodes during the thermal quench of single-jet MGI rapid shutdown of C-Mod shot 1120202009, and log-normal distribution function, which better models the shape of the TQ radiation pulse than a square pulse. Vertical lines represent the start and end of the "initial TQ flash" (see Section 6.5).

9.1.1 TQ radiation waveform

In past studies of disruptions and rapid shutdown on ITER (e.g. [2]), it is usually assumed that the the toroidally averaged irradiance will be constant during the TQ (a "square pulse" waveform). It should be noted that the average plasma brightness as measured by photodiodes through the thermal quench of MGI rapid shutdowns on Alcator C-Mod does not have this shape. A better model for the TQ radiation is a modified version of the probability density function (pdf) of the log-normal distribution [5]:

$$f(\tau) = \frac{A}{\tau\sigma\sqrt{2\pi}} \exp\left(\frac{-(\ln\tau)^2}{2\sigma^2}\right) \times (1-\tau) \tag{9.1}$$

where τ is the time coordinate, normalized to the duration of the TQ: $\tau \equiv (t - t_{start})/\tau_{TQ}$, t_{start} is the time of the start of the TQ, A is the amplitude of the function (set so that the time integral of f matches the actual stored thermal energy of the plasma which is radiated

during the TQ), and σ controls the skewness of the function.[1] Setting $\sigma = 1$ gives a good approximation of the shape of the radiation pulse in the TQ of MGI rapid shutdowns on Alcator C-Mod. This function is undefined for $\tau \leq 0$ and becomes negative for $\tau > 1$; thus it is only used on the interval $\tau \in (0,1)$.

Figure 9-1 shows measured plasma brightness through the TQ of a single-jet MGI rapid shutdown Alcator C-Mod shot 1120202009, as well as the model of TQ radiation (Equation 9.1). It can be seen that the model does not capture the radiation during the CR phase at right: accurate "engineering-quality" modeling of the heating of the wall of a large machine like ITER will require including all phases of the rapid shutdown, including pre-TQ, TQ, CR, and CQ.

9.1.2 Duration of thermal quench

In addition to the assumption about the shape of the waveform of radiation in the TQ, past studies of rapid shutdown on ITER have usually assumed that the thermal quench will have a length of 1 ms. This is based on a scaling of the TQ duration in *unmitigated* disruptions that was conducted for the original ITER Physics Basis. If it is assumed, based on the results presented in this work, that the energy transport in the TQ is actually caused by a large, rotating, saturated magnetic island, then two possible interpretations of how the TQ duration scales to larger machines are suggested.

In the first interpretation, the energy transport from the hot plasma core to the radiative edge during the TQ is caused by parallel thermal transport along stochastic (or "braided") magnetic field lines. This is the case if the magnetic surfaces are fully destroyed during the TQ, an interpretation which is supported by extended MHD simulation (see Chapter 8). This "Rechester–Rosenbluth" diffusion [6] has a diffusion coefficient D_R $[m^2\,s^{-1}]$ that does not scale with machine size, which means that the duration of the thermal quench will scale as the square of the machine size: $\tau_{TQ} \sim a^2 \sim R^2$ at constant plasma aspect ratio ε. This suggests a TQ length on JET of ≈ 7 ms and ITER of ≈ 30 ms, which is far longer than what is actually observed in JET MGI rapid shutdowns. Thus, it is concluded that while there likely exists Rechester–Rosenbluth heat diffusion across destroyed magnetic surfaces during the TQ of MGI rapid shutdowns, a different effect dominates and sets the duration of the TQ.

In this second interpretation, it is assumed that the energy transport in the TQ is due to bulk MHD flows caused by the rotating island. In this case, one would expect $\tau_{TQ} \sim v_\perp/a$, where $v_\perp$ is the bulk flow in the minor-radial direction produced by the MHD activity, and a is the minor radius of the plasma. As was discussed in Section 7.3, theory indicates that for rotating radiative islands, $v_\perp \sim \omega$, that is, the perpendicular flow velocity simply scales like the rotation rate of the island. This produces the peculiar outcome that $\tau_{TQ} \sim R/\omega$, and this the number of mode rotations in the TQ is independent of the rotation rate of the mode:

[1] The variable σ is actually the standard deviation of the variable's natural logarithm, but for the purposes of modelling TQ radiation, it simply controls the shape of the waveform.

$f\tau_{TQ} \sim \omega\tau_{TQ} \sim R$.[2] This would be a favorable result for ITER, however, as was discussed in Section 7.3, there are significant caveats to assuming that this theory applies to the rotating modes in the TQ of MGI rapid shutdowns.

In reality, having confidence in the duration of the TQ in MGI rapid shutdown on ITER will require scaling across a multi-machine database. Massive gas injection systems are now installed on the Alcator C-Mod, DIII-D, ASDEX Upgrade, TEXTOR, and JET tokamaks.[3] A study should be conducted of TQ duration in MGI rapid shutdowns on all these machines in order to build up a database and extrapolate to ITER.

9.1.3 Peak wall temperature on ITER

A 2 + 1 dimensional simulation of the ITER wall was conducted in order to illustrate the effects of a rotating brightness feature during the TQ on the temperature of the wall. The two spatial dimensions were toroidal angle ϕ [rad], depth into the wall x [m]. The ITER baseline $Q \approx 10$, $P_{fus} \approx 500$ MW plasma was assumed to radiate its entire stored thermal energy $W_{th} = 350$ MJ in a TQ duration of 1 ms, with a temporal waveform of the radiation given by Equation 9.1, with the skewness parameter $\sigma = 1$. Thus, integrating the irradiance E_e at the wall over the entire wall surface and the duration of the thermal quench:

$$W_{th} = \iint_{wall} dA \int_0^{\tau_{TQ}} E_e(\phi, t)\, dt \tag{9.2}$$

The equation solved in the wall was the one-dimensional heat equation (Equation 2.4), with material parameters for beryllium from Table 2-1. The boundary conditions were: at the surface ($x = 0$), the heat flux is equal to the irradiance E_e, and in the other direction, $T = T_0$ as $x \to \infty$. The simulation was carried out assuming a starting wall temperature of $T_0 = 590$ K (see Table 2-1) and it was run for 2 ms of time.

The irradiation on the wall is assumed to be peaked purely in the toroidal direction: no poloidal peaking was included. The toroidal radiation peaking was assumed to follow a constant plus a von Mises distribution, which is very similar to a Gaussian distribution but designed to work on a circular domain:

$$f(\phi) = b + a_v \frac{\exp(\kappa \cos(\phi - \mu))}{2\pi I_0(\kappa)} \tag{9.3}$$

with the constants b and a_v chosen to be 0.047 and 5.99 respectively, giving an instantaneous

[2] This is because in this model, a faster-rotating mode produces a proportionatly faster TQ.

[3] Additionally, there is an MGI system on the MAST spherical torus in the U.K., soon to be re-opened as MAST Upgrade, and there are plans to install such a system on the NSTX Upgrade spherical torus at the Princeton Plasma Physics Laboratory.

τ_{TQ} [ms]	$f\tau_{TQ}$	T_{max} [K]
0.5	1.5	2840
0.7	2.1	2243
1.0	3.0	1784
1.2	3.6	1681
1.4	4.2	1579
1.6	4.8	1485
1.8	5.4	1408
2.0	6.0	1360

Table 9-1 – Peak wall temperature obtained on the ITER wall during the simulated thermal quench of an MGI rapid shutdown for various TQ durations. Instantaneous toroidal peaking factor was 3.0 and the brightness mode rotated in the TQ at 3 kHz; $f\tau_{TQ}$ is the number of rotations the brightness mode makes during the TQ. In all cases, the total radiated energy was 350 MJ.

toroidal peaking factor of 3.0, and making the integral of $f(\phi)$ have a value of unity over $\phi \in [0, 2\pi]$. Thus, the toroidally averaged time-dependent irradiance $\bar{E}_e$ could be simply multiplied by this distribution to produce the time-dependent irradiance at every toroidal coordinate ϕ. The width parameter κ (not the same as the plasma elongation κ) was chosen to be 1.86, corresponding to a full-width at half-maximum of the radiation feature of about 70°. The peak location $\mu = \omega t$, so that the mode rotates at $\omega = 2\pi \times 3$ kHz, *i.e.* it rotates three times during the TQ. $I_0(\kappa)$ is the modified Bessel function of the first kind, of order zero. The inputs to the simulation are shown in Figure 9-2.

The results of the simulation can be seen in Figure 9-3. It can be seen that in this simulation, there is surface melting of the beryllium wall over the entire 360° of the tokamak. This is mainly because of the high instantaneous toroidal peaking factor (3.0) and the peaked temporal waveform of the radiation: even though the TQ duration is nominally 1 ms, most of the heat comes out in ≈ 400 μs. The toroidal peaking factor integrated through the entire TQ in this simulation is 1.07.

A scoping study was performed in order to determine the effect of TQ duration on the peak wall temperature, with a constant brightness mode rotation rate of 3 kHz. The results are summarized in Table 9-1. For simulated shutdowns in which the mode made many rotations during the TQ ($f\tau_{TQ} \gtrsim 3$), the peak wall temperature varies approximately as $T_{max} \sim \tau_{TQ}^{-1/2}$, consistent with the prediction of Equation 2.6 for short pulses of heat. This indicates that if the mode rotates many times during the TQ, it effectively causes the wall to behave as if the instantaneous toroidal peaking factor were much lower than its actual value of 3.0.

In order to more clearly show the effect of rotation, two simulations were run with an assumed TQ duration of 1.8 ms, and the same temporal waveform (Equation 9.1) as for the

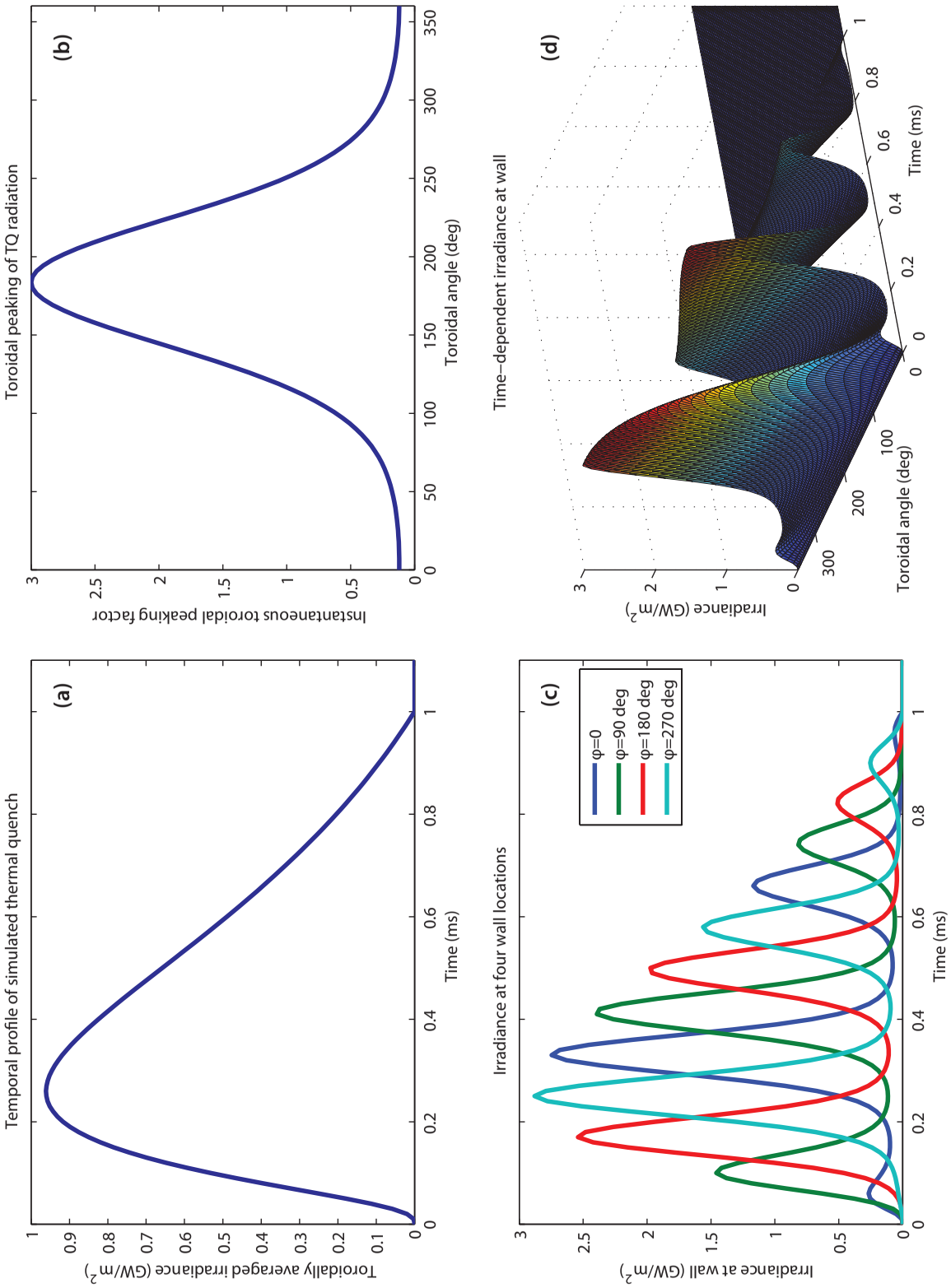

Figure 9-2 – (*Rotated figure.*) **(a)** Temporal waveform of toroidally averaged irradiance during simulated ITER thermal quench with rotating radiation mode; **(b)** Toroidal profile of irradiance (instantaneous TPF is 3.0); **(c)** Temporal profile of irradiance at four different toroidal locations; **(d)** Irradiance versus toroidal location and time, showing mode rotation at 3 kHz in $+\phi$ direction.

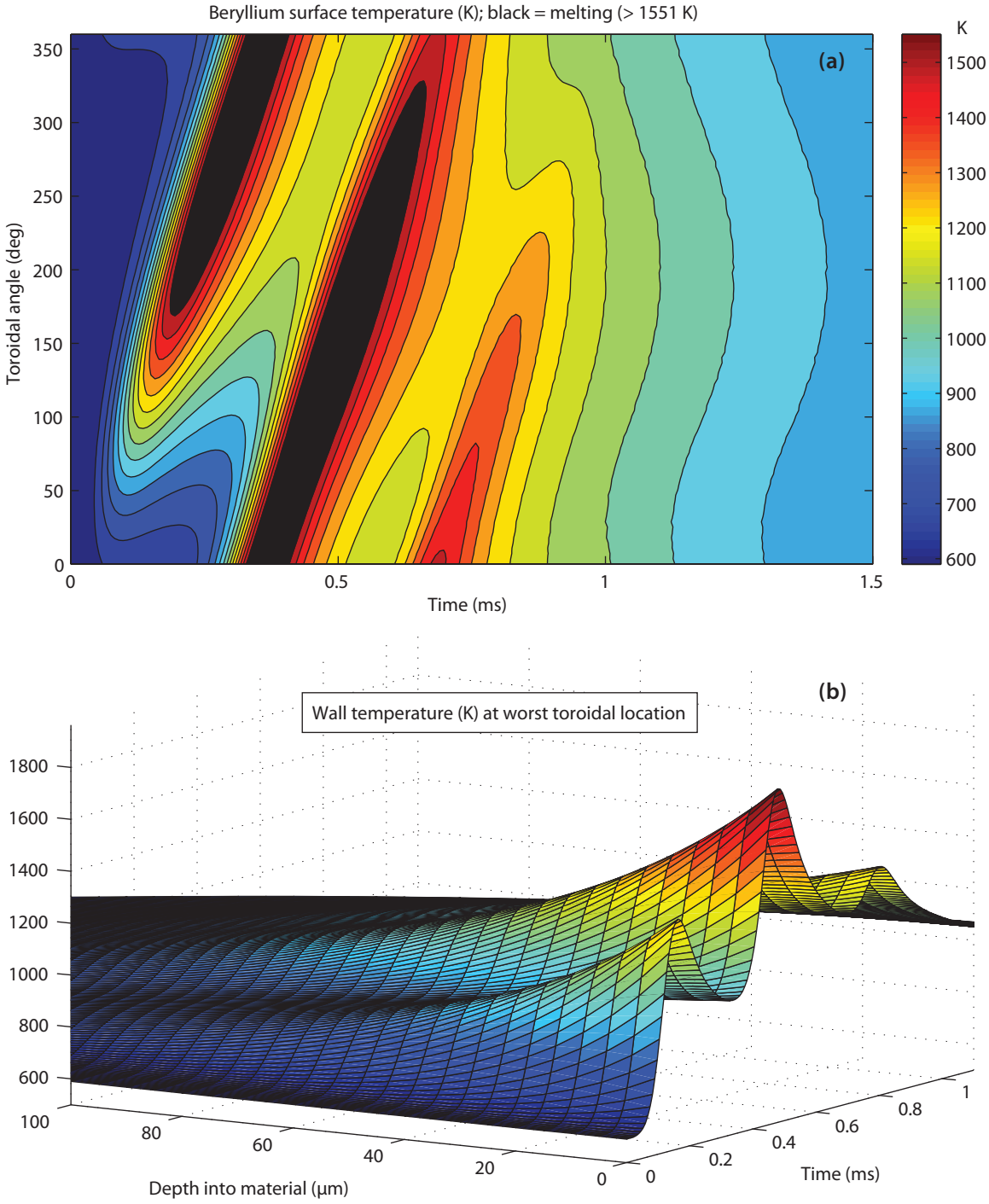

Figure 9-3 – **(a)** Contour plot of ITER wall surface temperature during MGI rapid shutdown with rotating radiation feature. Black shaded areas are molten beryllium. **(b)** Temperature of beryllium versus depth into material and time at worst toroidal location ($\phi = 140°$).

earlier simulations (except stretched in time). In the first simulation, the brightness mode was assumed to rotate at 0.9 kHz, so that its center completed 1.6 rotations during the TQ, and less than one rotation during the brightest part of the TQ radiation temporal waveform. In the second, the brightness mode rotated at 2.7 kHz (three times faster), so that it completed 4.9 rotations during the TQ. The results are shown in Figure 9-4.

It can be seen in panel (a) of Figure 9-4 that if the mode rotates slowly, surface melting is obtained over a significant portion of the beryllium wall. In contrast, if the mode rotates rapidly, then the energy is deposited evenly over the entire wall surface—although it shows up in two or three pulses at each toroidal location as the "spotlight" sweeps by—and the peak wall temperature obtained is below the melting temperature of beryllium.

These simulations are not intended to be a full engineering study of ITER wall behavior in MGI rapid shutdown. Instead, they are intended as a demonstration of the effect that brightness mode rotation can have on peak wall temperature. The peak wall temperature is a function of the instantaneous toroidal (and poloidal) radiation peaking factor, the duration of the thermal quench, and the rate of rotation of the brightness mode. It must be ensured that the ITER MGI rapid shutdown system reliably produces thermal quenches that are in the region of this three-dimensional space where the wall does not melt.

The three simplifications in these simulations which produce the largest inaccuracies are:

i. No poloidal radiation peaking was included; and

ii. If the wall melts, the latent heat of fusion (1.356×10^6 J kg^{-1} for beryllium) means some of the radiant energy would go into melting wall material instead of continuing to heat it. Thus, the simulation slightly overestimates temperature and amount of melting. But because this inaccuracy only exists if there is any melt in the first place, the simulation does correctly answer the question "will there be any wall melting?".

iii. The wall material properties were taken to be those of beryllium at 1000 K (see Table 2-1). Temperature-dependent material properties should be used.

Determining the true risk of wall melting on ITER will require taking into account four factors:

- The wall will be pre-heated because of the plasma discharge, as well as radiation during the pre-TQ phase.[4] In addition, even after the TQ is complete, the wall will continue to be heated by the CQ radiation. The CQ radiation is on a much longer timescale in ITER (see Section 2.8.4), but there is a larger stored poloidal magnetic field energy

[4] As was mentioned in Section 9.1, wall preheating in the pre-TQ is another reason why it is important to have multiple gas injectors: because the radiation in the pre-TQ becomes more symmetric when multiple injectors are used (see Figure 5-6), the use of multiple injectors will reduce concentrated preheating in a single toroidal location.

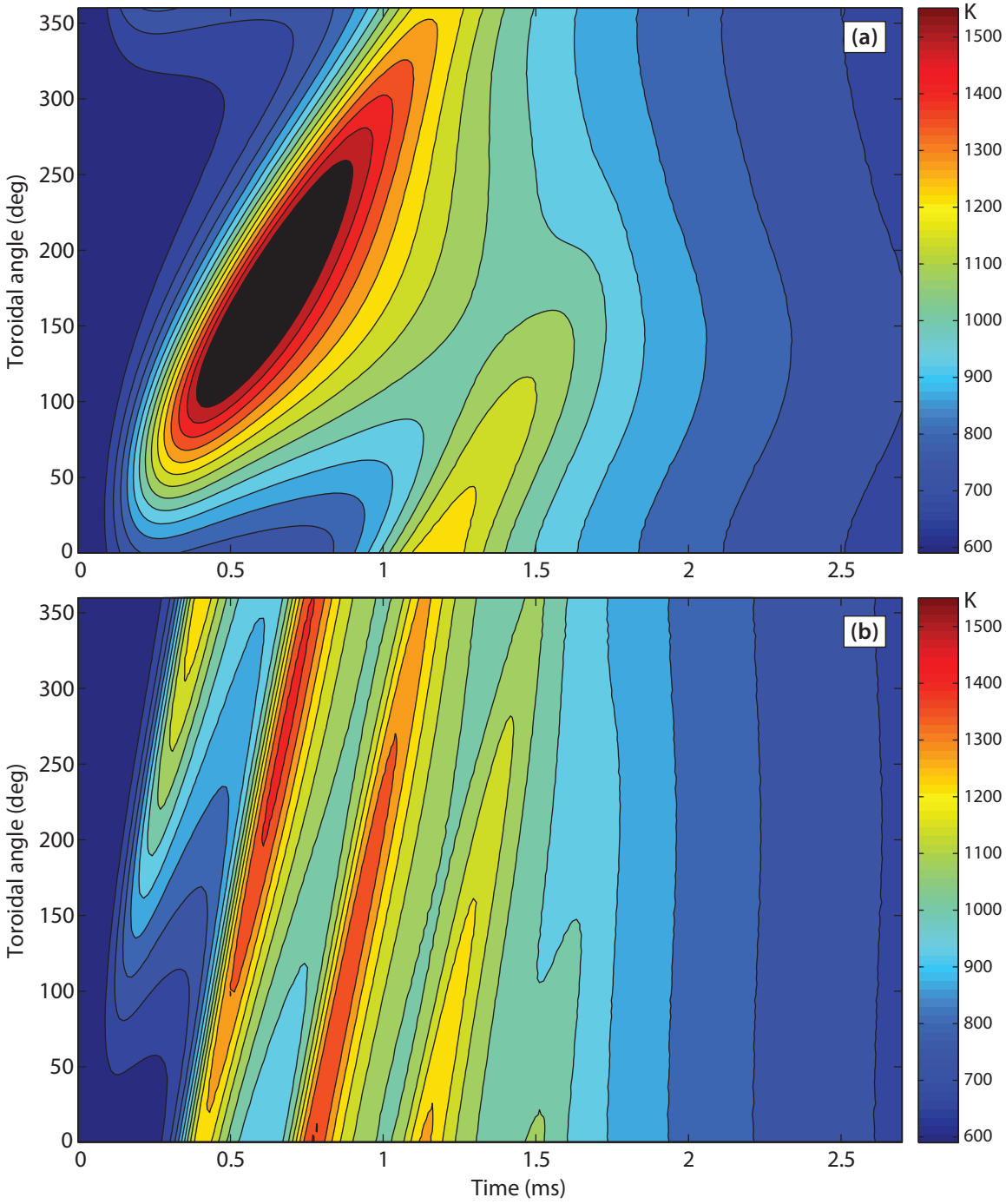

Figure 9-4 – The effect of brightness mode rotation on the peak wall temperature obtained during simulated MGI rapid shutdowns of ITER is shown. **(a)** TQ duration 1.8 ms, and mode rotation 0.9 kHz ($f\,\tau_{\mathrm{TQ}} \approx 1.6$). Surface melting is obtained over nearly half the toroidal extent of the wall. **(b)** The same TQ duration (1.8 ms), but with three times faster mode rotation (2.7 kHz), so that the mode makes ≈ 4.9 toroidal rotations during the TQ. The peak wall temperature obtained is 1430 K, and the wall does not melt.

than stored thermal energy in ITER, and this radiation is applied when the wall has already been preheated by the pre-TQ and TQ radiation, so the CQ radiation should be included in any engineering model of rapid shutdown on ITER.

- The true waveform of radiation during the TQ. Assuming a "square pulse" may be too optimistic.
- The duration of the TQ may be shorter than 1 ms. Scaling studies of MGI rapid shutdown across multiple machines are necessary to improve confidence in the TQ duration estimate.
- A rotating brightness feature should be included in the model in order to assess whether the wall will melt with a radiation pattern which is instantaneously toroidally peaked, but in which the brightness feature rotates rapidly around the machine.

These factors should be included in future engineering simulations of MGI rapid shutdown on ITER. In addition, it is suggested that the possibility of the MGI rapid shutdown system being triggered with plasma stored energy $W_{\mathrm{th}} > 350$ MJ due to thermal instability or "runaway" fusion power, in order to mitigate an inevitable beta-limit disruption (see Section 1.1.2), be considered when engineering the rapid shutdown system.

9.2 Summary of work

Major disruptions, now more commonly known as just "disruptions" have been a feature of tokamaks since the earliest experiments with these devices. Unmitigated disruptions will almost certainly cause damage to ITER and reactors, chiefly localized wall melting and potential stress damage to bolts and members from halo and vessel current forces. Thus, prediction and mitigation of disruptions is essential for future tokamaks. Massive gas injection is a proven technique for the rapid shutdown portion of a disruption mitigation system. Large quantities of high-Z noble gas are injected into the plasma, radiating the stored thermal and poloidal magnetic energy of the plasma over the entire plasma-facing first wall. However, this technique has been observed to produce an asymmetric radiation pattern: the plasma shines brighter in some areas of the wall than in others. A time-integrated peak-to-average brightness ratio, known as a *peaking factor*, of less than approximately 2.0–2.5 is necessary to prevent wall melting on ITER *even in the case of a successful rapid shutdown*.

Two toroidally separated massive gas injectors were installed on Alcator C-Mod, as well as a toroidal array of six wall-mounted photodiodes to observe the radiation in the thermal quench of MGI rapid shutdowns. MGI rapid shutdown experiments were conducted in the 2012 C-Mod experimental campaign. It was observed that the radiation in the TQ, rather than being stationary, often had a rotating brightness feature. The rotation rate of this bright

spot, normalized to the duration of the TQ, sets the time-integrated radiation peaking factor. If the mode rotates more than once during the TQ, then the overall radiation is more symmetric than if the mode rotates slowly, or not at all (locked).

There is a ubiquitous exponentially-growing $n = 1$ magnetic mode observed in the pre-TQ phase of MGI rapid shutdowns. It is suggested that this mode is a radiative tearing mode, which is a magnetic island whose growth is dominated by the impurity radiation term in the extended Rutherford model equation that is used to describe such modes. Existing theory correctly predicts that the radiative island should grow purely exponentially, but overestimates the growth rate of the mode.

Extended MHD modeling using the NIMROD code of an MHD rapid shutdown on Alcator C-Mod suggests that the toroidal radiation asymmetry in the TQ is caused by an $n = 1$ MHD mode convecting heat from the hot core of the plasma to the radiative edge (where the impurities mostly are) preferentially at one toroidal phase. However, in the computer model, the mode does not rotate. It is thus proposed that the rotating radiation feature observed in the TQ of MGI rapid shutdowns on Alcator C-Mod is produced by a rotating, saturated radiative island which is originally produced during the pre-TQ.

It was observed that the radiation feature was always stationary (locked), and the toroidal radiation asymmetry was worst, when the two gas injectors were fired so that the gas arrived at the plasma at close to the exact same time. However, firing one injector approximately 1.0–1.5 ms before the other reliably produced a rotating brightness mode and a low time-integrated radiation asymmetry.

Looking ahead to ITER, it is noted that ensuring that the MGI rapid shutdown system works reliably without a risk of damaging the wall, will probably require ensuring that the MHD mode which produces the brightness feature rotates more than once during the TQ. Furthermore, there is a risk of wall melting even in this case, since the waveform of radiation is not uniform in time. The lessons learned from this work must be taken into account in future engineering studies of disruption mitigation and rapid shutdown on large tokamaks such as ITER or reactors.

9.3 Unique contributions

The work presented in this thesis has contributed the following to the world fusion research program:

- **The first true multi-point measurements of toroidal peaking factor in massive gas injection rapid shutdown**. While the toroidal coverage was limited due to available wall space, no other tokamak has installed a toroidal array of photodiodes to investigate the toroidal radiation peaking in gas jet rapid shutdown.

- **The first observations of massive gas jet rapid shutdown with multiple gas injectors.** All previous published work on MGI rapid shutdown used a single gas injector.
- **The first experimental observations supporting the theory that the radiation asymmetry in the thermal quench is set by low-n MHD modes rather than simply toroidal spreading of gas.** This interpretation is now supported by modelling (extended MHD) as well as experiment.

9.4 Suggested future work and extensions

While this work represents a thorough investigation of the role of magnetohydrodynamic modes in setting radiation asymmetry in the thermal quench of gas jet rapid shutdowns, there are several avenues of research which could extend this work. These next steps could be conducted on Alcator C-Mod or other tokamaks, and would further the understanding of massive gas injection rapid shutdown, and improve the confidence in the ITER disruption mitigation system.

The first is to simply add *more* toroidal coverage. Typically, tokamak diagnostics assume toroidal symmetry, and thus only sample plasma parameters at a single toroidal location. Alcator C-Mod now has the only toroidal array of photodiodes optimized for examining disruption radiation. However, even this array did not cover the entire toroidal direction, because of limitations on wall space (see the photos in Appendix E for some views of how crowded the Alcator C-Mod outer wall is).

A mode with an $n = 1$ structure has a toroidal full width at half maximum (FWHM) of 90° to 180° (approximately 60° if considering an impurity-dominated radiation mode where $\varepsilon \sim n_e^2$). In this case, having detectors every 20–30°—that is, a toroidal array of 12–18 equally-spaced detectors—would ensure that these modes can be accurately resolved, even if they do not rotate during the thermal quench.

An important equipment upgrade if one is to validate results with 100% confidence for ITER will be to have multiple gas injectors with *exactly* the same valve hardware, and ideally at identical poloidal locations. On Alcator C-Mod, the two gas injectors were not identical, and this produced differences in the behavior when the gas jet stagger time was negative (F-jet fired first) or positive (B-jet fired first).

The most important next steps suggested by this work, however, are theoretical. Through a combination of computer modeling and analytic theory, it would be greatly desirable to understand exactly what is setting the radiation mode rotation during the TQ of MGI rapid shutdowns, in order to have confidence that this rotation can be controlled. In the absence of a validated theory, however, multi-machine database studies of MGI rapid shutdown should be conducted, in order to extrapolate quantities like mode rotation frequency or the duration of the thermal quench to ITER.

Future MGI rapid shutdown experiments on Alcator C-Mod should take the following suggestions into account:

- Vary q_{95} by changing the plasma current instead of by changing the toroidal field, so that the ECE radiometry can get the temperature at the location of the growing island. This will give a quantitative test of the RTM growth rates. Changing the plasma current will change the plasma poloidal magnetic field energy, but this does not appear to affect the mode rotation rate or radiation asymmetry in any case.
- Re-install the "halo Rogowskis" and have them operating at the same time as the wall-mounted toroidal photodiodes. This will help answer the question of whether the rotating halo current mode in the CQ is the same as the rotating brightness mode in the TQ.
- Install parallel digitizers for the fast magnetics pickup coils (Mirnov coils) at a lower gain, in order to resolve the magnetics signal through the CR phase of the MGI rapid shutdown, when the $\mathrm{d}B/\mathrm{d}t$ signal attains a huge amplitude and saturates the coils with their current setup.

9.5 Concluding remarks

It is hoped that this work can inform the engineering design of the essential disruption mitigation system on ITER and on future fusion reactors, and hasten the development of fusion energy for the benefit of humanity. Following this chapter, there are several appendices with additional information for other researchers seeking to replicate these results on other tokamaks.

References

[1] Baylor, L.R. *et al.* (2013). "ITER disruption mitigation system conceptual design review highlights – options for ITER." Presentation for ORNL VLT conference call, January 16, 2013. Slides available online at http://vlt.ornl.gov/research/20130116_Baylor.pdf

[2] Sugihara, M. *et al.* (2007). "Disruption scenarios, their mitigation and operation window in ITER." *Nuclear Fusion* **47**(4), 337–352. doi:10.1088/0029-5515/47/4/012

[3] R.R. Parker, personal communication, July 23, 2013.

[4] Barabash, V. *et al.* (1996). "Selection, development, and characterisation of plasma facing materials for ITER." *Journal of Nuclear Materials* **233-237**, Part 1, 718–723. doi:10.1016/S0022-3115(96)00323-6

[5] Chapter 14 "Lognormal distributions" in Johnson, N.L., Kotz, S., and Balakrishnan, N., *Continuous Univariate Distributions, Vol. 1*, 2nd ed. Wiley Series in Probability and Mathematical Statistics: Applied Probability and Statistics. New York: John Wiley & Sons, 1994. ISBN 978-0-471-58495-7.

[6] Rechester, A.B. and Rosenbluth, M.N. (1978). "Electron heat transport in a tokamak with destroyed magnetic surfaces." *Physical Review Letters* **40**(1), 38–41. doi:10.1103/PhysRevLett.40.38

Appendix A

Table of symbols

Symbol	Description	SI unit	Typical value
${}^{2}_{1}\mathrm{D}$	Nuclear symbol for deuterium	—	—
${}^{4}_{2}\mathrm{He}$	Symbol for helium nucleus (α particle)	—	—
${}^{1}_{0}\mathrm{n}$	Nuclear symbol for the neutron	—	—
${}^{3}_{1}\mathrm{T}$	Nuclear symbol for tritium	—	—
A	Area	m^2	—
A_{wall}	Total area of plasma-facing first wall	m^2	10–1000
B_θ	Poloidal magnetic field (a.k.a. B_{pol})	T	0.1–2
B_ϕ	Toroidal magnetic field (a.k.a. B_{tor})	T	2–8
C_{p}	Specific heat capacity of wall material	$\mathrm{J\,kg^{-1}\,K^{-1}}$	3.7×10^2
D_{R}	Rechester–Rosenbluth diffusion coefficient	$\mathrm{m^2\,s^{-1}}$	—
E_{e}	Total irradiance	$\mathrm{W\,m^{-2}}$	10^8
g	Nondimensional constant in dimensional version of Troyon beta limit	—	0.025
H_{e}	Radiant exposure	$\mathrm{J\,m^{-2}}$	$10^5\ \mathrm{J\,m^{-2}}$
I_{p}	Plasma current	A	1.0×10^6 (C-Mod)
J	Plasma current density	$\mathrm{A\,m^{-2}}$	1.0×10^6
k	Thermal conductivity of wall material	$\mathrm{W\,m^{-1}\,K^{-1}}$	90
$L_{\mathrm{rad}}(T)$	Temperature-dependent impurity line radiation coefficient	$\mathrm{W\,m^3}$	5×10^{-31}
m	Poloidal mode number (Fourier harmonic) of MHD modes	—	1–3
n_{D}	Density of deuterium ions	$\mathrm{m^{-3}}$	1×10^{20}
n	Toroidal mode number (Fourier harmonic) of MHD modes	—	0–2

Table of symbols continues on next page…

…Table of symbols continues from previous page

Symbol	Description	SI unit	Typical value
n, n_e	Plasma electron density	m^{-3}	1.5×10^{20} (C-Mod)
$\bar{n}_e$	Line-averaged electron density	m^{-3}	1.5×10^{20} (C-Mod)
$\langle n_e \rangle$	Volume-averaged electron density	m^{-3}	1.0×10^{20} (C-Mod)
$n_{e,\,max}$	Maximum electron density (density limit)	m^{-3}	6×10^{20}
n_{cs}	Density of charge state	m^{-3}	10^{20}
n_T	Density of tritium ions	m^{-3}	1×10^{20}
p	Plasma kinetic pressure	Pa	2.0×10^5 (C-Mod)
$\langle p \rangle$	Volume-averaged plasma pressure	Pa	0.5×10^5 (C-Mod)
P_{rad}	Total radiated power from plasma	W	10^9
PF	Peaking factor	—	3.0
q	Magnetic safety factor	—	2–10
q^*	Cylindrical safety factor	—	2–10
q_{95}	Safety factor at 95th percentile flux surface	—	2–10
$\vec{q}$	Vector heat flux in heat equation	$W\,m^{-2}$	—
R, R_0	Plasma major radius	m	0.5–8
S_f	Fusion power density	$W\,m^{-3}$	1×10^6 (ITER)
t	Time	s	—
t_{stag}	Gas jet stagger time	s	1×10^{-3}
T	Wall material temperature	K	—
T_0	Wall temperature at start of TQ	K	600
T, T_e	Plasma electron temperature	J	3×10^{-16}
T_{melt}	Wall material melting temperature	K	2820
TPF	Toroidal peaking factor	—	3.0
W_{th}	Plasma thermal energy	J	1×10^5 (C-Mod)
W_p	Plasma poloidal magnetic field energy	J	1×10^6
x	Distance into wall for one-dimensional heat transfer	m	10^{-6}
Z	Vertical coordinate	m	—
Z	Ion charge	—	1 (deuterium)
Z_{cs}	Charge of particular charge state	—	0–18
Z_{eff}	Plasma effective charge state	—	1–3
α	Alternate symbol for helium nucleus	—	—

Table of symbols continues on next page…

…Table of symbols continues from previous page

Symbol	Description	SI unit	Typical value
α	Thermal diffusivity	$m^2\,s^{-1}$	—
β	Plasma beta	—	0.02
β_N	Normalized beta	%	1–3
β_θ	Poloidal beta	—	0.6
γ	Growth rate (general)	s^{-1}	—
γ_B	Growth rate of perturbed magnetic field	s^{-1}	2×10^4
γ_E	Growth rate of mode energy	s^{-1}	4×10^4
γ_w	Growth rate of island width	s^{-1}	1×10^4
Δ'	Classical tearing mode stability index	—	−0.5
δ	Plasma triangularity	—	0–1
δ_L	Lower plasma triangularity	—	0.55
δ_U	Upper plasma triangularity	—	0.35
ε, ε_{rad}	Plasma emissivity	$W\,m^{-3}$	1×10^9
ε_0	Electric constant	$F\,m^{-1}$	$\approx 8.854 \times 10^{-12}$
$\bar{\varepsilon}_{rad}$	Average plasma emissivity	$W\,m^{-3}$	1×10^9
$\tilde{\varepsilon}_{rad}$	Net plasma emissivity in island	$W\,m^{-3}$	1×10^8
η	Plasma electrical resistivity	$\Omega\,m$	5×10^{-6}
θ	Poloidal coordinate	rad	$0–2\pi$
κ	Plasma elongation	—	1.0–1.8
λ	Wavelength	m	—
μ_0	Magnetic constant	$H\,m^{-1}$	$4\pi \times 10^{-7}$
ν	Frequency (photons)	Hz	—
ρ	Normalized minor radius	—	0–1
ρ	Material density	$kg\,m^{-3}$	1×10^4
τ	Time scale (general)	s	—
τ_{CQ}	Current quench duration	s	$\approx 10^{-3}$ (C-Mod)
τ_{TQ}	Thermal quench duration	s	4×10^{-4} (C-Mod)
Φ	Radiant flux	W	—
ϕ	Toroidal coordinate	rad	$0–2\pi$
ψ	Poloidal flux	Wb	−0.1–0.5 (C-Mod)
Ω	Solid angle	sr	—

THIS PAGE INTENTIONALLY LEFT BLANK

Appendix B

Definitions of selected terms

B-jet. The gas injector installed at B-port in Alcator C-Mod. One of two gas injectors on the machine for the 2012 experimental campaign. This was the original gas jet installed in 2005. See also **F-jet**.

Current rearrangement phase. Phase of an MGI rapid shutdown proposed in this work. This phase is between the end of the thermal quench, marked by the fall of core soft X-ray emissivity to near zero, and the beginning of the current quench, marked by the peak of the measured plasma current (which indicates that the plasma current profile has flattened). See Section 6.5.

Current quench. The final phase of an unmitigated disruption or a rapid shutdown, in which the cold, resisitve plasma ramps down on its L/R timescale.

Disruption mitigation. The entire system on a tokamak in which an inevitable disruption has its effects ameliorated. One part of a disruption mitigation system is **rapid shutdown**.

F-jet. The gas injector installed at F-port in Alcator C-Mod for the 2012 experimental campaign. See also **B-jet**.

Fast magnetics. Mirnov coils, used for measuring the time derivative of the local poloidal magnetic field $\dot{B}_\theta$ at a fast digitization rate (2.5 MHz).

Island. See **Magnetic island**.

Magnetic island. When a non-axisymmetric perturbation is added to an axisymmetric toroidal plasma, the magnetic surfaces are distorted so that a secondary, three-dimensional separatrix appears inside the toroidal plasma. This is known as a "magnetic island". Such islands can be produced spontaneously if the plasma current profile is too steep; this is known as a **tearing mode**.

Massive gas injection. Rapid shutdown technique for fusion devices in which large quantities of high-Z noble gas are injected into the plasma in order to radiate the plasma stored energy (thermal + poloidal magnetic) over a large fraction of the plasma-facing first wall. This technique, along with injection of large shattered "killer" pellets, are the leading candidates for the rapid shutdown system in ITER.

Mirnov coils. See **Fast magnetics**.

NIMROD. Computer code for global time-dependent nonlinear extended MHD simulation of fusion plasmas. See Chapter 8.

Peaking factor. The ratio of the peak irradiance (or radiant exposure) at the wall to the average irradiance (or radiant exposure). This gives a measure of the severity of radiation asymmetry in the thermal quench of an MGI rapid shutdown of a tokamak plasma.

Pre-thermal quench (pre-TQ). The initial phase of a rapid shutdown, in which the injected impurities are cooling the edge of the plasma. This phase ends when the cooling front gets to the $q = 2$ surface, at which point an $m = 2$, $n = 1$ MHD mode is destabilized, which grows and triggers the thermal quench (TQ).

Radiative tearing mode. An exponentially-growing magnetic island in a tokamak plasma, defined by the radiative term in the extended Rutherford model of neoclassical resistive islands being dominant over all other terms.

Rapid shutdown. The process by which a tokamak plasma is rapidly terminated, ideally dissipating its energy radiatively over the entire plasma-facing first wall. This term is used in this work instead of the more common *disruption mitigation* in order to emphasize that a rapid shutdown system is simply one component of a disruption mitigation system.

Tearing mode. Resistive plasma instability driven by the energy in a current gradient (which is usually measured in a tokamak by the magnetic shear $s \equiv (r/q)\,\mathrm{d}q\,\mathrm{d}r$. Produces a magnetic island on a resonant surface. There are several terms in the Rutherford model, which describes the nonlinear evolution of the width of the tearing-mode island. If the radiative term dominates, then the instability is known as a **radiative tearing mode**.

Thermal quench. During this phase of a rapid shutdown, the plasma thermal energy is rapidly lost by radiation. Because the impurities are still largely in the edge of the plasma at this time (a "radiative mantle"), the thermal quench consists of energy being transported from the hot plasma core to the radiative, cold plasma edge. It is proposed in this work that the same MHD flow which causes this energy transport produces the rotating brightness feature which controls the radiation asymmetry.

Appendix C

Disruption mitigation miniproposals

On the following pages are reproduced the two Alcator C-Mod miniproposals relating to disruption mitigation and rapid shutdown which were written by Geoffrey M. Olynyk. Miniproposals are the method by which experimental time (run-time) is granted on the Alcator C-Mod tokamak by the Experimental Planning Committee (EPC). Further information is given in Table 4-1.

Miniproposal 675: 8 pages
Miniproposal 714: 7 pages

Alcator C-Mod

Mini-Proposal

MP No. 675

Subject: **Initial disruption mitigation experiments with two gas jets**

From: G.M. Olynyk, R.S. Granetz, D.G. Whyte, M.L. Reinke, I.H. Hutchinson

Group: Disruption mitigation

Date: November 11, 2011

Approved by: **Date approved:**

1 Purpose of experiments

Include immediate goal of the experiments, scientific importance and/or programatic relevance. Refer to any relevant program milestones or ITER R&D commitments. This is the "sales pitch" for your use of a C-Mod run day.

The goal of this experiment is twofold: (1) to commission the second disruption mitigation gas jet; and (2) to begin to study the performance of the Alcator C-Mod disruption mitigation system with the second gas jet installed, especially as regards the toroidal radiation asymmetries observed in earlier gas jet experiments. This miniproposal continues an ongoing line of research [1, 2, 3, 4, 5, 6] into massive gas jet disruption mitigation (MGI-DM), aimed at understanding the physics of what occurs during a mitigated disruption, and informing the design of disruption mitigation systems for ITER and for future reactors.

2 Background

Discuss physics basis of the proposed research, prior results at Alcator or elsewhere, and any related work being carried out separately (in other Alcator C-Mod miniproposals).

2.1 Tokamak disruptions

Major disruptions (today usually just called "disruptions") are events in tokamak plasma discharges in which the stored thermal energy of the plasma is suddenly lost (over $\approx$ ms timescales, $\ll \tau_E$) and not recovered by re-heating; the toroidal plasma current then resistively ramps down on approximately an L/R timescale. The loss of stored energy (plasma pressure) is known as the "thermal quench" (TQ), and the subsequent ramping-down of plasma current is known as the "current quench" (CQ). In tokamaks today, disruptions are a common event, with a significant fraction of plasma discharges ending this way [1]. (This fraction is known as "disruptivity.")

Due to its general definition (roughly: any event that suddenly ends the plasma discharge with a loss of stored thermal energy and subsequent termination of the plasma current), there are many classes of disruptions, such as density-limit disruptions (thought to be a radiative instability), stability limit disruptions (in which a parameter like β or q crosses a stability limit), or vertical displacement events (VDEs, in which control of the vertical position of the plasma column is lost). In all cases, the stored thermal (pressure) and magnetic (current) energy in the plasma can be deposited onto localized plasma-facing surfaces. In shaped plasmas, this deposition is often localized to the divertor region due to the heat conducting down field lines in the scrape-off layer to the divertor, or due to vertical position control being lost (either after the TQ, or in the case of a VDE, before/simultaneous with the TQ).

This localized deposition of energy—nearly 1 MJ in C-Mod, and scaling as R^3 to larger machines—has the potential to cause PFC damage in ITER and in reactors, requiring unscheduled maintenance to remove the leading edges that are created due to melting of high-Z metallic PFCs. In addition, currents flowing in the cold, force-free plasma ($\vec{J} \times \vec{B} \approx 0$) short out through the vacuum vessel, causing "halo currents" to flow, which interact with the toroidal magnetic field and produce large loads on the vacuum vessel and divertor components.

2.2 Disruption mitigation

Because of the potential damage to plasma-facing surfaces from unmitigated disruptions, research has proceeded into how to mitigate their effects. Several techniques have been developed, such as "killer pellet" injection, shattered pellet injection, liquid jet injection, or the technique used on Alcator C-Mod, massive gas jet disruption mitigation (MGI-DM).

On Alcator C-Mod, the MGI-DM system consists of a high-pressure gas plenum connected by a fast valve and a simple length of stainless steel pipe to the edge of the plasma. When the system is triggered[1], a large amount of gas ($> 10^{23}$ electrons, typically a mixture of 85% Ar + 15% He) is injected suddenly into the plasma, which triggers a disruption.

The difference is that this *induced* disruption repeatably radiates the stored energy of the plasma over the *entire* first wall. The addition of such a large amount of highly radiative species (argon) along with the helium to increase the sound speed of the delivered gas [6], quickly reduces the plasma temperature to 5–10 eV, increasing the resistivity of the post-TQ plasma and thus decreasing the duration of the CQ. Time traces of some key parameters during a gas jet mitigated disruption (C-Mod shot 1090925014, part of MP 567) are shown at right in figure 1.

The C-Mod disruption mitigation system has been upgraded in the Summer 2011 opening, and now consists of two independent gas jets,

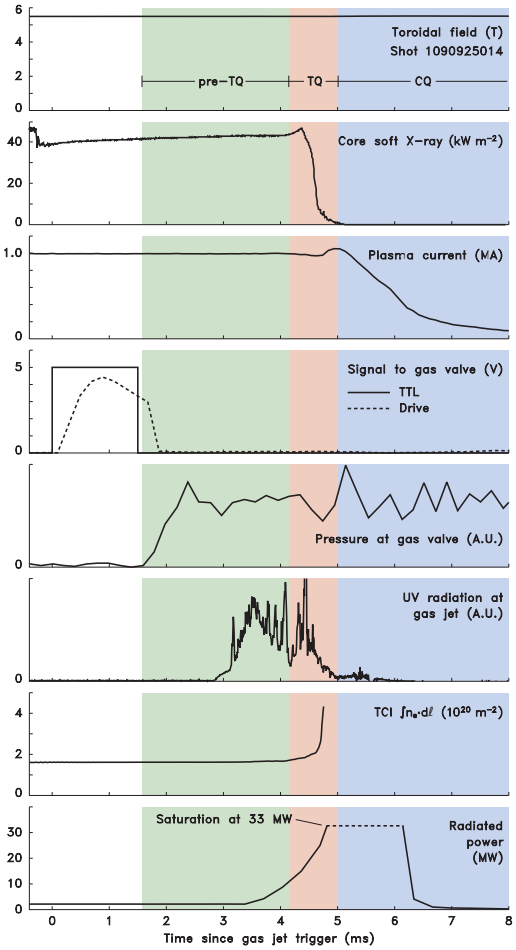

Figure 1 – Time traces of key parameters during a gas jet mitigated disruption on Alcator C-Mod. From top: toroidal field (which remains unchanged at its pre-disruption value of 5.4 T throughout the disruption); core soft X-ray emission (a proxy for core plasma temperature); plasma current; the logic signal and actual drive voltage measured at the fast gas valve; pressure in the gas jet tube just downstream from the fast gas valve; radiation measured by an AXUV diode in a chord passing through the plasma just in front of the gas jet mouth; line-integrated plasma density measured by two-color interferometry; and radiated power measured by the 2π bolometry diode. Phases of the disruption (pre-TQ, TQ, and CQ) are colored in green, red, and blue respectively.

[1] On Alcator C-Mod, the disruption mitigation system is currently pre-programmed. In "disruption prediction" experiments, and in future reactors, the mitigation system will be triggered by the plasma CODAC and/or machine protection systems. These experiments are not currently performed on C-Mod.

each able to be charged with their own gas mixture and triggered at independent times. The goal of this experiment is to commission the new gas jet equipment, but also to compare the behavior of mitigated disruptions using both gas jets to that of mitigated disruptions triggered by the original, single gas jet.

2.3 Radiation asymmetry in mitigated disruptions

It has been found in experiments on Alcator C-Mod and elsewhere that the energy is not radiated *evenly* over the entire plasma-facing surface during gas jet mitigated disruptions: it has significant toroidal and poloidal asymmetries [4]. Mitigated disruptions on C-Mod are investigated using the diagnostics shown in figure 2.

The yellow-shaded chords in the `AXA` and `AXJ` arrays in figure 2 have been used in past experiments [7] to diagnose the radiation asymmetry. When the total time-integrated radiation seen through the entire disruption (TQ and CQ) is compared between `AXA` and `AXJ`, ratios varying from 1.1–2.4 are seen, with `AXA` always receiving more radiation (likely because the `AXA` chords "see" the gas jet, while the `AXJ` chords look the other way). Figure 3 shows time traces of the radiation power seen on the two diode arrays for a very symmetric, and a highly asymmetric disruption mitigation experiment.

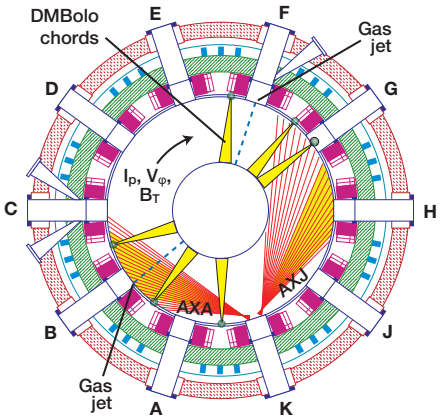

Figure 2 – Disruption mitigation system and relevant diagnostic systems on Alcator C-Mod. `ECE` is second-harmonic X-mode electron-cyclotron emission diagnostic; `XTomo` is soft X-ray tomography array; `AXA` and `AXJ` are arrays of AXUV diodes. Green circles at edge of plasma represent fast magnetics pickup coils (B_p coils) used for identifying the toroidal mode number (n) of magnetics modes during the pre-thermal quench phase of mitigated disruption.

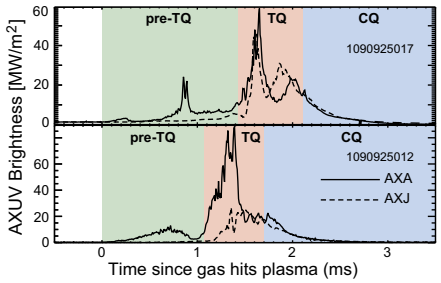

Figure 3 – Comparison of radiation seen on AXUV diode arrays `AXA` and `AXJ` for two disruption mitigation shots. At top, a mitigated disruption with a high degree of symmetry ($\int$`AXA`/$\int$`AXJ` = 1.16) and at bottom, a highly asymmetric mitigated disruption ($\int$`AXA`/$\int$`AXJ` = 2.39).

It should be noted that the AXUV diodes used to diagnose radiation asymmetry in these experiments have reduced sensitivity between approximately 400 and 50 nm wavelength (violet visible light to vacuum UV). Thus, the radiation asymmetry seen by the AXUV diodes does not serve as proof of the absolute total radiation asymmetry. However, the total time-integrated radiation energy seen by a 2π bolometer of the gold-on-kapton foil type [8] is assumed to correlate with the time-integrated radiation seen by a 2π AXUV diode (known as the "2π bolometer diode") and thus that the radiation during mitigated disruptions seen by the AXUV diodes is a good proxy for the total radiation across the entire spectrum.

The issue of radiation asymmetry in mitigated disruptions is extremely important for ITER, since it is estimated that a peak-to-average ratio of the radiated power during the TQ of 2 or greater could lead to localized beryllium first wall melting [9].

One of the main goals of the second gas jet system installed on Alcator C-Mod (see section 2.4) is to determine if using multiple gas jets (or by phasing the multiple gas jets, using different gases in each one, etc.) can reduce the radiation asymmetry. This is in addition to the other interesting science that can come out of the use of multiple gas jets, such as its effect on halo currents, TQ and CQ duration, radiated energy fraction (that is, the fraction of plasma stored energy that is radiated during the mitigated disruption), etc.

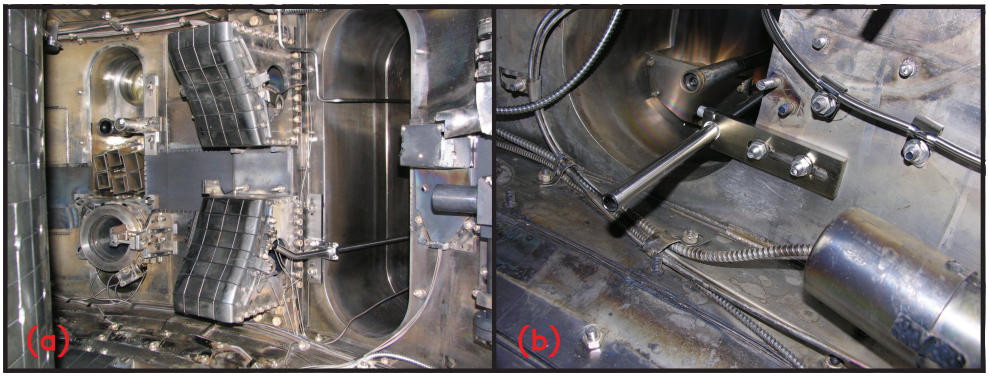

Figure 4 – (a) Original gas jet at B-port; (b) New gas jet at F-port

2.4 The second gas jet system

The second gas jet system, essentially an identical copy of the first one, albeit at a slightly different poloidal location due to equipment constraints (see figure 5) has been installed at F-port during the Summer 2011 opening. Photographs of the original gas jet (at B-port) and the new one (at F-port) are shown in figure 4.

See miniproposal 424 [10] for additional information about the rationale for the gas jet disruption mitigation system. In general, this experiment aims to begin to test all of the elements of an effective gas jet disruption mitigation system with both one and two gas jets:

- Reduction of halo currents vs. unmitigated disruptions
- Radiated energy fraction
- Current quench duration
- Radiated energy asymmetry
- Pre-thermal quench duration
- Presence of MHD modes during pre-TQ phase (and the link to the radiated energy asymmetry [5])

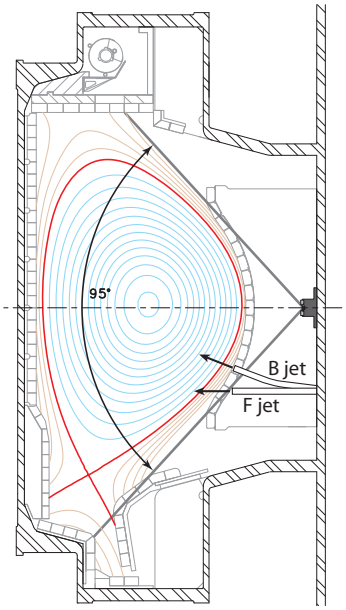

Figure 5 – Poloidal location of gas jets and new DMBolo diagnostic.

3 Approach

What your experiment will actually do, and why you will do it that way. Describe the methodology to be employed and explain the rationale for the choice of parameters. Describe the analysis techniques to be employed in interpreting the data, if applicable. If the approach is standard or otherwise self-evident, this section may be absorbed into the Experimental Plan.

For these initial experiments with one and two gas jets, we will run a typical, non-disruptive 800 kA, 5.4T fiducial target plasma, with RF heating in the second phase (not required in the first phase). We will pre-emptively fire in gas jets using the now-standard 85% He + 15% Ar disruption mitigation gas. It is anticipated that several shots will be required to set the timing of the gas jets relative to each other.

In addition, the new disruption mitigation bolometry (DMBolo) system will likely need adjustments (to transimpedance gain) after each of the first few shots.

We will then study how the thermal and current quench times, vertical and horizontal plasma motion, halo currents, and radiated energy efficiency ($W_{\rm rad}/W_{\rm th}$) are affected by the use of one or two gas jets, and the relative timing between the two gas jets. Most importantly, the DMBolo system will collect information about the toroidal asymmetry in the radiated energy during the mitigated disruption.

I-mode target plasmas are specified for the second (RF-heated) phase of this experiment because of their greater reproducibility of target conditions at the time of the gas jet firing compared to H-modes.

4 Resources

4.1 Machine and plasma parameters

Give values or range for all of the following:

Toroidal field **Plasma current**	5.4 T 800 kA
Working gas species	Deuterium (D_2)
Density	$\bar{n}_{\rm e} \approx 1.5-2.0 \times 10^{20}$ m^{-3} $n\ell 04 \approx 0.8-1.2 \times 10^{20}$ m^{-2}
Equilibrium configuration (if possible, refer to database equilibria)	Reference shot 1110113020 (LSN for L-mode) 1110323027 (USN for I-mode if RF available)
Pulse length, typical current and density waveforms, etc. (refer to database or sketch desired waveforms)	As in shot 1110113020 or 1110323027.
Boronization required? (if yes, specify whether overnight or between-shot, how recently needed, and any special conditions.)	If RF is available, run any time after the first boronization of the campaign. If no RF available, boronization is not required.

4.2 Auxiliary systems

List requirements for the following Alcator C-Mod auxiliary systems:

ICRF (power, pulse length, phasing)	Not required for inital L-mode experiments; for I-mode targets, request 1.0–3.0 MW, turning on at $t = 0.6$ s, until (induced) disruption at $t = 1.0$ s
LHCD (power, pulse length, phasing)	Not required
Pellet injection (list species)	N/A
Impurity injection (laser blow-off)	Not required.
Diagnostic neutral beam	Not required.
Special gas puffing	Disruption mitigation gas jets at B-port and F-port with 85% He / 15% Ar gas mixture
Cryopump	Not required
Non-axisymmetric coils (list connections and current)	Not required
Other	None

4.3 Diagnostics

List required diagnostics, and any special setup or configuration required, e.g. non-standard digitization rate.

Only a base set of diagnostics (magnetics, TCI) will be *required*, however, Thomson, fast ECE (FRCECE), fast CXRS, and IR imaging are desired if possible. The full set of bolometric diagnostics (foil bolometers and AXUV diodes, both 2π and radial), plus the DMBolo system (disruption mitigation AXUV diodes), and the fast magnetics pickup coils should be operational.

Sensitive diagnostics should have their gate valves or shutters closed prior to this run to avoid damage due to the large pressure pulse created by the gas jet injectors.

4.4 Neutron budget

Estimate the neutron dose rate at the site boundary. Give basis for estimate (e.g. refer to previous shots).

Based on the target shot planned to be used for the initial phase of this run (1110113020, with no RF heating), it is anticipated that the neutron production rate will be below 1.0×10^{11} s^{-1}, and thus total neutron production for the day will be very low.

If RF is available and the I-mode target shot (1110323027) is used, the neutron production should be approximately 0.6–1.0×10^{13} s^{-1} during ICRF operation (from 0.6–1.0 s during each shot). Thus, total neutron production for the day (20 useful shots) should stay below the occupational warning limit of 10^{14} neutrons.

5 Experimental plan

5.1 Run sequence plan

Specify total number of runs required, and any special requirements, such as consecutive days, Monday runs, extended run period (10 hours maximum), etc.

We anticipate that this experiment will require two ordinary-length run days: one for L-mode target plasmas and one for RF-heated I-mode targets. The first of these run days can be during the preliminary phase of the campaign, when not all diagnostic and heating systems are fully functioning.

The use of the gas jet disruption mitigation system has in the past led to the loss of one or more subsequent shots, reducing the number of useful discharges in a run day, although this was not the case in one recent experiment (run 1090925).

5.2 Shot sequence plan

For each run day, give detailed specification for proposed shot sequence: number of shots at each condition, specific parameters and auxiliary systems requirements, etc. Include contingency plans, if appropriate.

The first run day will consist of a planned 20–24 useful shots. In all cases, the gas jet system will be triggered at $t = 1.0$ s ($\pm$ a few milliseconds for staggered triggering of each gas jet).

1. **Commissioning of gas jets.** Load LSN target (1110113020) and make field/current adjustments as necessary. Fire gas jet (with standard 85% Ar, 15% He disruption mitigation gas mixture) into identical 800 kA, 5.4 T, $n\ell 04 \approx 0.8 \times 10^{20}$ m^{-2} plasmas (see section 4.1). Repeat twice with each of two gas jets (B- and F-port). Fire gas jet at B-port, then (new) gas jet at G-port, then B-port, then G-port. (*4 shots total*)

2. **Simultaneous operation of two gas jets.** Fire both gas jets at the same time into identical plasma. Repeat three times to figure out any unexpected offsets in the timing of each jet. Attempt to get the two gas jets to fire at the exact same time. Up to four shots allocated for this. (If it is attained earlier, move on to step 3.) (*3–4 shots total*)

3. **Staggered gas jet operation scan.** This is a scan of the advancement time between triggering to each gas jet. Defining $\Delta t \equiv t_{\mathrm{trig,G}} - t_{\mathrm{trig,B}}$ (*i.e.*, the length of time between the triggering signal being sent to the B-port and the G-port gas jets, such that a positive Δt means that the G-port gas jet is fired *after* the B-port jet), repeat into identical (800 kA, 5.4 T, $n\ell 04 \approx 0.8 \times 10^{20}$ m^{-2}) plasma with $\Delta t = -2.0$, -1.0, 1.0, and 2.0 ms. ($\Delta t = 0$ was already covered in the last step.) (*4–6 shots total*).

4. **q-scan.** Repeat with B-port gas jet alone; G-port gas jet alone; both gas jets at the same time ($\Delta t = 0$); and both gas jets with $\Delta t = \pm 1.0$ ms at 5.4 T with currents of 600 kA, 1.0 MA, and 1.2 MA. Adjust density to maintain fixed T_{e}. This step will be completed on the first day only if time permits. (*9 shots total*).

On the second day, we first complete step 4 from the first run day (if not completed then), and perform a scan of W_{th} in I-mode (target 1110323027) using 1.0–3.0 MW of ICRF power from D and E antennas (additional power from J antenna if available). Finally, if possible, the current is varied in order to perform a q-scan in I-mode.

1. **Complete L-mode q-scan from day 1.** See step 4 from first run day.

2. **Two gas jets into RF-heated I-mode plasmas.** Load target I-mode shot (1110323027) at 800 kA, 5.4 T, upper single null topology. Repeat staggered gas jet and single gas jet operation into I-mode target according to lessons learned from first day. (*4–6 shots total*).

3. **$\mathbf{W_{th}}$ scan in I-mode.** Increase heating from 1.5 to 3.0 MA (or even further, depending on availibility of J-antenna) and fire gas jet at $t = 1.0$ s. (*2–3 shots*).

4. **q-scan in I-mode plasmas** Increase current to 1.0 and 1.2 MA and fire gas jet at $t = 1.0$ s. (*2–3 shots*).

6 Anticipated results

Discuss possible experimental outcomes and implications. Indicate if the experiment may be expected to lead to publications, milestone completions, improved operating techniques, etc. Indicate if the experiments are intended to contribute to a joint research effort, or an external database.

It is anticipated that interesting results will be obtained by the use of two gas jets, regardless of their success in reducing the radiation asymmetry. If the use of the two gas jets (in general, or due to specific timing between the jets) is successful at reducing the radiation asymmetry, this would be a very important result for ITER. If it is unsuccessful, it would still be interesting from a physics perspective, and might shed light on the link between MHD modes and the radiation asymmetry that was identified in 2010 [5].

This research will be presented as a poster or talk at conferences (APS-DPP 2012 and possibly HTPD 2012). In addition, understanding the cause of the observed radiation asymmetry in gas jet mitigated disruptions has been identified as a high-priority issue for ITER (see, e.g., [11]). The results of this work will directly inform the choice of the number of gas jets in the ITER design. It is anticipated that the experimental observations of disruption mitigation with two gas jets will lead to a peer-reviewed publication. If the observations lead to a theory of what is occurring during a mitigated disruption, and/or what is causing the radiation asymmetry, a second publication could result. This experiment will also contribute to G.M. Olynyk's thesis work.

References

[1] Granetz, R.S. *et al.* (2006). "Gas jet disruption mitigation studies on Alcator C-Mod". *Nuclear Fusion* **46**(12), 1001–1008. doi:10.1088/0029-5515/46/12/003

[2] Whyte, D.G. *et al.* (2007). "Disruption mitigation on Alcator C-Mod using high-pressure gas injection: Experiments and modeling toward ITER". *Journal of Nuclear Materials* **363–365**, 1160–1167. doi:10.1016/j.jnucmat.2007.01.149

[3] Granetz, R.S. *et al.* (2007). "Gas jet disruption mitigation studies on Alcator C-Mod and DIII-D". *Nuclear Fusion* **47**(9), 1086–1091. doi:10.1088/0029-5515/47/9/003

[4] Reinke, M.L. *et al.* (2008). "Toroidally resolved radiation dynamics during a gas jet mitigated disruption on Alcator C-Mod". *Nuclear Fusion* **48**(12), 125004. doi:10.1088/0029-5515/48/12/125004

[5] Olynyk, G.M. *et al.* (2010). "MHD activity during the pre-thermal quench phase of gas jet mitigated disruptions on Alcator C-Mod". Poster at 52$^{\text{nd}}$ Annual Meeting of the APS Division of Plasma Physics, Chicago, Illinois, November 8–12, 2010. Abstract #TP9.071.

[6] Bakhtiari, M. *et al.* (2011). "Using mixed gases for massive gas injection disruption mitigation on Alcator C-Mod". *Nuclear Fusion* **51**(6), 063007. doi:10.1088/0029-5515/51/6/063007

[7] Reinke, M.L. and Hutchinson, I.H. (2008). "Two-dimensional radiated power diagnostics on Alcator C-Mod". *Review of Scientific Instruments* **79**(10), 10F306. doi:10.1063/1.2965018

[8] Müller, E.R. and Mast, F. (1984). "A new metal resistor bolometer for measuring vacuum ultraviolet and soft x radiation." *Journal of Applied Physics* **55**(7), 2635–2641. doi:10.1063/1.333272

[9] Sugihara, M. *et al.* (2007). "Disruption scenarios, their mitigation and operation window in ITER." *Nuclear Fusion* **47**(4), 337–352. doi:10.1088/0029-5515/47/4/012

[10] Granetz, R. *et al.* (2005). "Initial tests of disruption mitigation using a gas jet." Alcator C-Mod Mini-Proposal N$^{\underline{\text{o}}}$ 424, 2005-05-11. Available on PSFC website at `http://www.psfc.mit.edu/research/alcator/miniproposals/424.pdf`

[11] Huijsmans, G. (2011). "Task on disruption mitigation: Radiation asymmetry and runaway mitigation by massive gas injection in ITER scenarios". Task no. 6A2EMG, v. 1 (for bid), date 2011-08-10.

Alcator C-Mod

Mini-Proposal

MP No. 714

Subject: **MHD effects on massive gas injection disruption mitigation**

From: G.M. Olynyk, R.S. Granetz, D.G. Whyte

Group: MHD (disruption mitigation)

Date: July 20, 2012

Approved by: **Date approved:**

1 Purpose of experiments

Include immediate goal of the experiments, scientific importance and/or programatic relevance. Refer to any relevant program milestones or ITER R&D commitments. This is the "sales pitch" for your use of a C-Mod run day.

The purpose of this experiment is to determine what effect the important MHD parameters—elongation, configuration (diverted/limited) and safety factor—have on the effectiveness of massive gas injection disruption mitigation. In particular, we hypothesize that in low-elongation plasmas (nearly circular), the low-n MHD modes that grow during the pre-TQ phase of mitigated disruptions will grow more quickly, and the radiation asymmetry will be lower (i.e. more symmetric). It is also suspected that changing from diverted to inner-wall limited configuration can have an effect on the *variability* of the radiation asymmetry.

2 Background

Discuss physics basis of the proposed research, prior results at Alcator or elsewhere, and any related work being carried out separately (in other Alcator C-Mod miniproposals).

It is known from previous experiments that in lower-single-null elongated, shaped plasmas, there is a link between toroidal radiation asymmetry and the growth rate of low-n MHD modes in the pre-TQ phase of mitigated disruptions [1]. This is shown in Figure 1. To date, this link has not been explained theoretically.

In 2010, an experiment was run in which the disruption mitigation gas jets were fired into low-elongation limited plasmas. The purpose of the experiment was to test for runaway electron confinement during mitigated disruptions, and thus no radiation asymmetry data is available from that day. However, the growth rates of the $n = 1$ MHD modes were recorded and are shown in Figure 2.

In addition to having no radiation asymmetry data from the 2010 runaway-confinement experiment, other important figures of merit for disruption mitigation include divertor heat load, halo current, and runaway confinement. However, for this run, the divertor thermocouples and IR thermography was not enabled, and the halo-current Rogowski coils were not digitized. Thus, all we have from this previous run is the suggestive correlation between elongation and $n = 1$ MHD mode growth rate.

Simulation using an extended MHD code (NIMROD) indicates [2] that last closed flux surface elongation has a large effect on the MHD activity during mitigated disruptions. Island formation and flux surface rehealing are significantly modified in low-elongation (circular) plasmas – flux surfaces are re-healed to a

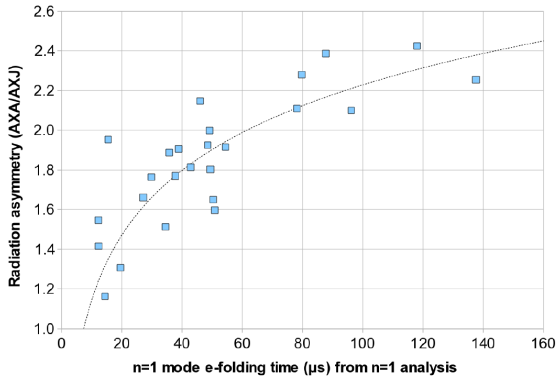

Figure 1 – The toroidal radiation asymmetry in mitigated disruptions seems to correlate positively with the growth time (inverse of growth rate) of the $n = 1$ electromagnetic mode as measured by a toroidal array of fast magnetic pickup coils.

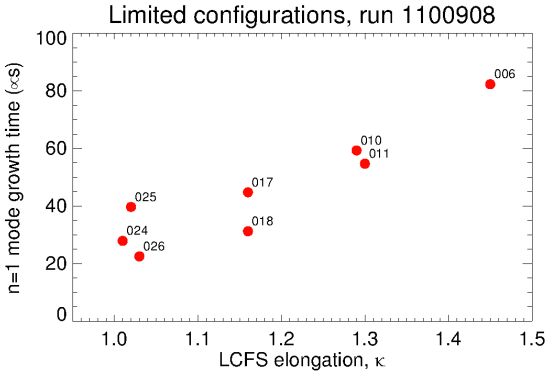

Figure 2 – Link between $n = 1$ MHD mode growth rate and plasma elongation (κ). It can be seen that low-elongation plasmas generally have faster-growing MHD modes, which implies that these low-elongation plasmas will have more symmetric thermal quench radiation.

greater extent in low-elongation plasmas. Given that it appears that the MHD activity also is linked to the radiation asymmetry, this suggests that elongation (κ) is a natural candidate as a "knob" for mitigated disruption radiation asymmetry.

In addition, the safety factor (q_{95}/q^*) is another important MHD stability parameter, and is thought to play a role in mitigated disruptions [3, 4]. The current theory is that the thermal quench (TQ) phase of the mitigated disruption is triggered when the cooling front from the gas jet has penetrated in to the $q = 2$ surface, causing a current channel contraction and destabilizing an internal (2,1) reconnection event.

Given these previous results and theory, it is desired to run a dedicated experiment in which the most important MHD parameters are modified, and the effect on $n = 1$ mode growth rate and disruption toroidal radiation asymmetry is measured. Specifically, elongation κ, safety factor q^*, and magnetic configuration (diverted or limited) will be varied.

3 Approach

What your experiment will actually do, and why you will do it that way. Describe the methodology to be employed and explain the rationale for the choice of parameters. Describe the analysis techniques to be employed in interpreting the data, if applicable. If the approach is standard or otherwise self-evident, this section may be absorbed into the Experimental Plan.

This miniproposal contains enough shots for two run days, organized into a "primary" set to be run on the first day, and an "auxiliary" set to be run on the second day. To maximize the chances of success, we will run L-mode plasmas with a small amount of ICRF heating (1 MW) to increase stored energy. We will pre-emptively fire in gas jets using the now-standard 85% He + 15% Ar disruption mitigation gas.

The plan is to conduct a seven-point scan of elongation in the limited configuration. Then, a five-point scan of safety factor will be done in the diverted configuration. A "binary scan" (*i.e.* diverted/limited) of X-point configuration will be done at the highest elongation and a single safety factor. Finally, each shot will be repeated twice with a single gas jet, and once with two gas jets firing simultaneously. This corresponds to a total of 42 physics shots. In addition, time will be spent at the beginning of each run day to tune and calibrate the gas jets.

These goals are split up into a number of phases so that useful results can be obtained even with a single run day.

4 Resources

4.1 Machine and plasma parameters

Give values or range for all of the following:

Toroidal field	5.6 T
Plasma current	560 kA–1.0 MA
Working gas species	Deuterium (D_2)
Density	$\bar{n}_e \approx 1.5-2.0 \times 10^{20}$ m^{-3} $n\ell 04 \approx 0.8-1.2 \times 10^{20}$ m^{-2}
Equilibrium configuration (if possible, refer to database equilibria)	See shot sequence plan
Pulse length, typical current and density waveforms, etc. (refer to database or sketch desired waveforms)	See shot squence plan
Boronization required? (if yes, specify whether overnight or between-shot, how recently needed, and any special conditions.)	Run any time after the first boronization of the campaign.

4.2 Auxiliary systems

List requirements for the following Alcator C-Mod auxiliary systems:

ICRF (power, pulse length, phasing)	1 MW from E-antenna (transmitter #2) only, turning on at $t = 0.6$ s, until (induced) disruption at $t = 1.0$ s
LHCD (power, pulse length, phasing)	Not required
Pellet injection (list species)	N/A
Impurity injection (laser blow-off)	Not required.
Diagnostic neutral beam	Not required.
Special gas puffing	Disruption mitigation gas jets at B-port and F-port with 85% He / 15% Ar gas mixture. Argon from B-side lower gas puff in order to get core rotation from HiReX Jr.
Cryopump	Not required
Non-axisymmetric coils (list connections and current)	Not required
Other	None

4.3 Diagnostics

List required diagnostics, and any special setup or configuration required, e.g. non-standard digitization rate.

Essential diagnostics for this run will consist of the base C-Mod diagnostics (magnetics, TCI, plus all TorVac systems including thermocouple gauge and B-side lower MKS gauge), the DMBolo disruption-optimized diode array, plus ordinary bolometry (AXUV diodes and foils, with diode gains reduced for disruption mitigation brightnesses), fast magnetics (especially the low-n coils on stalks), soft X-ray tomography array 3, and FRCECE radiometer for fast profiles of electron temperatures, and HiReX Jr for core rotation.

Desired diagnostics include Thomson scattering, soft X-ray tomography array 1, divertor thermocouples and IR imaging, and core CXRS for impurity temperature and rotation. No beam-based diagnostics will be available as the diagnostic neutral beam is shut off and locked out for gas jet disruption mitigation runs.

Sensitive diagnostics should have their gate valves or shutters closed prior to this run to avoid damage due to the large pressure pulse (up to 1 torr) created by the gas jet injectors.

5 Experimental plan

5.1 Run sequence plan

Specify total number of runs required, and any special requirements, such as consecutive days, Monday runs, extended run period (10 hours maximum), etc.

The intention is to get a useful set of data from a single "primary" run day, and to get additional detail (basically, fill in the scans and get the two-gas-jet shots) using a second "auxiliary" run day if available. This is of course contingent on successful machine and diagnostic operation.

The past several run days in which the gas jet disruption mitigation system was fired (1071220, 1090924, 1090925, 1100908, 1120202, 1120622) have convincingly shown that the use of the gas jet does not cause a loss of subsequent plasmas. It does delay the shot cycle due to the time required to pump out the

torus from several hundred millitorr of pressure. Generally, it is possible to achieve about 20–25 gas jet disruption mitigation shots in one run day.

5.2 Shot sequence plan

For each run day, give detailed specification for proposed shot sequence: number of shots at each condition, specific parameters and auxiliary systems requirements, etc. Include contingency plans, if appropriate.

The first ("primary") run day will consist of a planned 18–23 useful gas jet mitigated disruptions. In all cases, both gas jets will be triggered at $t = 1.0$ s ($\pm$ a few milliseconds for staggered triggering of each gas jet so that the gas front arrives at the plasma at the same time from each jet).

1. **Gas jet shakedown / base case diverted target.** Load LSN target from previous gas jet runs (1120622012) – field 5.6 T, current 1.0 MA. Auxiliary heating (1 MW ICRF from E-antenna, transmitter #2 only) is to turn on at $t = 0.6$ s and remain on $t = 1.0$ s. Fire B-port gas jet only (with standard 85% Ar, 15% He disruption mitigation gas mixture) into plasma at $t = 1.0$ s. Verify that all diagnostics are working properly. Repeat as necessary to get 2 good mitigated disruptions. (*2–3 shots.*)

2. **Establish low-elongation limited plasma.** Load $\kappa = 1.3$ target shot (1100908011). Set field to 5.6 T and current to 756 kA (thus $q^* \approx 3.80$). Apply ICRF heating, 1.0 MW from E-antenna only from $t = 0.6$ s on. Fire B-port gas jet only at $t = 1.0$ s. Repeat as required to get good gas jet mitigated disruption. (*1–2 shots.*)

3. **Scan of elongation at constant safety factor.** Here we do a scan of the elongation in the inner-wall limited configuration, at constant safety factor (q^*). All shots have $B_t = 5.6$ T, and 1.0 MW ICRF heating from E-antenna only starting at $t = 0.6$ s. Single gas jet (B-jet only) is fired at $t = 1.0$ s in all cases. Shots as follows. Elongations in the middle of the range (1.1 and 1.5) to be attempted first; the extreme elongations (1.0 and 1.6) to be attempted at end, in case these plasma shapes cannot be established.:

Elongation (κ)	**Current (kA)**	**Target shot (notes)**
1.3	756	(*Already covered in part 2*)
1.5	913	1100908006 (increase κ to 1.50)
1.1	621	1100908017 (reduce κ to 1.10)
1.0	562	1100910025
1.6	1000	Extend from $\kappa = 1.5$ shot

   This scan should then be repeated in the order (κ = 1.3, 1.5, 1.1, 1.0, and then 1.6). It is anticipated that some shots will be required to develop the high-elongation limited plasmas. (*9–11 shots total.*)

4. **Safety factor scan at constant elongation in diverted configuration.** As with previous step, all shots have $B_t = 5.6$ T, and 1.0 MW ICRF heating from E-antenna only starting at $t = 0.6$ s. Single gas jet (B-jet only) is fired at $t = 1.0$ s. Use LSN target (1120622012) but modify current.

Current (MA)	**Safety factor (q^*)**	**Notes**
0.6	6.33	
0.8	4.75	
1.0	3.80	(*Already covered in part 1*)
1.2	3.17	

   Repeat in order of increasing current (I_p = 0.6, 0.8, 1.2 MA) so that there are two good single-jet mitigated disruptions at each current. (*6–7 shots total.*)

The result of this first "primary" run day is a fairly comprehensive scan of the important MHD parameters for disruption mitigation, with good radiation asymmetry data with a single gas jet only.

On the second ("auxiliary") day, we first extend the scans from steps 3 and 4 of the first run day, and then repeat everything with both gas jets. This run consists of a planned 20 useful shots.

5. **Establish two gas-jet operation.** Load 1.0 MA, 5.6 T, $q^* = 3.80$, LSN target (1120622012). ICRF heating 1.0 MW from E-antenna only, starting at $t = 0.600$ s. Fire B-jet only (1 shot) and then F-jet only (1 shot) at $t = 1.000$ s to confirm timing and operation of both jets. Repeat as necessary to establish reliable gas jet operation. (*2–4 shots.*)

6. **Extended elongation scan with one gas jet.** Here we continue the scan in the limited configuration from part 3 of the first run day. All shots have $B_t = 5.6$ T and $q^* = 3.80$. 1.0 MW ICRF heating is to be applied from E-antenna only, starting at $t = 0.6$ s to (induced) disruption at $t = 1.0$ s.

Elongation (κ)	**Current (kA)**	**Target shot (notes)**
1.4	831	1100908006 (reduce κ to 1.50)
1.2	685	1100908017 (increase κ to 1.10)

   Repeat each shot twice with single (B-port) gas jet. (*4–5 shots.*)

7. **Extended safety factor scan with one gas jet.** Load 1.2 MA LSN target from previous run day. All parameters identical except increase current to 1.4 MA ($q^* = 2.71$). Fire single gas jet into plasma. Repeat so we have two data points at this current. (*2 shots.*)

8. **Repeat of elongation and safety factor scans with two gas jets.** See table below. In all cases, we are repeating previous shots, except we fire with two gas jets, with timing such that the gas front arrives at the same time. The purpose here is to reveal the effect of using two gas jets vs. a single gas jet at various values of the important MHD parameters. All shots have $B_t = 5.6$ T, 1.0 MW of ICRF heating from E-antenna only, starting at $t = 0.6$ s to (induced) disruption at $t = 1.0$ s.

Configuration	κ	I_p (MA)	q^*
Limited	1.0	0.562	3.80
Limited	1.1	0.621	3.80
Limited	1.2	0.685	3.80
Limited	1.3	0.756	3.80
Limited	1.4	0.831	3.80
Limited	1.5	0.913	3.80
Limited	1.6	1.000	3.80
Diverted	1.6 (LSN)	0.6	6.33
Diverted	1.6 (LSN)	0.8	4.75
Diverted	1.6 (LSN)	1.0	3.80
Diverted	1.6 (LSN)	1.2	3.17
Diverted	1.6 (LSN)	1.4	2.71

   (*12 shots.*)

This second "auxiliary" run day thus has a total of 20–23 useful shots.

6 Anticipated results

Discuss possible experimental outcomes and implications. Indicate if the experiment may be expected to lead to publications, milestone completions, improved operating techniques, etc. Indicate if the experiments are intended to contribute to a joint research effort, or an external database.

It is anticipated that these scans will help reveal the details of the link between MHD mixing and radiation asymmetry in gas jet mitigated disruptions. This data will directly contribute to an invited talk at APS-DPP 2012 (and an associated *Physics of Plasmas* paper). In addition, it will form an important part of G.M. Olynyk's Ph.D thesis.

Another paper is also possible if the link between MHD and radiation asymmetry is figured out in detail. This is a very important topic for ITER and an explanation of the link would constitute significant progress.

References

[1] Olynyk, G.M. *et al.* (2010). "MHD activity during the pre-thermal quench phase of gas jet mitigated disruptions on Alcator C-Mod." Poster at 52$^{\text{nd}}$ Annual Meeting of the APS Division of Plasma Physics, Chicago, Illinois, November 8–12, 2010. Abstract #TP9.071.

[2] Izzo, V.A. *et al.* (2011). "Runaway electron confinement modelling for rapid shutdown scenarios in DIII-D, Alcator C-Mod and ITER." *Nuclear Fusion* **51**(6), 063032. doi: 10.1088/0029-5515/51/6/063032

[3] Hollmann, E.M. *et al.* (2007). "Observations of q-profile dependence in noble gas injection radiative shutdown times in DIII-D." *Physics of Plasmas* **14**(1), 012502. doi: 10.1063/1.2408404

[4] Thornton, A.J. *et al.* (2012). "Plasma profile evolution during disruption mitigation via massive gas injection on MAST." *Nuclear Fusion* **52**(6), 063018. doi: 10.1088/0029-5515/52/6/063018

Appendix D

Reproductions of some key computer code

The codes reproduced in this appendix are written in the IDL 7.0 language. IDL, the Interactive Data Language, is, as of 2013, a product of Exelis VIS, a wholly owned subsidiary of the company ITT Exelis.

Code: DMAG_CROSSCOR.PRO

```
;+
;
; DMAG_CROSSCOR does cross-correlation on the DMBolo channels for a single shot
;  and makes plots. You get to set the time range over which it's done.
;
; NAME:
;
;   DMAG_CROSSCOR
;
; CALLING SEQUENCE:
;
;   DMAG_CROSSCOR, s [, TSTART=<double>] [, TEND=<double>] [, T0=<double>]
;    [, TRANGE=<double>] [, EX_RANGE=<double>] [, MAX_SPEED=<double>]
;    [, BAD_CHANS=<list>] [, /USE_AXJ] [, /SUB_MEAN] [, /CURSOR] [, /NOPLOT]
;
; INPUTS:
;
;   s       DMAG structure as output from DMAG_LOAD. (Must be a single, that is,
;           scalar, structure, not a vector or array.)
;
; OUTPUTS:
;
;   [none, other than the plots]
;
; OPTIONAL INPUTS and SWITCHES:
;
;   TSTART    Time at which to start the analysis. (Default is to start the
;             analysis at the first time point in the DMAG structure.)
;
;   TEND      Time at which to end the analysis. (Default is to end the
;             analysis at the last time point in the DMAG structure.)
;
```

```
;   TO          "Offset" time for plots. If this keyword is set, then all times
;               are plotted relative to this offset time, in milliseconds.
;               (Default is to plot absolute times in seconds.)
;
;   TRANGE      For the cross-correlation plots, set this keyword to force the
;               plots to have an x-range of +/- TRANGE (in microseconds). The
;               default is to use a plot range of half the difference between the
;               last and first time points in the time range used for analysis.
;
;   EX_RANGE    Range around zero (+/- EX_RANGE) to exclude when finding the
;               maximum in the cross-correlation function. Input in MICROSECONDS.
;
;   MAX_SPEED Maximum possible rotational speed (in kHz) of any rotating
;               mode. This keyword is exclusive of EX_RANGE, that is, you cannot
;               set them both or it will throw an error. This is the better
;               keyword to use, since this takes into account the fact that some
;               diode pairs are closer together than others (as opposed to just
;               blanket excluding small times).
;
;   BAD_CHANS List of bad DMBolo channels. These channels are exluded from the
;               analysis. Note that these are specified as channel numbers from
;               the list {1, 2, 3, 4, 5, 6}, i.e. BAD_CHANS=[3,6]. Default is to
;               use all channels.
;
;   /USE_AXJ    Include the AXJ data in the DMAG structure as a proxy for another
;               DMBolo channel at phi = 90 degrees. Note that this doesn't
;               really work all that well. The AXJ channels do not sample at a
;               single toroidal location but rather a broad toroidal swath about
;               45 degrees in extent; thus the cross-correlation to the other
;               channels (which are more delta-function-like) is not great.
;
;   /SUB_MEAN Subtract the mean of the DMBolo channels from each channel before
;               doing the cross-correlation analysis.
;
;   /CURSOR     Gives you a cursor at the end in order to do a fit to the
;               cross-correlation data.
;
;   /NOPLOT     Don't make plots; just print results.
;
; DESCRIPTION and NOTES:
;
;   - [none yet]
;
; DEPENDENCIES:
;
;   CLOSEST.PRO [G.M. Olynyk]
;   COLOUR.PRO [G.M. Olynyk]
;   DIFF.PRO [G.M. Olynyk]
;   GREEK.PRO [D. Fanning / Coyote Library]
;   TIMESERIES.PRO [G.M. Olynyk]
;   UNDEFINE.PRO [D. Fanning / Coyote Library]
;
```

```
; Program originally written 2013-05-17 by Geoffrey M. Olynyk for thesis work.
;
;-

PRO dmag_crosscor, s, TSTART=tstart, TEND=tend, T0=t0in, TRANGE=tr, $
  EX_RANGE=er, MAX_SPEED=ms, BAD_CHANS=bc, USE_AXJ=ua, SUB_MEAN=sm, CURSOR=c, $
  NOPLOT=npp

; Number of bad channels:
IF KEYWORD_SET(bc) THEN nbc = Size(bc, /N_ELEMENTS) ELSE nbc=0

nshots = Size(s, /N_ELEMENTS)

; Check inputs and throw an error if necessary.
IF nshots GT 1 THEN MESSAGE, $
  "This function only works on single shots."

IF KEYWORD_SET(er) AND KEYWORD_SET(ms) THEN MESSAGE, $
  "You can only set one of EX_RANGE and MAX_SPEED at a time."

IF TAG_NAMES(s[0],/STRUCTURE_NAME) NE "DMAG" THEN MESSAGE, $
  "You must pass a DMAG structure as input to this function."

; If they set the keywords
IF KEYWORD_SET(tstart) THEN ts=DOUBLE(tstart) ELSE ts=DOUBLE(Min(*s.dmbolo.t))
IF KEYWORD_SET(tend) THEN te=DOUBLE(tend) ELSE te=DOUBLE(Max(*s.dmbolo.t))

; If they set a T0, set a boolean that says we want an offset.
IF KEYWORD_SET(t0in) THEN BEGIN
  t0 = DOUBLE(t0in)
  offset = 1b
ENDIF ELSE BEGIN
  t0 = !Values.D_NaN
  offset = 0b
ENDELSE

; Extract data from structures for easier access.
t = DOUBLE(*s.dmbolo.t)
IF KEYWORD_SET(tstart) THEN i1 = closest(t, ts) ELSE i1=0
IF KEYWORD_SET(tend) THEN i2 = closest(t, te) ELSE i2=Size(t,/N_ELEMENTS)-1

t = t[i1:i2]
nt = Size(t, /N_ELEMENTS)

f = (*s.dmbolo.eps)[i1:i2,*]
nc = s.dmbolo.nchans
all_chans = Indgen(nc)+1
UNDEFINE, i1
UNDEFINE, i2

shot = s.shot
phi = s.dmbolo.phi
```

```
; If we have some bad channels, then remove them.
IF nbc GT 0 THEN BEGIN
  bci = BYTARR(nc) + 1b
  FOR i=0,nbc-1 DO bci = bci* (all_chans NE bc[i])
  gc = Where(bci)
ENDIF ELSE BEGIN
  gc = INDGEN(nc)
ENDELSE

f = f[*, gc]
phi = phi[gc]
good_chans = all_chans[gc]
nc = Size(gc, /N_ELEMENTS)

; 2013-05-22: Append the AXJ data if they asked for it.
; Note that the time base is the same for AXJ and DMBolo because it's on the
; same digitizer.

IF KEYWORD_SET(ua) THEN BEGIN
  axj_full = *s.axj.axj
  t_axj = *s.axj.t

  i1 = closest(t_axj, ts)
  i2 = closest(t_axj, te)

  axj = axj_full[i1:i2] * 275.e6
  phi_axj = 90. * !Pi / 180.

  ; Append the data to the various arrays here:
  phi = [phi, phi_axj]
  f = [[f], [axj]]
  nc = nc+1
  good_chans = [good_chans,7]
ENDIF

; 2013-05-21: If they call the SUBTRACT_MEAN keyword, we subtract the mean of
;           the DMBolo channels from each channel.

f_mean = REPLICATE(0.d, nt) ; Start with zeroes for mean
IF KEYWORD_SET(sm) THEN BEGIN
  FOR i=0,nt-1 DO f_mean[i] = Mean(f[i,*])
  FOR j=0,nc-1 DO f[*,j] = f[*,j] - f_mean
  UNDEFINE, i
  UNDEFINE, j
ENDIF

; Here we actually do the cross correlation by calling C_CORRELATE:
Lag = Indgen(2*(nt-2)+1)-(nt-2)
nl = Size(Lag, /N_ELEMENTS)

; 2013-05-20: Give the user the option to manually specify the range over which
```

```
; the cross-correlation will be plotted.
IF KEYWORD_SET(tr) THEN trange = DOUBLE(tr)*2.d-6 ELSE trange = t[nt-1] - t[0]
dt = DOUBLE(Mean(diff(t)))

; Number of points in range; we will use this later when deciding whether to
; plot points or a solid line:
nr = round(trange/dt)

; Make empty arrays to hold results.
ccor    = DBLARR(nl, nc, nc)
ccmax   = FLTARR(nc,nc)
ccargmax = FLTARR(nc,nc)

; For every pair of diodes, there is a corresponding phi difference.
dphi = FLTARR(nc,nc)
FOR i=0,nc-1 DO BEGIN
  FOR j=0,nc-1 DO BEGIN
    dphi[i,j] = phi[j]-phi[i]
    IF dphi[i,j] LT -1.*!Pi THEN dphi[i,j] = dphi[i,j] + 2.*!Pi
    IF dphi[i,j] GT !Pi THEN dphi[i,j] = dphi[i,j] - 2.*!Pi
  ENDFOR
ENDFOR

; If the user sets one of the two keywords EX_RANGE or MAX_SPEED then
; we get the maximum speed / minimum time for analysis.

; Make blank arrays to hold:
max_f    = DBLARR([nc,nc])
max_omega = DBLARR([nc,nc])
min_t    = DBLARR([nc,nc])

; By default, we don't exclude any points.
exclude = 0b

IF KEYWORD_SET(er) THEN BEGIN
  exclude = 1b
  FOR i=0,nc-1 DO BEGIN
    FOR j=0,nc-1 DO BEGIN
      max_f[i,j]    = DOUBLE(1.d / (er*1.d-6))
      max_omega[i,j] = DOUBLE(max_f[i,j] * 2.d * !Pi)
      min_t[i,j]    = DOUBLE(er * 1.d-6)
    ENDFOR
  ENDFOR
ENDIF

IF KEYWORD_SET(ms) THEN BEGIN
  exclude = 1b
  FOR i=0,nc-1 DO BEGIN
    FOR j=0,nc-1 DO BEGIN
      max_f[i,j]    = DOUBLE(ms * 1.d3)
      max_omega[i,j] = DOUBLE(max_f[i,j] * 2.d * !Pi)
      min_t[i,j]    = DOUBLE(ABS(dphi[i,j]) / max_omega[i,j])
```

```
    ENDFOR
  ENDFOR
ENDIF

; Do the cross-correlation and pick out the maxima.
FOR i=0,nc-1 DO BEGIN
  FOR j=0,nc-1 DO BEGIN
    ccor[*,i,j] = C_CORRELATE(f[*,i], f[*,j], Lag, /DOUBLE)

    ; To find the maximum, we exclude +/- MIN_T around 0:
    IF (exclude AND (i NE j)) THEN BEGIN
      incrange = where(abs(Lag)*dt GT min_t[i,j])
      IF incrange[0] EQ -1 THEN MESSAGE, $
        'No data points outside of excluded range (EX_RANGE)'
      ccmax[i,j] = Max(ccor[incrange,i,j])
      ccargmax[i,j] = DOUBLE(Lag[incrange[!C]]) * dt ; Use system variable hack.
    ENDIF ELSE BEGIN
      ccmax[i,j] = Max(ccor[*,i,j])
      ccargmax[i,j] = DOUBLE(Lag[!C]) * dt ; Use system variable hack.
    ENDELSE
  ENDFOR
ENDFOR
UNDEFINE, i
UNDEFINE, j

IF KEYWORD_SET(npp) THEN GOTO, theEnd
;; PLOTTING SECTION REMOVED FOR THESIS

theEnd:
END
```

Code: DMAG_TPF.PRO

```
;+
;
; DMAG_TPF For getting the toroidal peaking factor (TPF) of a C-Mod rapid
;  shutdown using DMBolo data.
;
; PROCEDURE NAME:
;
;   DMAG_TPF
;
; CALLING SEQUENCE:
;
;   DMAG_TPF, s, t_int, [, TPF=<float>] [, TSTART=<double>] [, TEND=<double>]
;     [, T0=<double>] [, BAD_CHANS=<list>] [, /USE_AXJ] [, /NOPLOT]
;
; INPUTS:
;
;   s       DMAG structure as output from DMAG_LOAD. (Must be a single, that is,
;           scalar, structure, not a vector or array.)
```

```
;
;   t_int  2-element vector containing times (absolute times)
;
; OUTPUTS:
;
;   TPF       Variable which will be set equal to the calculated TPF.
;
; OPTIONAL INPUTS and SWITCHES:
;
;   TSTART    Time at which to start the analysis. (Default is to start the
;             analysis at the first time point in the DMAG structure.)
;             Note this is an absolute time, in seconds.
;
;   TEND      Time at which to end the analysis. (Default is to end the
;             analysis at the last time point in the DMAG structure.)
;             Note this is an absolute time, in seconds.
;
;   T0        "Offset" time for plots. If this keyword is set, then all times
;             are plotted relative to this offset time, in milliseconds.
;             (Default is to plot absolute times in seconds.) This offset time
;             is an absolute time, in seconds.
;
;   BAD_CHANS List of integers representing bad DMBolo channels which shouldn't
;             be used for the analysis. Note that these are in the range {1,6}.
;
;   /USE_AXJ  Use the AXJ chord as a proxy for a seventh DMBolo channel.
;
;   /NOPLOT   Don't make plots, just return results. Note that if you don't use
;             the TPF=<float> keyword, and you set the /NOPLOT switch, the
;             procedure won't return anything useful.
;
; DESCRIPTION and NOTES:
;
;   - [none yet]
;
; DEPENDENCIES:
;
;   CLOSEST.PRO [G.M. Olynyk]
;
;   COLOUR.PRO [G.M. Olynyk]
;
; Procedure originally written 2013-05-21 by Geoffrey M. Olynyk for thesis work.
;
;-

PRO dmag_tpf, s, t_int, TPF=tpf_out, TSTART=ts, TEND=te, T0=tz, $
  BAD_CHANS=bc, USE_AXJ=ua, NOPLOT=np

; Check that the input is a scalar DMAG structure.
; Throw an error if it is not.
IF TAG_NAMES(s[0],/STRUCTURE_NAME) NE "DMAG" THEN MESSAGE, $
  "You must pass a DMAG structure as input to this function."
```

```
IF Size(s, /N_ELEMENTS) GT 1 THEN MESSAGE, $
  "This function only works on single shots."

; If they set the keywords for the time, then use them, otherwise we use
; the entire set of data in the DMAG structure.

IF KEYWORD_SET(ts) THEN tstart=DOUBLE(ts) $
  ELSE tstart=DOUBLE(Min(*s.dmbolo.t))
IF KEYWORD_SET(te) THEN tend=DOUBLE(te) $
  ELSE tend=DOUBLE(Max(*s.dmbolo.t))

IF Size(t_int, /N_ELEMENTS) NE 2 THEN MESSAGE, $
  'Input T_INT must be a two-element vector'

ti1 = DOUBLE(t_int[0])
ti2 = DOUBLE(t_int[1])

; Extract data from input structure.
t_raw = *s.dmbolo.t
phi_raw = s.dmbolo.phi
axj_raw = *s.axj.axj
i1 = closest(t_raw, tstart)
i2 = closest(t_raw, tend)
t = DOUBLE(t_raw[i1:i2])

AXJ_P_TO_V_EXPR = 275.e6
axj = axj_raw[i1:i2] * AXJ_P_TO_V_EXPR

f_raw = *s.dmbolo.eps
f_with_bad_chans = f_raw[i1:i2,*]

; Throw out bad channels.
nc_raw = (Size(f_with_bad_chans))[2]
all_chans = Indgen(nc_raw)+1

IF KEYWORD_SET(bc) THEN BEGIN
  ; If they have specified bad channels.
  nbc = Size(bc, /N_ELEMENTS) ; Number of bad channels
  bci = BYTARR(nc_raw) + 1b
  FOR i=0,nbc-1 DO bci = bci* (all_chans NE bc[i])
  gc = Where(bci)
  f   = f_with_bad_chans[*,gc]
  phi = phi_raw[gc]
  nc = Size(gc, /N_ELEMENTS)
ENDIF ELSE BEGIN
  ; If there are no bad channels.
  nbc=0 ; number of bad channels = 0
  nc = nc_raw
  gc = Indgen(nc)
  phi = phi_raw
  f = f_with_bad_chans
```

```
ENDELSE

CHAN_NAMES = StrArr(nc)
FOR i=0,nc-1 DO CHAN_NAMES[i] = 'DMBolo ' + StrTrim(gc[i]+1,2)

; If they wish to use the AXJ data, append it now.
IF KEYWORD_SET(ua) THEN BEGIN
  phi_axj = 90. * !Pi / 180.
  phi = [phi, phi_axj]
  f = [[f], [axj]]
  nc = nc+1
  gc = [gc,6]
  all_chans = [all_chans, 7]
  CHAN_NAMES = [CHAN_NAMES, 'AXJ']
ENDIF

; Okay now we can actually do the integration.
j1 = closest(t, ti1)
j2 = closest(t, ti2)
wrad = FLTARR(nc)
FOR i=0,nc-1 DO wrad[i] = FLOAT(INT_TABULATED(t[j1:j2], f[j1:j2,i]))

UNDEFINE, j1
UNDEFINE, j2
UNDEFINE, i

wrad_ave = TOTAL(wrad, /NAN) / FLOAT(nc)
asym = wrad / wrad_ave
pf = MAX(asym, /NAN)

; Put it into the output if they request.
tpf_out = pf

; If they don't want plots, just skip to end
IF KEYWORD_SET(np) THEN GOTO, theEnd
;;; PLOTTING SECTION REMOVED FOR THESIS PUBLICATION.

theEnd:
END
```

Code: FITNMODES.PRO

```
;+
; FITNMODES fits arbitrary n-modes to magnetics data.
;
; CALLING SEQUENCE:
;   s = FITNMODES(B, t, coils, phi, nmax [, /NODC])
;
; INPUTS:
;   B       FLTARR  Coil signals
;   t       FLTARR  s
```

```
;   coils   STRARR  String vector containing names of coils (72 of them)
;   phi     FLTARR  Vector containing phi values of coils (in DEGREES)
;   nmax    INT     Maximum value of n to consider.
;
; OUTPUTS:
;   s       STRUCT  Structure containing fit.
;
; OPTIONAL INPUTS and SWITCHES:
;   /NODC   Don't include n=0 (constant) component.
;
; DEPENDENCIES:
;   EREHW.PRO [G.M. Olynyk]
;
; Function originally created 2013-05-06 by Geoffrey M. Olynyk for thesis work.
;-

FUNCTION fitnmodes, B_in, t_in, coils_in, phi_in, nmax, NODC=nodc

; Sanitize inputs to make sure we don't modify them.
B = B_in
t = t_in
coils = coils_in
; angles get converted to radians:
phi = phi_in * !pi / 180.

; Extract one vector of B values for shorthand:
B0 = B[0,*]

; UPPER COILS:
; top row of low-N coils (angles are in DEGREES here):
; BP_KA_TOP (index 65) phi=015.20 theta=+18.0
; BP_AB_TOP (index 67) phi=349.84 theta=+18.0
; BP_BC_TOP (index 68) phi=300.13 theta=+18.0
; BP_EF_TOP (index 70) phi=189.91 theta=+18.0
; limiter coils at theta = +16.1 degrees:
; BP06_ABK (index 05) phi=329.40 theta=+16.1
; BP18_ABK (index 17) phi=339.60 theta=+16.1
; BP06_GHK (index 35) phi=128.10 theta=+16.1
; BP21_GHK (index 50) phi=138.30 theta=+16.1

upper_coils = Where(COILS EQ "BP_KA_TOP" OR COILS EQ "BP_AB_TOP" OR $
  COILS EQ "BP_BC_TOP" OR COILS EQ "BP_EF_TOP" OR $
  COILS EQ "BP06_ABK" OR COILS EQ "BP18_ABK" OR $
  COILS EQ "BP06_GHK" OR COILS EQ "BP21_GHK")

; make vector of indices of upper coils which meet three conditions
; (a) Are in the upper_coils list
; (b) Are not in the bad_coils() list
; (c) Have data

u = Where((erehw(upper_coils,72)) * (~erehw(bad_coils(),72)) * Finite(B0))
```

```
; LOWER COILS:

; lower row of low-N coils (angles are in DEGREES here):
; BP_KA_BOT (index 66) phi=015.20 theta=-18.0
; (note there is no BP_AB_BOT)
; BP_BC_BOT (index 69) phi=300.13 theta=-18.0
; BP_EF_BOT (index 71) phi=189.91 theta=-18.0

; limiter coils at theta = -16.1 degrees:
; BP07_ABK (index 06) phi=329.40 theta=-16.1
; BP19_ABK (index 18) phi=339.60 theta=-16.1
; BP10_GHK (index 39) phi=128.10 theta=-16.1
; BP24_GHK (index 53) phi=138.30 theta=-16.1

lower_coils = Where(COILS EQ "BP_KA_BOT" OR $
  COILS EQ "BP_BC_BOT" OR COILS EQ "BP_EF_BOT" OR $
  COILS EQ "BP07_ABK" OR COILS EQ "BP19_ABK" OR $
  COILS EQ "BP10_GHK" OR COILS EQ "BP24_GHK")
IF lower_coils EQ -1 THEN nl=0

; Generate some variables holding counts of various things:
sb = SIZE(B)
nt = sb[1] ; number of time steps
nb = sb[2] ; number of fast magnetics coils including invalid ones
nu = size(u,/N_ELEMENTS) ; number of valid upper coils
nl = size(l,/N_ELEMENTS) ; number of valid lower coils

; Generate vector of valid lower coils (see discussion of upper coils):
IF nl GT 0 THEN $
  l = Where((erehw(lower_coils,72)) * (~erehw(bad_coils(),72)) * Finite(B0))

; Here we actually fit n-modes to the coil data we have:
IF KEYWORD_SET(NODC) THEN BEGIN ; if no n=0 mode
  IF NMAX LT 1 THEN MESSAGE,"You have specified NMAX<1 and NODC"
  N = INDGEN(NMAX)+1
ENDIF ELSE BEGIN ; if we include the n=0 mode
  IF NMAX LT 0 THEN MESSAGE,"You have specified NMAX<0"
  N = INDGEN(NMAX+1)
ENDELSE

NN = SIZE(N,/N_ELEMENTS)
NX = 2*NN ; number of sine and cosine coefficients to solve for

; Create arrays to do the linear algebra for the least-squares fits:
MAT = FLTARR(NX,NX,NT) ; big matrix
MBLOCK1 = FLTARR(NN,NN,NT) ; matrix sub-block 1
MBLOCK2 = FLTARR(NN,NN,NT) ; matrix sub-block 2
MBLOCK3 = FLTARR(NN,NN,NT) ; matrix sub-block 3
Y = FLTARR(NX,1,NT) ; to hold constants
R = FLTARR(NX,1,NT) ; to hold results
; As with MNMODES.PRO, we solve for R in the equation MAT#R = Y
; except here we have to do it twice because we do it for upper and
```

```
; lower coil sets separately.

; Reform the B matrix to be the right dimensionality:
B = REFORM(TRANSPOSE(TEMPORARY(B)),[NB,1,NT])

; Rebin the phi vector (holds phi-values for each coil) so that it is
; the right dimensions for our linear algebra:
PHIAR = REBIN(PHI,[NB,1,NT])

; Check to make sure that we have at least three coils on the upper
; and/or lower coil set, or else throw an error:
IF NL LT NX && NU LT NX THEN MESSAGE,"Not enough coils to do fit"

; UPPER COILS
IF NU GE NX THEN BEGIN ; check if we have enough coils on upper set

; Create arrays to hold the results of the fit for upper coils:
AU = FLTARR(NN,NT)
CU = FLTARR(NN,NT)

; Fill in the big matrix. As for MNMODES, this requires a double
; nested loop, but it runs pretty quick, so I'm not going to try to
; figure out how to optimize it. -G. Olynyk

FOR X=0,NN-1 DO BEGIN ; enter loop
  CN1 = N[X] ; current primary n-number

  FOR Z=0,NN-1 DO BEGIN ; enter subloop

    CN2 = N[Z] ; current secondary n-number

  ; Sub-block 1 (sine-sine terms):
    MBLOCK1[X,Z,*] = TOTAL(SIN(CN1*PHIAR[u,0,*]) * $
                           SIN(CN2*PHIAR[u,0,*]), 1)

  ; Sub-block 2 (cosine-cosine terms):
    MBLOCK2[X,Z,*] = TOTAL(COS(CN1*PHIAR[u,0,*]) * $
                           COS(CN2*PHIAR[u,0,*]), 1)

  ; Sub-block 3 (sine-cosine terms):
    MBLOCK3[X,Z,*] = TOTAL(SIN(CN1*PHIAR[u,0,*]) * $
                           COS(CN2*PHIAR[u,0,*]), 1)
  ENDFOR

  ; Fill in the constants vector (Y) for all time steps at once,
  ; for the sine and cosine coefficients, for the upper coils:

  Y[X,*,*]     = TOTAL(B[u,*,*] * SIN(CN1*PHIAR[u,*,*]),1)
  Y[X+NX/2,*,*] = TOTAL(B[u,*,*] * COS(CN1*PHIAR[u,*,*]),1)

ENDFOR
```

```
; Put subblocks into big matrix for upper coils:
MAT[0:(NN-1),0:(NN-1),*] = MBLOCK1 ; top-left block (sine-sine)
MAT[(NX/2):(NX-1),(NX/2):(NX-1),*] = MBLOCK2 ; bottom-right block (cos-cos)
MAT[0:(NN-1),(NX/2):(NX-1),*] = MBLOCK3 ; top-right block (sin-cos)
MAT[(NX/2):(NX-1),0:(NN-1),*] = TRANSPOSE(MBLOCK3,[1,0,2]) ; bottom-left block (sin-cos)

; Solve linear system MAT#R=Y for R using Cramer's rule:
FOR Q=0L,NT-1 DO R[*,*,Q] = CRAMER(MAT[*,*,Q],Y[*,*,Q])

; Put results from the R array (NX-by-1-by-NT) into the output arrays
; A and C (which are NN-by-NT)

FOR X=0,NN-1 DO BEGIN
  AU[X,*] = R[X,*,*]
  CU[X,*] = R[X+NX/2,*,*]
ENDFOR

ampU   = SQRT(AU^2 + CU^2)
deltaU = ATAN(AU,CU)

ENDIF ; this is the loop where we checked if we had enough upper coils

; LOWER COILS
IF NL GE NX THEN BEGIN ; if we have at least three coils on lower set

; Create arrays to hold the results of the fit for lower coils:
AL = FLTARR(NN,NT)
CL = FLTARR(NN,NT)

; Fill in the big matrix. As for MNMODES, this requires a double
; nested loop, but it runs pretty quick, so I'm not going to try to
; figure out how to optimize it. -G. Olynyk

FOR X=0,NN-1 DO BEGIN ; enter loop
  CN1 = N[X] ; current primary n-number

  FOR Z=0,NN-1 DO BEGIN ; enter subloop

    CN2 = N[Z] ; current secondary n-number

  ; Sub-block 1 (sine-sine terms):
    MBLOCK1[X,Z,*] = TOTAL(SIN(CN1*PHIAR[1,0,*]) * $
                           SIN(CN2*PHIAR[1,0,*]), 1)

  ; Sub-block 2 (cosine-cosine terms):
    MBLOCK2[X,Z,*] = TOTAL(COS(CN1*PHIAR[1,0,*]) * $
                           COS(CN2*PHIAR[1,0,*]), 1)

  ; Sub-block 3 (sine-cosine terms):
    MBLOCK3[X,Z,*] = TOTAL(SIN(CN1*PHIAR[1,0,*]) * $
                           COS(CN2*PHIAR[1,0,*]), 1)
  ENDFOR
```

```
  ; Fill in the constants vector (Y) for all time steps at once,
  ; for the sine and cosine coefficients, for the lower coils:

  Y[X,*,*]     = TOTAL(B[l,*,*] * SIN(CN1*PHIAR[l,*,*]),1)
  Y[X+NX/2,*,*] = TOTAL(B[l,*,*] * COS(CN1*PHIAR[l,*,*]),1)
ENDFOR

; Put subblocks into big matrix for lower coils:
MAT[0:(NN-1),0:(NN-1),*] = MBLOCK1 ; top-left block (sine-sine)
MAT[(NX/2):(NX-1),(NX/2):(NX-1),*] = MBLOCK2 ; bottom-right block (cos-cos)
MAT[0:(NN-1),(NX/2):(NX-1),*] = MBLOCK3 ; top-right block (sin-cos)
MAT[(NX/2):(NX-1),0:(NN-1),*] = TRANSPOSE(MBLOCK3,[1,0,2]) ; bottom-left block (sin-cos)

; Solve linear system MAT#R=Y for R using Cramer's rule:
FOR Q=0L,NT-1 DO R[*,*,Q] = CRAMER(MAT[*,*,Q],Y[*,*,Q])

; Put results from the R array (NX-by-1-by-NT) into the output arrays
; A and C (which are NN-by-NT)

FOR X=0,NN-1 DO BEGIN
  AL[X,*] = R[X,*,*]
  CL[X,*] = R[X+NX/2,*,*]
ENDFOR

ampL   = SQRT(AL^2 + CL^2)
deltaL = ATAN(AL,CL)

ENDIF ; this is the loop where we checked if we had enough lower coils

; For now, just use the upper coil set since it has more coils
; Maybe later have to take an average of the two or something.
; G. Olynyk 2010-06-22
A=AU
C=CU
AMP = ampU
DELTA = deltaU

; Create a structure to insert into the input structure to return
s = { NMODEDATA, $ ; structure name
         N:N, A:TRANSPOSE(A), C:TRANSPOSE(C), $
         AMP:TRANSPOSE(AMP), DELTA:TRANSPOSE(DELTA) }
RETURN, s

END
```

Appendix E

Additional equipment photographs

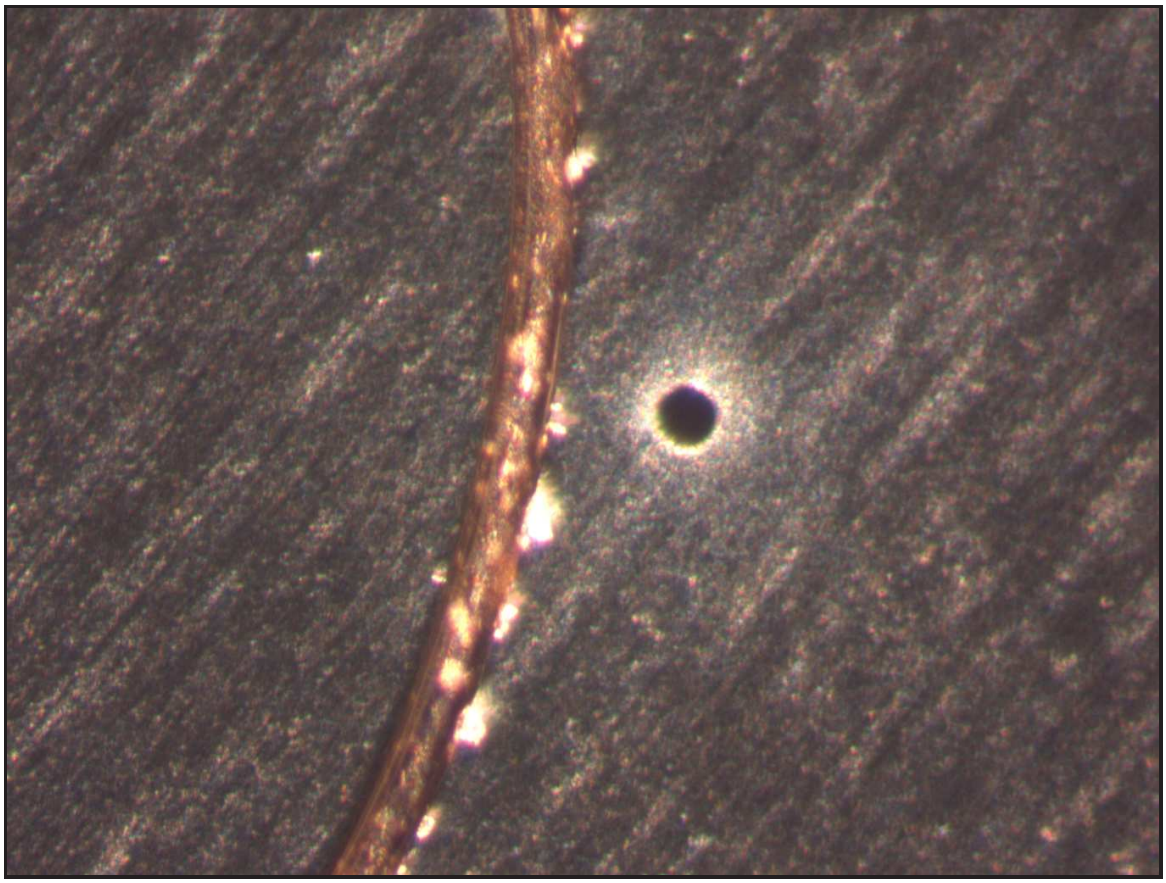

Photo 1 – The 100 μm aperture diameter in each Lenox Laser HP-3/8-DISC-MLY-100 molybdenum aperture disc was verified by comparing it to a 38 AWG copper wire (nominal diameter 101 μm). Optical micrograph #2 of aperture #207 (G.M. Olynyk numbering), taken August 12, 2011.

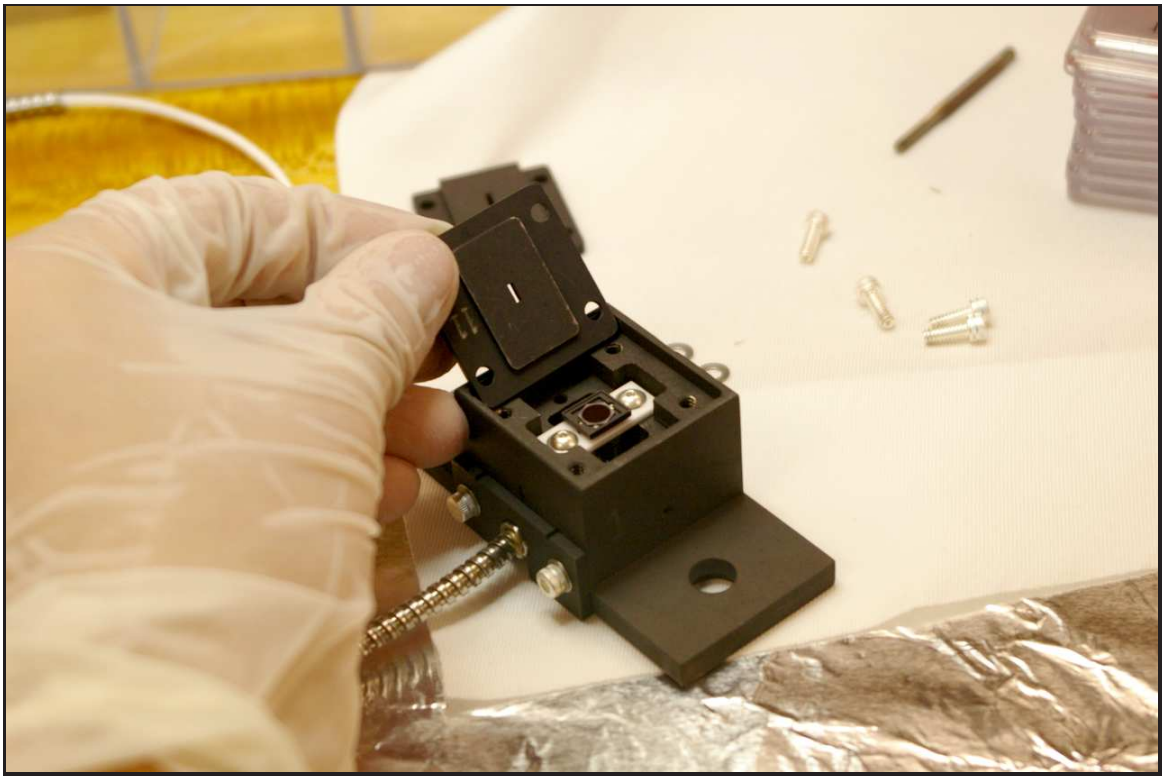

Photo 2 – Final assembly of the wall-mounted photodiode boxes on August 29, 2011.

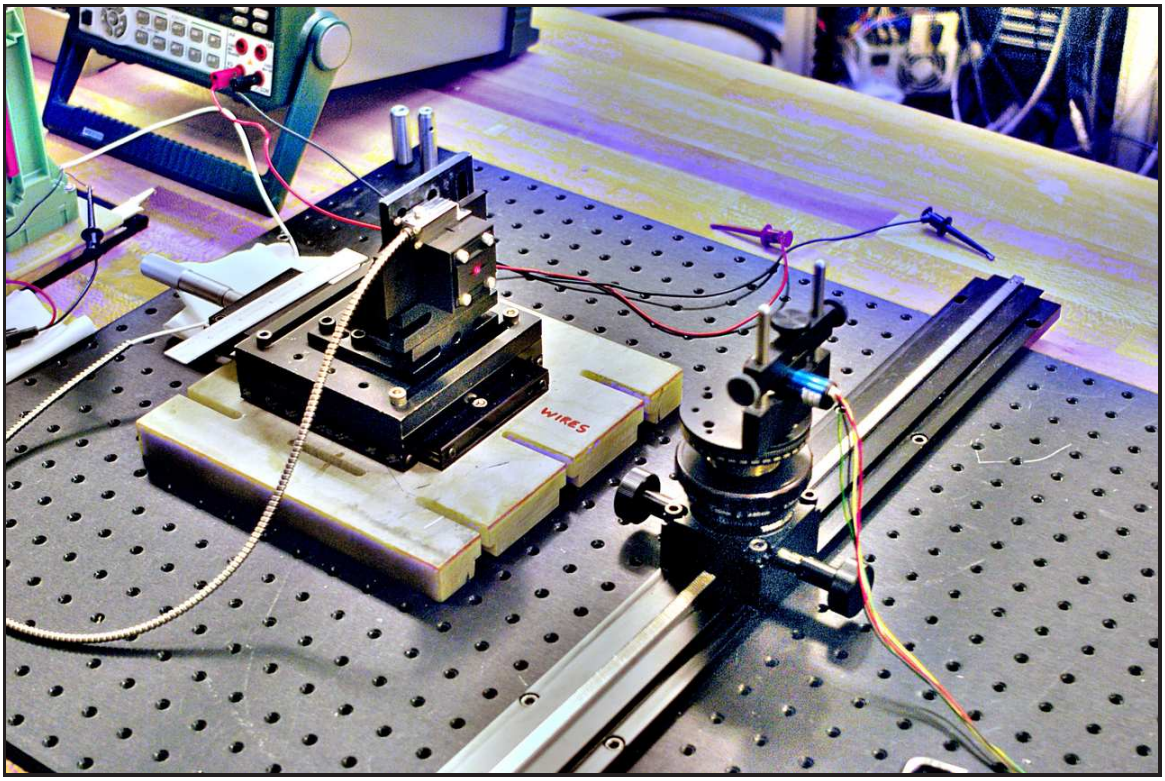

Photo 3 – Geometric calibration of the photodiode boxes in order to determine view area, September 3, 2011. Contrast-enhanced.

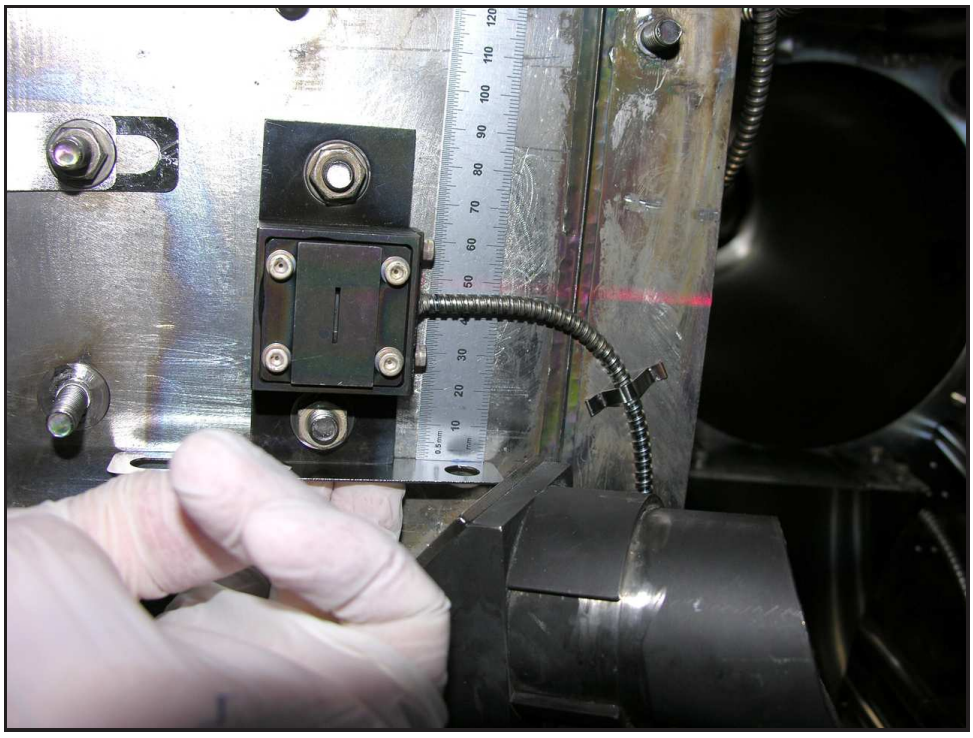

Photo 4 – Checking the geometric position of the diode boxes on the C-Mod vessel wall using a laser level, April 6, 2012.

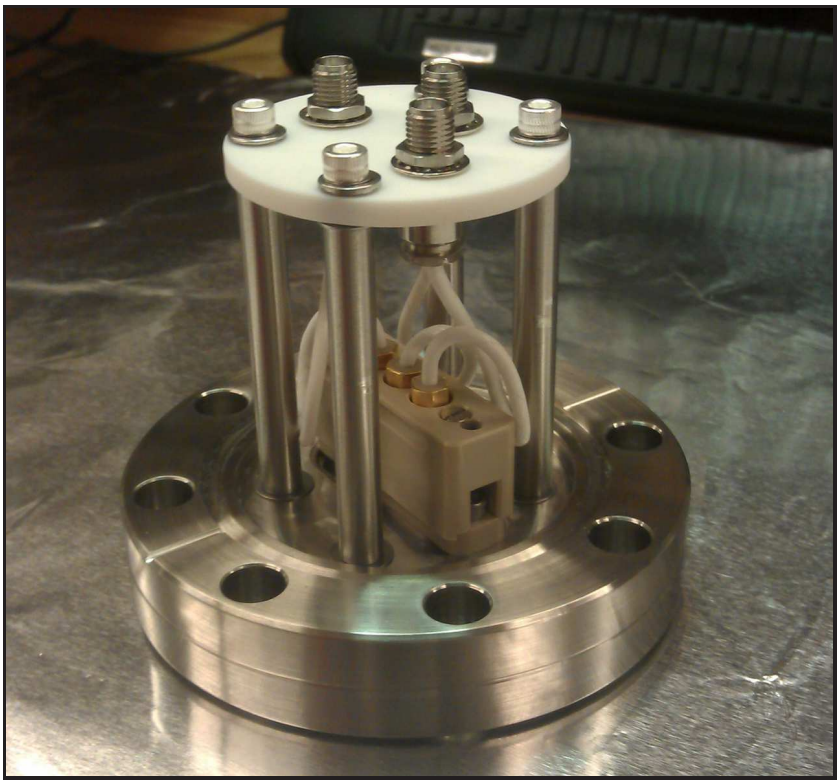

Photo 5 – Custom-built "triple PEEK" vacuum feedthrough to carry diode data out of Alcator C-Mod with fully coaxial signal path. Assembled and ready for installation, August 16, 2011. See Appendix F for manufacturing drawings for feedthrough.

THIS PAGE INTENTIONALLY LEFT BLANK

Appendix F

Equipment drawings

The following equipment drawings are reproduced here, for reference:

- Manufacturing drawings for wall-mounted diode boxes (6 drawings)
- Manufacturing drawings for electrical vacuum feed-through (3 drawings)
- International Radiation Detectors, Inc. AXUV100 photodiode. IRD no longer exists as an independent company; their products are now sold by Opto-Diode Inc., a member of the ITW Photonics Group.
- Alcator C-Mod standard transimpedance amplifier electrical schematic

PARTS LIST (PER ASSEMBLY)				
ITEM	PART NUMBER	DESCRIPTION	MATERIAL	QTY
1	DMBOLO-01-001	DIODE BOX BODY	Stainless Steel, 304L	1
2	(IRD) AXUV20A	AXUV20A DIODE WITH CERAMIC SOCKET		1
3	(McMaster) 9713K53	#4 BELLEVILLE DISC SPRING	Stainless steel	2
4	(UC) BU-406-A	#4-40UNC x 0.375" VENTED BUTTON-HEAD SOCKET CAP SCREW	Ag-plated S/S	2
5	DMBOLO-01-003	APERTURE BACKPLATE	Stainless Steel, 304L	1
6	(McMaster) 92373A103	SPRING PIN, 1/16" DIA. x 3/16" LENGTH	Stainless steel	2
7	(Lenox) HP-3/8-DISC-MLY-100	FOIL APERTURE, 9.5 MM DIAMETER	Molybdenum	1
8	DMBOLO-01-002	DIODE BOX COVER	Stainless Steel, 304L	1
9	DMBOLO-01-004	TUBING ADAPTER	Stainless Steel, 304L	1
10	DMBOLO-01-005	TUBING CLAMP PLATE	Stainless Steel, 304L	1
11	(McMaster) 9713K55	#6 BELLEVILLE DISC SPRING	Stainless steel	6
12	(UC) C-608-A	#6-32UNC x 0.500" VENTED SOCKET CAP SCREW	Ag-plated S/S	6
13	(Pemflex) SL-SS-002	1/8" NOM. SQUARELOK INSTRUMENTATION TUBING		1

REVISION HISTORY			
REV	DESCRIPTION	DATE	APPROVED
0	ISSUED FOR CONSTRUCTION	2011-06-15	RV
1	DIODE BOX COUNTERBORE	2011-07-24	

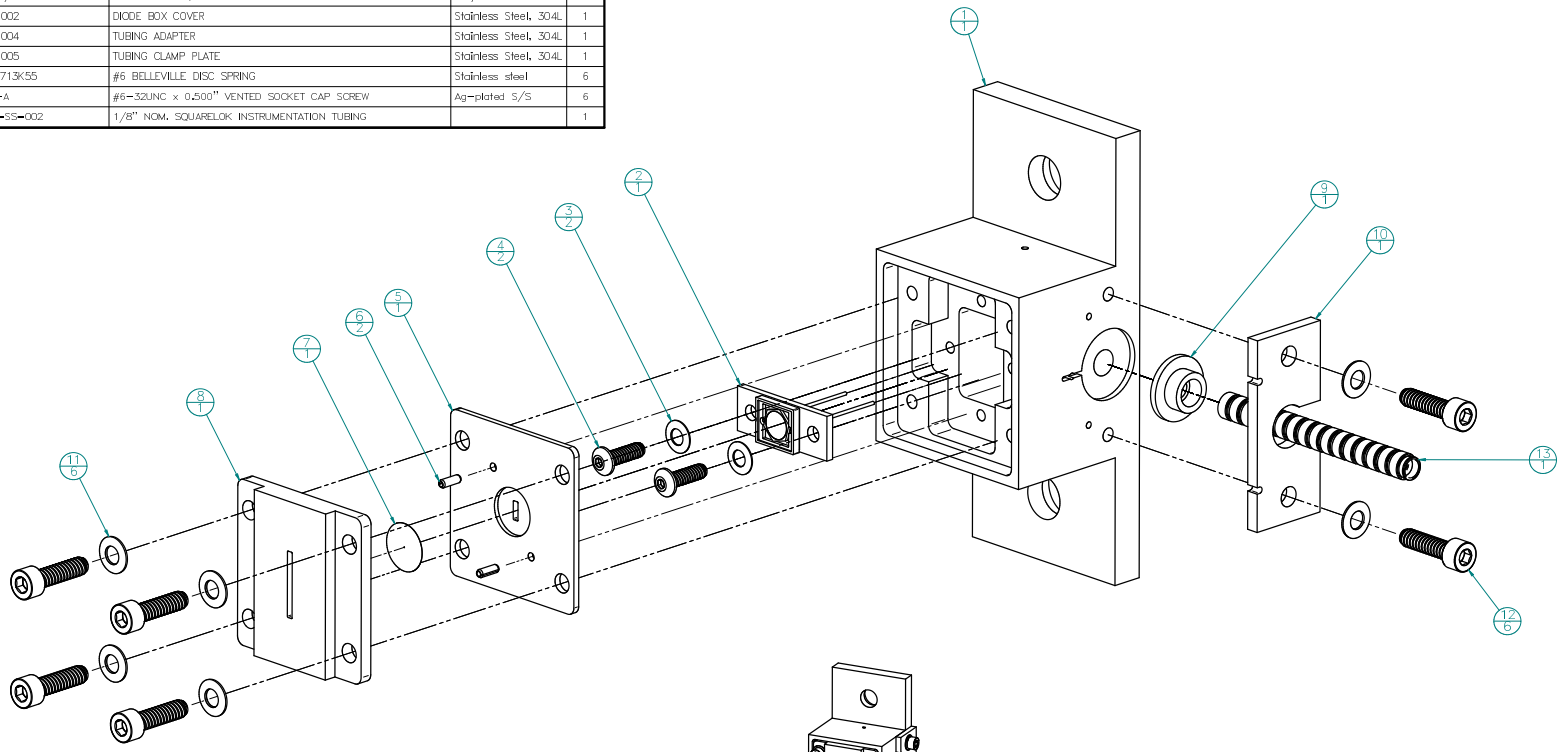

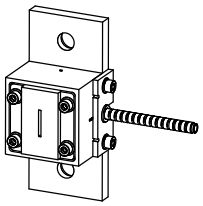

1:1 ASSEMBLED

	NAME	DATE
DRAWN	G. Olynyk	2011-06-08
CHECKED		
APPROVED		

TOLERANCES UNLESS OTHERWISE SPECIFIED
DECIMALS ANGLES ±0°15'
3 PLACES ±.005" SURFACE FINISH 125
2 PLACES ±.010" REMOVE ALL BURRS
1 PLACES ±.100" BREAK SHARP EDGES
DO NOT SCALE DRAWING

PLASMA SCIENCE & FUSION CENTER
MASSACHUSETTS INSTITUTE OF TECHNOLOGY

TITLE: DMBOLO AXUV diode boxes
GENERAL ARRANGEMENT

SIZE: D | DWG NO: DMBOLO-01-000 | REV: 1

FILENAME: DMBOLO-01-000.dft

SCALE: 5:2 | WGT: | SHEET 1 OF 1

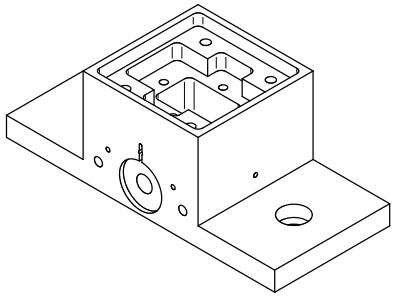

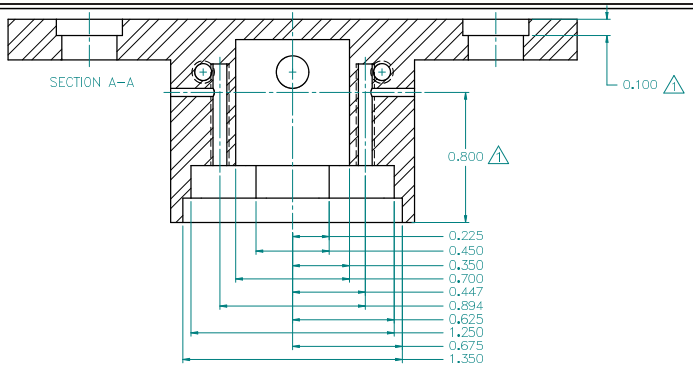

REVISION HISTORY			
REV	DESCRIPTION	DATE	APPROVED
0	ISSUED FOR CONSTRUCTION	2011–06–15	RV
1	TAPPED HOLE DEPTH, LOCATION OF VENT HOLES, MOUNT HOLE DIAMETER AND COUNTERBORE, SURFACE FINISH	2011–07–24	

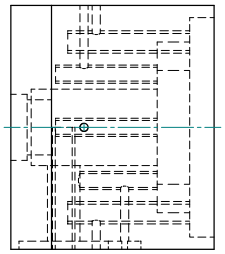

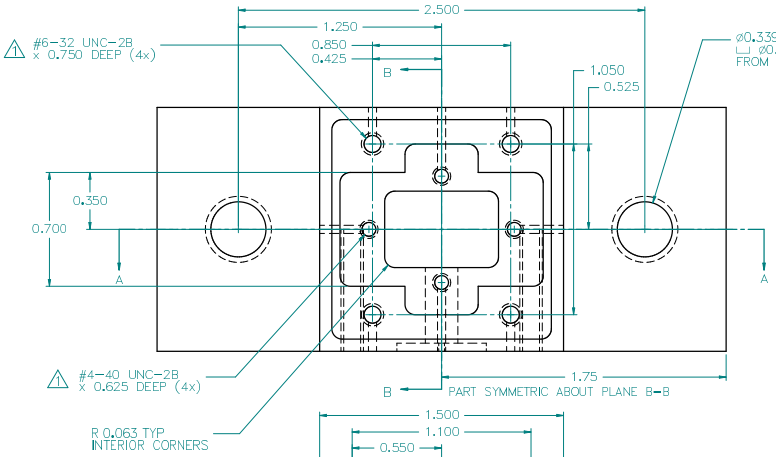

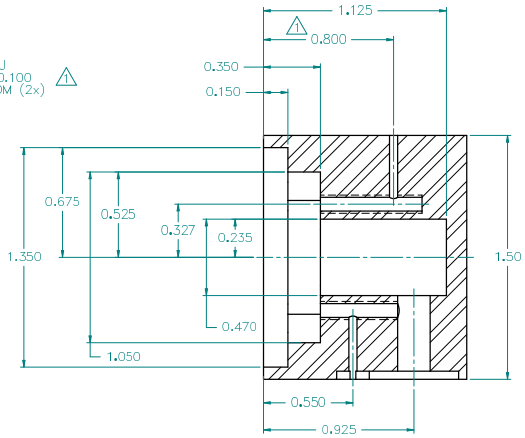

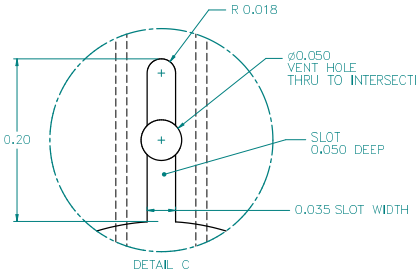

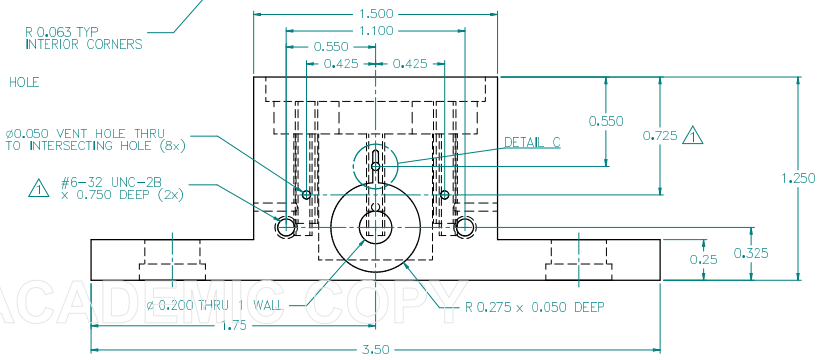

NOTES:
1. MATERIAL: 304L STAINLESS STEEL
2. QUANTITY REQUIRED PER ASSEMBLY: 1

	NAME	DATE
DRAWN	G. Olynyk	2011–06–08
CHECKED		
APPROVED		

TOLERANCES UNLESS OTHERWISE SPECIFIED
DECIMALS ANGLES ±0°15'
3 PLACES ±.005" SURFACE FINISH 125
2 PLACES ±.010" REMOVE ALL BURRS
1 PLACES ±.100" BREAK SHARP EDGES
DO NOT SCALE DRAWING

PLASMA SCIENCE & FUSION CENTER
MASSACHUSETTS INSTITUTE OF TECHNOLOGY

TITLE DMBOLO AXUV diode boxes
DIODE BOX BODY

SIZE D | DWG NO DMBOLO–01–001 | REV 1
FILENAME: DMBOLO–01–001.dft
SCALE: 3:1 | WGT: | SHEET 1 OF 1

REVISION HISTORY			
REV	DESCRIPTION	DATE	APPROVED
0	ISSUED FOR CONSTRUCTION	2011-06-15	RV
1	STANDARD SURFACE FINISH	2011-07-24	

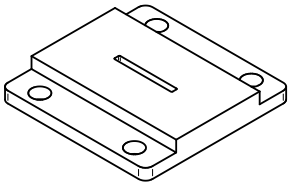

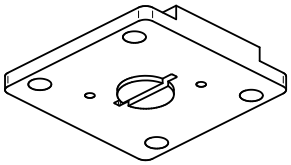

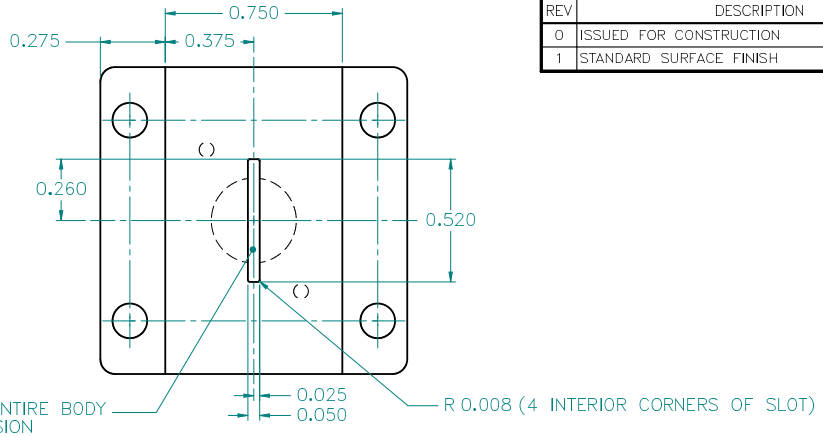

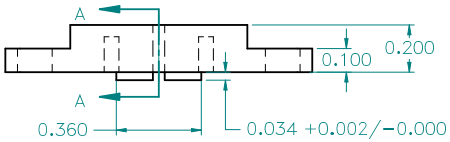

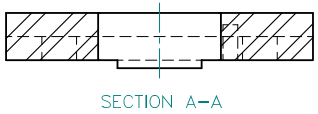

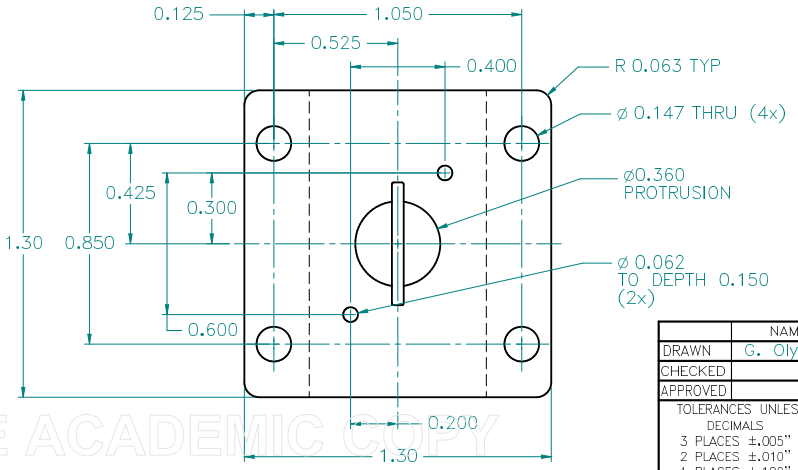

NOTES:
1. MATERIAL: 304L STAINLESS STEEL (1)
2. QUANTITY REQUIRED PER ASSEMBLY: 1

	NAME	DATE
DRAWN	G. Olynyk	2011-06-08
CHECKED		
APPROVED		

TOLERANCES UNLESS OTHERWISE SPECIFIED
DECIMALS — ANGLES ±0°15'
3 PLACES ±.005" — SURFACE FINISH 125
2 PLACES ±.010" — REMOVE ALL BURRS
1 PLACES ±.100" — BREAK SHARP EDGES
DO NOT SCALE DRAWING

PLASMA SCIENCE & FUSION CENTER
MASSACHUSETTS INSTITUTE OF TECHNOLOGY

TITLE DMBOLO AXUV diode boxes
DIODE BOX COVER

SIZE	DWG NO	REV
C	DMBOLO-01-002	1

FILENAME: DMBOLO-01-002.dft

SCALE: 3:1 | WGT: 1.2 oz | SHEET 1 OF 1

REVISION HISTORY			
REV	DESCRIPTION	DATE	APPROVED
0	ISSUED FOR CONSTRUCTION	2011-06-15	RV
1	STANDARD SURFACE FINISH	2011-07-24	

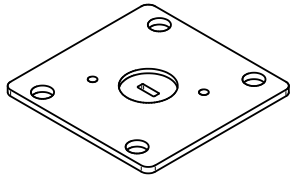

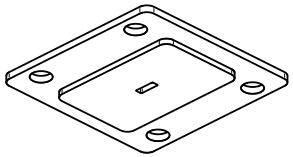

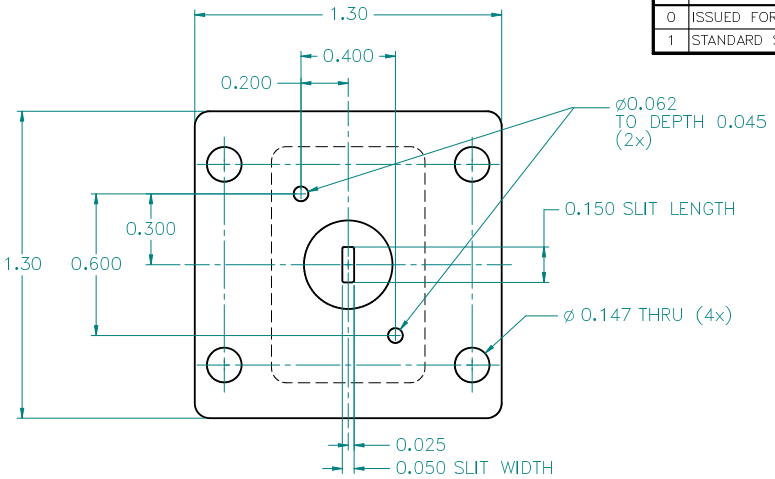

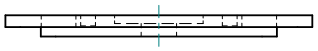

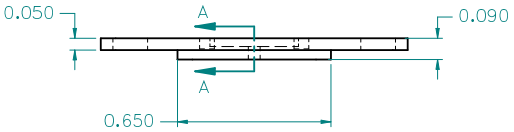

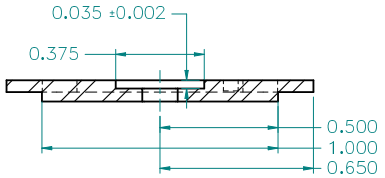

SECTION A–A

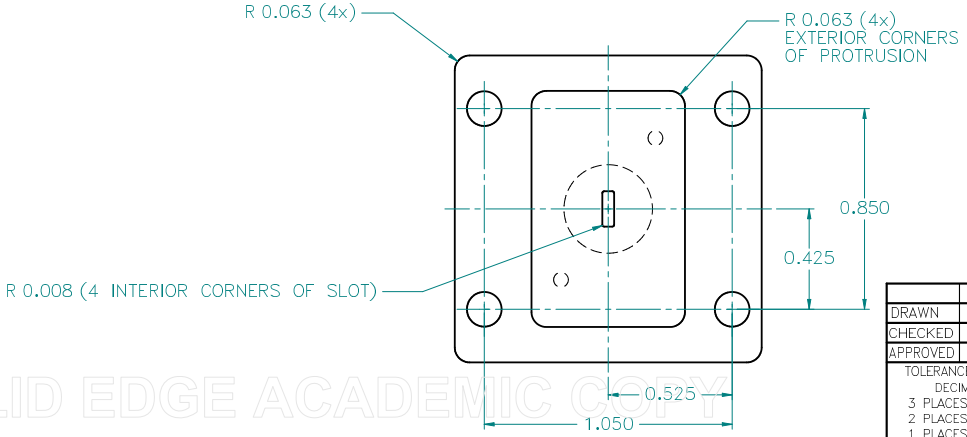

NOTES:
1. MATERIAL: 304L STAINLESS STEEL
2. QUANTITY REQUIRED PER ASSEMBLY: 1

	NAME	DATE
DRAWN	G. Olynyk	2011-06-08
CHECKED		
APPROVED		

TOLERANCES UNLESS OTHERWISE SPECIFIED
DECIMALS — ANGLES ±0°15'
3 PLACES ±.005" — SURFACE FINISH 125
2 PLACES ±.010" — REMOVE ALL BURRS
1 PLACES ±.100" — BREAK SHARP EDGES
DO NOT SCALE DRAWING

PLASMA SCIENCE & FUSION CENTER
PSFC MASSACHUSETTS INSTITUTE OF TECHNOLOGY MIT

TITLE DMBOLO AXUV diode boxes
APERTURE BACKPLATE

SIZE	DWG NO	REV
C	DMBOLO-01-003	1

FILENAME: DMBOLO-01-003.dft

SCALE: 3:1 | WGT: 0.48 oz | SHEET 1 OF 1

REVISION HISTORY			
REV	DESCRIPTION	DATE	APPROVED
0	ISSUED FOR CONSTRUCTION	2011-06-15	RV
1	STANDARD SURFACE FINISH	2011-07-24	

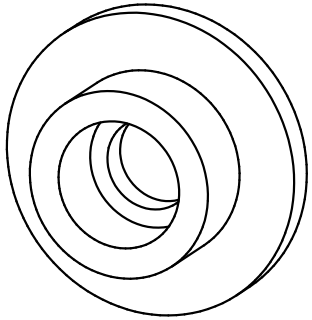

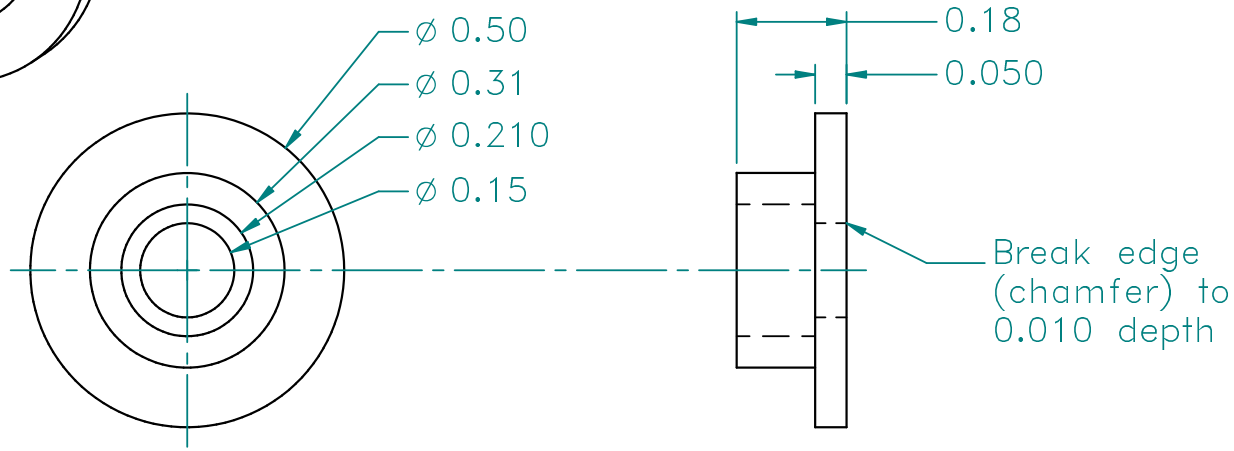

NOTES:
1. MATERIAL: 304L STAINLESS STEEL
2. QUANTITY REQUIRED PER ASSEMBLY: 1

	NAME	DATE
DRAWN	G. Olynyk	2011-06-08
CHECKED		
APPROVED		

TOLERANCE UNLESS OTHERWISE SPEC'D
DECIMALS
3 PLACES ±.005"
2 PLACES ±.010"
1 PLACES ±.100"
ANGLES ±0°15'
SURFACE FINISH 125
REMOVE ALL BURRS
BREAK SHARP EDGES
DO NOT SCALE DRAWING

PLASMA SCIENCE & FUSION CENTER
PSFC MASSACHUSETTS INSTITUTE OF TECHNOLOGY MIT

TITLE DMBOLO AXUV diode boxes
TUBING ADAPTER

SIZE	DWG NO	REV
A	DMBOLO-01-004	1

FILENAME: DMBOLO-01-004.dft

SCALE: 4:1 | WGT: 0.06 oz | SHEET 1 OF 1

REVISION HISTORY			
REV	DESCRIPTION	DATE	APPROVED
0	ISSUED FOR CONSTRUCTION	2011-06-15	RV
1	STANDARD SURFACE FINISH	2011-07-24	

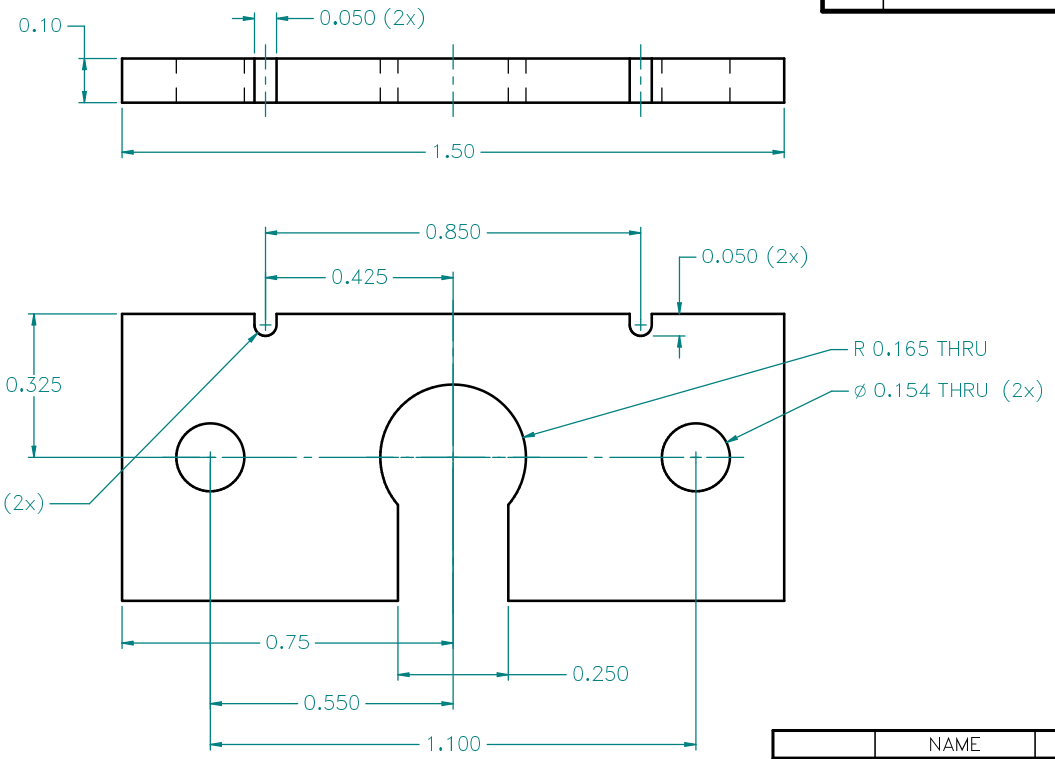

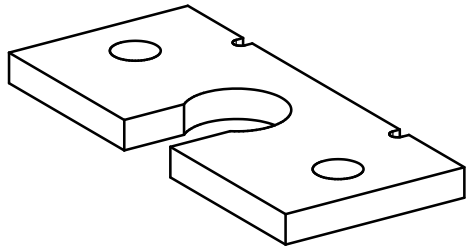

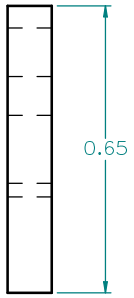

NOTES:
1. MATERIAL: 304L STAINLESS STEEL
2. QUANTITY REQUIRED PER ASSEMBLY: 1

	NAME	DATE
DRAWN	G. Olynyk	2011-06-08
CHECKED		
APPROVED		

TOLERANCES UNLESS OTHERWISE SPECIFIED
DECIMALS
3 PLACES ±.005"
2 PLACES ±.010"
1 PLACES ±.100"
ANGLES ±0°15'
SURFACE FINISH 125
REMOVE ALL BURRS
BREAK SHARP EDGES
DO NOT SCALE DRAWING

PLASMA SCIENCE & FUSION CENTER
PSFC MASSACHUSETTS INSTITUTE OF TECHNOLOGY MIT

TITLE DMBOLO AXUV diode boxes
TUBING CLAMP PLATE

SIZE	DWG NO	REV
B	DMBOLO-01-005	1

FILENAME: DMBOLO-01-005.dft

SCALE: 4:1 | WGT: 0.37 oz | SHEET 1 OF 1

PARTS LIST (PER ASSEMBLY)				
ITEM	PART NUMBER	DESCRIPTION	MATERIAL	QTY
1	(Accu-Glass) 6-100186	CF 3.375 WITH 3-PIN D-TYPE COAXIAL FEEDTHROUGH	S/S 304	1
2	(McMaster) 9713K58	#10 BELLEVILLE DISC SPRING	S/S 18/8	4
3	DMBOLO-02-001	SMA BULKHEAD STANDOFF	S/S 304L	4
4	(McMaster) 92141A008	#6 GENERAL PURPOSE WASHER	S/S 18/8	8
5	DMBOLO-02-002	SMA BULKHEAD MOUNT PLATE	MACOR	1
6	(McMaster) 92320A031	#6 UNTHREADED SPACER, 1/4" OD, 5/32" LG	S/S 18/8	4
7	(McMaster) 92161A024	#6 TRIPLE-WAVE WASHER	S/S 18/8	4
8	(UC) C-608-A	#6-32UNC x 0.500" VENTED SOCKET CAP SCREW	AG-PLATED S/S	4

REVISION HISTORY			
REV	DESCRIPTION	DATE	APPROVED
0	ISSUED FOR CONSTRUCTION	2011-07-20	RV

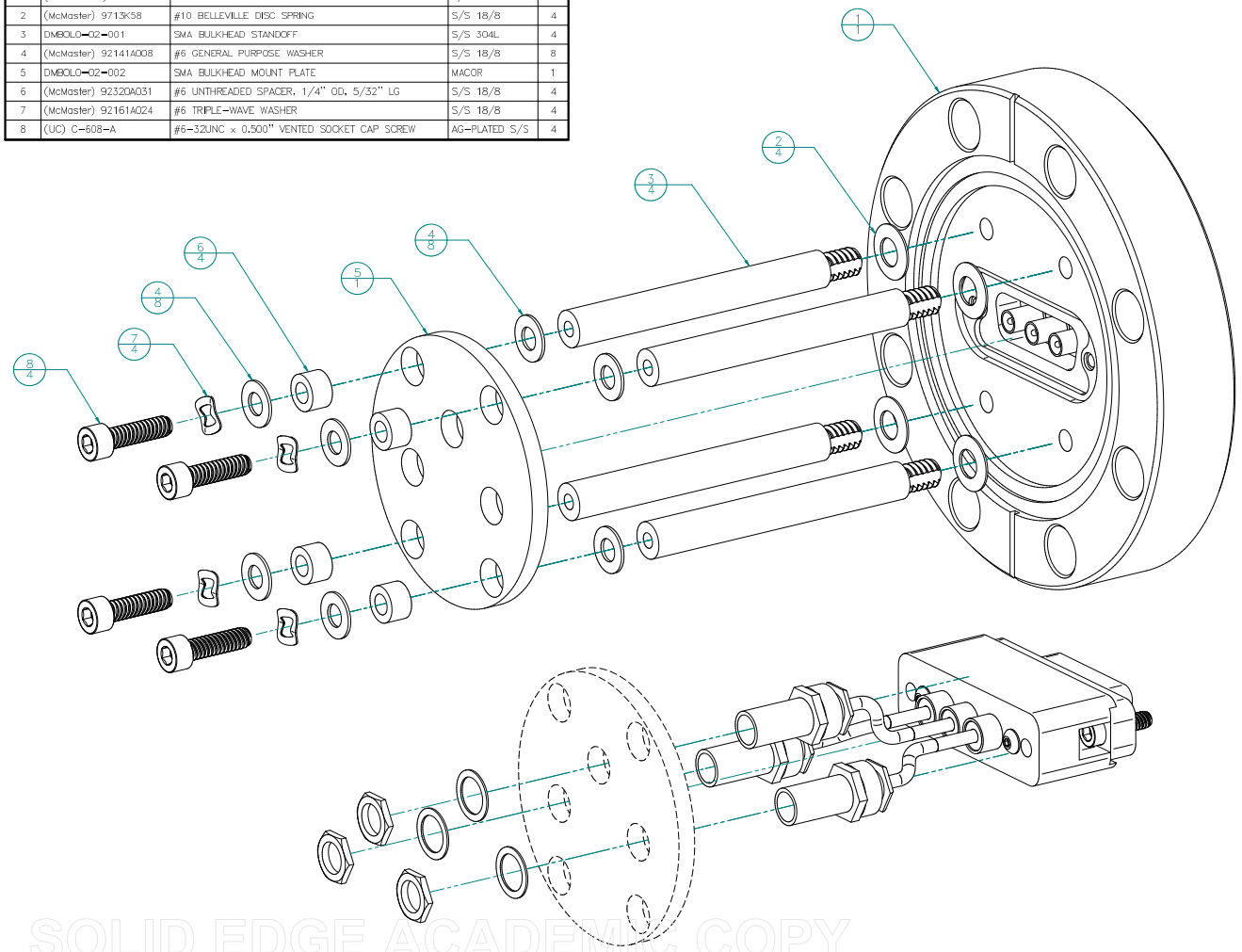

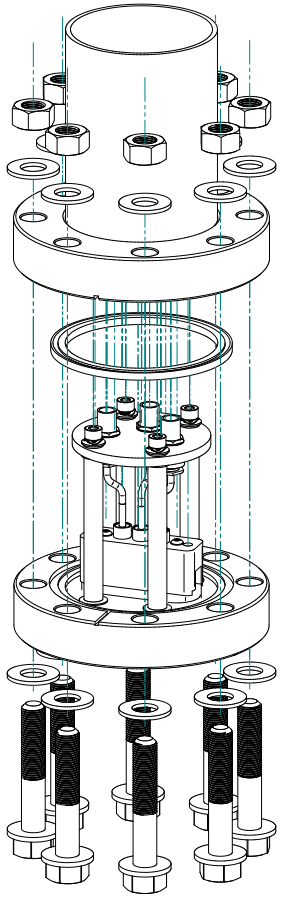

ELECTRICAL ASSEMBLY

	NAME	DATE
DRAWN	GMO	2011-07-14
CHECKED		
ENG APPR.		
MGR APPR.		

UNLESS OTHERWISE SPECIFIED
DIMENSIONS ARE IN INCHES
ANGLES ±0°15'
2 PL ±0.010" 3 PL ±0.005"

Plasma Science and Fusion Center
Massachusetts Institute of Technology

TITLE: DMBOLO triple vacuum feedthrough
GENERAL ARRANGEMENT

SIZE: D | DWG NO: DMBOLO-02-000 | REV: 0

FILENAME: DMBOLO-02-000.dft

SCALE: | WGT: | SHEET 1 OF 1

REVISION HISTORY			
REV	DESCRIPTION	DATE	APPROVED
0	ISSUED FOR CONSTRUCTION	2011-07-20	RV

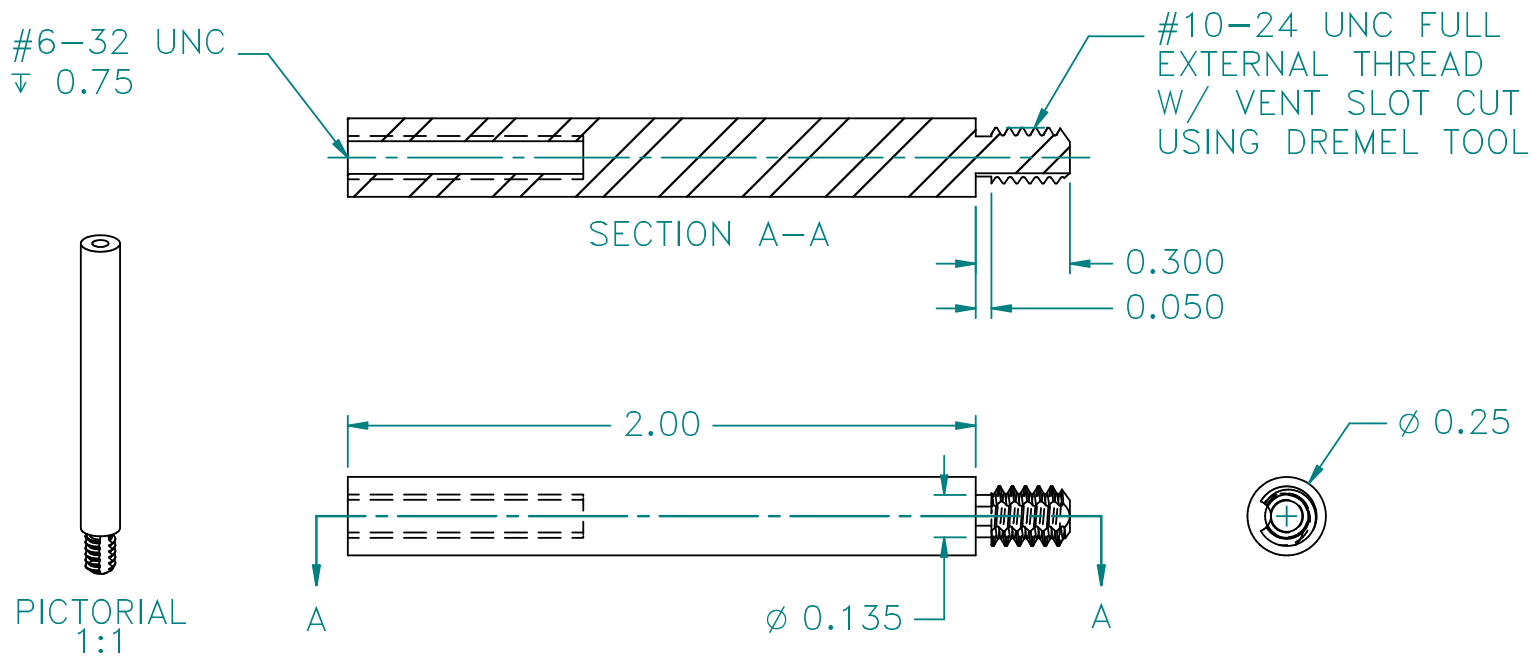

NOTES:

1. MATERIAL: 304L STAINLESS STEEL
2. REMOVE ALL BURRS & SHARP EDGES
3. QUANTITY REQUIRED PER ASSEMBLY: 4
4. UNLESS OTHERWISE SPECIFIED, ALL SURFACES 125

	NAME	DATE
DRAWN	GMO	2011-06-21
CHECKED		
ENG APPR		
MGR APPR		

UNLESS OTHERWISE SPECIFIED
DIMENSIONS ARE IN INCHES
ANGLES ±0°15'
2 PL ±0.010" 3 PL ±0.005"

Plasma Science and Fusion Center
Massachusetts Institute of Technology

TITLE DMBOLO triple vacuum feedthrough
SMA BULKHEAD STANDOFF

SIZE	DWG NO	REV
A	DMBOLO-02-001	0

FILENAME: DMBOLO-02-001.dft

SCALE: 2:1 WGT: 0.5 oz SHEET 1 OF 1

REVISION HISTORY			
REV	DESCRIPTION	DATE	APPROVED
0	ISSUED FOR CONSTRUCTION	2011-07-20	RV

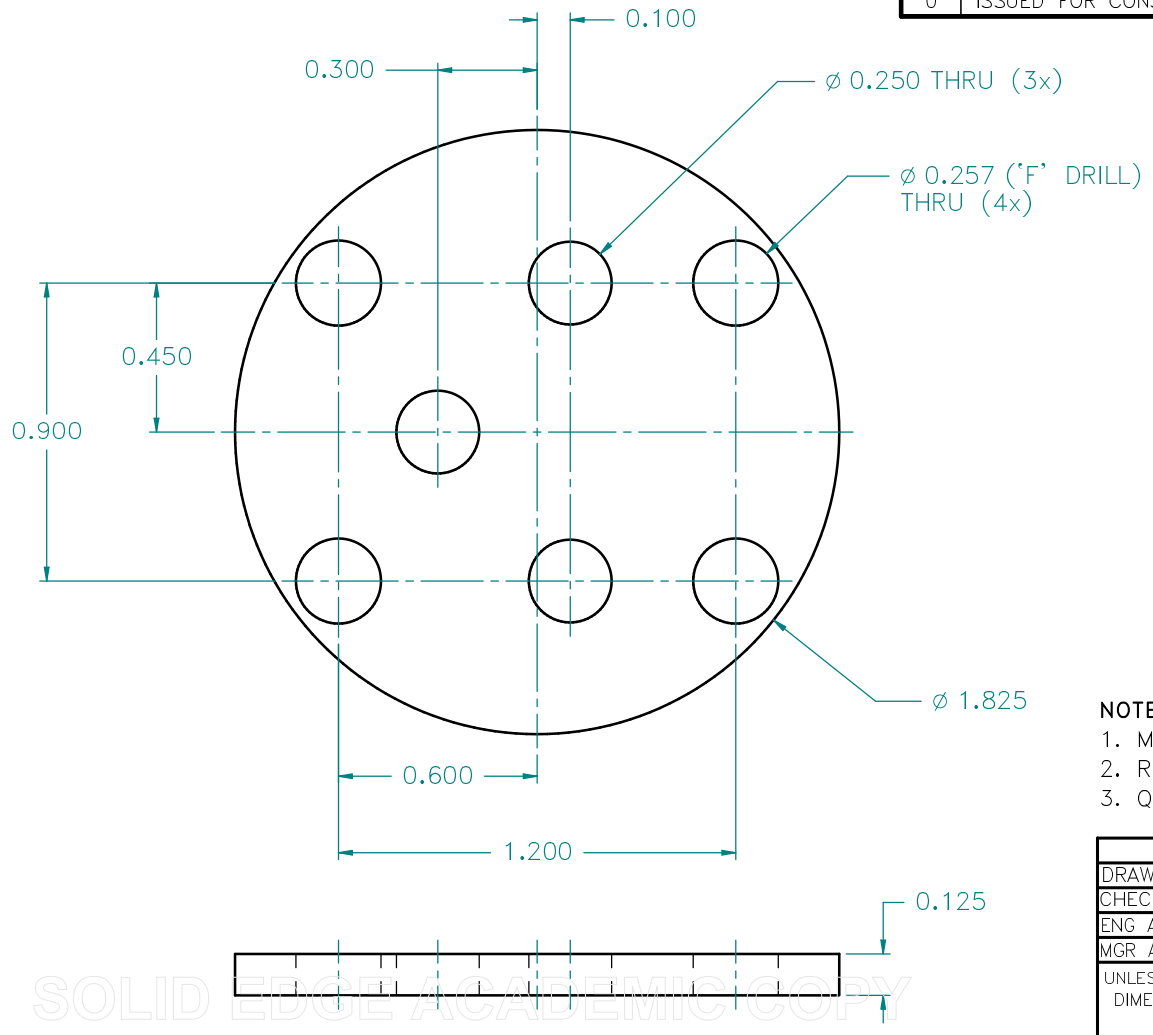

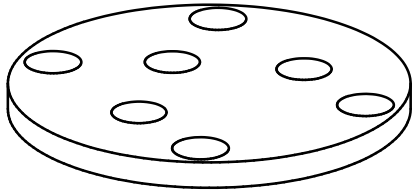

NOTES:

1. MATERIAL: **MACOR** MACHINABLE GLASS CERAMIC
2. REMOVE ALL BURRS & SHARP EDGES
3. QUANTITY REQUIRED PER ASSEMBLY: 1

	NAME	DATE
DRAWN	GMO	2011-07-07
CHECKED		
ENG APPR		
MGR APPR		

UNLESS OTHERWISE SPECIFIED
DIMENSIONS ARE IN INCHES
ANGLES ±0°15'
2 PL ±0.010" 3 PL ±0.005"

Plasma Science and Fusion Center
Massachusetts Institute of Technology

TITLE DMBOLO triple vacuum feedthrough
SMA BULKHEAD MOUNT PLATE

SIZE	DWG NO	REV
B	DMBOLO-02-002	0

FILENAME: DMBOLO-02-002.dft

SCALE: 3:1 | WGT: | SHEET 1 OF 1

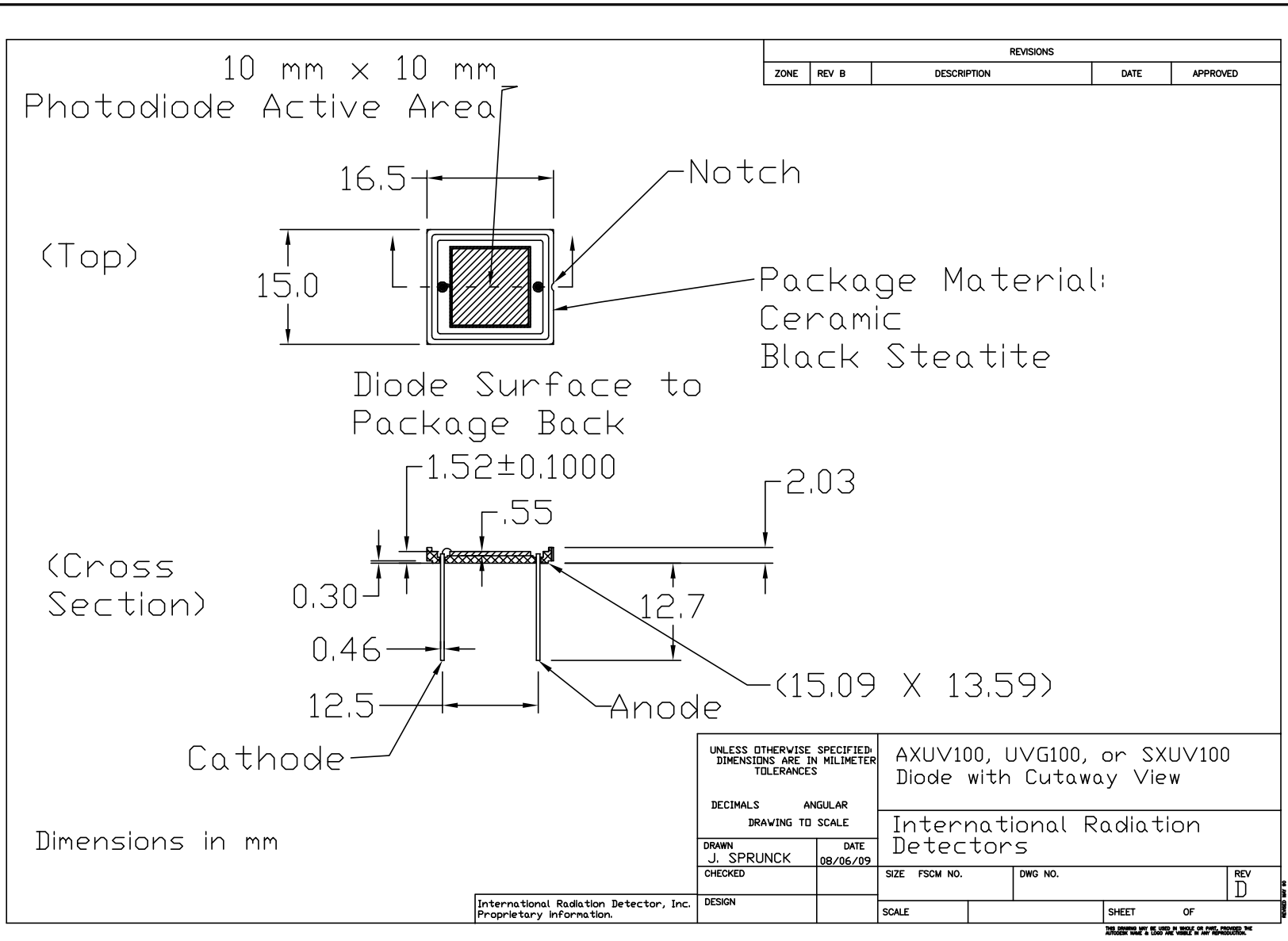
REVISIONS
ZONE
REV B
DESCRIPTION
DATE
APPROVED
10 mm x 10 mm
Photodiode Active Area
16.5
Notch
(Top)
15.0
Package Material:
Ceramic
Black Steatite
Diode Surface to
Package Back
1.52±0.1000
.55
2.03
(Cross
Section)
0.30
12.7
0.46
(15.09 X 13.59)
12.5
Anode
Cathode
Dimensions in mm
UNLESS OTHERWISE SPECIFIED:
DIMENSIONS ARE IN MILIMETER
TOLERANCES
DECIMALS
ANGULAR
DRAWING TO SCALE
DRAWN
J. SPRUNCK
DATE
08/06/09
CHECKED
DESIGN
AXUV100, UVG100, or SXUV100
Diode with Cutaway View
International Radiation
Detectors
SIZE
FSCM NO.
DWG NO.
REV
D
SCALE
SHEET
OF
International Radiation Detector, Inc.
Proprietary information.

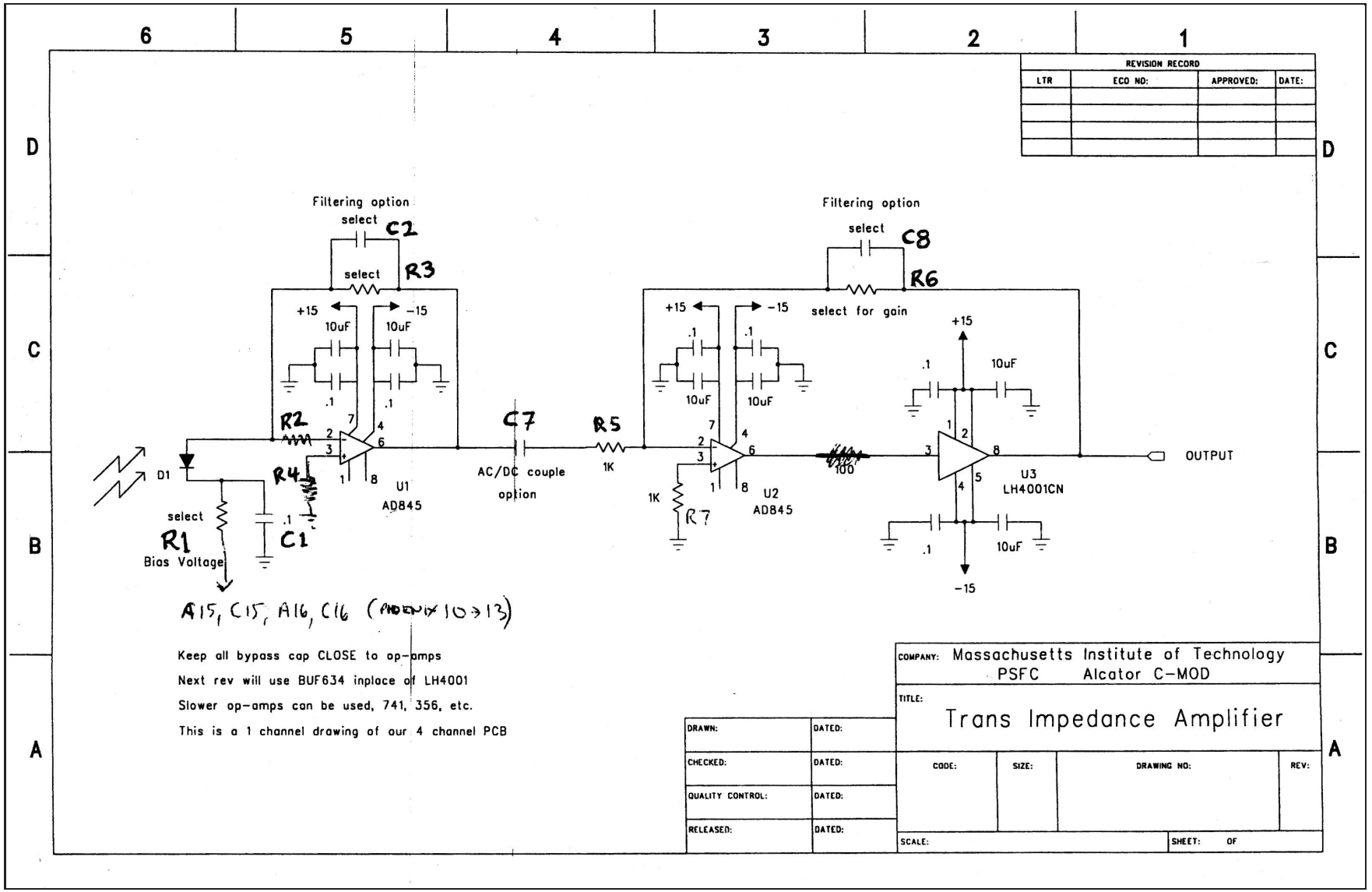
6
5
4
3
2
1
D
C
B
A
REVISION RECORD
LTR
ECO NO:
APPROVED:
DATE:
Filtering option
select
C2
select
R3
+15
-15
10uF
10uF
.1
.1
R2
R4
D1
select
R1
Bias Voltage
C1
.1
U1
AD845
C7
AC/DC couple
option
R5
1K
Filtering option
select
C8
R6
select for gain
+15
-15
.1
.1
10uF
10uF
1K
R7
U2
AD845
100
+15
.1
10uF
U3
LH4001CN
.1
10uF
-15
OUTPUT
A15, C15, A16, C16 (Appendix 10-13)
Keep all bypass cap CLOSE to op-amps
Next rev will use BUF634 inplace of LH4001
Slower op-amps can be used, 741, 356, etc.
This is a 1 channel drawing of our 4 channel PCB
COMPANY: Massachusetts Institute of Technology
PSFC Alcator C-MOD
TITLE:
Trans Impedance Amplifier
DRAWN:
DATED:
CHECKED:
DATED:
QUALITY CONTROL:
DATED:
RELEASED:
DATED:
CODE:
SIZE:
DRAWING NO:
REV:
SCALE:
SHEET: OF